MAGNETIC-FIELD-RESILIENT TRANSMONS FOR TOPOLOGICAL QUANTUM COMPUTATION

Inaugural-Dissertation

zur Erlangung des Doktorgrades
der Mathematisch-Naturwissenschaftlichen Fakultät
der Universität zu Köln

vorgelegt von

Jonas KRAUSE

Master of Science (ETH) in Physik,
Eidgenössische Technische Hochschule Zürich, Schweiz,
geboren in Nürtingen, Deutschland.

Köln, 2024

Composition of the doctoral committee:

Prof. Dr. Simon Trebst,	Universität zu Köln, chairperson
Prof. Dr. Yoichi Ando,	Universität zu Köln, advisor & reviewer
Prof. Dr. Erwann Bocquillon,	Universität zu Köln, reviewer

Accepted by the Faculty of Mathematics and Natural Sciences of the University of Cologne. Defended on September 10, 2024.

CONTENTS

SUMMARY

Topological quantum computation based on Majorana zero modes (MZMs) offers inherent fault tolerance for a discrete set of logical gate operations, which may help to reduce the overhead of quantum error correction in future quantum computing platforms. However, the unambiguous detection of MZMs proves to be notoriously difficult due to a complex interplay of superconductors and semiconductor or topolological-insulator materials with magnetic fields. Circuit QED (cQED) in turn offers well-established dispersive readout and control techniques that couple coherent resonator states containing many photons to single quanta in a superconducting circuit and provide quantum-non-demolition, single-shot measurements with high signal-to-noise ratio. The cQED platform is moreover very versatile and can accomodate any low-loss materials and nanostructures to form hybrid devices. Integrating topological-superconductor platforms that are predicted to host MZMs to superconducting circuits is therefore a promising route to hunting down the elusive Majorana fermions. In particular, the transmon circuit can couple to the fermion parity of a topological qubit based on MZMs. Transmons can resolve charge dynamics in the circuit with sub-microsecond resolution and their spectrum is modified significantly when MZMs couple via the transmon's Josephson junction (JJ). Moreover, the integration of topological qubits to transmon circuits can enable universal quantum computation with MZMs by complementing the discrete topologically protected gate operations with near-fermion-parity-protected gate operations.

A challenge to overcome, however, is that the generation of MZMs typically requires the readout circuit to sustain relatively large magnetic fields. Transmons based on conventional Al/AlO_x/Al JJs are usually operated in a setting that is well-shielded from magnetic fields, and prior to this work the use of unconventional JJs such as JJs based on Graphene or semiconductor nanowires has been put forward for magnetic-field resilience. The latter types of JJs typically suffer from poor coherence and low control over their fabrication, however. This thesis therefore investigates to what extent transmons based on Al/AlO_x/Al JJs can serve for readout and control of future Majorana qubits. To this end, the magnetic-field dependence of spectrum and coherence times as well as the parity-switching time of aluminum transmons is measured. The measured devices are designed for enhanced magnetic field compatibility: Thin bottom and top aluminum layers of nominally 10 nm and 18 nm, respectively, give high critical fields, narrow leads to the JJ minimize vortex losses and the transmons are placed in a three-dimensional copper cavity resonator, which is unaffected even by strong magnetic fields.

As a result, both single-JJ and SQUID transmons can be operated coherently in parallel magnetic fields $B_\parallel$ approaching 1 T with microsecond lifetimes over the entire measurable range. To preserve coherence, accurate in-plane alignment of the magnetic field is paramount. The magnetic-field-dependence of the energy spectrum is described by a combination of gap suppression and a Fraunhofer-like modulation of the junction's critical current, both of which lead to a decrease in the transmon's Josephson energy E_J. With decreasing E_J/E_C-ratio, where E_C is the transmon's charging energy, the transmons become more and more susceptible to charge noise. Also flux noise increases with magnetic field, likely due to vibrations of the sample with respect to the magnet. The parity-switching time τ_p of a SQUID transmon is measured in parallel magnetic fields up to 0.41 T, with a limited suitable range of

E_J/E_C-ratios and an instability at the top flux sweetspot of the SQUID limiting further measurements. Measurements of the temperature dependence of τ_p at selected values of $B_\parallel$ complement the data. Using a comprehensive model that consistently describes both the field and temperature dependence of τ_p we demonstrate that the superconducting-gap asymmetry between top and bottom aluminum layer plays a crucial role in the observed non-monotonic behavior of τ_p. Besides giving a deeper insight into the parity-switching mechanisms in conventional transmon qubits, the measurements presented in this thesis establish that Al/AlO_x/Al JJs can be used in architectures for the parity-readout and manipulation of topological qubits based on MZMs.

The long-term goal being the integration of MZMs to magnetic-field-resilient transmons then, transmons based on topological-insulator (TI) nanowire JJs are investigated in a parallel reseach effort. All TI-based transmon devices tested so far suffer from heavy microwave losses and do not achieve the strong coupling limit. Instead, the transmons act as a sink for resonator photons leading to a drastic reduction of the cavity Q-factor upon resonance via the inverse Purcell decay. This prevents unambiguous spectroscopic measurements of the transmon frequencies, let alone time-domain measurements of the transmon coherence times. Likely a soft induced gap in the TI allows for unproximitized resistive channels in parallel to the supercurrent-carrying channels. To mitigate and avoid the observed losses, alternative device designs are put forward that may profit from an in-situ fabricated interface between superconductor and TI or rely on a weak coupling of MZMs via a nearby Al/AlO_x/Al JJ.

1

MAGNETIC-FIELD-RESILIENT TRANSMONS FOR TOPOLOGICAL QUANTUM COMPUTATION

This introductory chapter outlines the evolution of concepts in topological quantum computation and circuit QED (cQED) with a focus on their connection: the detection and manipulation of Majorana zero modes (MZMs) using magnetic-field-resilient transmon circuits. Morover, the chapter defines quality criteria for transmon circuits to be met such that they can actually be useful for the study of MZMs. Against this background, the specific research questions driving this work are discussed.

1

While quantum processors based on superconducting circuits, trapped ions and neutral atoms are reaching qubit numbers > 100 and single-qubit gate fidelities > 99.9%, the quest for a noise-resilient and scalable platform for quantum computing is ongoing. Local noise at the level of a single qubit quickly accumulates with more and more interconnected qubits, ultimately preventing robust quantum information processing and creating the need for quantum error correction. Instead, topological quantum computing based on braiding of non-abelian anyons may offer a platform inherently protected from local noise thus reducing the overhead of quantum error correction. Among the most prominently discussed possible realizations of non-abelian anyons are Majorana zero-modes (MZMs) forming in topological-superconductor devices. However, at the time of writing this thesis, there is no unambiguous evidence for the observation of MZMs, let alone for their braiding. Readout and control of MZMs require complex devices and the required interplay of superconductors and semiconductor or topolological-insulator materials with magnetic fields proves to be notoriously hard to handle and understand. The research presented in this thesis aims to facilitate further progress by establishing the cQED readout protocol for MZMs using magnetic-field-resilient transmon circuits. The introductory chapter starts out with a review of fundamental concepts to summarize the state of the field. This will set the stage for further specification of the research problem addressed in this thesis and gives rise to the precise formulation of research aims, objectives and questions, the significance and finally, the limitations.

1.1. MAJORANA ZERO MODES FOR QUANTUM COMPUTATION

When Kitaev proposed that non-abelian anyonic excitations of a two-dimensional quantum system can be used for fault-tolerant quantum computation [1] he sparked huge interest in the physical realization of such peculiar excitations. A promising solid-state realization of non-abelian anyons are Majorana zero modes (MZMs) forming at phase boundaries or defects of topological superconductors, i.e. effectively spinless superconductors with p-wave pairing symmetry. Here, research first focussed on fractional quantum hall systems and intrinsic $p_x + ip_y$-wave superconductors [2], but the former proved to be hard to control experimentally and the latter seems to be exceedingly rare in nature and sensitive to disorder [3]. It was as a breakthrough, therefore, when Fu and Kane realized that is is possible to engineer an effectively spinless superconducting phase resembling intrinsic $p_x + ip_y$-wave superconductors: the two-dimensional surface states of a 3D topological insulator support topological superconductivity when being proximitized with an ordinary s-wave superconductor and should therefore support MZMs at vortices [4]. This idea did not only fuel reseach in topological insulators, but also inspired proposals to alternatively proximitize two-dimensional semiconductor quantum wells with strong spin-orbit coupling with s-wave superconductors, also resulting in topological superconductivity [5, 6]. Looking for an experimentally even more accessible platform, Oreg [7] and Lutchyn [8] proposed to proximitize semiconductor nanowires instead, effectively realizing Kitaevs toy model of a topological quantum wire hosting MZMs at its ends [9]. Cook and Franz then re-transferred the idea of topological quantum wires back to the realm of topological insulators, showing that the quantized surface states of a topological-insulator nanowire support topological superconductivity when the nanowire is pierced by a magnetic flux and proximitized with an ordinary s-wave superconductor [10]. In our lab, we focus on topological-

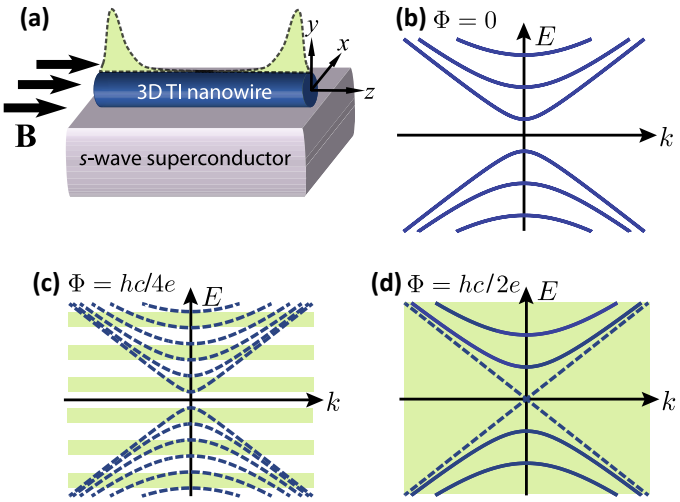

Figure 1.1: Illustration of the Cook and Franz proposal. **(a)** A 3D topological-insulator (TI) nanowire is proximity-coupled to an ordinary *s*-wave superconductor and threaded by a magnetic field B parallel to the wire. **(b)** At zero field, the spectrum of the TI surface states consists of doubly-degenerate subbands (solid lines), which **(c)** start to split into non-degenerate bands (dashed lines) with increasing magnetic flux. If the chemical potential lies within in the green shaded regions an odd number of bands is occupied and topological superconductivity may be induced, resulting in localized Majorana zero modes (MZMs) at the wire ends (see panel **(a)**). **(d)** For half a flux quantum an odd number of surface state bands is occupied for any chemical potential in the bulk band gap. Figure adapted from [3].

insulator platforms for MZMs. Figure 1.1 shows a schematic of the platform proposed by Cook and Franz, as well as its surface-state spectrum.

Many of the aforementioned proposals require in-plane magnetic fields on the order of several hundreds of mT to realize a topological superconducting phase. The trick is to overcome the "fermion doubling problem" [3] and freeze out the spin degree of freedom, such that the electronic states that are to be proximitized become effectively spinless. For instance, in the case of a topological-insulator nanowire, the magnetic field lifts the spin degeneracy of the subbands enabling an effectively spinless regime (see Fig. 1.1 **(b)**-**(d)**). In the case of semiconductor platforms the magnetic field induces a Zeeman-gap to the spin-orbit-split bands, which breaks time-reversal symmetry [6, 8]. Coupling to ferromagnetic insulators is considered in Ref. [5] instead, but from an experimental point of view an external magnetic field is advantageous: First, it avoids possible complications due to to an additional interface between the ferromagnetic insulator and the topological superconductor. Second, it provides an experimental tuning knob to tune in and out of the topological regime in-situ, faciltating targeting and identification of the topologically non-trivial phase. However, the applied external magnetic field also requires magnetic-field resilience of the readout and control circuitry. This is one of the main drivers of this thesis.

Before coming to the readout and control circuitry for MZMs it is helpful to briefly summarize some basic ideas of topological quantum computation based on MZMs, agnostic of their physical realization. A fermionic annihilation (creation) operator f ($f^\dagger$) can be expressed in terms of two potentially well separated MZMs γ_1 and γ_2, reading $f = \gamma_1 + i\gamma_2$ ($f^\dagger = \gamma_1 - i\gamma_2$). A pair of MZMs hence forms a two-level system: it can be occupied by an eletron or not. If the MZMs are well separated, the occupation comes at zero energy cost as the corresponding fermionic creation operator does not enter the system's Hamiltonian [9]. The groundstate of a superconductor with a single pair of MZMs is therefore two-fold degenerate, allowing for an

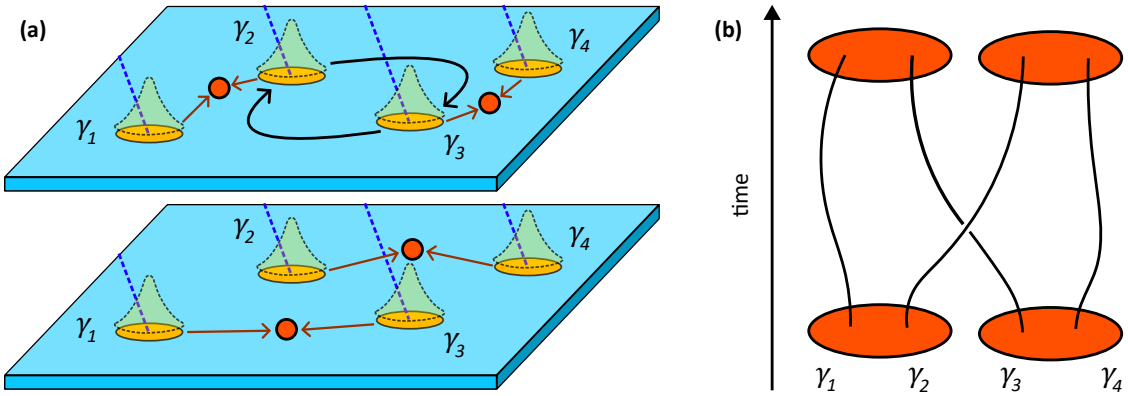

Figure 1.2: Schematic illustrating a topological quantum computation. **(a)** Two pairs (γ_1, γ_2) and (γ_3, γ_4) can each host a zero-energy fermion (red circle). Single qubit gates can be realized by braiding, i.e. a particle exchange of two MZMs either by physically moving them around each other (upper panel) or by changing the measurement basis to (γ_1, γ_3) and (γ_2, γ_4) (lower panel). **(b)** The world lines of the exchange operation are the same in both cases and give the braiding operation its characteristic name.

even (Cooper-pairs only) or an odd (Cooper-pairs plus occupied pair of MZMs) number of zero-energy fermions. However, the parity of the number of zero-energy fermions in a topological superconductor is conserved; to change it zero-energy fermions "have to be physically added to or removed from the superconductor" [11]. Consequently, a single pair of MZMs cannot form a topological qubit as its state would be fixed by the conservation of fermion parity.

The simplest form of a topological qubit involves two pairs of MZMs (see Fig. 1.2). Each pair can host one zero-energy electron and for even fermion parity of the superconductor the qubit's basis states are $|00\rangle$ and $|11\rangle$, i.e. both pairs unoccupied and both pairs occupied, respectively. For odd fermion parity, the basis states are $|10\rangle$ and $|01\rangle$, i.e. either one pair is occupied or the other. Without loss of generality, the remainder of this introduction pursues the case of two pairs of MZMs with a total even fermion parity. The topological qubit's state then reads

$$|\psi\rangle = \alpha\,|00\rangle + \beta\,|11\rangle\,, \tag{1.1}$$

with $|\alpha|^2 + |\beta|^2 = 1$.

Single qubit gates can be realized by braiding. Braiding is the particle exchange of two MZMs in a two-dimensional plane, or two-dimensional grid of nanowires. Being non-abelian anyons, the annihilation and creation operators of MZMs obey

$$\gamma_i = \gamma_i^\dagger \tag{1.2}$$

$$\{\gamma_i, \gamma_j\} = 2\delta_{ij} \tag{1.3}$$

and hence exchanging MZMs from the same basis pair (e.g. braiding γ_1 and γ_2 in Fig. 1.2) applies a phase factor [12]

$$|00\rangle \longrightarrow e^{i\pi/4}\,|00\rangle \tag{1.4}$$

$$|11\rangle \longrightarrow e^{-i\pi/4}\,|11\rangle\,. \tag{1.5}$$

Exchanging an MZM of one of the basis pairs of MZMs with an MZM of the other one, i.e.

braiding γ_2 and γ_3 in Fig. 1.2, can be used for bit-flip operations:

$$|00\rangle \longrightarrow \frac{1}{\sqrt{2}}(|00\rangle + i\,|11\rangle) \tag{1.6}$$

$$|11\rangle \longrightarrow \frac{1}{\sqrt{2}}(-i\,|00\rangle + |11\rangle)\,. \tag{1.7}$$

There are two striking features of these operations [2]: First, unlike gate operations on conventional qubit systems braiding is an operation that only allows for digital errors: Either the MZMs are exchanged, or they are not. Second, braiding consitutes transitions between degenerate ground states, and local perturbations do not have matrix elements within this ground-state manifold. The platform is hence predicted to be very robust. However, the topologically protected braiding operations alone are insufficient for universal quantum computation. As the gates form a finite group, they can not be used to synthesize arbitrary unitaries. For universal quantum computation, braiding needs to be complemented with topologically unprotected operations, e.g. a $\pi/8$-phase gate and a joint read-out of the fermion parity of four MZMs [2]. An elegant realization of these topologically unprotected operations that introduces only minimal decoherence uses transmon circuits, which will be introduced next.

1.2. CIRCUIT QED AND MAJORANA ZERO MODES - A MARRIAGE STORY

In a parallel research effort, the field of circuit QED (cQED) evolves as a platform not only for quantum computation and communication, but also for quantum sensing. In particular, cQED can help to resolve charge dynamics in the circuit with sub-microsecond resolution turning it into a tool of choice to study MZMs. This section briefly summarizes basic ideas underlying the cQED framework with an emphasis on its applicability to the study and control of MZMs.

1.2.1. CAVITIES AND ATOMS

When Blais et al. first introduced the cQED architecture they framed it as a solid-state realization of cavity QED [13]. In cavity QED, atoms are coupled to photons in optical cavities to enhance the interaction of light and matter, yielding unprecedented control of the coupled system's quantum nature [14]. Similarly, cQED exploits resonant structures to couple single photons to quantum objects. Instead of atoms and optical cavities, however, it uses superconducting circuits that can act both as linear microwave resonators or as non-linear artificial atoms, depending on their geometry and architecture. Summarizing a comprehensive review article by Blais et al. [15], the subsequent paragraphs briefly outline how resonators and artificial atoms are realized in cQED.

The resonators can be lumped-element harmonic LC-oscillators, coplanar waveguide resonators or 3D cavity resonators, all of which have discrete electromagnetic oscillation modes with resonance frequencies ω_r^m, where m indexes the mode. At low thermal energies, $k_\mathrm{B}T \ll \hbar\omega_\mathrm{r}^m$, a resonance mode m with small linewidth κ (or high quality factor $Q = \omega_\mathrm{r}^m/\kappa \sim 10^3$ to 10^9) reaches the quantum limit. It may then be initialized in its quantum-mechanical ground state by waiting a time of order $O(1/\kappa)$ and its excitation spectrum is described by the quantum harmonic oscillator Hamiltonian,

$$H = \hbar\omega_\mathrm{r}^m(a^\dagger a + 1/2)\,, \tag{1.8}$$

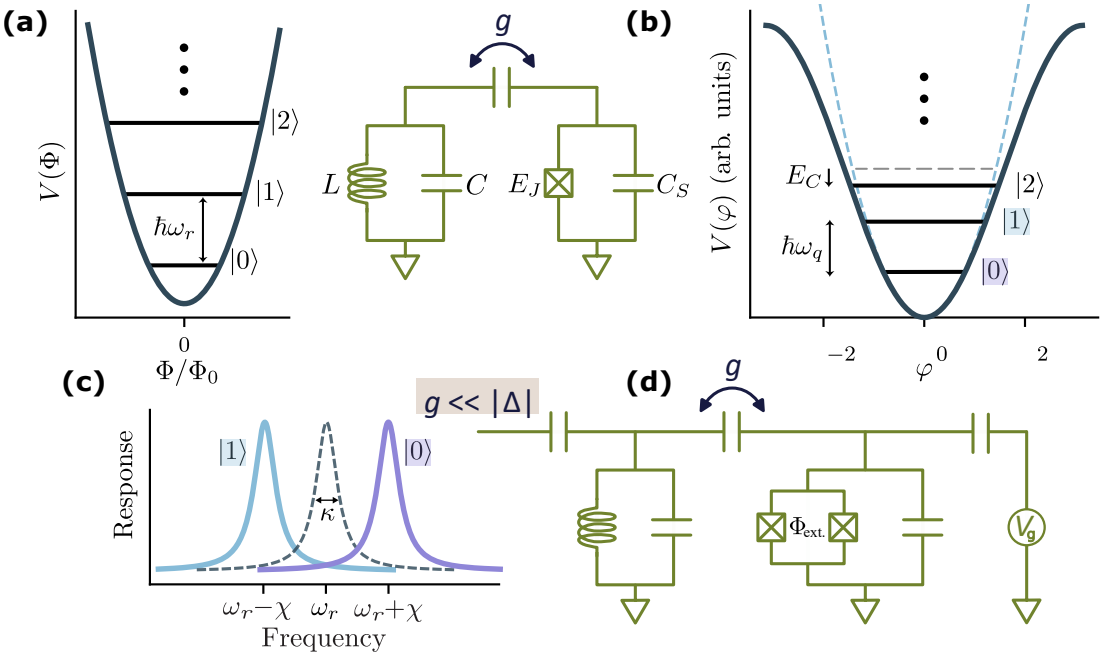

Figure 1.3: Circuit QED in a nutshell. **(a)** Harmonic potential and spectrum of a quantized LC circuit with equistant level spacing $\hbar\omega_\mathrm{r}$. **(b)** Replacing the linear inductance by the non-linear inductance of a Josephson junction (JJ) one obtains a transmon or Cooper-pair-box circuit, which has a cosine potential and hence anharmonic spectrum. Here, the groundstate and the first excited state can be individually addressed by a microwave transition at frequency $\hbar\omega_\mathrm{q}$ and form the basis state of a qubit. As indicated by the green circuit diagram, resonator and transmon circuit may be coupled capacitively at a rate g. Figure panels **(a)** and **(b)** reprinted with permission from [15]. Copyright (2021) by the American Physical Society. **(c)** In the dispersive coupling regime then, $g \ll |\Delta| = |\omega_\mathrm{q} - \omega_\mathrm{r}|$, the transmon imparts a qubit-state-dependent shift $\pm\chi$ on the resonator frequency. **(d)** Additional control knobs can be integrated to the circuit: The single JJ can be replaced by a SQUID loop formed by two parallel JJs. Then, the SQUIDs Josephson energy E_J can be tuned by a perpendicular magnetic flux Φ_ext. A charge bias line applying a voltage V_g controls n_g in Eq. (1.9).

with creation and annihilation operators $a^\dagger$, a and eigenstates satisfying $a^\dagger a|n\rangle = n|n\rangle$, $n = 0, 1, 2, \ldots$. Figure 1.3 **(a)** shows the harmonic potential and spectrum of a quantized LC circuit, which besides describing a lumped-element resonator also is the circuit representation of a single mode of a coplanar waveguide resonator or of a 3D cavity resonator (see [15] for details). Lumped element and coplanar waveguide resonators require superconducting electrodes on a low-loss dielectric substrate to give high Q factors. A 3D cavity resonator generally has higher Q-factors as most of its field energy is stored in the vacuum avoiding dielectric losses at interfaces and surfaces; it can therefore also be made from normal metal. The experiments in this thesis use a 3D copper cavity resonator for magnetic-field compatibility. It does not reach the high quality factors of superconducting resonators but it is entirely unaffected by the magnetic field. Superconducting resonators generally become limited by vortices and their frequencies are affected by the gap dependence with magnetic field.

The artificial atoms are made of superconducting islands connected by Josephson junctions (JJs), which act as a low-loss, non-linear inductor. Additionally, the islands couple capacitively, the coupling strength being determined by their geometry. The system is thus very similar to the above discussed LC-oscillator but the quadratic potential energy term is replaced by the energy-phase relation of the Josephson junction (Fig. 1.3 **(b)**). The most simple form is a cosine term which is obtained for tunnel junctions with many weakly transmitting channels. The superconducting circuit then forms a man-made mesoscopic quantum object with a non-linear

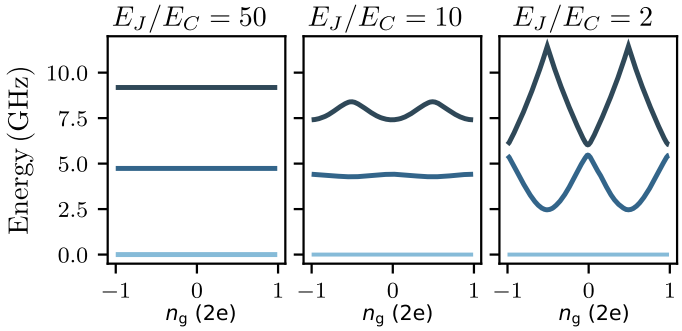

Figure 1.4: Transmon and Cooper-pair-box regimes. With decreasing E_J/E_C-ratio the charge dispersion of the energy levels (their dependence on n_g) increases. The transition frequencies then become more and more sensitive to fluctuations in n_g. The transmon regime ($E_J/E_C \gg 1$) hence provides the most stable conditions for qubit operation, however at the cost of a reduced anharmonicity. More charge-sensitive regimes can be used to sense charge fluctuations, as explained in Section 1.2.2. Figure reprinted with permission from [15]. Copyright (2021) by the American Physical Society.

excitation energy spectrum, which is why it is called artificial atom. Its spectrum is described by the Cooper-pair box Hamiltonian,

$$H = 4E_C(\hat{N} - n_g)^2 - E_J\, cos(\hat{\varphi})\,, \tag{1.9}$$

where E_C is the charging energy of one island with respect to the other island or to ground and E_J is the junction's Josephson energy. The Cooper-pair-number operator $\hat{N}$ counts the number of Cooper pairs having tunneled across the JJ and the phase operator $\hat{\varphi}$ describes the superconducting phase difference across the JJ. The charge bias n_g can be set by a voltage gate or more generally the charge environment of the circuit, which can furthermore be subject to slow drift and fluctuations. Figure 1.4 illustrates the spectrum of Eq. (1.9) for different E_J/E_C-ratios as a function of n_g. Due to the non-linearity of the spectrum, each transition can be individually addressed, and the ground and first-excited state can form a qubit. The transmon regime, $E_J/E_C \gg 1$, provides the least non-linearity, but the most stable conditions for qubit operation: Here, the charge dispersion, the dependence of the energy levels on n_g, is exponentially suppressed with E_J/E_C [16]. Consequently, fluctuations in n_g do not lead to large fluctuations in the transition frequencies. Conversely, however, this also means that operating the circuit in a lower E_J/E_C regime turns a transmon into an excellent sensor for charge fluctuations. It is precisely this feature that is useful for readout and control of MZMs.

Before coming there, however, the analogy of cQED to cavity QED is completed by considering the interaction between a single resonator mode and a transmon. This paragraph still draws heavily on the review article by Blais et al. [15]. The transmon couples capacitvely to the resonator with coupling constant g (Fig. 1.3 **(a)**-**(b)**). Reducing the transmon to a two-level system of ground and first-excited state, the system can be described by the well-known Jaynes-Cummings Hamiltonian,

$$H_{JC} = \hbar\omega_r \hat{a}^\dagger \hat{a} + \frac{\hbar\omega_q}{2}\hat{\sigma}_z + \hbar g(\hat{a}^\dagger \hat{\sigma}_- + \hat{a}\hat{\sigma}_+)\,, \tag{1.10}$$

capturing the coherent exchange of single quanta between light and matter, which are resonator photons and excitations in the transmon circuit in this case. Upon resonance, $\Delta = \omega_q - \omega_r \simeq 0$, the eigenstates of Eq. (1.10) correspond to strongly hybridized resonator-qubit modes. For

explicit readout and control of the transmon state the system is therefore usually operated in the dispersive regime, $\Delta = \omega_q - \omega_r \gg g$. Here, the eigenstates of Eq. (1.10) can be meaningfully identified with a transmon and a resonator mode. In the dispersive limit, the transmon-resonator Hamiltonian reads

$$H = \hbar\omega_r' \hat{a}^\dagger \hat{a} + \frac{\hbar\omega_q'}{2}\hat{\sigma}_z + \hbar\chi \hat{a}^\dagger \hat{a}\hat{\sigma}_z . \tag{1.11}$$

In comparison with Eq. (1.10) there are two modifications: First, the effect of higher transmon levels is non-negligible in the dispersive limit and leads to a slight renormalization of the resonator and qubit frequencies,

$$\omega_r' = \omega_r - \frac{g^2}{\Delta - E_C/\hbar}, \quad \omega_q' = \omega_q + \frac{g^2}{\Delta} . \tag{1.12}$$

Second, and most remarkably, in the interaction term the transmon exerts a qubit-state-dependent shift $\pm\chi$ on the resonator frequency,

$$\chi = -\frac{g^2 E_C/\hbar}{\Delta(\Delta - E_C/\hbar)} . \tag{1.13}$$

The effect is illustrated in Fig. 1.3 **(c)**. As the resonator frequency can be probed with high accuracy, this shift provides an excellent readout of the transmon state. The interaction term now commutes with the transmon state observable $\hat{\sigma}_z$, which implies that the readout can furthermore be quantum-nondemolition (QND).

So far, summarizing the review article by Blais et al. [15], we have just demonstrated that we can rebuild a cavity QED architecture using superconducting circuits. The interesting question in view of this thesis, however, is whether cQED can open up new areas of application and thus go beyond a mere solid-state reproduction of cavity QED. First of all, the cQED architecture is extremely flexible in design. Varying the coupling strength between resonator and artificial atom amounts to changing the geometry of the superconducting islands The same holds for E_C. Then, on the fabrication side, E_J can be targeted reliably, ranging from few GHz to tens or hundreds of GHz: The workhorse of cQED are superconductor-insulator-superconductor (SIS) JJs made from a sandwich structure of aluminum, aluminum oxide, and aluminum. Using shadow evaporation under two different angles and an intermittent in-situ oxidation they can be fabricated without breaking vacuum, resulting in a high-quality tunnel barrier and hence extremely low intra-JJ losses. The Josephson coupling between the two aluminum layers is determined by the JJ dimensions, as well as the oxidation time and pressure. Besides, as illustrated in Fig. 1.3 **(d)** a split-junction design can be used to form a superconducting quantum interference device (SQUID). Then, E_J can be tuned by perpendicular magnetic flux threading the SQUID [17, 16]. As a result, the same device can in-situ be tuned from the transmon regime to a more offset-charge-sensitive regime and back again. Most strikingly, however, cQED can accomodate any low-loss materials and nanostructures that one can think of. This enables the conception of hybrid devices, integrating quantum dots, spin qubits, nano-mechanical oscillators, unconventional JJs, or MZMs to the circuits. In view of this thesis, in particular the latter two are of relevance and the remainder of this section focusses on proposals how transmons enable universal topological quantum computation and how they

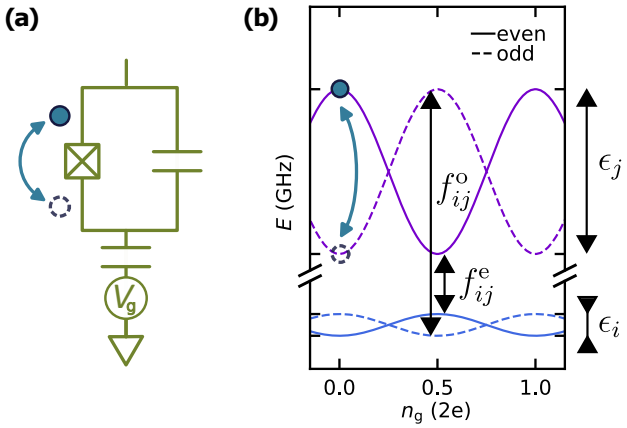

Figure 1.5: Transmon as a parity meter. **(a)** A single fermion can be to either side of the transmon's JJ. **(b)** Depending on the fermionic configuration, the transmon spectrum is either described by the "even" manifold (solid lines) or by the "odd" manifold (dashed lines). Coherent microwave transitions at frequencies f^{e}_{ij} and f^{o}_{ij} are only possible within each manifold. However, incoherent tunneling of single quasiparticle excitations across the junction is ubiquitous (quasiparticle poisoning), resulting in sdden jumps of the transmon frequencies from f^{e}_{ij} to f^{o}_{ij} and vice versa. Also deliberate changes to the fermionic configuration in circuits containing MZMs result in frequency jumps. The transmon can therefore act as a readout circuit for the fermion parity of topological qubits, provided that the quasiparticle poisoning time is much larger than the topological gate operations. Figure panel adapted from [18] (own work). Copyright (2024) by the American Physical Society.

can add to the experimental detection of MZMs.

1.2.2. THE TRANSMON AS A PARITY METER

As laid down in Section 1.1, a topological Majorana qubit builds on the fermionic occupation of pairs of MZMs, and braiding changes the occupation configuration while conserving the total fermion parity of the system. Key to reading out the state of a Majorana qubit are hence measurements of the fermionic occupation of pairs of MZMs. The transmon in turn is an excellent sensor for charge dynamics in the circuit: Due to the dependence of its energy levels on n_g, it can sense tunneling events of single quasiparticles across the transmon's JJ (see Fig. 1.5 **(a)**). The transmon Hamiltonian (Eq. (1.9)) is $2e$-periodic, where e is the elementary charge. Intuitively, however, the spectrum may be repeated at steps of $1e$, where the interleaved manifolds differ in their fermionic charge configuration and are labeled "even" and "odd" (see Fig. 1.5 **(b)**). Here, the labels "even" and "odd" do not indicate the fermion parity of the individual transmon islands but refer to the transmon parity, which is the number of single quasiparticles that have tunneled across the junction modulo two [19]. It is important to note that the "even" and "odd" manifolds are not coupled by Eq. (1.9); coherent microwave transitions are only possible within each manifold with transition frequencies f^{e}_{ij} and f^{o}_{ij}. However, the two manifolds are incoherently connected by the tunneling of single quasiparticle excitations across the junction [20, 21, 22]. An incoherent tunneling event then results in a sudden jump of the transmon frequencies from f^{e}_{ij} to f^{o}_{ij} or vice versa; the magnitude of this jump depends on the E_J/E_C-ratio and the level indices i and j. This frequency jump forms the basis of proposals to use transmon circuits for readout and control of MZMs: Just as incoherent tunneling of quasiparticles changes the fermion parities of the transmon islands and results in a frequency jump, a deliberate shuttling of (occupied) pairs of MZMs from one island should do so, too. The subsequent sections discuss a choice of relevant theory proposals that exploit this idea.

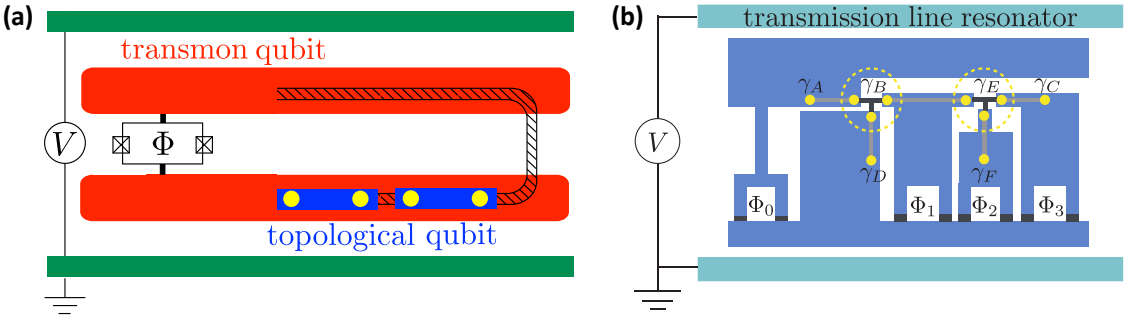

Figure 1.6: **(a)** "top-transmon" proposal by Hassler et al. [23] combining a transmon qubit with a topological qubit. Two superconducting islands (red) are coupled by a flux-tuneable split-JJ and form a SQUID transmon. MZMs (yellow) in a topological-superconductor nanowire (blue) can be shuffled from one transmon island to another by gate electrodes (not shown). This results in an occupation-dependent shift $f^{\mathrm{e}}_{ij} \leftrightarrow f^{\mathrm{o}}_{ij}$ of the transmon frequencies, which can be used for readout of the topological qubit and a phase gate on the topological qubit (see text). Tuning E_{J} via the SQUID loop the coupling between transmon and topological qubit can be switched on and off exponentially. Figure panel reproduced from [23], permission request pending. ©IOP Publishing. **(b)** Flux-controllable circuit for braiding. Topological tri-junctions couple MZMs (yellow) from different superconducting islands (dark blue). Each islands $E_{\mathrm{J}}/E_{\mathrm{C}}$-ratio can furthermore be tuned by flux-tuneable split-JJs to a regime that is either charge-sensitive and therefore parity-protected, i.e. couples strongly MZMs on the same island, or to a charge-insensitive regime, where the coupling of MZMs at the tri-junction dominates. This enables shuffling the MZMs around in the pi-shaped topological network. Figure panel reprinted with permission from [24]. Copyright (2013) by the American Physical Society.

1.2.3. cQED FOR TOPOLOGICAL QUANTUM COMPUTING

The connection to cQED experiments for topological qubits based on MZMs was made early on: In their "top-transmon" proposal Hassler et al. demonstrate that a transmon qubit can couple to the Fermion-parity of a Majorana qubit and can therefore realize parity-protected σ_z-rotations and readout of the topological qubit [23]. These can be the required operations to complement braiding and hence enable universal topological quantum computation. Figure 1.6 **(a)** shows the device that the authors propose, it combines a SQUID transmon with a topological qubit. The SQUID transmon, as above, consists of two superconducting islands coupled by a split JJ, and the topological qubit consists of a nanowire that can locally be depleted by gate electrodes (which are not shown). In a parallel magnetic field, MZMs are predicted to appear at the ends of undepleted sections of the wire and can be shuffled from one island to the other assuming full control of the gate electrodes beneath the wire. In their device, the offset charge n_{g} in the Cooper-pair box Hamiltonian Eq. (1.9) can be tuned by applying a voltage V between the center conductor and the ground plane of a coplanar waveguide resonator. However, the shuttling of a pair of MZMs from one island to the other can also change n_{g}: If the MZMs host one electron, n_{g} shifts by 0.5, i.e. half a Cooper pair. As Fig. 1.4 illustrates this shift in n_{g} alters the transition energy between successive transmon levels significantly if the $E_{\mathrm{J}}/E_{\mathrm{C}}$-ratio is small and it leaves the transition energy almost unchanged for high $E_{\mathrm{J}}/E_{\mathrm{C}}$-ratios. The coupling between the transmon and the topological qubit can hence be switched on and off exponentially using the flux degree of freedom to tune E_{J}. The authors propose the following protocol for reading out the topological qubit:

1. The topological qubit may be in any superposition $|\psi\rangle = \alpha|00\rangle + \beta|11\rangle$. Flux ϕ is set to zero such that $E_{\mathrm{J}} = \max(E_{\mathrm{J}}(\phi))$, i.e. transmon and topological qubit are maximally decoupled

2. Tune $\phi = 0.5\Phi_0$, and hence $E_{\mathrm{J}} = \min(E_{\mathrm{J}}(\phi))$. The transmon is now sensitive to changes in

n_g.

3. Move one pair of MZMs to the other island and measure the transmon frequency. The frequency depends on whether or not the pair of MZMs was occupied and the measurement projects the topological qubit onto $|00\rangle$ or $|11\rangle$.

4. Reset ϕ to 0.

If the time that the transmon spends in an offset-sensitive regime is short, quasiparticle-tunneling across the JJs is unlikely to happen, and the authors call the operation to be "parity-protected" in the sense that subgap excitations in the individual electrodes cannot affect the readout result [25]. The joint parity readout of four MZMs is analogously performed by moving all four MZMs from one island to the other. The remaining missing ingredient for universal quantum computation then is a $\pi/8$-phase gate. The protocol is almost the same as for readout, but without the projective frequency measurement. Instead, the coupled system of transmon and topological qubit evolves freely in the offset-charge sensitive regime for a waiting time τ,

$$\alpha|00\rangle + \beta|11\rangle \rightarrow \alpha e^{i(E_n-\epsilon_n/2)\tau/\hbar}|00\rangle + \beta e^{i(E_n+\epsilon_n/2)\tau/\hbar}|11\rangle\,. \tag{1.14}$$

During this unitary time evolution, the transmon is in state $|n\rangle$ with energy E_n and peak-to-peak value of the charge dispersion $\epsilon_n = E_n(n_g = 0.5) - E_n(n_g = 0)$. The time evolution corresponds to a θ-phase gate with $\theta = \tau\epsilon_n/2\hbar$. A $\pi/8$-phase gate corresponds to a waiting time of $\tau = \pi\hbar/4\epsilon_n$ ~10.3 ns to 1.3 ns for $\epsilon_n/\hbar$ ~10 MHz to 100 MHz.

It is worth noting, that the protocol devised by Hassler at al. can also be performed using a single-JJ transmon instead of a SQUID-transmon: For higher transmon levels ϵ_n increases exponentially with the level index n. Instead of tuning the E_J/E_C-ratio with a flux loop to increase charge sensitivity, an alternative approach is therefore to pulse the transmon to higher levels, measure its parity, and then pulse back again. We make use this approach in Chapter 3. In our setup, flux noise increases with parallel magnetic field (see Chapter 2) and for high-field parity readout it may therefore be beneficial to avoid a SQUID loop.

The "top-transmon" proposal focusses on the realization of the non-Clifford gates necessary for universal quantum computation with MZMs, but it does not explicitly treat the topologically protected operations. Moreover, it requires shuttling of the MZMs from one island to another, which from an experimental point of view is quite difficult to achieve: The gates are easily screened by the superconductor and defects may introduce local variations of the chemical potential. Tackling both issues at once, Hyart et al. provide a fully flux-controlled cQED circuit suited to demonstrate non-abelian exchange statistics of MZMs, i.e. initialization, braiding and readout of a topological qubit [24]. At its core, the device comprises topological tri-junctions coupling MZMs on different superconducting islands (see Fig. 1.6 **(b)**). Effectively, this forms a two-dimensional network of topological nanowires in which MZMs can be shuffled around to realize a braiding operation. Each island is furthermore connected to a large superconducting island by a flux-tuneable split-JJ. Using these SQUIDs, the E_J/E_C-ratio of each island can be tuned separately, which as before exponentially modifies the charge-sensitivity of the island. Each island can be tuned to a regime that is either charge-sensitive and therefore parity-protected, i.e. couples strongly MZMs on the same island, or it can be tuned to a charge-insensitive regime, where the coupling of MZMs at the tri-junction dominates. This enables

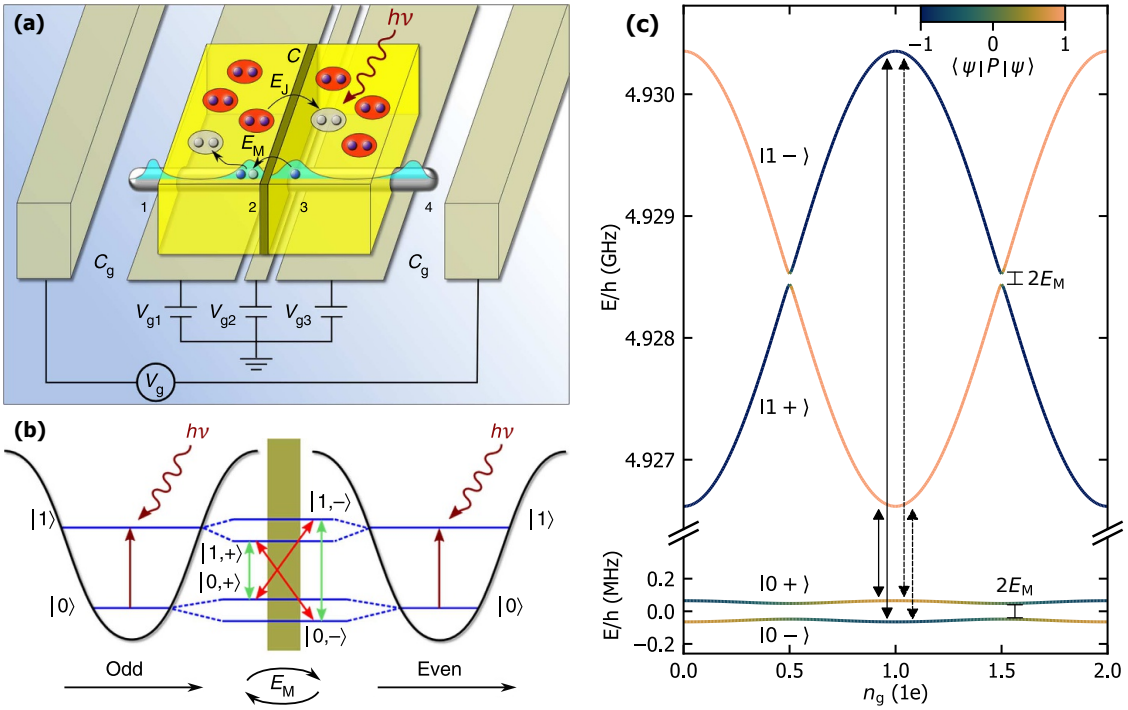

Figure 1.7: Majorana transmon proposal by Ginossar et al. [26]. **(a)** Sketch of SNS (S: superconductor, N: normal conductor) JJ with topological-superconductor wire segments hosting MZMs (teal). The innermost MZMs 2 and 3 overlap and introduce coherent tunneling of single electrons with a coupling strength E_M. **(b)** A finite E_M couples the formerly disconnected spectral manifolds of "even" and "odd" parity, introducing hybridized states $|0,\pm\rangle$ and $|1,\pm\rangle$. Four instead of two microwave transitions are allowed now. Figure panels **(a)** and **(b)** are adapted from [26] and reproduced with permission from Springer Nature. **(c)** Energy levels of Majorana transmon for $E_J = 9\,\text{GHz}$, $E_C = 0.4\,\text{GHz}$, $E_C = 50\,\text{kHz}$ as a function of n_g. The colorscale represents the degree of parity-hybridization in terms of the expectation value of the transmon-parity operator, $-1 \leq \langle\Psi|\hat{P}|\Psi\rangle \leq +1$. Energy levels $|n\pm\rangle$ with n being the transmon level index are separated by an anticrossing of magnitude E_M.

shuffling the MZMs around in the pi-shaped topological network. In view of this thesis, an important point is, that the SQUIDs that are used to tune the E_J/E_C-ratio of each island do not need to be topological but can be conventional tunnel junctions.This also holds for the "top-transmon"-proposal. To comply with the magnetic fields used to push the nanowires in the topological regime, however, these junctions (and more generally the readout circuitry) need to be magnetic-field resilient. This is one of the underlying motivations for investigating the magnetic field resilience of transmons based on tunnel junctions.

1.2.4. cQED FOR HYBRID DEVICES

Besides realizing protocols for topological quantum computing, cQED provides an excellent platform to study hybrid devices, integrating micro- and mesoscopic quantum systems to circuits. In particular, transmons with topological JJs can help to unambiguously detect MZMs. For concreteness, we consider here the case of an SNS (S: superconductor, N: normal conductor) nanowire JJ as defined by proximitizing two segments of a nanowire with a superconductor leaving a gap and hence an unproximitized region in between (see Fig. 1.7 **(a)**). As before, the nanowire is made from topological-insulator material or a strongly spin-orbit coupled semiconductor, and the proximitized segments attain a topological regime when threaded by a sizeable magnetic flux. In the topological regime, the proximitized segments host MZMs γ_1, γ_2, γ_3, γ_4 at their ends, with γ_2 and γ_3 overlapping significantly.

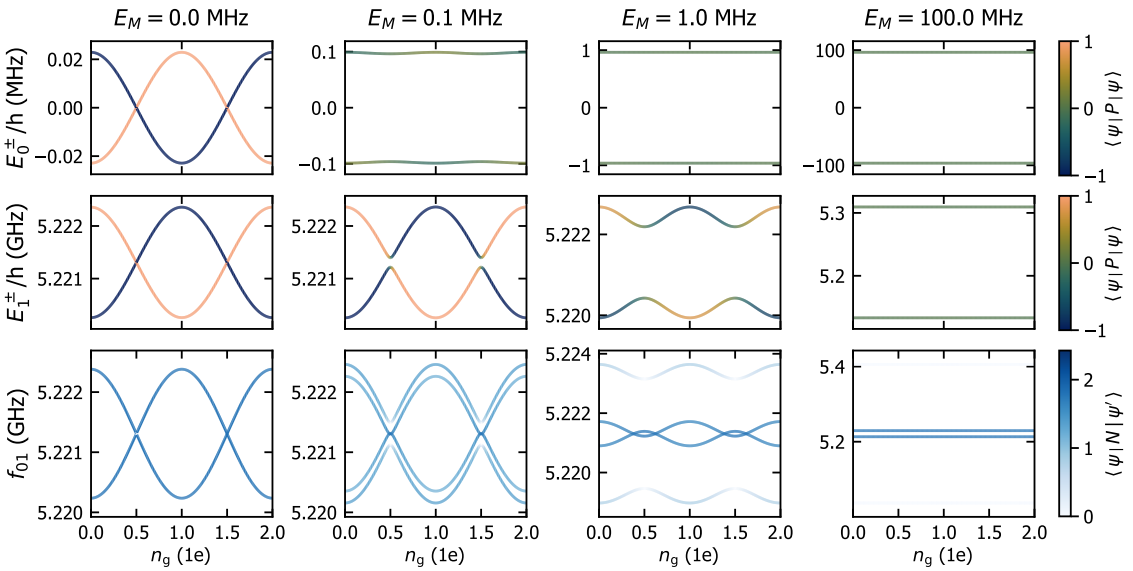

Figure 1.8: Simulation of the Majorana transmon's level spectrum ($E_0^{\pm}$ and $E_1^{\pm}$) and transition frequencies $f_{01} = (E_1^{\pm} - E_0^{\pm})/h$ for different values of E_M. Here, $E_J = 10\,\text{GHz}$ and $E_C = 0.4\,\text{GHz}$. As before, the levels are color-coded by the expectation value of the transmon-parity operator, $\langle\Psi|\hat{P}|\Psi\rangle$. The transition frequencies are color-coded by the strength of the transitions' dipole moments $\langle\Psi|\hat{D}|\Psi'\rangle \propto \langle\Psi|\hat{N}|\Psi'\rangle$. For $E_M = 0$ the normal transmon spectrum is recovered with uncoupled "even" and "odd" parity sectors. These sectors hybridize with increasing E_M, resulting in a doubling of the transition frequencies. The separation of the hybridized levels is eventually entirely dominated by E_M and their charge dispersion becomes flat.

As first laid down in [26] and further elaborated in [27, 28, 29] the presence of MZMs in an SNS-JJ changes the transmon spectrum drastically. In addition to the coherent tunneling of Cooper pairs, which gives rise to the $E_J\,cos(\hat{\varphi})$-term in Eq. (1.9), the overlap of γ_2 and γ_3 introduces coherent tunneling of single electrons. In a simplified picture, disregarding a finite mutual overlap of the other MZMs and ignoring the microscopic details of Andreev reflections the Majorana transmon hamiltonian reads

$$H = 4E_C(\hat{N} - n_g)^2 - E_J\,cos(\hat{\varphi}) + i2E_M\gamma_2\gamma_3\,cos(\hat{\varphi}/2)\,. \tag{1.15}$$

Here, E_M is the coupling strength between γ_2 and γ_3. Crucially, as illustrated in Fig. 1.7 **(b)** the last term coherently couples the "even" and "odd" transmon-parity sectors. The formerly disconnected energy levels for "even" and "odd" transmon parity hybridize and show an avoided crossing of order E_M, and microwave transitions between the parity sectors are possible (see Fig. 1.7 **(c)**).

Depending on the values of E_J, E_C and E_M the coupling between "even" and "odd" transmon parity thus leads to new spectral lines appearing. Figure Fig. 1.8 shows the (hybridized) levels $E_0^{\pm}$ and $E_1^{\pm}$ as well as the predicted spectral lines $f_{01} = (E_1^{\pm} - E_0^{\pm})/h$ for different values of E_M. Here, $E_J = 10\,\text{GHz}$ and $E_C = 0.4\,\text{GHz}$ are the same for all panels. To illustrate the parity hybridization of the energy levels $E_0^{\pm}$ and $E_1^{\pm}$ are color-coded by the expectation value of the transmon-parity operator, $-1 \leq \langle\Psi|\hat{P}|\Psi\rangle \leq +1$, where -1 corresponds to "odd" transmon parity and $+1$ to "even" transmon parity. For $E_M = 0$ we recover the normal transmon level spectrum where "even" and "odd" parity sectors are entirely disconnected and no coherent microwave transitions are allowed between the two sectors. Consequently, $\langle\Psi|\hat{P}|\Psi\rangle = \pm 1$ and only two transitions show up in the f_{01}-panel. In two-tone spectroscopy usually both

transitions are visible due to frequent incoherent tunneling of quasiparticles on the timescale of the measurement (see Chapter 3). Ramping up E_M separate energy levels $E_0^\pm$ and $E_1^\pm$ form, which become more and more parity-hybridized. The separation of the hybridized levels is eventually entirely dominated by E_M and their charge dispersion becomes flat. As the charge dispersion is stronger for higher level index, the effect becomes appearent later for $E_1^\pm$ compared to $E_0^\pm$. In the f_{01}-panel, the spectral lines double. The color bar indicates the strength of the transitions' dipole moments $\langle\Psi|\hat{D}|\Psi'\rangle \propto \langle\Psi|\hat{N}|\Psi'\rangle$. For intermediate values of E_M all four transitions are predicted to show up very clearly in spectroscopic measurements, with characteristically varying spectral weights. For values of E_M on the order of E_C, however, the outer transitions fade out.

Equation 1.15 is a powerful and yet simplified toy model describing the effect of MZMs inside the JJ on a transmon spectrum. A more detailed description of the system would not only account for the overlap of γ_2 and γ_3 but also for a finite mutual overlap of all other MZMs. Furthermore, a nanowire SNS JJ typically has a non-sinusoidal current-phase relationship $I_c(\varphi)$ [30]. A refined approach models $I_c(\varphi)$ in an Andreev picture, with few channels of high transparency. For instance, refs. [28, 29] solve the full Bogoliubov-de-Gennes Hamiltonian for the case of a semiconductor nanowire. This is particularly useful to model and understand the magnetic-field dependence of a Majorana-transmon's spectrum. A similar model is currently being set up for topological-insulator nanowires within a collaboration of our group with the Forschungszentrum Jülich.

1.2.5. A SUGGESTIVE REMARK ON SNR

Condensing the preceding sections into a single claim, transmons can resolve charge dynamics in the circuit with sub-microsecond resolution and their spectrum is modified significantly in the presence of coherent electron tunneling. This turns cQED into a tool of choice to study MZMs. In particular, the dispersive technique is key to high fidelity, low noise readout and control. The use of coherent resonator states containing many photons to readout and control single quanta in the artificial atom offers several advantages over more direct DC coupling [15]: The measurement on-off ratio is exceptionally high and well controlled by switching on and off classically generated microwave tones and the inevitable dissipation due to the measurement [31] happens away from the qubit at room temperature. As the readout is performed at a resonator frequency ω_r far detuned from the qubit frequency ω_q probetone photons are not easily absorbed by the qubit. Moreover, the resonator acts as a filter for noise at ω_r and the Purcell decay of the qubit is highly reduced compared to a situation where the qubit couples to a continuum or multi-mode environment. All of this turns dispersive readout into a QND measurement, where the backaction is quantum-limited.

Additionally, an excellent amplification chain exists for signals in the range of 4 GHz to 8 GHz typically used for cQED experiments, consisting of circulators, quantum-limited parametric amplifiers (JPA or TWPA) and low-noise high-electron-mobility transistor (HEMT) amplifiers. In particular, the quantum-limited parameteric amplifiers drastically improve single-shot measurements of the transmon state [32, 33], resulting in superior fidelities and/or extremely short readout times of tens of nanoseconds, overcoming the fidelity-limiting effect of qubit relaxation during measurements [34]. This is of particular relevance for potentially

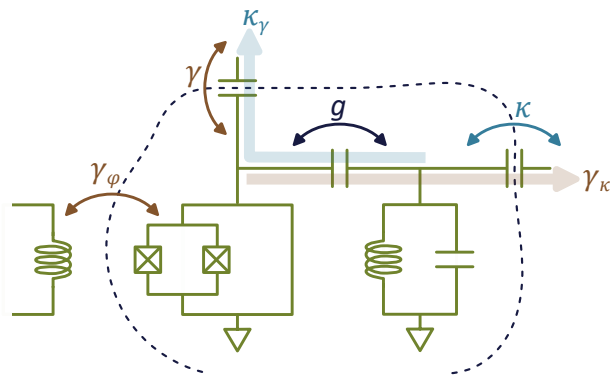

Figure 1.9: Schematic of coupling and loss mechanisms for a transmon circuit coupled to a resonator at a rate g. The resonator couples at a rate κ to the outside world, the transmon at a rate γ. Being coupled by g, the loss of a photon in the resonator can lead to energy relaxation of the transmon and vice versa. The corresponding relaxation rates $\gamma_\kappa = (g/\Delta)^2\kappa$ and $\kappa_\gamma = (g/\Delta)^2\gamma$ are known as the (inverse) Purcell decay. Furthermore, dephasing of the transmon (e.g. due to flux or charge noise, or photon shot noise) is considered at a rate γ_φ.

lossy transmons based on topological JJs. The experiments presented in this thesis did not yet incorporate a parametric amplifier and the single-shot fidelities attained in Chapter 3 are sufficient for transmon-parity measurements with cycle times limited by relaxation-based qubit reset. The newly installed TWPA is tested for magnetic-field resilience [35] and would now also allow for continuous, back-to-back monitoring of the transmon parity due to improved QND-ness of the readout.

The dispersive technique aided by near-quantum limited signal amplification allows a degree of control and isolation of the quantum system that is hard to achieve with other measurement techniques, such as tunneling spectroscopy. At the same time the latter represent a good complement to cQED-based approaches to the detection and manipulation of MZMs and often offer simpler device integration. In particular, the operation of a transmon for readout and control of MZMs sets rather stringent criteria on the device quality, as will become clear in the subsequent section. Finally, while this thesis focusses on the transmon as an artificial atom, the benefits of dispersive readout may also be applied to other prominent Majorana platforms. For instance, the charge dipole of a Majorana box qubit can couple to a resonator, too, and allows therefore for dispersive cQED readout, with promising results demonstrated recently by Microsoft Azure Quantum [36].

1.3. FIGURES OF MERIT: WHEN IS A TRANSMON GOOD ENOUGH TO STUDY MZMS?

Having advertised cQED and more precisely transmons for the detection and manipulation of MZMs, a discussion of figures of merit for transmons is in order: Which criteria should transmon circuits meet to be useful for the study of MZMs?

Despite the above discussed favorable SNR the resonator-transmon system is not an isolated quantum system, but couples to the outside world. On the one hand, this is to some extent intended to enable readout and control of the system. On the other hand, the coupling introduces loss channels and noise, which, in the case of on-chip sources of loss and noise, are not even useful for readout and control. Figure 1.9 illustrates some of the relevant coupling and loss mechanisms. The resonator couples at a rate κ to the outside world, the transmon at

a rate γ. Note that κ and γ are not independent: As transmon and resonator are coupled at a rate g, the loss of a photon in the resonator can lead to energy relaxation of the transmon and vice versa. The corresponding relaxation rates $\gamma_\kappa = (g/\Delta)^2\kappa$ and $\kappa_\gamma = (g/\Delta)^2\gamma$ are known as the (inverse) Purcell decay. Furthermore, dephasing of the transmon (e.g. due to flux or charge noise, or photon shot noise) is considered at a rate γ_φ.

These coupling and dephasing rates connect to the characteristic time scales that quantify qubit coherence: the energy-relaxation time T_1, the dephasing time T_2^*. T_1 is the characteristic time scale for a qubit to decay from its excited state to the ground state, or, in the case of non-negligible thermal population, to equilibrate to a thermally mixed state $\rho = \alpha\,|0\rangle\langle 0| + \beta\,|1\rangle\langle 1|$. The dephasing time T_2^* describes the characteristic lifetime of a coherent superposition $|\psi\rangle = 1/\sqrt{2}\,(|0\rangle + |1\rangle)$, it is measured in a Ramsey sequence. An echo pulse may be applied in the middle of the Ramsey-sequence, rotating the qubit state by π and canceling out noise contributions that are slow compared to the qubit frequency. The resulting echo-dephasing time is denoted T_2^{echo} and is useful to characterize noise that is fast compared to the qubit frequency. Connecting to the previously discussed coupling and loss rates, at zero temperature $T_1 = 1/\gamma$, and $T_2 = 1/\gamma_2 = \left(\gamma/2 + \gamma_\varphi\right)^{-1}$.

Having introduced the qubit coherence times and coupling rates to the environment, we can now define criteria that constrain useful cQED regimes for the detection of MZMs.

The most basic requirement compares the transmon-resonator interaction with the linewidth of resonator and transmon, $g > \kappa, \gamma_2$. In this so-called strong-coupling regime the light-matter interaction is strong enough to enable coherent exchange of a single quantum between resonator and transmon [15]. For circuits using conventional aluminum tunnel junctions this regime has first been demonstrated by Wallraff et. al [37] and is since then well-established, but in the case of hybrid devices employing unconventional JJs the situation is less clear-cut. In these junctions, sub-gap excitations may carry normal currents in parallel to the supercurrent. The resulting parallel resistance leads to poor transmon coherence and consequently also to a large inverse purcell decay κ_γ. In this situation, the cavity Q-factor broadens when the qubit is close in frequency. In the course of my PhD project we tried to incorporate various types of topological-insulator JJs to transmon circuits, but could not achieve the strong coupling regime yet. Example data is shown in Chapter 4 of this thesis, and concrete plans how to move forward are sketched in Chapter 6.

Measuring the fermion parity of transmons for readout of a topological qubit as well as resolving coherent single electron tunneling through topological JJs sets an even more stringent requirement on transmon coherence. The transmon linewidth needs to be smaller than the parity-frequency splitting, $\gamma_2 < \epsilon_n/h, E_M/h$. Only then a parity-split spectrum can be resolved. Moreover, single-shot parity measurements rely on superpositions that require $T_2 > (\epsilon_n/h)^{-1}$. Typical cQED experiments focussing on quantum computing with superconducting circuits are well shielded from external magnetic fields: Fluctations in the magnetic field may dephase the qubit and vortices and increased quasiparticle densities may introduce losses. In our setup, however, we want to be able to apply and sweep magnetic fields on the order of 1 T. To understand and mitigate losses and noise introduced by the magnetic field Chapter 2 investigates the field dependence of spectrum and coherence times of a transmon based on aluminum tunnel JJs.

Finally, the ultimate limit on topological quantum computing with MZMs is set by quasiparticle poisoning. As opposed to the coherent tunneling of single zero-/low-energy electrons in a topological JJ, which is mediated by MZMs, incoherent quasiparticle poisoning refers to stocchastic tunneling of quaisparticle excitations above the superconducting gap. This process randomizes the fermion parity of superconducting islands and thus affects the readout to its very core. Here, too, the magnetic field may be detrimental and affects quasiparticle poisoning. Chapter 3 therefore investigates quasiparticle effects in magnetic-field resilient aluminum transmons.

1.4. RESEARCH QUESTIONS

Concluding this introductory chapter I would like to lay down the specific research questions that this work adresses. The above mentioned cQED proposals to study and manipulate MZMs require the readout circuit to sustain relatively large magnetic fields. And, while some parts of the proposed circuits require topological JJs, large parts of the readout and control circuitry can be realized with conventional aluminum tunnel JJs. Typically, however, transmons based on aluminum JJs have been operated in the absence of magnetic fields, and prior to this work the use of unconventional JJs, e.g. based on Graphene [38] or semiconductor nanowires [39, 40], has been put forward for magnetic-field resilience. At the same time, transmons based on non-tunnel JJs often show poor coherence, which we also had to discover ourselves. To what extent is it therefore possible to use transmons based on tunnel JJs for readout and control of Majorana qubits? Which effects dominate the spectrum and coherence times as well as the quasiparticle-poisoning time of aluminum transmons in a magnetic field? And finally, how can we optimize devices and setup for enhanced magnetic-field resilience? The long-term goal being the integration of MZMs to magnetic-field-resilient transmons, these research questions are furthermore complemented by efforts to fabricate and measure transmons based on topological-insulator JJs.

All these questions are being addressed while setting up a cQED lab almost from scratch. Chapter 2 demonstrates that thin-film aluminum transmons can be operated coherently at fields up to 1 T, and we learn about how to push them to even higher fields. One of the two devices is a SQUID transmon, and its coherent operation in magnetic fields is not only required for the above mentioned proposals by Hassler et al. [23] or Hyart et al. [24]. As the SQUID transmon frequency is very sensitive to fluctuations in the perpendicular flux, we can moreover investigate the magnetic field-dependence of slow and fast flux noise in our setup using measurements of the qubit dephasing times T_2^* and T_2^{echo}. While such investigations can in principle elucidate the microscopic origins of on-chip flux noise our data is agnostic to this matter, likely because T_2^{echo} is limited by photon shot noise in the resonator. Our findings do suggest however that vibrations of the magnet relative to the sample and noise from magnet current sources could become a limiting factor, when operating the SQUID transmon away from its top or bottom flux sweetspot. Chapter 3 demonstrates readout of the transmon parity in moderate magnetic fields up to 0.41 T and we learn a lot about how to improve the device and the setup to enable parity readout with high quality tunnel-JJs in higher magnetic fields. As a byproduct, we co-discover a slightly non-sinusoidal current-phase relationship in Al tunnel JJs leading to higher Josephson harmonics. Finally, while the project initially encompassed

also the successful integration of topological-insulator JJs to transmons it became evident that this research avenue requires efforts exceeding the scope of this thesis. In Chapter 4 I summarize the present status of our efforts to fabricate and measure TI-based transmons and give example data illustrating their poor coherence. In Chapter 6 I propose instead two devices which make use of tunnel-JJs as much as they can, and could still possibly show interesting Majorana physics.

2

Magnetic-field resilience of 3D transmons with thin-film Al/AlO$_x$/Al Josephson junctions approaching 1 T

As briefly discussed in Section 1.1 the generation of MZMs typically requires the presence of magnetic fields, often on the order of hundreds of mT. To profit from the dispersive readout and control techniques that cQED offers, and to be able to couple transmon circuits to the fermion parity of a Majorana qubit, magnetic-field resilience of the circuitry is therefore key. The workhorse of transmon qubits are Al/AlO$_x$/Al JJs, with coherence and yield unrivalled by other types of JJs that have been put forward for magnetic field resilience, such as JJs based on Graphene [38] or semiconductor nanowire JJs [39, 40]. The objective of the work presented in this chapter is to investigate the magnetic-field-resilience of transmons based on Al/AlO$_x$/Al JJs. To this end, the field dependence of spectrum and coherence times of a single-JJ and a SQUID transmon are measured and the results indicate that thin-film aluminum transmons can remain sufficiently coherent for qubit operation at considerable magnetic fields on the order of 1 *T. In that sense, this chapter lays the foundation for the subsequent chapters, which focus on the parity-readout protocol for future Majorana qubits and the integration of topological-superconductor nanowires to transmons. Besides, while devices and setup are already partly optimized for magnetic-field resilience, the data give valueable insights on how to further improve.*

This chapter has been published in Phys. Rev. Applied *as:*

J. Krause[*]**, C. Dickel**[*]**, E. Vaal, M. Vielmetter, R. Bounds, J. Feng, G. Catelani, J. M. Fink, Y. Ando**, *Magnetic Field Resilience of Three-Dimensional Transmons with Thin-Film Al/AlO$_x$/Al Josephson Junctions Approaching 1 T*, Phys. Rev. Applied **17** 034032 (2022).

Author contributions *The project was conceived by C.D. and Y.A.. J.K. and C.D. fabricated the device and took the measurements. The data was analyzed by J.K. and C.D. with help from G.C and E.V.. The manuscript was written by J.K., C.D., and G.C. with input from all coauthors.*

Data availability *The raw data are stored on the institute network servers. A Git repository hosted on the group Gitlab server contains the compressed data in csv format and Jupyter notebooks for their analysis.*

[*]These authors contributed equally to this work

Magnetic-field-resilient superconducting circuits enable sensing applications and hybrid quantum-computing architectures involving spin or topological qubits and electro-mechanical elements, as well as studying flux noise and quasiparticle loss. We investigate the effect of in-plane magnetic fields up to 1 T on the spectrum and coherence times of thin-film 3D aluminum transmons. Using a copper cavity, unaffected by strong magnetic fields, we can solely probe the magnetic-field effect on the transmons. We present data on a single-junction and a SQUID transmon, that were cooled down in the same cavity. As expected, transmon frequencies decrease with increasing fields, due to a suppression of the superconducting gap and a geometric Fraunhofer-like contribution. Nevertheless, the thin-film transmons show strong magnetic-field resilience: both transmons display microsecond coherence up to at least 0.65 T, and T_1 remains above 1 µs over the entire measurable range. SQUID spectroscopy is feasible up to 1 T, the limit of our magnet. We conclude that thin-film aluminum Josephson junctions are a suitable hardware for superconducting circuits in the high-magnetic-field regime.

2.1. INTRODUCTION

Josephson junctions (JJ) based on aluminum and its oxide (Al/AlO_x/Al) have three key properties that have made them the workhorse of circuit QED (cQED) [13]. They are routinely fabricated to high quality; their Josephson energy E_J can be estimated from the room temperature resistance [41]; the E_J can be controlled with high yield to specifications [42] using standard electron beam lithography, and even tuned post fabrication [43, 44]. These properties have enabled various advances in quantum engineering, for example, the scaling up of quantum processors to ~50 qubits [45] and the fabrication of sophisticated Josephson parametric amplifiers [46]. The cQED framework allows for elucidating the quantum mechanical interaction of various systems with photons, enabling us to understand those systems from a new perspective. As standard JJ circuits continue to advance, cQED is also applied to more exotic systems like non-conventional JJs, mechanical elements, magnons, quantum dots, spin qubits or Majorana zero modes [47].

When the cQED methods are to be applied to phenomena or systems requiring strong magnetic fields, the magnetic-field compatibility of components used in cQED becomes an issue. So far, this issue has been explored as need arose. One component that is particularly useful is a superconducting quantum interference device (SQUID): Two JJs in parallel form a SQUID. They are an important tool in, e.g., metrology [48], and a key building block in many cQED quantum computing architectures [49, 50, 51]. Compatibility of a SQUID with high magnetic fields enables, e.g., studying spin ensembles or even single spins. In this context, SQUIDs based on constriction junctions have demonstrated operation up to 6 T [52]. There is currently a lot of interest in using SQUIDs in external magnetic fields to couple mechanical oscillators to superconducting circuits [53, 54, 55, 56, 57, 58, 59]. Magnetic fields are also a requirement for integrating many spin-qubit architectures with cQED [60, 61], and for many Majorana zero mode realizations [8, 10] where cQED methods could be used for the readout [23]. To couple to quantum dots and topological qubits, magnetic field resilient superconducting resonators have been realized [62, 63, 64]. But the exploration of superconducting qubits in magnetic fields has so far largely relied on semiconductor nanowire JJs [39, 65, 40], graphene JJs [38] or JJs based on granular aluminum [66], with qubits based on carbon nanotube JJs likely following soon [54, 67]. A notable exception is Ref. [68], which explored a standard single-junction Al/AlO_x/Al transmon in a magnetic field, but the findings would suggest that coherence times are already severely limited at 20 mT of in-plane field. So far, alternative-JJ qubit designs have reached higher magnetic fields, but have not consistently achieved the reliability, quality, and targeting of E_J that Al/AlO_x/Al-JJ qubits routinely achieve.

In this article, we explore the magnetic field dependence of the Josephson energy E_J, and the coherence of transmon qubits [16] with standard Al/AlO_x/Al JJs in a 3D copper cavity [69, 70]. The 3D copper cavity is essentially unaffected by the magnetic field and thus allows for exploring the magnetic field dependence of the transmon without additional complications. Planar superconducting resonators are themselves vulnerable to magnetic fields, which proved to be a limiting factor in Ref. [68]. We first show the spectrum as a function of out-of-plane magnetic fields and demonstrate how the limitations imposed on qubit coherence by vortices require precise alignment. With the use of a vector magnet, we can align the magnetic-field axis to

the sample plane with high precision. Thus, we can measure the transmon spectrum and coherence as a function of exact in-plane magnetic field. We track the transition frequencies of the transmons over a range of ~1–7 GHz in in-plane magnetic fields of up to 1 T. Based on the spectrum, we try to understand the geometric effects and the magnetic field dependence of the superconducting gap. One of the transmons has a SQUID loop; therefore, we can investigate combining very sensitive SQUIDs with large magnetic fields. Overall, even the SQUID transmon maintains sufficient coherence for many of the applications mentioned above. Thus, we show that Al/AlO_x/Al JJs can be operated in high magnetic fields to give coherent qubits matching the demonstrated field compatibility of non-standard SNS JJs [40].

2.2. EXPERIMENTAL SET-UP

In Fig. 2.1, we display the 3D copper cavity containing both transmons, the transmon geometries and a sketch relating the JJ geometry to the magnetic field axes. The cavity design is based on Ref. [71]. There is one asymmetric SQUID transmon and one single-JJ transmon; each have their own merits: On the one hand, the SQUID transmon is sensitive to µT out-of-plane fields $B_\perp$, allowing a precise alignment of the magnetic field parallel to the device plane. It is also tunable, meaning measurements will cover a wide frequency range allowing to estimate frequency effects at a similar magnetic field. On the other hand, the single-JJ transmon is less sensitive to flux noise and to the magnetic-field misalignment, and thus it serves as a control device for the SQUID transmon. As shown in Fig. 2.1 **(b)**, the 3D transmons have long narrow leads to the JJ, making it vortex resilient, even though the big capacitor pads do not have intentional vortex trapping sites. Having no magnetic shields, we opted for a small SQUID loop area of 3.4 µm^2.

The JJs are made with a standard Dolan-bridge design [72] with double-shadow evaporation, but for field compatibility we chose a thickness of only 10 nm for the first aluminum layer and 18 nm for the second layer. The JJs presented were made in the same fabrication run; scanning electron micrographs of the junction region can be found in Section 2.A. The design leads to large spurious JJs (see Fig. 2.1 **(c)**) between the two superconducting films, which could complicate the in-plane magnetic field dependence [68]. For more detailed information on the device and on the experimental setup see Ref. [73].

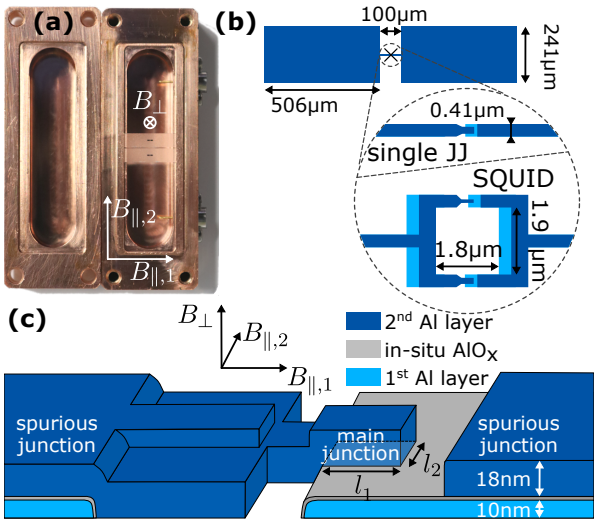

Figure 2.1: **(a)** 3D copper cavity with two transmons, referred to as single Josephson junction (JJ) and SQUID. **(b)** Transmon top view with zoom-in on the junction region for both the single JJ and the SQUID device. **(c)** Sketch of a Dolan-bridge JJ relating the magnetic field coordinate system ($B_{\parallel,1}$,$B_{\parallel,2}$,$B_\perp$) to the JJ geometry.

2.3. OUT-OF-PLANE MAGNETIC FIELD DEPENDENCE

For every in-plane magnetic field shown in this paper, we sweep the out-of-plane magnetic field, $B_\perp$. In contrast to Ref. [74], where vortex-quasiparticle interplay is explored, we do not perform field cooling; rather, we change the magnetic field with the sample remaining at base temperature, as in Ref. [75]. The out-of-plane-field datasets at different in-plane fields are qualitatively similar, even at the highest fields where all quantities can be measured. As an example, Fig. 2.2 **(a)** shows two-tone spectroscopy peaks of the transmon frequencies for a $B_\perp$ range of ~1 mT at $B_{\parallel,1} = 0.17$ T (a $B_{\parallel,1} = 0$ T dataset can be found in Ref. [73]). We always measure both the first and the second excitation energies of the transmons, f_{01} and $f_{02}/2$, to be able to estimate the E_J and the charging energy E_C. [39, 68]. While the frequency of the single-JJ transmon changes only ~10 MHz over this range in $B_\perp$, the SQUID transmon frequency oscillates between top and bottom limits, the sweetspots. The sweetspots are determined by the sum and difference of the E_Js of the constituent JJs. The models for the $B_\perp$ dependence of the spectrum for both transmons can be found in Section 2.E.

We also measure the relaxation time T_1 and the Ramsey and Hahn-echo dephasing times T_2^* and T_2^{echo}

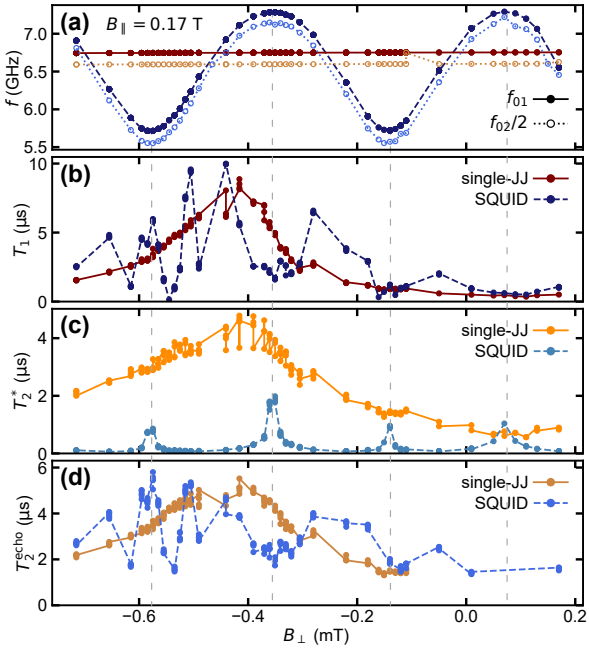

Figure 2.2: Out-of-plane magnetic field dependencies of both transmons, shown here for $B_{\parallel,1} = 0.17$ T. **(a)** First and second transmon transitions f_{01} and $f_{02}/2$. The SQUID transmon changes with out-of-plane magnetic fields $B_\perp$ which thread the SQUID loop. As its constituting JJs are asymmetric, the frequencies oscillate between top and bottom limits, the sweetspots. **(b)** Energy relaxation time T_1. High T_1 times are found in a $B_\perp$-interval from −0.7 mT to −0.25 mT, deviating from the nominal $B_\perp = 0$ based on the SQUID alignment procedure. **(c)** Ramsey dephasing time T_2^*. At the sweetspots, the SQUID frequency is less sensitive to flux noise and T_2^* is enhanced. **(d)** Echo dephasing time T_2^{echo}. In the interval of high T_1, T_2^{echo} is generally not $2T_1$-limited for both transmons.

of the transmons for different $B_\perp$ at a fixed $B_{\parallel,1}$. One can see in Fig. 2.2 **(b)**-**(d)** that both transmons show higher coherence at a finite $B_\perp$ (around $B_\perp \simeq 0.4$ mT. The $B_\perp = 0$ point is based on aligning the parallel magnetic field based on the SQUID oscillation (Section 2.B). Therefore we have to sweep $B_\perp$ at every in-plane magnetic field and map out the value at which T_1 is maximized; we call this B_0 and consider it to be an offset in the perpendicular field dependence. The offset B_0 seems to follow a roughly linear trend as a function of $B_{\parallel,1}$. This is an interesting observation, likely related to vortex physics, but we do not have a concrete understanding at this point (for more details, see Section 2.C).

Apart from the existence of B_0, to understand the effect of $B_\perp$ on T_1, we consider loss due to superconducting vortices coupling to the transmon current (see Section 2.D for details) and the Purcell limit imposed by the cavity (see Section 2.G). For the single-JJ transmon, the frequency remains practically constant when sweeping $B_\perp$, thus the change in T_1 is likely due to vortices. The loss scales linearly with $B_\perp - B_0$ sufficiently far away from the maximum T_1, but the onset of vortex loss is not linear. For the SQUID transmon, we consistently find T_1 to be lower at the top sweetspot than at the bottom sweetspot. Looking at the frequency dependence of T_1, we find that for high frequencies it is Purcell limited (see Section 2.G). The B_0 values for a given $B_{\parallel,1}$ are similar for both transmons (see also Section 2.B).

The dephasing times for both transmons do not reach $2T_1$ in the high T_1 interval. Close to the cavity resonance frequency, photon shot noise from the cavity is a limiting factor to T_2^{echo} (see Section 2.G). Compared to the single-JJ transmon the SQUID shows drastically reduced T_2^* with a clear sweetspot enhancement. For the T_2^{echo}, the sweetspot enhancement is less clear. Thus, the SQUID transmon data points to slow noise in $B_\perp$, limiting T_2^* but not T_2^{echo}.

2.4. IN-PLANE MAGNETIC FIELD DEPENDENCE OF THE SPECTRUM

Next we consider the in-plane magnetic field dependencies of the two transmons. Here we focus on the data obtained for the $B_{\parallel,1}$ direction. For every in-plane-field, $B_{\parallel,1}$, we sweep $B_\perp$ to perform a full set of measurements as explained in Section 2.3. First, we show how the transmon spectra evolve in parallel magnetic fields. As one can see in Fig. 2.3 **(b)**, both transmons decrease in frequency at higher magnetic fields. As the magnetic field increases, the difference between the top and bottom sweetspot frequencies increases (Fig. 2.3 **(a)**), indicating that the E_Js of the two constituting JJs evolve differently. For high $B_{\parallel,1}$, we observe large charge-parity splitting due to the decreasing E_J/E_C-ratio. Thus, for $B_{\parallel,1} = 0.88$ T, the two parity branches of f_{01} are plotted.

Having measured f_{01} and $f_{02}/2$ for both transmons we can estimate E_J (and E_C) as described in Section 2.E. For the high-field/low-E_J/E_C-ratio regions, charge-parity splitting is used to estimate E_J. The resulting E_J as a function of $B_{\parallel,1}$ is shown in Fig. 2.3 **(c)** and **(d)** for the single-JJ and SQUID transmon, respectively. A naïve estimate based on the Ginzburg-Landau (GL) theory for the superconducting gap provides neither qualitative nor quantitative agreement for the in-plane field dependence of E_J (Fig. 2.3 **(c)**). We therefore combine GL theory with a

	$E_J(B_{\parallel,1}=0)$	B_{Φ_0}	l_2
Single-JJ	24.7 GHz	0.83 T	231 nm
SQUID JJ_1	23.5 GHz	0.90 T	206 nm
SQUID JJ_2	6 GHz	1.65 T	122 nm

Table 2.1: Parameters of the three JJs. To determine B_{Φ_0}, the in-plane field for which a superconducting flux quantum is threading the JJ, we fit Eq. (2.1) to the data in Fig. 2.3 **(c)** and **(d)** assuming the same GL critical field $B_\parallel^c = 1.03\,\mathrm{T}$ for all JJs. Then B_{Φ_0} should be inversely proportional to the junction finger width l_2, as determined by SEM imaging.

Fraunhofer term describing the flux penetration into an extended junction

$$E_J(B_\parallel) = E_{J0}\sqrt{1-\left(\frac{B_\parallel}{B_\parallel^c}\right)^2}\left|\mathrm{sinc}\left(\frac{B_\parallel}{B_{\Phi_0}}\right)\right|, \qquad (2.1)$$

where E_{J0} denotes the Josephson energy at zero field, $B_\parallel^c$ the in-plane Ginzburg-Landau critical field, and B_{Φ_0} the in-plane field for which one superconducting flux quantum ($= h/2e$) threads the JJ. B_{Φ_0} is inversely proportional to the in-plane cross section of the junction, defined by its finger width l_2 (see Fig. 2.1 **(c)**) and a constant insulator thickness. As the JJs differ in finger width, each JJ has a different B_{Φ_0}. Assuming the same critical field $B_\parallel^c = 1.03\,\mathrm{T}$ for all three junctions, we find the independently measured junction dimensions are consistent with the estimated B_{Φ_0} (Table 2.1). Taking the values for l_2 and B_{Φ_0} we can calculate the height of the in-plane cross section threaded by $B_{\parallel,1}$ which amounts to a plausible 10 nm. In particular for the asymmetric SQUID transmon this model fits the distinctive behavior of the individual JJs forming the SQUID loop (Fig. 2.3 **(d)**): The larger JJ shows a rapid decrease in E_J followed by a slight upturn for $B_{\parallel,1} > 0.9\,\mathrm{T}$ that is consistent with the emergence of a second Fraunhofer lobe. The smaller JJ in turn is less affected by flux penetration and its E_J decreases slowly and monotonically. While a full BCS modeling of the superconducting gap for thin films could further improve the fits, it is clear that junction geometry plays a role also for conventional $Al/AlO_x/Al$ JJs and should be considered when targeting them for operation in high magnetic fields. The overall JJ footprint should be small and it should especially be narrow in the axis parallel to the magnetic field.

In Fig. 2.3 **(b)** there is a gap in the SQUID data between 0.4 T and 0.5 T and the single-JJ data is more noisy in this area. In this region, no clear SQUID oscillations can be observed when sweeping $B_\perp$. Measurements of the cavity frequency as a function of $B_\perp$ are not reproducible and the cavity frequency is only stable for several minutes, making qubit spectroscopy for both qubits challenging. However, the data points that could be gathered for the single-JJ transmon are generally consistent with the data outside this region. This instability can also be observed when measuring in the $B_{\parallel,2}$ direction, but it arises already at low fields around 20 mT. It is for this reason that we focus on the $B_{\parallel,1}$ direction here. Details on these instabilities for $B_{\parallel,1}$ and $B_{\parallel,2}$ can be found in Ref. [73]. We suspect spurious JJs inherent in our simple fabrication are responsible; it would be beneficial to avoid them when

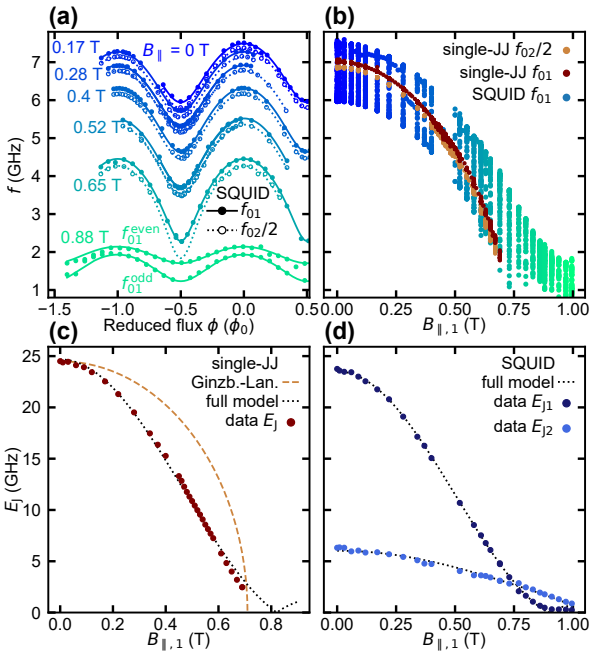

Figure 2.3: Spectroscopy for in-plane magnetic fields. **(a)** Examples of the flux dependence of the SQUID transmon frequency: For every $B_{\parallel,1}$, we sweep $B_\perp$ to tune the SQUID transmon. We measure f_{01} and $f_{02}/2$. With increasing $B_{\parallel,1}$ (color scale corresponds to that in panel **(b)**), both frequencies decrease, and eventually the $f_{02}/2$ transition can no longer be measured. For high $B_{\parallel,1}$, f_{01} is split for even and odd charge parity, which is shown for $B_{\parallel,1} = 0.88\,\mathrm{T}$. **(b)** SQUID f_{01} and single-JJ f_{01}, $f_{02}/2$ transmon transitions versus in-plane magnetic field $B_{\parallel,1}$. **(c)** extracted Josephson energy E_J for the single-JJ transmon. We correct for different systematic errors, for details see Section 2.E. A simple Ginzburg-Landau (GL) theory for the superconducting gap provides neither qualitative nor quantitative agreement. Combining GL theory with the flux penetration into an extended junction, Eq. (2.1), we obtain better agreement (dotted line). **(d)** Josephson energies E_J for the two Josephson junctions forming the asymmetric SQUID transmon. The larger junction E_{J1} is consistent with a second Fraunhofer lobe emerging for $B_{\parallel,1} > 0.9\,\mathrm{T}$.

exploring large magnetic fields [68].

Eventually our measurements become limited by the decreasing signal-to-noise ratio as the dispersive shifts of the transmons become small. Therefore we did not measure the single-JJ transmon at magnetic fields above 0.69 T. However, we can measure characteristic SQUID oscillation over the entire field range of 1 T that is available to us, as the distinctive frequency modulation helps to identify the SQUID transmon transitions. Unfortunately, because values of B_{Φ_0} of the SQUID junctions are above or close to $B_{\parallel}^{c}$, the upturn in E_{J1} for $B_{\parallel,1} > 0.9$ T is relatively weak.

2.5. IN-PLANE MAGNETIC FIELD DEPENDENCE OF THE COHERENCE TIMES

Now we turn from the energy spectrum of the transmons to the coherence as a function of $B_{\parallel,1}$. At each $B_{\parallel,1}$, data sets as the one shown in Fig. 2.2 were taken. To eliminate the $B_\perp$ dependence, Fig. 2.4 (**a**) and (**b**) show the highest 5 % of all T_1, T_2^* and T_2^{echo} measured at each $B_{\parallel,1}$. As seen in Fig. 2.2, the $B_\perp$ for the maximum T_1, T_2^* and T_2^{echo} do not necessarily coincide.

We observe microsecond T_1 over the entire $B_{\parallel,1}$-range measurable in time domain. While the single-JJ transmon T_1 is essentially constant up to 0.4 T, the SQUID transmon T_1 shows a slight improvement with a maximum T_1 of more than 30 µs for $B_{\parallel,1} = 0.34$ T. At that point, the perpedicular field offset B_0 for maximum T_1 coincides with the bottom sweetspot, and as we noted earlier (see Section 2.3) the bottom sweetspot T_1 is usually longer than at the top sweetspot. A slight T_1 improvement is also expected because at higher fields and lower frequencies, the Purcell effect is reduced (see Section 2.G). In the instability region between 0.4 T and 0.5 T, the few data points for the single-JJ transmon (and one data point for the SQUID device) suggest a reduction in T_1. While the single-JJ transmon T_1 stabilizes at a slightly lower 2 - 4 µs after the instability region, the SQUID transmon T_1-dependence for high fields is less clear. We do not understand the sudden drop in T_1 for the SQUID transmon, nor the gradual improvement in T_1 that follows. From $B_{\parallel,1} > 0.65$ T onwards we were unable to perform time domain measurements at the bottom sweetspot as the frequency became too low. Before that our data represents the maximum T_1 across the entire SQUID oscillation; for the highest fields, we lose the lowest frequencies. Quasiparticle-induced decay does not seem to limit our transmons even for the highest magnetic fields, where the superconducting gap is smallest. For details see Section 2.G, where we compare our estimate for the closing of the superconducting gap (Section 2.4) with the qubit lifetimes at high $B_{\parallel,1}$.

We now discuss qubit dephasing. While in general microsecond coherence is maintained up to at least 0.7 T, it is clear that T_2^{echo} is not T_1-limited. To better understand the limiting factors, we calculate the pure dephasing rate $\Gamma_\phi = 1/T_2 - 1/(2T_1)$ for both Ramsey and echo experiments. Fig. 2.4 **(c)** and **(d)** shows $\Gamma_\phi^{\text{echo}}$ as a function of $B_{\parallel,1}$. Here we do no longer restrict the discussion to the top 5 % measured coherence times. Both devices show a qualitatively and quantitatively consistent trend: For in-plane magnetic fields up to 0.4 T, $\Gamma_\phi^{\text{echo}}$ shows a slight decrease, meaning improved coherence. We partially attribute this effect to photon shot noise in the cavity (see Section 2.G), which limits the transmons less as their frequency decreases with increasing field (dashed line). The data would suggest an effective cavity temperature of 76 mK, which is far above the dilution refrigerator base temperature of ~ 10 mK. This could likely be improved by better shielding and filtering. For fields above 0.52 T, we observe increasing qubit dephasing, likely due to charge noise. The transmons approach the low E_J/E_C limit and the charge dispersion $f_{01}(n_g = 0) - f_{01}(n_g = 0.5)$ increases (dashed lines). Here n_g is the charge offset entering the Cooper-pair-box Hamiltonian (see Section 2.E). With increasing charge dispersion, the transmons become proportionally more sensitive to charge noise [16].

As previously noted, the SQUID T_2^* shows a strong sweetspot enhancement; we can therefore characterize the noise in $B_\perp$ as a function of $B_{\parallel,1}$ by performing a sensitivity analysis (see Section 2.F). Here, pure Ramsey dephasing Γ_ϕ^* is analyzed as a function of the SQUID frequency sensitivity $|df_{01}/dB_\perp|$ (Fig. 2.4 **(e)**). For every in-plane magnetic field $B_{\parallel,1}$ we observe a linear dependence $\Gamma_\phi^* = a|df_{01}/dB_\perp| + b$. The inset shows the slope a as a function of $B_{\parallel,1}$, which suggest that noise in $B_\perp$ increases linearly with $B_{\parallel,1}$. The observed noise level and trend are independent of the current source powering the $B_{\parallel,1}$ magnet coil; we compare the Oxford Instruments Mercury iPS to a low-noise Keithley current source (which cannot reach the currents required for higher fields). This suggests the noise is not due to the current source of the $B_{\parallel,1}$ magnet. A possible explanation could be vibrations in the setup that convert $B_{\parallel,1}$ to $B_\perp$. Vibrations are usually low frequency and the

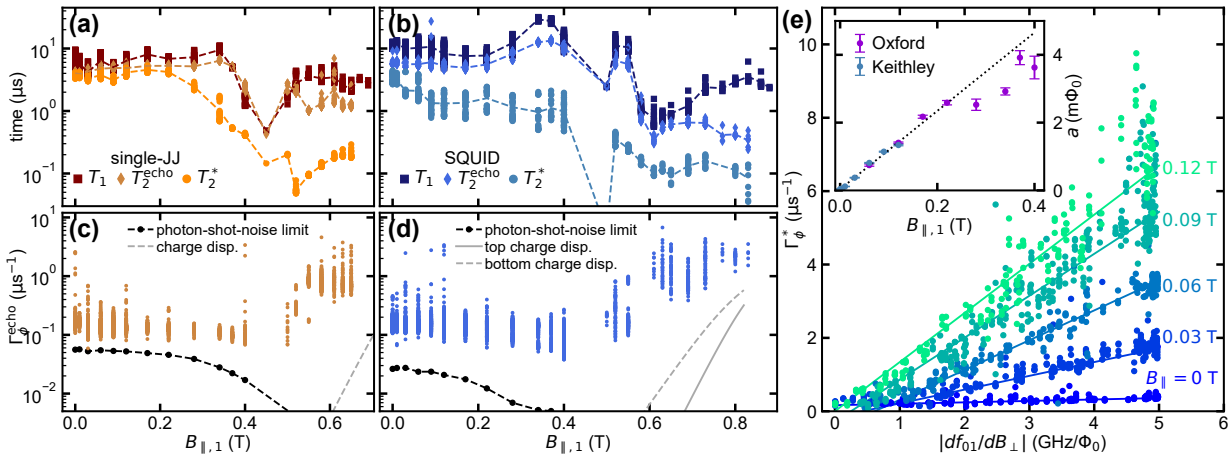

Figure 2.4: Transmon qubit coherence as a function of $B_{\parallel,1}$. $B_\perp$ was varied at each $B_{\parallel,1}$ and we show the highest 5 % of all T_1, T_2^{echo}, T_2^* for **(a)** single-JJ and **(b)** SQUID transmon at each $B_{\parallel,1}$. Dashed lines indicate the mean of the high-coherence data at each field. Microsecond coherence is maintained up to at least 0.7 T, with T_1 above 1 µs over the entire measurable range. **(c)** and **(d)** Pure echo dephasing rates $\Gamma_\phi^{\text{echo}} = 1/T_2^{\text{echo}} - 1/(2T_1)$ versus parallel magnetic field $B_{\parallel,1}$. For low magnetic fields (high frequencies) $\Gamma_\phi^{\text{echo}}$ is limited by photon shot noise. In high magnetic fields the transmons approach the low E_J/E_C limit and the charge dispersion $f_{01}(n_g = 0) - f_{01}(n_g = 0.5)$ increases, eventually limiting the coherence. **(e)** The pure Ramsey dephasing rate Γ_ϕ^* as a function of the SQUID frequency sensitivity $|df_{01}/dB_\perp|$. For every in-plane magnetic field $B_{\parallel,1}$ we observe a linear dependence $\Gamma_\phi^* = a|df_{01}/dB_\perp| + b$. The inset shows the slopes a as a function of $B_{\parallel,1}$, which suggest that the noise in $B_\perp$ increases linearly with $B_{\parallel,1}$. The observed noise level and trend are independent of the current source connected to the $B_{\parallel,1}$ magnet coil (named Oxford and Keithley in the legend). We believe this noise is caused by mechanical vibrations (see text).

noise in $B_\perp$ would increase proportionally with $B_{\parallel,1}$. Γ_ϕ^* would be sensitive to this kind of low-frequency noise. We attempted to confirm this theory by measuring while turning off the pulse-tube cooler, which is likely the main source of vibrations in the dilution refrigerator, but the turning off led to flux jumps and we could not recalibrate in the time the fridge stayed cold.

A similar analysis was performed for T_2^{echo} measurements but $\Gamma_\phi^{\text{echo}}$ as a function of $|df_{01}/dB_\perp|$ is essentially flat, likely because it is mainly limited by photon shot noise or other noise sources that are not $B_\perp$ dependent (see Section 2.G). Due to the asymmetry of the SQUID, $|df_{01}/dB_\perp|$ has an upper limit [76], for a more symmetric SQUID one could increase the $|df_{01}/dB_\perp|$ until flux noise would become a dominant noise source. The asymmetry was useful for extracting the magnetic-field dependence of the individual JJs, but for studying flux noise, a symmetric SQUID would be beneficial. The fact that $\Gamma_\phi^{\text{echo}}$ does not show a strong $B_{\parallel,1}$ dependence is consistent with noise due to mechanical vibrations limiting Γ_ϕ^*, because mechanical vibrations are expected to be low-frequency and the noise can be largely echoed away. A similar situation is reported in Ref. [77].

2.6. CONCLUSION

The present results show that for many applications in magnetic fields up to 0.4 T, the standard Al-AlO$_x$-Al JJs can be a viable option. In this regime T_1 and T_2^{echo} times remained largely unaffected in our transmons, but accurate in-plane alignment of the magnetic field is paramount to preserve coherence. We use thin aluminum films to increase the in-plane critical field and narrow leads to minimize vortex losses. For higher fields, coherence times are reduced compared to low-field levels, but the standard Al/AlO$_x$/Al transmon can be operated at magnetic fields up to 1 T, comparable to semiconductor nanowire transmons [40], while exhibiting better coherence times. For the $B_{\parallel,1}$ direction, the frequency dependence of the transmon was found to be reasonably well described by a simple model, which considers the gap closing according to the Ginzburg-Landau theory, and a Fraunhofer-like geometrical contribution. In addition, we have shown that the operation of a SQUID transmon is possible in high in-plane fields, although vibrations of the magnet relative to the sample and noise from magnet current sources could become a limiting factor. These challenges seem solvable with better vibrational damping of the dilution refrigerator and the use of persistent current magnets. However, between 0.4 T and 0.5 T,

regular SQUID oscillations could not be observed and the cavity frequency was unstable. We speculate this is due to spurious JJs inherent in the Dolan bridge fabrication.

With thinner films and possibly shifting to a JJ fabrication that minimizes spurious JJs, such as Manhattan style JJs [78] or JJs that are made with two lithography steps [79], it would be possible to make an Al-AlO$_x$-Al JJ transmon that can work above 1 T. If the target magnetic field is known in advance and the film properties are largely characterized, one can account for the reduction in E_J due to suppression of the superconducting gap. Then, the Al-AlO$_x$-Al JJ advantages of high quality, decent yield and targeting will remain available even in experiments that require high magnetic fields. In future, it would be interesting to look into charge parity dynamics and thermal excitation in the transmon at higher fields [80]. Strong in-plane magnetic fields present an additional tuning knob in cQED, which could help understand the physics of the quasiparticles coupling to the transmon. We also believe that with slight improvements in the setup, it would be possible to measure the effect of magnetic fields on flux noise and shed light on the nature of the spin ensembles that are believed to cause it [81].

ACKNOWLEDGMENTS

We would like to thank Ida Milow for her internship in the lab and contributions to our code base. We thank T. Zent and L. Hamdan for technical assistance and D. Fan for help with setting up the aluminum evaporator. We thank A. Salari, M. Rössler, S. Barzanjeh, M. Zemlicka, F. Hassani, and M. Peruzzo for contributions in the early stages of the experiment. This project has received funding from the European Research Council (ERC) under the European Union's Horizon 2020 research and innovation program (grant agreement No 741121) and was also funded by the Deutsche Forschungsgemeinschaft (DFG, German Research Foundation) under CRC 1238 - 277146847 (Subproject B01) as well as under Germany's Excellence Strategy - Cluster of Excellence Matter and Light for Quantum Computing (ML4Q) EXC 2004/1 - 390534769

2.A. DEVICE FABRICATION, GEOMETRY AND FILM THICKNESS

The two transmon devices are standard 3D transmons with a Dolan-bridge Josephson junction (JJ) [72]. They were fabricated in a single electron-beam lithography step and a double-shadow evaporation using a Plassys MEB 550S evaporator. The aluminum has 5N purity. To be able to mix and match, many transmon with varying JJ parameters were fabricated in the same run on a large sapphire piece and then diced. Thus, the two transmons in this experiments, while on two disconnected sapphire pieces, should have very similar aluminum film and junction properties. The JJ geometry for both with all relevant measurements can be seen in the SEM pictures (Fig. 2.5). Because the taking of SEM pictures alters or destroys the JJs, the actual devices were imaged after measurements were completed. In the junction test prior to the fabrication of the devices, the relative spread of the room temperature resistances was on the order of 4 %. We believe this to be largely due to the lithography rather than film roughness or a non-uniform oxide layer. In the test, 79 out of 96 JJs were working, but we were limited by trying to make small JJs for large SQUID asymmetry. The reliability of our fabrication process is also confirmed by the fact that the critical current densities of the three junctions studied (proportional to the ratio of E_Js in Table 2.1 over the junction areas from Fig. 2.5) are approximately the same.

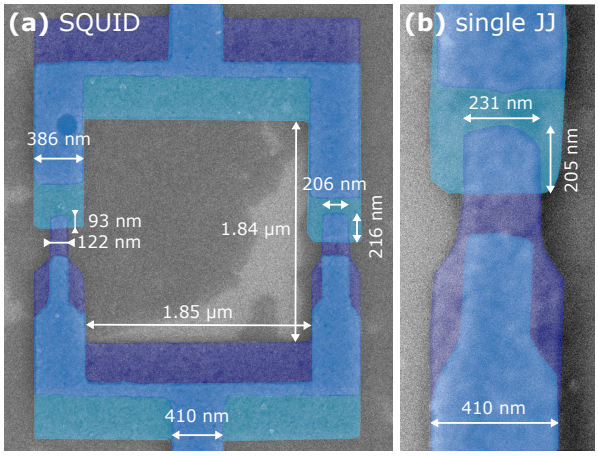

Figure 2.5: False-colored SEM pictures of **(a)** the SQUID loop of the SQUID transmon and **(b)** single JJ of the single-JJ transmon. Bottom aluminum layer is overlayed with a turquoise layer, while the top layer is overlayed with a violet layer, leaving the overlap region colored blue. Measurements of the different dimensions are indicated (some taken from other images with larger resolution).

Crucially, the film thicknesses for the two evaporations were nominally 10 nm and 18 nm for the bottom and top layers, respectively. Reducing the film thickness further should be possible using the same evaporator. For previous devices with film thicknesses

of 15 nm (bottom layer) and 30 nm (top layer), the in-plane critical field was on the order of 250 mT to 300 mT. In contrast, Al films of thickness $d \sim 7$ nm can remain superconducting up to 3 T [82]. As shown there, at this thicknesses the orbital effect of the parallel field and the Zeeman splitting contribute approximately equally to suppressing superconductivity. It is only for thicker films that one can use the relation [17]

$$B_{\parallel}^{c} = B_c \frac{\sqrt{24}\lambda}{d}, \tag{2.2}$$

with B_c the thermodynamic critical field and λ the (effective) penetration depth, which qualitatively explain the increase in critical field with decreasing thickness. Nonetheless, using the low-temperature value of the critical field for aluminum ($B_c = 10$ mT), estimating the mean free path ℓ to be of the order of the thickness, and using $\lambda \approx \lambda_L \sqrt{\xi_0/\ell}$, with the London penetration depth $\lambda_L = 16$ nm and the coherence length $\xi_0 = 1600$ nm, we find from Eq. (2.2) the estimate $B_{\parallel}^{c} \approx 1$ T for the $d = 10$ nm thick film in our devices. For comparison, the same procedure for $d = 15$ nm and 30 nm gives $B_{\parallel}^{c} \approx 0.5$ and 0.2 T, compatible with our measurements.

We note that the numerical results for the order parameter presented in Ref. [82] can be well approximated, not too close to the parallel critical field, by the Ginzburg-Landau formula

$$\Delta(B_{\parallel}) = \Delta_0 \sqrt{1 - \left(\frac{B_{\parallel}}{B_{\parallel}^{c}}\right)^2}, \tag{2.3}$$

although with a (fitted) critical field larger than the one obtained numerically. While this justifies the phenomenological use of Eq. (2.3) in analyzing the data, in our devices a further complication arises due to proximity effect between two films of different thickness; however, modeling of this effect is beyond the scope of the present work.

2.B. ALIGNMENT OF MAGNETIC AXES TO SAMPLE

Here we illustrate the alignment procedure to align our magnet axes precisely to the in-plane direction of our sample. We used the SQUID oscillation offset as a signal, to construct the two in-plane axis $B_{\parallel,1}$ and $B_{\parallel,2}$ from the physical magnet axes B_x, B_y, B_z. In our case the magnet B_x corresponds roughly to $B_\perp$. The current source connected to the B_x coil has a finer resolution and lower noise than the one connected to B_y and B_z. We therefore only used the B_x coil to correct the extra out-of-plane field caused by B_y and B_z and not vice versa. This is a simple rotation that we apply in software before setting the values.

To determine the alignment we took a 2D map of the cavity frequency as a function of B_x and B_y (or B_z). These measurements are fast and we can scan the B_x field for several B_y with few visible jumps. A linear change in the offset of the SQUID oscillation along the B_x axis with changing B_y is due to an additional out-of-plane component of B_y. Then a linear fit is performed to find the misalignment which is then corrected by an additional B_x field as a function of B_y. The resulting axis is our $B_{\parallel,1}$. An aligned data set can be seen in Fig. 2.6 **(a)**, a color plot of the cavity resonance frequency normalized line by line vs $B_\perp$ and $B_{\parallel,1}$. The stable offset of the oscillation over a large range of $B_{\parallel,1}$ suggests that we have aligned our magnetic field axis to better than 0.05°. We determined the initial misalignment to be −0.61° between the B_y and $B_{\parallel,1}$ axis. For very low field there is usually a small deviation which we attribute to small residual ferromagnetism in the vicinity of our sample being magnetized. A more concrete example with misaligned and aligned data for the $B_{\parallel,2}$ direction can be found in Ref. [73].

2.C. UNUSUAL $B_\perp$-DEPENDENCE OF T_1 AND THE MAXIMUM QUBIT FREQUENCY

The alignment of the magnet axes on the SQUID oscillation seems natural and gives a straightforward linear alignment procedure. While one would expect T_1 as well as the qubit frequency (meaning the superconducting gap) to be maximal at the nominal $B_\perp = 0$ (which depends on the alignment), we observed that they take their maximum values at finite values of $B_\perp$; furthermore, these values are different for the maximum T_1 and the maximum qubit frequency.

When looking at the $B_\perp$ corresponding to the largest T_1 at a given $B_{\parallel,1}$ for both transmons (Fig. 2.6 **(b)** and **(c)**, we see that it increasingly deviates from $B_\perp = 0$. In the following, we focus on the single-JJ transmon T_1 data, because it shows more clear peaks as there is no additional frequency dependence that complicates the picture. We designate the $B_\perp$ corresponding to optimal T_1 as B_0. B_0 changes linearly with $B_{\parallel,1}$, such that we can estimate the angle

with respect to the sample plane which is roughly −0.15° (data labeled T_1^{maximum} in Fig. 2.6 **(a)**). The dependence of T_1 on $B_\perp$ is likely due to vortex creation, which takes place largely in the large capacitor pads. We show in Section 2.D, that apart from this offset it appears that the data is consistent with the vortex hypothesis. Initially we believed that there could be hysteresis in the vortex system, which could lead to an offset in B_0. So when changing $B_{\parallel,1}$, we tried to scan $B_\perp$ back and forth approaching the estimated $B_\perp$ = 0 mT point, a procedure laid out in Ref. [83]. However, this procedure did not make a big difference. Some data on the hysteresis in $B_\perp$ at $B_{\parallel,1} = 0$ can be found in Ref [73] and while we see hysteresis in the SQUID offset and in the T_1 data, it is not necessarily identical. Ultimately we found that B_0 seemed to be stable for up and downscan in $B_{\parallel,1}$, therefore it appears that hysteresis does not fully explain the effect. This effect could be investigated in more detail, we did, e.g., not explore the negative direction in $B_{\parallel,1}$, but it is beyond the scope of this work.

Peculiarly, the $B_\perp$ value corresponding to the maximum frequency of the single-JJ transmon seems to also linearly deviate from $B_\perp = 0$ at different $B_{\parallel,1}$, corresponding to an angle of 0.8° with respect to the in-plane direction (see inset of Fig. 2.9 **(a)**). Two example data sets for the frequency of the single-JJ transmon as a function of magnetic field can be found in Fig. 2.9. If one assumes that only E_J is field dependent, the maximum frequency corresponds to the maximum superconducting gap immediately at the JJ. Possibly due to flux focusing in the vicinity of the JJ, which has a step in the $B_{\parallel,1}$ direction, there is an additional angle with respect to the sample plane. While the differences in angle between the SQUID, the vortex system and the maximum frequency of the single-JJ transmon are small in absolute terms, they are clearly distinguishable in our data.

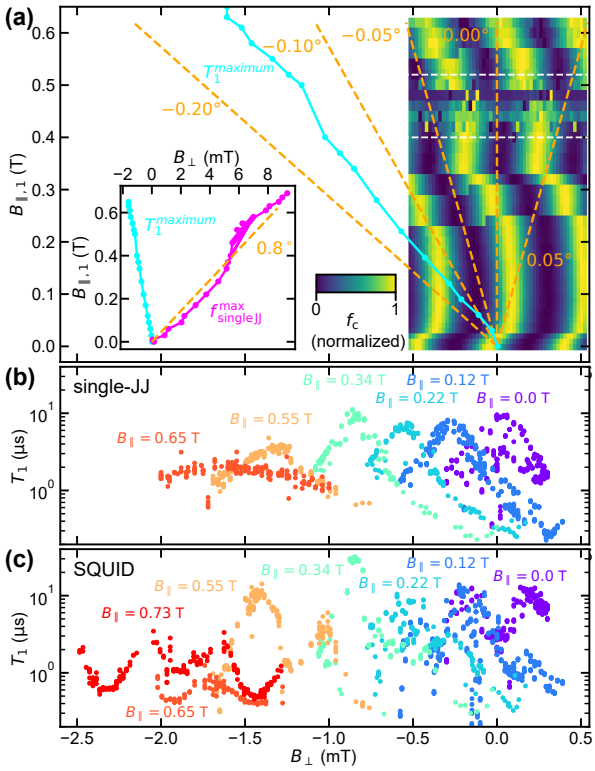

Figure 2.6: **(a)** Cavity frequency (line-by-line normalized for contrast) as a function of $B_\perp$ and $B_{\parallel,1}$ (color plot). We observe clear SQUID oscillations in the cavity frequency with a stable period for a large range of magnetic field. Occasional jumps can change the flux offset of the oscillations. The region between the two dashed white lines shows no stable SQUID oscillations. For perfect alignment, the oscillation offset should be constant for different $B_{\parallel,1}$. Orange dashed lines corresponding to different angular misalignment are given as a guide to the eye. We conclude that our alignment should be within ±0.05° with respect to the plane of the SQUID. The cyan line indicates the $(B_\perp, B_{\parallel,1})$ values corresponding to the maximum T_1 of the single-JJ transmon. The maximum T_1 values follow an axis at a ∼−0.15° angle with respect to the sample plane. The inset additionally shows the $(B_\perp, B_{\parallel,1})$ values corresponding to the estimated maximum frequency of the single-JJ transmon (magenta) which follows an axis that is at a ∼0.8° angle with respect to the sample plane. **(b)** and **(c)** Example data sets of T_1 as a function of $B_\perp$ for single-JJ and SQUID transmon respectively for different $B_{\parallel,1}$.

2.D. VORTEX LOSS IN OUT-OF-PLANE MAGNETIC FIELDS

In Fig. 2.4, we plot the best T_1 times as a function of $B_{\parallel,1}$; however, reaching the longest possible T_1 crucially depends on finding the appropriate $B_\perp$ value for a given $B_{\parallel,1}$, as we discuss in Section 2.B, pointing to the possible role of vortices. Indeed, as shown both in resonators [84] and transmons [75], the loss is proportional to the number of vortices; above a certain threshold field B_{th}, this number increases linearly with $B_\perp$. However, vortices can enter into the large transmon capacitor pads already at fields smaller than B_{th} [84, 85], leading to a more gradual onset of vortex dissipation. To phenomenologically capture this behavior, we fit the vortex contribution to dissipation Γ_v with the formula

$$\Gamma_v = \sqrt{p^2 \tilde{B}_\perp^2 + q^2} - q, \tag{2.4}$$

where p and q are fit parameters, which we discuss below, and $\tilde{B}_\perp = B_\perp - B_0$, with the offset B_0 being the value of the perpendicular field where T_1 is the largest for a given $B_{\parallel,1}$ (see Section 2.C). We show in Fig. 2.7

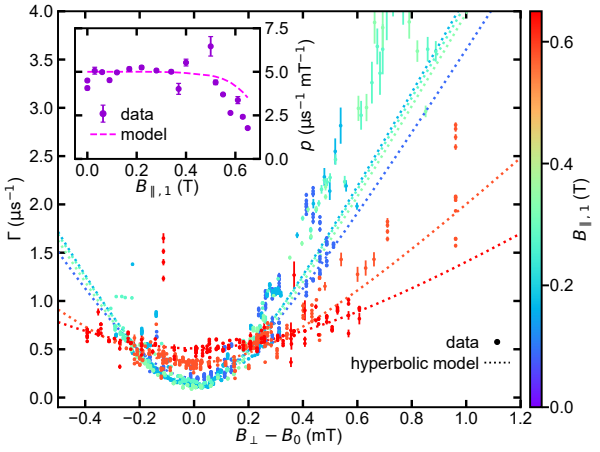

Figure 2.7: Single-JJ transmon relaxation rate $\Gamma = 1/T_1$ vs $B_\perp - B_0$ for various $B_{\parallel,1}$. The data are fitted using a phenomenological hyperbolic model (Eq. (2.4). The inset shows the fitted asymptotic slope p of Eq. (2.4). Interestingly, for $B_{\parallel,1} \geq 0.5\,\mathrm{T}$ the slope shows a significant drop for high $B_{\parallel,1}$. We can model this decrease in p (dashed pink line) which we mainly attribute to the decreasing qubit frequency.

the total relaxation rate $\Gamma = 1/T_1$ as function of $B_\perp - B_0$ for several values of the parallel field; note that $\Gamma = \Gamma_0 + \Gamma_v$ includes also the non-vortex contribution Γ_0. Data over a wider range of perpendicular field, showing more clearly a regime of linear dependence of Γ_v on $B_\perp$, is reported in Ref. [73].

In fitting the data of Fig. 2.7, we fix $q = 1.3\,\mu\mathrm{s}^{-1}$, while we treat p as a parallel field-dependent quantity. The inset in Fig. 2.7 presents the value of p as a function of $B_{\parallel,1}$; The coefficient p is the slope in the linear regime of Γ_v vs $B_\perp$. As discussed in Ref. [84], the value of the slope is affected by the so-called flux-flow viscosity η and the presence of pinning centers that can lead to vortex creep. Considering the model for the flow resistivity of Ref. [84] (see also [86]), we can write

$$p = p_0 \frac{1}{\sqrt{1-(B_\parallel/B_\parallel^{\mathrm{crit}})^2}} \frac{F(f(B_\parallel)/f_d,\epsilon)}{F(f(0)/f_d,\epsilon)}, \tag{2.5}$$

where by construction p_0 is the slope at zero parallel field, $f(B_\parallel)$ is the transmon frequency as function of the parallel field, f_d is the depinning frequency, marking the crossover from elastic to viscous response of the vortices, and $0 \leq \epsilon \leq 1$ is the dimensionless creep parameter. For aluminum, the latter two quantities take the values $f_d = 4\,\mathrm{GHz}$ and $\epsilon = 0.15$ [84]. The function F is defined as

$$F(x,\epsilon) = \frac{\epsilon + x^2}{1 + x^2}. \tag{2.6}$$

Finally, the factor in the middle of Eq. (2.5) arises as follows: the loss is inversely proportional to the viscosity η, and the latter is proportional to the upper critical field $B_{c2} = \Phi_0/(2\pi\xi^2)$, where $\xi \approx \sqrt{\hbar D/\Delta}$ is the coherence length in a disordered superconductor, with D the diffusion constant (physically, the loss increases with the square of coherence length because the latter determines the radius of the vortex core). Therefore, we expect $p \propto 1/\Delta(B_\parallel)$, a factor that we estimate using Eq. (2.3).

The curve in the inset of Fig. 2.7 has been plotted using Eq. (2.5), with the qubit frequency obtained from the data in Fig. 2.3 **(b)** and $B^{\mathrm{c}}_{\parallel,1} = 1.03\,\mathrm{T}$, see the caption of Table 2.1. Hence $p_0 = 5\,\mu\mathrm{s}^{-1}\,\mathrm{mT}^{-1}$ is the only free parameter, which has been fixed by fitting the data for $B_\parallel \leq 0.4\,\mathrm{T}$; for comparison, accounting for their different frequencies through the function F of Eq. (2.6), the two qubits measured in Ref. [75] have $p_0 = 0.5$ and $1.2\,\mu\mathrm{s}^{-1}\,\mathrm{mT}^{-1}$. The curve captures the experimental drop of the slope with parallel field, implying that the decrease in dissipation at low frequency due to pinning has a stronger effect compared to the increase due to the expansion of the vortex cores. Based on this result, we expect that by introducing pinning sites or vortex-trapping holes in the pads, the qubit can be made more robust to out-of-plane fields and less sensitive to misalignment, although care must be taken in not increasing dielectric losses [87].

Returning now to Eq. (2.4), the parameter q can be related to the threshold field by $B_{\mathrm{th}} \sim q/p$; however, this identification is meaningful only at zero parallel field, since at higher field (and hence lower frequency) p is suppressed due to pinning. In this way, we estimate $B_{\mathrm{th}} \sim q/p_0 \approx 0.26\,\mathrm{mT}$, similar to the value at which decrease in T_1 starts in Ref. [75]. In that case, this value is related there to the lower critical field for vortex entry into a region of the capacitor pads, close to the JJs, of lateral size $\sim 10\,\mu\mathrm{m}$. However, this explanation is not applicable to our device, since there are no features with comparable dimensions, and we expect vortex entry in the pads already at a few μT. We speculate that B_{th} could be related to the number of vortices exceeding the number of pinning sites. We do not expect vortices to enter the thin leads to the JJs in our device, because the lead width $w = 410\,\mathrm{nm}$ is only a few times the coherence length $\xi \sim 0.85\sqrt{\xi_0 \ell} \approx 108\,\mathrm{nm}$ (see Section 2.A). In fact, an order-of-magnitude estimate for the field of vortex entry into the leads B_v applicable in the case $w \gg \xi$ is $B_v = \Phi_0/w^2 \approx 10\,\mathrm{mT}$ [85]. Although the condition $w \gg \xi$ is not satisfied, this value suggests that vortices are not present in the leads in the few mT range of perpendicular field explored in this work.

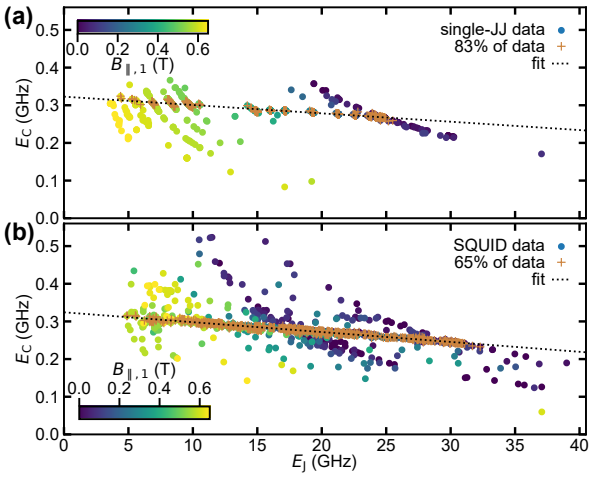

Figure 2.8: **(a)** Single-JJ and **(b)** SQUID transmon E_C as a function of E_J. This data was extracted from pairwise spectroscopic measurements of f_{01} and $f_{02}/2$. For every pair, we fit the transitions to a numerical Cooper-pair box Hamiltonian, giving a value for E_J and E_C (see text). We find a clear correlation of E_C and E_J: 65 % of all SQUID data and 80 % of all single JJ qubit data gather around a linear trend to within 10 MHz. The outliers can be due to a number of effects: bad peak fits (e.g. picking a wrong photon number peak), flux or n_g jumps between the f_{01} and $f_{02}/2$ measurements. Fitting a linear dependence we can infer E_C from E_J.

2.E. ESTIMATION OF E_J AND E_C FROM SPECTROSCOPY DATA

In Fig. 2.3 we show E_J as a function of $B_{\parallel,1}$. Here we want to elaborate on how we estimate E_J and E_C from the measured transmon spectrum. We also consider systematic errors, such as additional dependence on $B_\perp$ and cavity dressing.

E_J and E_C can be extracted from f_{01} and $f_{02}/2$ by fitting the measured transitions to a numerical Cooper-pair box Hamiltonian in the charge basis

$$H = 4E_C \sum_{n=-k}^{k} (n-n_g)^2 |n\rangle\langle n| + \frac{1}{2}E_J \sum_{n=-k}^{k} (|n\rangle\langle n+1| + |n+1\rangle\langle n|), \tag{2.7}$$

with charge states $|n\rangle$, where n stands for the difference in Cooper pairs between the two islands. A voltage gate or environmental noise can introduce a charge offset n_g. k is the truncation in the charge basis; we usually truncate at $k = 20$, thus include 41 states. That way we obtain accurate results in both the transmon regime and the low E_J/E_C regime, where $f_{01} \approx \sqrt{8E_JE_C} - E_C$ stops being a good approximation. Every pair of f_{01} and $f_{02}/2$ measurements will then give a value for E_J and E_C. The data are shown in Fig. 2.8.

The data shows a clear correlation between E_J and E_C because the participation of the cavity capacitance depends on the impedance matching between the cavity and transmon mode and therefore on E_J. The coupling between cavity and transmons is also not constant but depends on E_J and E_C. The dependence looks very similar for both transmons and we can assume a linear dependence of E_C on E_J. The outliers in the data set can be due to a number of effects: bad peak fits (e.g. picking a wrong photon number peak), flux or n_g jumps between the f_{01} and $f_{02}/2$ measurements or hysteresis in the magnetic field. Throughout the experiment we used continuous wave spectroscopy. The powers were constantly adapted as the qubit-cavity detuning grew trying to maintain a balance between visibility and minimizing the shifts due to the readout tone and the AC stark shift.

Both the single-JJ and the SQUID transmon transitions vary with $B_\perp$. Furthermore, our large spectroscopy dataset has outliers. As we sweep a small range in $B_\perp$ for every $B_{\parallel,1}$, we can identify and reject outliers easily. To obtain a robust estimate of $E_J(B_{\parallel,1})$, we do not extract all individual values for E_J from all f_{01} and $f_{02}/2$ pairs, but rather fit a model to all transitions measured at a given $B_{\parallel,1}$ as a function of $B_\perp$. In the following we will give the models we used for the $B_\perp$ dependence for the two transmons.

For the single-JJ transmon, the out-of-plane field dependence is dominated by a suppression of the superconducting gap. As in the case of the in-plane magnetic field, we model it using Ginzburg-Landau dependence of the gap on field [17]

$$E_J(B_\perp) \propto \Delta(B_\perp) = \Delta(0)\sqrt{1-\left(\frac{B_\perp}{B_\perp^c}\right)^2}. \tag{2.8}$$

Using the same form as in Eq. (2.3) seems appropriate since, as discussed at the end of Section 2.D, we do not expect vortices to play a role in the leads to the JJ at least up to $B_\perp \sim 10$ mT, which covers the range of perpendicular field in our measurements. Note that the critical field $B_\perp^c$ of the junction leads should not be confused with the upper critical field B_{c2} of the much wider pads introduced in Section 2.D.

When simultaneously applying an in-plane and an out-of-plane magnetic field the effective $B_\perp^c(B_{\parallel,1})$ is reduced. In Ginzburg-Landau theory for thin films, for any angle θ to the film plane, the critical field $B_c(\theta)$ lies

in between $B_\perp^c$ and $B_{\parallel,1}^c$ and satisfies [17]

$$\left|\frac{B_c(\theta)\sin\theta}{B_\perp^c}\right| + \left(\frac{B_c(\theta)\cos\theta}{B_{\parallel,1}^c}\right)^2 = 1. \tag{2.9}$$

Example data for the single-JJ transmon transitions as a function of $B_\perp$ can be found in Fig. 2.9. We only measured spectroscopy for a ~ 10 mT range in $B_\perp$ at $B_{\parallel,1} = 0$ T and at $B_{\parallel,1} = 0.58$ T. At other fields, we generally measured a range of ~ 2 mT in $B_\perp$ around the high-coherence interval, because we want to mainly make the case that high coherence can be maintained. But the frequency maximum as a function of $B_\perp$ for the single-JJ transmon increasingly deviates from the maximum coherence time (see Section 2.B). In Fig. 2.9 **(b)**, the transmon frequency in the high-coherence interval around −1.5 mT is about 150 MHz lower than the maximum frequency we measured. To account for this, we try to estimate the maximum E_J at every $B_{\parallel,1}$ by fitting all data we have in $B_\perp$ for this $B_{\parallel,1}$. In the fit, we fix $B_\perp^c$ and $B_{\parallel,1}^c$ and use Eq. (2.9) to extract the effective $B_\perp^c(B_{\parallel,1})$ at each $B_{\parallel,1}$. The free parameters are the maximum E_J, the E_C and the offset in $B_\perp$. For the highest fields this suggests a ~10 % correction on the E_J. Note that when we model the magnetic field dependence of the transmon frequencies, we consider the field dependence of E_J and therefore of the superconducting gap right at the JJ. In fact, Eq. (2.8) accounts for the gap suppression due to the perpendicular component of the field. This mechanism would result in the first term of Eq. (2.9) to be a square, as the second term, rather than an absolute value; the absolute value originates from the effect of vortices [17]. As we discussed, it is unclear what ultimately determines the perpendicular critical field in the leads, and hence which formulation is the correct one. In the measured range of parallel field, the two approaches give effective $B_\perp^c$ differing by at most 25 %, so we opted to use the well-known Eq. (2.9). In future experiments this could be easily explored by measuring larger ranges in $B_\perp$ for each $B_{\parallel,1}$.

For the SQUID transmon, the effective E_J will depend on $B_\perp$ and on the two individual Josephson energies E_{J1} and E_{J2} according to:

$$E_J(B_\perp) = E_{J,\Sigma}\sqrt{\alpha_{JJ}^2 + \left(1-\alpha_{JJ}^2\right)\cos\left(\frac{\pi B_\perp}{B_{\Phi_0,\mathrm{SQUID}}}\right)^2}, \tag{2.10}$$

with $E_{J,\Sigma} = E_{J1} + E_{J2}$, the JJ asymmetry parameter $\alpha_{JJ} = |E_{J1} - E_{J2}|/(E_{J1} + E_{J2})$ and the out-of-plane field $B_{\Phi_0,\mathrm{SQUID}}$ that corresponds to a flux quantum through the SQUID loop. Intuitively the Josephson energies at the top (bottom) sweetspot correspond to the sum (difference) of the individual E_Js. Neglecting the suppression of the superconducting gap with $B_\perp$ that we have noted for the single-JJ transmon above, one can fit this dependence to a SQUID oscillation and get a result for E_{J1} and E_{J2}. In the fitting model, we use the linear relation of E_J and E_C extracted before. The suppression of the superconducting gap with $B_\perp$ can be neglected because of the large difference between $B_\perp^c \approx 30$ mT and $B_{\Phi_0,\mathrm{SQUID}} \approx 0.43$ mT. We also do not observe that the sweetspot frequencies vary as strongly with $B_\perp$ as the frequency of the single-JJ transmon.

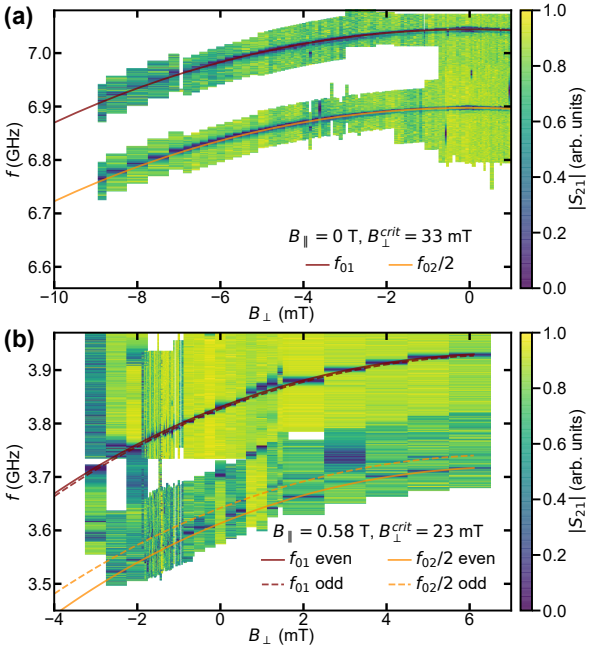

Figure 2.9: Single-JJ transmon f_{01} and $f_{02}/2$ as a function of $B_\perp$ for $B_{\parallel,1} = 0$ T **(a)** and for $B_{\parallel,1} = 0.58$ T **(b)**. The data for **(a)** was taken in a previous cooldown in a different but nominally identical dilution refrigerator. We use this data to estimate $B_\perp^c$ using a fit of a simple Ginzburg-Landau model. The effective $B_\perp^c$ is lower in **(b)** as the superconductivity is also suppressed by the in-plane field.

Close to the cavity frequency, the anharmonicity of the transmon is modified by hybridization with the cavity. To estimate this effect and correct for it, we fit a two-qutrit-one-cavity Hamiltonian of the form

$$H = H_0 + H_{\mathrm{coupling}} + H_{qq}. \tag{2.11}$$

Here, H_0 is the uncoupled Hamiltonian for two qutrits and a resonator,

$$\begin{aligned} H_0 = {} & \hbar\omega_c a^\dagger a \\ & + \omega_{01,1}\,|1\rangle_1\langle 1|_1 + \omega_{02,1}\,|2\rangle_1\langle 2|_1 \\ & + \omega_{01,2}\,|1\rangle_2\langle 1|_2 + \omega_{02,2}\,|2\rangle_2\langle 2|_2\,, \end{aligned} \tag{2.12}$$

with $\omega_c = 2\pi f_{cav}$ the cavity angular frequency and creation/annihilation operators ω_c, a and $a^\dagger$. $H_{coupling}$ then models the qutrit-cavity interaction in the rotating-wave approximation, but avoiding the dispersive approximation:

$$H_{coupling} = \hbar g_1 \left[\left(|0\rangle_1 \langle 1|_1 + \sqrt{2}\,|1\rangle_1 \langle 2|_1 \right) a + \text{c.c.} \right] + \hbar g_2 \left[\left(|0\rangle_2 \langle 1|_2 + \sqrt{2}\,|1\rangle_2 \langle 2|_2 \right) a + \text{c.c.} \right]. \tag{2.13}$$

Here, $g_{1,2}$ denote the coupling strength between the respective qutrit and the cavity. Finally, H_{qq} would be a direct qubit-qubit interaction. However, we measured the qubit-qubit avoided crossings at several fields and can bound the interaction to below 1 MHz. For the fit, we only used data away from the avoided crossing and neglected this term. Having a data set of dressed transitions ω_c, $\omega_{01}^{(q1)}$, $\omega_{02}^{(q1)}/2$, $\omega_{01}^{(q2)}$ and $\omega_{02}^{(q2)}/2$ we fit the respective energy levels of Eq. (2.11) to these transitions (see Fig. 2.10 **(a)**). Approximating the bare cavity frequency by its high power limit, $f_{cav} = 8.107\,\text{GHz}$, we obtain the cavity-qutrit couplings and bare qutrit frequencies. The couplings $g_{1,2}$ show a slight frequency dependence, which is expected as the transmon dipole moment is dependent on E_J and E_C [16]. In the fit range, we can approximate $g_{1,2}/2\pi = 57\,\text{MHz} + 0.01\,f_{01}$, meaning $g_{1,2}/2\pi$ ranging from 100 MHz to 130 MHz. Refitting the estimated bare SQUID frequency dependence with $B_\perp$, we obtain more accurate values for the transmon E_J and E_C. The bare and dressed values for E_C and E_J are compared in Fig. 2.10 **(b)** and **(c)**. The downward correction of E_J is less than 3 %. With increasing field, the correction becomes even smaller, as the qubit frequencies and consequently the hybridization with the cavity mode decrease. The E_J presented in the main text is based on the bare levels when the transmon frequencies are close to the cavity.

For the highest fields, charge-parity splitting becomes a dominant effect in the transmon spectrum, as the E_J/E_C ratio becomes small. In spectroscopy, we observe peaks for the odd and even parity subspace and the charge offset n_g randomly changes. Example data sets and fits for single-JJ and SQUID qubit are shown in Fig. 2.11 **(a)** and **(b)**. The Hamiltonian remains the same as Eq. (2.7), but we evaluate it for $n_g = 0$ and $n_g = 0.5$ to have the two parity branches. Populations of those two states as well as the exact value of n_g are random and drift. In order to extract E_J and E_C in this regime we fitted transitions from the charge-parity split Hamiltonian to bound the experimental data.

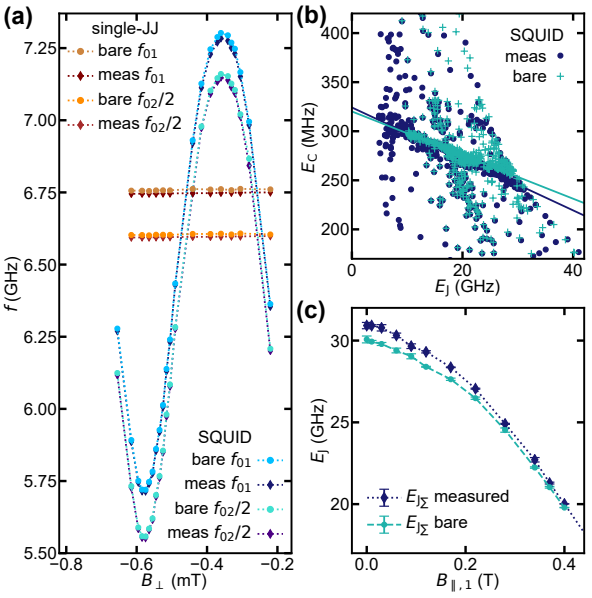

Figure 2.10: Estimating bare transmon parameters. **(a)** Fitting a two-qutrit-one-cavity Hamiltonian to the measured frequencies, we can estimate the bare transmon frequencies. Closer to the cavity resonance frequency ($f_c = 8.1$ GHz), the hybridization is stronger leading to a larger correction. **(b)** The E_C-E_J correlation, as described in Fig. 2.8 gives a slightly altered linear trend for E_Cs from bare frequencies. **(c)** Refitting the estimated bare SQUID flux arches we obtain a downward correction of E_J by 3 %. With increasing field the correction becomes smaller, as the qubit frequencies and consequently the hybridization with the cavity mode decrease.

2.F. SENSITIVITY ANALYSIS OF NOISE IN $B_\perp$

Any noisy parameter that tunes the transmon frequency reduces its coherence. The SQUID transmon frequency and therefore its coherence are sensitive to noise in the perpendicular magnetic field component $B_\perp$. This noise can be on-chip flux noise or setup-related, e.g. noise in the current source powering the magnet coils or vibrations of the sample with respect to the vector magnet. The sensitivity $|df_{01}/dB_\perp|$ determines the extent to which noise in $B_\perp$ reduces the transmon coherence. To calculate it, we fit the the flux dependence of the SQUID frequency using Eq. (2.10). For every frequency, we calculate $|df_{01}/dB_\perp|$ from the fitted curve (Fig. 2.12 **(a)**). We can then plot the $|df_{01}/dB_\perp|$ as a function of SQUID transmon frequency f_{01} (Fig. 2.12 **(b)**). The main parameters that contribute to the $|df_{01}/dB_\perp|$ as a function of frequency are the SQUID period $B_{\Phi_0,\text{SQUID}}$, and top and bottom sweetspot frequencies (as well as E_C to a lesser degree). The sensitivity is given in units of GHz/Φ_0, because

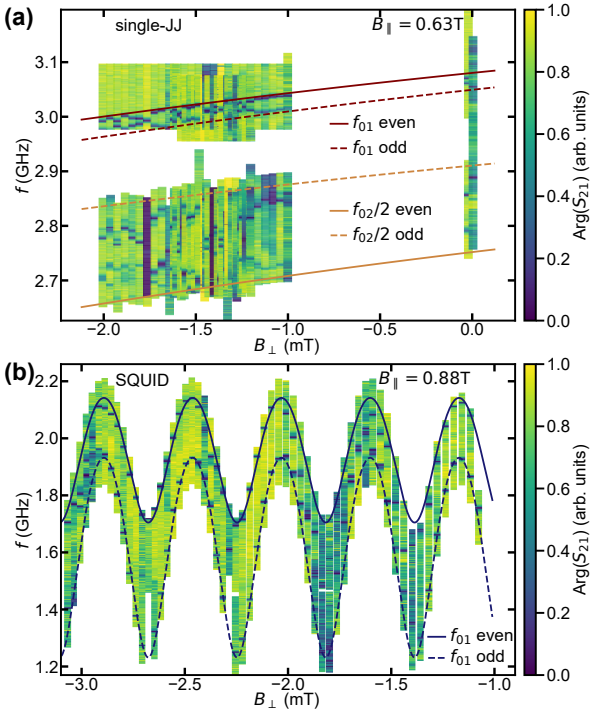

Figure 2.11: Example data for extracting E_J and E_C from charge-parity splitting for the single-JJ (panel **(a)**) and SQUID transmon (panel **(b)**). Only the maximum splitting between the peaks needs to be estimated as any value in between can be observed for different n_g in the Hamiltonian. The changes in n_g that modulate the splitting are happening at a timescale slower than the measurements, therefore one can observe the opening and closing of the charge-parity. For the single-JJ example, we could also observe $f_{02}/2$, for the SQUID example we were in a regime where we could no longer observe $f_{02}/2$ and had to rely solely on f_{01}.

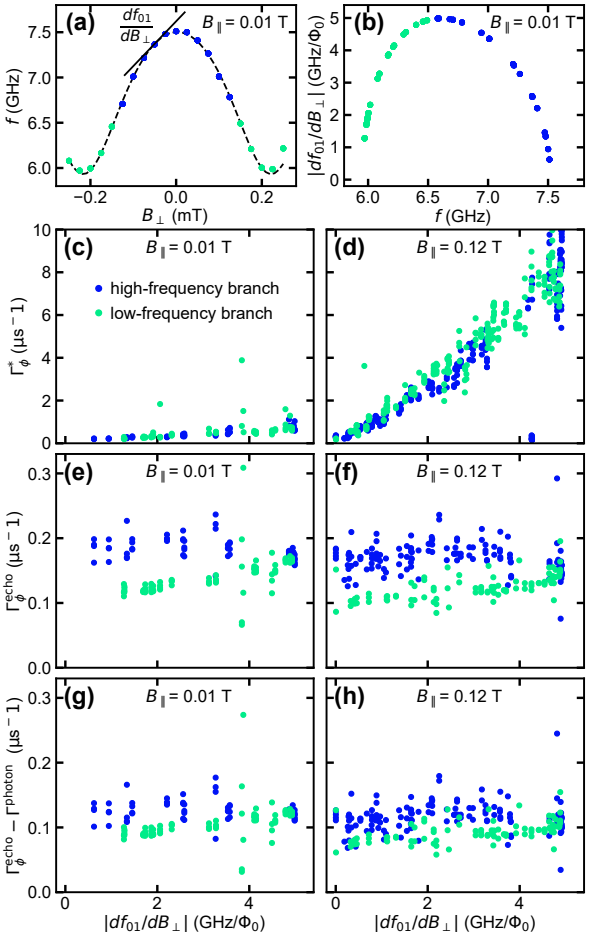

Figure 2.12: **(a)** f_{01} of the SQUID qubit vs. the out-of-plane field $B_\perp$ for an example flux oscillation of the SQUID at in plane field $B_{\parallel,1} = 0.01\,\mathrm{T}$. The tangent line indicates the sensitivity at that point. **(b)** out-of-plane field sensitivity $|df_{01}/dB_\perp|$ as a function of frequency for the complete in plane field dataset. Data in all figures are color coded for the low-frequency and high-frequency sensitivity branch. **(c)** and **(d)** The pure Ramsey dephasing rates of the SQUID qubit as a function of $|df_{01}/dB_\perp|$ at $B_{\parallel,1} = 0.01\,\mathrm{T}$ and $B_{\parallel,1} = 0.12\,\mathrm{T}$. **(e)** and **(f)** The pure echo dephasing rates of the SQUID qubit as a function of $|df_{01}/dB_\perp|$ at $B_{\parallel,1} = 0.01\,\mathrm{T}$ and $B_{\parallel,1} = 0.12\,\mathrm{T}$. **(g)** and **(h)** The pure echo dephasing rates of the SQUID qubit subtracting our estimate of photon shot noise as a function of $|df_{01}/dB_\perp|$ at $B_{\parallel,1} = 0.01\,\mathrm{T}$ and $B_{\parallel,1} = 0.12\,\mathrm{T}$.

the fitted model also contains the periodicity in $B_\perp$, thus we can rescale the x-axis in units of Φ_0.

To quantify the transmon coherence, we calculate the pure dephasing time

$$\frac{1}{T_2} = \Gamma_\phi + \frac{1}{2T_1} \tag{2.14}$$

to separate the contribution of the dephasing rate and the lifetime. Having measured T_1, T_2^* and T_2^{echo} as a function of $B_\perp$ over at least one period of the SQUID, we can plot Γ_ϕ against $|df_{01}/dB_\perp|$. Fig. 2.12 **(c)** and **(d)** illustrate the case for Γ_ϕ^*, and Fig. 2.12 **(e)** and **(f)** for $\Gamma_\phi^{\mathrm{echo}}$. We observe a linear dependence on sensitivity

$$\Gamma_\phi = a\left|\frac{df_{01}}{dB_\perp}\right| + b, \tag{2.15}$$

where a describes slow noise that scales with $B_\perp$ and the offset b accounts for flux-independent noise contributions. As illustrated in the four examples Fig. 2.12 **(c)**-**(f)** we generally find such a linear trend for the Ramsey data, but not for the echo experiments where we can see a clear difference between the high-frequency and low-frequency branch of the sensitivity. Therefore, it is only for Γ_ϕ^* that we can extract the noise parameters a and b for each in-plane magnetic field and analyze them as a function of $B_{\parallel,1}$. The result for a are shown and discussed in Section 2.5.

Compared to the Ramsey experiments, $\Gamma_\phi^{\mathrm{echo}}$ should be more robust against low-frequency noise and give insights into faster noise like on-chip flux noise as opposed to slow setup-related vibrational

noise. However, as shown in Section 2.G the echo dephasing rates are partially limited by photon shot noise in the cavity which is strongly frequency dependent. Assuming this photon-shot-noise contribution, we subtract it as a frequency-dependent background. With the background subtraction, the gap between the upper and lower sensitivity branch (which differ in frequency) is reduced, as seen in Fig. 2.12 **(g)** and **(h)**. For the Ramsey data, the two branches of the sensitivity are consistent with the same linear trend to begin with, because the noise in $B_\perp$ is more strongly limiting Γ_ϕ^*. However, the photon-shot-noise subtracted $\Gamma_\phi^{\text{echo}}$ becomes relatively flat, so there is likely another $B_\perp$-independent noise source limiting $\Gamma_\phi^{\text{echo}}$. There is also no strong change in $\Gamma_\phi^{\text{echo}}$ as a function of $B_{\parallel,1}$, until we reach fields where we also become more charge sensitive. Thus our data cannot give information on the characteristic $1/f$-like flux noise ubiquitous in cQED [88, 81]. If this noise originates from local paramagnetic fluctuators, it is expected to depend on applied magnetic fields [77], therefore repeating this experiment with improved coherence times could give insights into this.

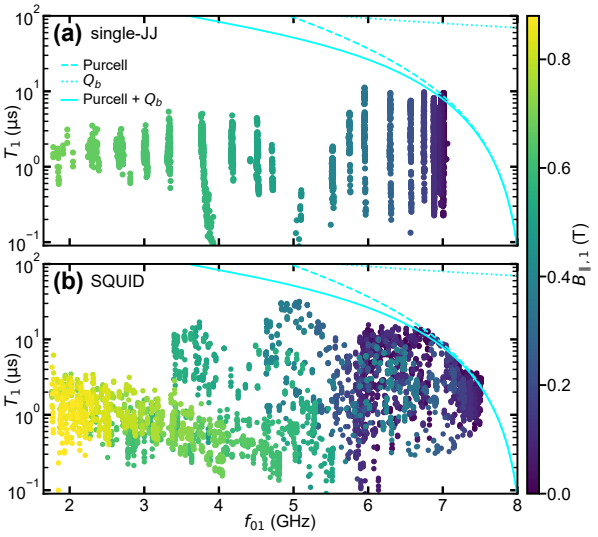

Figure 2.13: T_1 vs transmon f_{01} for every in-plane magnetic field for both the single-JJ (panel **(a)**) and the SQUID transmon (panel **(b)**). Purcell decay to the cavity mode is limiting both qubits at high frequencies. For similar frequencies but different $B_{\parallel,1}$, single-JJ and SQUID transmon show very different features, e.g. a dip and a peak around 5.0 GHz. The observed lifetimes are not following a frequency dependent loss model contrary to Ref. [39].

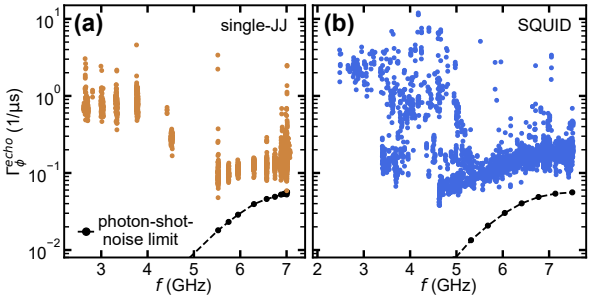

Figure 2.14: **(a)** The pure echo dephasing rate of the single JJ transmon against the transmon transition frequency. The black circles model photon shot noise with $T_{\text{cav}} = 76$ mK. **(b)** Similar to **(a)**, but for the SQUID transmon.

2.G. ADDITIONAL RELEVANT LIMITS ON COHERENCE

Here, we will present our understanding of additional relevant limits on transmon relaxation time and coherence in this work. While the qubits are not reaching the current state of the art in coherence times, this is likely largely due to insufficient shielding and filtering (see Ref. [73]). We will discuss Purcell and quasiparticle limits on T_1 and show evidence that T_2^{echo} is limited by photon shot noise. In the main text above, we already discussed mechanical vibrations as a likely culprit limiting T_2^* at high $B_{\parallel,1}$. Vortex loss is discussed in Section 2.D. We do not discuss the limits imposed on qubit dephasing by charge noise and quasiparticle dynamics in more detail in this work, but they might be different from transmons with thicker aluminum films.

2.G.1. LIMITS TO T_1

An important factor to consider in the qubit energy relaxation is frequency. Fig. 2.13 shows all measured T_1 values as a function of frequency for both qubits. There are several frequency-dependent mechanisms limiting T_1. The Purcell effect imposes a limit based on the coupling to the readout cavity $T_1^{\text{Purcell}} = \delta^2/(g^2\kappa)$, where $\delta = f_{01} - f_{\text{cav}}$ is the detuning between qubit and cavity mode, g is the qubit-cavity coupling, and κ the cavity linewidth. Instead of κ, the quality factor $Q_{\text{tot}} = 2\pi f_{\text{cav}}/\kappa$ is often quoted. We find $Q_{\text{tot}} \approx 5800$ at low fields but at $B_{\parallel,1} \geq 0.5$ T we find $Q_{\text{tot}} \approx 3800$. Surprisingly, the measured f_{cav} and Q_{tot} together with our estimates for g give a Purcell limit that some of our measured T_1 values exceed. Over a larger range, transmons limited by dielectric loss often exhibit an overall trend in T_1 that roughly follows the form $T_1^{\text{b}} = Q_{\text{b}}/2\pi f_{01}$, where Q_{b} is a background quality factor [89]. We cannot observe such a trend convincingly but did include it in Fig. 2.13 as a guide to the eye, setting $Q_{\text{b}} = 3.5 \times 10^6$.

As the magnetic field suppresses the supercon-

ducting gap, it is important to consider quasiparticle-induced relaxation. To estimate this effect, the superconducting gap needs to be estimated in absolute terms. As discussed in Section 2.4 we estimate the in-plane critical field to be $B_{\parallel}^{c} = 1.03\,\mathrm{T}$. Assuming a Ginzburg-Landau closing of the superconducting gap (Eq. (2.3)), we find the gap to be reduced by only ~50 % at $B_{\parallel,1} = 0.88\,\mathrm{T}$. The data taken during the cooldown suggests $T_{\mathrm{crit}} \approx 1.2\,\mathrm{K}$ which we can use to estimate the gap at zero magnetic field via $\Delta_0 = 1.764\, k_{\mathrm{B}} T_{\mathrm{crit}}$ [90, 17]. With these values we can calculate an estimate for the quasiparticle-induced relaxation rate [91]

$$\Gamma_{\mathrm{qp}} = 2\frac{8E_{\mathrm{J}}E_{\mathrm{C}}x_{\mathrm{qp}}}{f_{01}}\sqrt{\frac{2\Delta}{hf_{01}}}, \tag{2.16}$$

where

$$x_{\mathrm{qp}} = \sqrt{2\pi\frac{k_{\mathrm{B}}T_{\mathrm{R}}}{\Delta}}\exp\left(-\frac{\Delta}{k_{\mathrm{B}}T_{\mathrm{R}}}\right) \tag{2.17}$$

is the normalized quasiparticle density assuming a thermal equilibrium temperature T_{R}. Here, h is the Planck constant and k_{B} is the Boltzmann constant. The remaining free parameter is the quasiparticle bath temperature T_{R}. At 0.88 T we measure a T_1 of 2.4 µs for the SQUID transmon, which is at a frequency of 1.8 GHz. With these values we can roughly bound T_{R} to be ≤ 90 mK. More importantly, we do not observe any sharp decrease in T_1 with $B_{\parallel,1}$ that would signal loss mechanism becoming dominant [39]. This suggests that up to the highest field we measured, T_1 is not significantly limited by quasiparticles, yet.

2.G.2. LIMITS TO T_2

Turning to echo coherence times T_2^{echo}, we will now estimate the limit imposed by photon shot noise in the cavity. As can be seen in Fig. 2.4, $\Gamma_\phi^{\mathrm{echo}}$ slightly decreases with $B_{\parallel,1}$ for $B_{\parallel,1} < 400\,\mathrm{mT}$. Looking at $\Gamma_\phi^{\mathrm{echo}}$ as a function of qubit frequency (Fig. 2.14) is more revealing in this context. A dependence on qubit frequency is expected using a model for photon shot noise [70, 92]. In the dispersive limit, the qubit-cavity interaction is reduced to a term of the form $\chi a^\dagger a \sigma_z$. Accordingly, the qubit frequency depends on the cavity photon number $a^\dagger a$ via the dispersive shift χ, which for a transmon is given by

$$\chi = g^2\alpha_{\mathrm{tr}}\left[\frac{1}{\delta(\delta+\alpha_{\mathrm{tr}})} - \frac{1}{(\delta-2f_{01})(\delta-\alpha_{\mathrm{tr}}-2f_{01})}\right], \tag{2.18}$$

where $\alpha_{\mathrm{tr}} = f_{12} - f_{01}$ is the negative transmon anharmonicity. Thus, thermal fluctuations in the cavity photon number lead to a dephasing rate

$$\Gamma^{\mathrm{photon}} = \frac{\kappa}{2}\mathrm{Re}\left[\sqrt{\left(1+\frac{2i\chi}{\kappa}\right)^2 + \left(\frac{8i\chi n_{\mathrm{th}}}{\kappa}\right)} - 1\right]. \tag{2.19}$$

The thermal cavity photon number $n_{\mathrm{th}} = \left(\exp(hf_c/k_{\mathrm{B}}T_{\mathrm{cav}}) - 1\right)^{-1}$ is given by Bose-Einstein statistics. The only free parameter is the cavity temperature T_{cav}. As the photon shot noise limit on T_2^{echo} mainly depends on the transmon frequency, we show $\Gamma_\phi^{\mathrm{echo}}$ versus f_{01} for both transmons in Fig. 2.14. Using $T_{\mathrm{cav}} = 76\,\mathrm{mK}$ we approximately reproduce the smallest $\Gamma_\phi^{\mathrm{echo}}$ we measured for the single-JJ transmon. The data point is admittedly an outlier, but both the underlying T_1 and T_2^{echo} measurements have good signal-to-noise ratio and fits, however, the T_1 could have fluctuated. In that case the photon shot noise would likely be more severe. Even for this low estimate, at qubit frequencies above 5 GHz, photon shot noise is a significant contribution to T_2^{echo}.

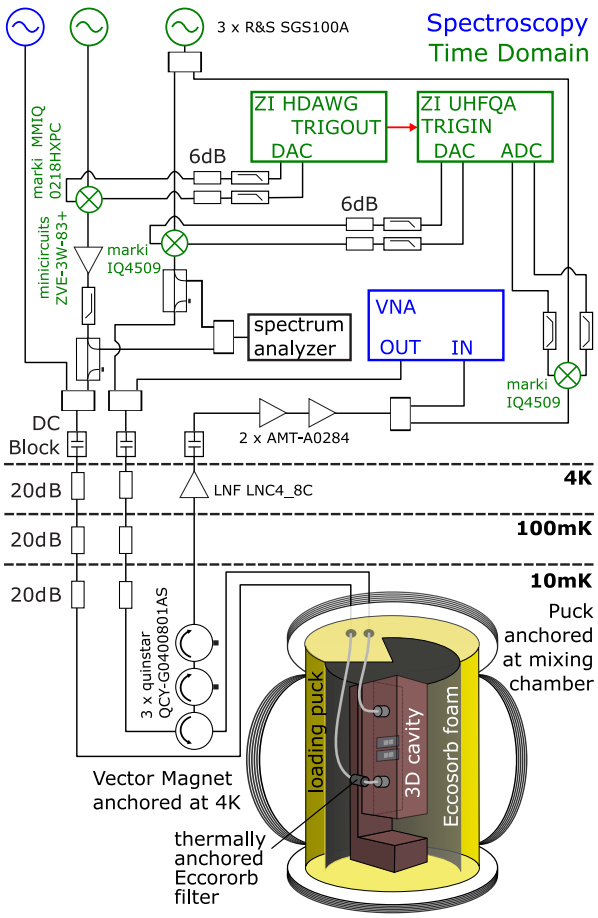

Figure 2.15: Wiring diagram of the experiment with the setup for qubit spectroscopy using a two-port VNA and an additional microwave source and the time-domain setup using ADCs, DACs and Mixers.

Supplementary Material for "Magnetic-field resilience of 3D transmons with thin-film Al/AlO$_x$/Al Josephson junctions approaching 1 T"

This supplement provides experimental details and additional data supporting the claims in the main text.

2.H. EXPERIMENTAL SETUP

The transmons are mounted in a 3D cavity which is loaded into a bottom-loading dilution refrigerator (Triton 500, Oxford Instruments) with a nominal base temperature of ~10 mK. The radiation shielding in this dilution refrigerator is likely not optimal and could partially account for the somewhat limited T_1 relaxation times and high cavity temperature. With the strong magnetic fields applied in this work, usual magnetic shielding used in cQED experiments consisting of μ-metal and superconducting boxes around the samples could not be used. We use Eccosorb LS-26 foam inside the loading puck to improve radiation shielding (see Fig. 2.15). In a similar setup, radiation as a limiting factor was suspected [93]. A detailed wiring diagram of the experiment can be found in Fig. 2.15. The fridge wiring is loosely based on [94]. While the maximum T_1 reported here is ~30 µs, we previously measured 60 µs on a different single-JJ transmon with a frequency of ~4 GHz in a nominally identical dilution refrigerator, therefore we do not believe our setup to impose a general strong T_1 limit.

A 3-axis vector magnet is used to apply magnetic fields to the sample. In this paper we do not give data for field cooled transmon, but we note that when we performed an initial cooldown with the high-field current supply of the magnet connected to the out-of-plane axis this already lead to frequency jumps in the transmons. Therefore, during cooldowns the magnet power supply was always turned off and the magnet was grounded. Everything was turned on once base temperature was reached. Not all magnet axes were connected at all times in order to minimize noise. For the in-plane axis we mainly used the Oxford Instruments Mercury iPS power supply, which can supply sufficient current to reach a magnetic field of 1 T . We also used a Keithley 2461 as a current source to compare the noise level. The Keithley 2461 can only reach magnetic fields of 0.16 T. For the out-of-plane axis, we used a Keithley 2450 for the data presented in the main text which can only reach 0.016 T. For the data presented in Fig. 2.18, we used the Keithley 2461 for the out-of-plane magnetic field coil.

The 3D cavity is machined from oxygen free copper. It has two symmetrically coupled ports, making it possible to measure it both in reflection and transmission. We mostly used reflection measurements as they allow an estimation of the intrinsic quality factor.

2.I. LARGE OUT-OF-PLANE MAGNETIC FIELDS AND HYSTERESIS

In this section, we discuss the large $B_\perp$ regime looking at the qubit coherence and the persistence of SQUID oscillations as well as hysteresis in $B_\perp$ as a factor complicating experiments. Fig. 2.16 shows data on cavity frequency f_c and transmon frequency f_{01} as well as T_1 for both transmons as a function of $B_\perp$. Data taking started immediately after a thermal cycle and only the magnet coil corresponding to $B_\perp$ was connected. This data was obtained in a separate cooldown in a different

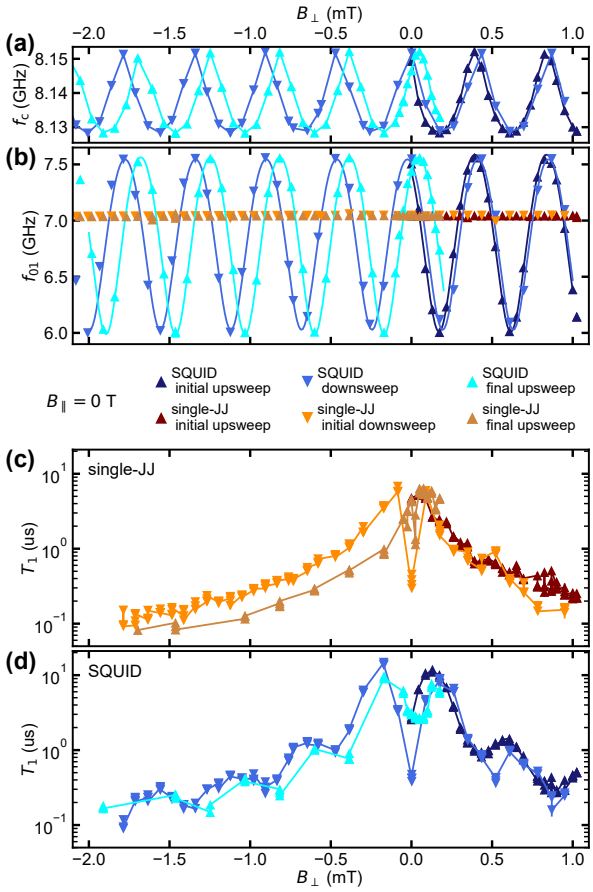

Figure 2.16: **(a)** and **(b)** Cavity frequency f_c and the qubit frequency f_{01} for both transmons as a function of $B_\perp$ for $B_\parallel = 0$. The Data were taken by scanning up from $B_\perp = 0$ mT, then down to outside the plot range and back up to $B_\perp$ =0.2 mT, with different markers and colors for the segments. f_c clearly follows the SQUID transmon oscillations. For the initial upsweep and downsweep the hysteresis is visible but small, but upon the return from larger negative $B_\perp$ hysteresis is a considerable fraction of a flux quantum. **(c)** and **(d)** T_1 for the single-JJ and SQUID transmon as a function of $B_\perp$. The SQUID data shows oscillations that are due to the frequency dependence of T_1, generally showing longer T_1 at the bottom sweetspot. Strangely, T_1 drops for both qubits on the way back to $B_\perp$ =0 mT. These data were taken in an initial cooldown in another nominally identical dilution refrigerator, thus qubit frequencies slightly vary compared to the data reported in the main text.

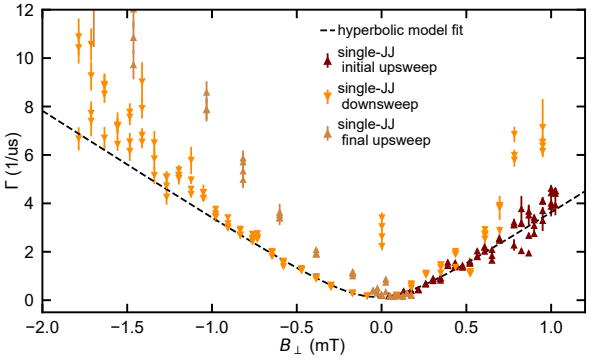

Figure 2.17: Relaxation rate Γ as a function of $B_\perp$. The data are the same as in Fig. 2.16 **(c)**. The dashed line shows a fit of the hyperbolic model (see main text). It is obvious that hysteresis is an important factor here, thus we fit the model through the downsweep data that was taken without changing sweep direction.

nominally identical dilution refrigerator. The data is color coded for the different scan segments (0 mT to 1 mT, 1 mT to −10 mT and −10 mT to 0.2 mT). Time domain measurements were stopped around −2 mT, so for the large field excursion we do not plot the entire curve. For the initial two scans, only extending to a small range of $B_\perp$, the change in field direction leaves visible but small hysteresis. However, after the excursion to large $B_\perp$ on the downward scan, the upward scan coming back shows a hysteresis that is a significant part of a flux quantum. Notably, in the scanned range here, we do not observe flux jumps. It is important to mention in passing, that in Fig. 2.16 where qubit spectroscopy data is plotted as well as cavity measurements, it is obvious that the cavity oscillations follow the SQUID transmon oscillations which repels the cavity. Later on, we will look at oscillations in the cavity frequency and assume that they are due to the SQUID oscillation in the qubit.

For this data we can also look at $\Gamma = 1/T_1$ as a function of $B_\perp$ for the single-JJ transmon (see Fig. 2.17). This larger range in $B_\perp$ shows more clearly that an expected linear dependence of Γ on $B_\perp$ can only be seen for larger $B_\perp$. We can only measure Γ precisely over roughly two orders of magnitude here, for small T_1, the error bars on Γ become large.

In order to estimate the out-of-plane critical field, we measured the dependence of the cavity frequency on $B_\perp$ expecting a breakdown of SQUID oscillations (Fig. 2.18). There is a clear change in the SQUID oscillation pattern around 23 mT. At this point, the cavity quality factor Q_{tot} also decreases. The most likely explanation for this decrease is the transition from superconducting to normal state of the capacitor pads: from $B_{c2} \equiv \Phi_0/(2\pi\xi^2) = 23$ mT, we find $\xi \approx 120$ nm, in good agreement with the rough estimate made in Appendix D of the main text.

Unexpectedly, the oscillations in Fig. 2.18 remain visible across the range that we measured, suggesting that superconductivity might persist up to $B_\perp = 60$ mT. The period of the oscillations becomes smaller suggesting the effective area of the SQUID loop increases, which one would expect, as more field penetrates the superconductor. Flux jumps become more frequent

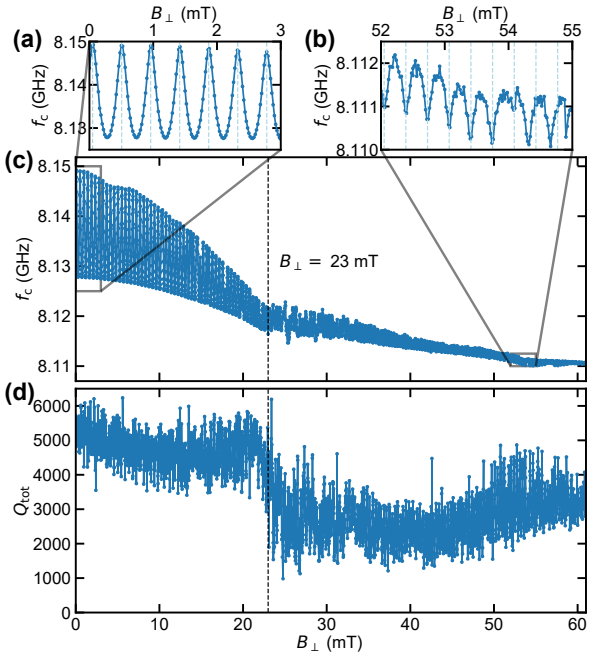

Figure 2.18: **(c)** Cavity frequency as a function of $B_\perp$. Zoom-in panels ((**a**) and (**b**)) show the low-field and high-field regime. While there is clearly a change in the oscillations around $B_\perp \approx 23$ mT, oscillations persist in our measurable range. However, the period decreases from ~0.455 mT to ~0.34 mT (dashed vertical lines). **(d)** Cavity total quality factor Q_{tot} as a function of $B_\perp$. Q_{tot} is reduced from ~5000 to ~2500 around $B_\perp \approx 23$ mT, also suggesting a change in the system at that point. Interestingly, towards large $B_\perp$, Q_{tot} seems to recover. The Q_{tot} data is noisy here because the cavity reflection measurements were done with a large bandwidth to save time.

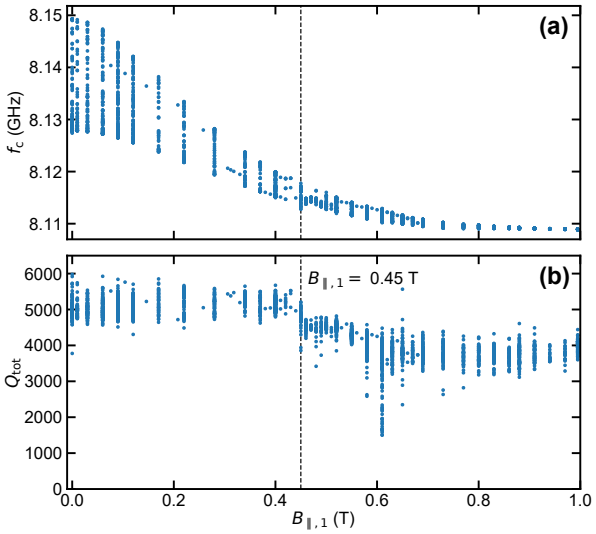

Figure 2.19: **(a)** Cavity frequency f_{cav} as a function of $B_{\parallel,1}$. We show the cavity measurements taken for the qubit spectroscopy and time domain measurements of the main text but reject some outliers as it is a large dataset. At each $B_{\parallel,1}$ there is a range of f_{cav} for different $B_\perp$. **(b)** Cavity total quality factor Q_{tot} as a function of $B_{\parallel,1}$. We see an almost step-like drop in Q_{tot} around $B_{\parallel,1} \approx 0.45$ T.

at higher fields. It is plausible that the critical fields for the large capacitor pads is different from that of the thin leads and JJ region. However, our estimate for the perpendicular critical field based on a Ginzburg-Landau theory fit to the magnetic-field dependence of the single-JJ transmon frequency yields $B_\perp^c \approx 33$ mT (presented in the main text). While spectroscopy was only performed up to $B_\perp \sim 8$ mT and Ginzburg Landau theory is approximate in this regime, we do not believe that superconductivity can still be present at the highest fields reached in our measurements. A possible explanation for the observed oscillations could be the Altshuler-Aronov-Spivak effect [95]. This effect should be relevant in rings with circumference longer than the mean free path ℓ and at most of the order of the phase coherence lenght L_ϕ. In our device, the circumference is about 8 µm and $\ell \sim 10$ nm (see main text). Estimates for L_ϕ in aluminum at temperatures around T_c and zero magnetic field are of the order of 1-2 µm [96, 97]. On one hand, it is not unreasonable to expect L_ϕ to be longer well below T_c (cf. [98]); on the other hand, L_ϕ should be suppressed by the applied field to a fraction of a micron. Although superconducting fluctuations could in part compensate for such a suppression (see also [99]), confirmation or refutation of our hypothesis is left to future work.

It is interesting to compare the f_{cav} and Q_{tot} as a function of $B_\perp$ with the cavity data as a function of $B_{\parallel,1}$ (Fig. 2.19). These cavity measurements were taken during the qubit spectroscopy and time domain measurements presented in the main text. At each $B_{\parallel,1}$ a range of measurements with different $B_\perp$ were taken, therefore there is usually a range of different f_{cav} and Q_{tot}. The data looks qualitatively remarkably similar to Fig. 2.18. While the reduction in f_{cav} with $B_{\parallel,1}$ is just due to the reduced frequencies of the transmons presented in the main text, the drop in the maximum Q_{tot} around $B_{\parallel,1} \approx 0.45$ T is unexpected. It is less severe than the drop in Q_{tot} as a function of $B_\perp$, but contrary to the data in Fig. 2.18, we do not reach the estimate for $B_{\parallel,1}^c$. From the other measurements presented in the main text, we can also exclude that this is an effect of misalignment of the magnet axes to the sample.

2.J. SQUID OSCILLATION STABILITY VS $B_{\parallel,1}$ AND $B_{\parallel,2}$

One of the more puzzling observations presented here is the SQUID oscillation instability. SQUID oscillations

are usually a robust feature that would only disappear if superconductivity is fully suppressed in the circuit or in one or both of the constituting JJs. While we can see clear SQUID oscillations for $B_{\parallel,1}$ in the range from 0 T-1 T, there is an instability region roughly between 0.4 T and 0.5 T. The step-like drop in the Q_{tot} of the cavity (Fig. 2.19) occurs at $B_{\parallel,1} \approx 0.45$ T in the instability region. In this region we also observed that the cavity did not remain stable in time with jumps in its resonance frequency occurring every few minutes. Therefore we did not perform detailed time-domain measurements in this region and did not have good measurements of the SQUID transmon. Spectroscopy measurements of the single-JJ transmon (where the frequency could be roughly predicted) were possible in between cavity jumps. We speculate the instability of the cavity frequency is due to the SQUID transmon being unstable in frequency, but we cannot exclude other options such as direct coupling to spin baths conclusively. Interestingly, there are outliers in our data where the cavity is at higher frequencies than would be consistent with the range of dispersive shifts for the expected maximum SQUID frequency.

The spin hypothesis arose because for a g-factor of ~2, spin precession frequencies could become resonant with the qubits or cavity in the magnetic field range we explored. However, we do see the cavity instability and disappearance of SQUID oscillations at different fields for $B_{\parallel,2}$ (Fig. 2.20). Fig. 2.20 **(a)** shows the SQUID oscillations in f_{cav} as a function of $B_{\perp}$ (normalized line by line) for back and forth scans of $B_{\parallel,2}$ in the -40 mT to 40 mT region. Already at fields with $|B_{\parallel,2}|$ >20 mT, the regular SQUID oscillations disappear. Instead, the cavity frequency seems to jump randomly and repeated scans are not reproducible. It is for this reason, that we have not studied the qubit spectroscopy and coherence as a function of $B_{\parallel,2}$. There seems to be a bistability in the SQUID oscillation offset at low fields, possibly due to residual ferromagnetism in the vicinity that can be sensed by the SQUID. The cavity connectors are nickel coated, so they could be responsible. Interestingly, around $B_{\parallel,2} > 0.55$ T regular SQUID oscillations reappear (Fig. 2.20 **(b)**) up to the highest fields we measured. While the in-plane alignment of the magnetic field is good for low $B_{\parallel,2}$ (Fig. 2.20 **(a)**), indicated by the constant SQUID oscillation offset for different $B_{\parallel,2}$, at high fields (Fig. 2.20 **(b)**), the oscillation offset in $B_{\perp}$ changes linearly with $B_{\parallel,2}$ suggesting that the field is not applied perfectly in plane with the SQUID loop. We have also included the data of f_{cav} as a function of $B_{\perp}$ for different B_z, just changing the current in one physical coil without using the B_x coil to align the field in the sample plane (Fig. 2.21). This dataset covers a different range and clearly shows the large range where SQUID oscillations are not visible as well as the apparent difference of the alignment angle for low and high field.

The anisotropy for different in-plane axes weakens the case for spins and we believe it points towards the spurious junctions in the leads as culprits, since the spurious JJ geometry is asymmetric for different in-plane directions. The spurious JJs in the transmons are not as well defined as the ones discussed in Ref. [68], as in this case the entire leads as well as the capacitor pads are formed by the two aluminum layers with the oxide in between. Given that the leads from the capacitor pads to the JJ are essentially a spurious JJ, it makes sense to consider the Fraunhofer pattern for this region. The lead width was measured in SEM pictures to be 410 nm and the SQUID arms are of similar size. The field to thread a flux quantum through the spurious JJ in the leads and SQUID arms in the $B_{\parallel,1}$ direction is on the order of 0.45 T, if we assume an insulator thickness similar to the one of the JJs discussed in the main text. This seems to coincide with the instability region in $B_{\parallel,1}$ between 0.4 T and 0.5 T. In the Fraunhofer lobe region, the supercurrent is suppressed and the devices become very field sensitive, which could also to some extent explain the unstable behavior. The expected E_J for the spurious JJs is very large, such that away from the fields where supercurrent is suppressed, the effects could be negligible. It seems to contradict this theory that the single-JJ transmon, which has identical leads to the SQUID transmon, can often be found close to where it would be expected in spectroscopy in the instability region. But the strong anisotropy would be consistent with the asymmetric shape of the spurious JJs in the $B_{\parallel,1}$ and $B_{\parallel,2}$ directions. Looking at the device from the $B_{\parallel,2}$ direction the length of the spurious JJ is huge (the leads are 100 µm long) and thus much lower fields could cause Fraunhofer lobes. In the large capacitor pads and maybe even the leads, pinholes likely limit the overall area that could be considered as one continuous JJ. The onset at 20 mT in the $B_{\parallel,2}$ direction would correspond to a length scale of 10 µm. It is puzzling that stable SQUID oscillations are observed again from $B_{\parallel,2} > 0.6$ T to the maximum measured field of 0.9 T. Given the confusing and unstable data, we did not investigate this further.

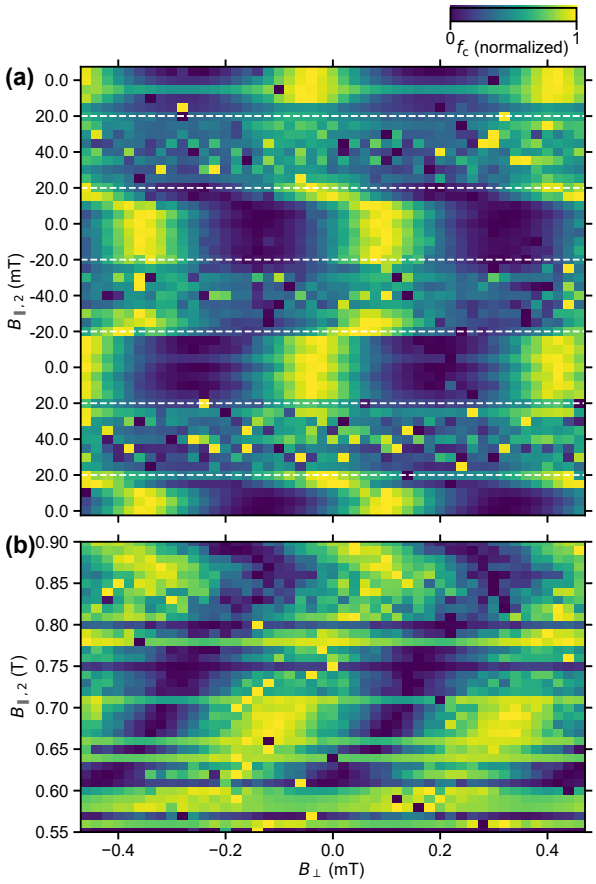

Figure 2.20: **(a)** Cavity frequency as a function of $B_\perp$ and $B_{\parallel,2}$. The data are normalized line-by-line. These data were taken in a low $B_{\parallel,2}$ regime scanning from 0 mT to +40 mT to -40 mT to 40 mT and back to 0 mT. In the region from 20 mT to 40 mT (and −20 mT to −40 mT) oscillations disappear and the cavity frequency as a function of the magnetic fields looks random. Dashed lines that mark the boundaries of the stable oscillation regime are added for clarity. The alignment looks good as the SQUID offset is essentially stable as $B_{\parallel,2}$ is changed. **(b)** Cavity frequency (line-by-line normalized for contrast) as a function of $B_\perp$ and $B_{\parallel,2}$ for large $B_{\parallel,2}$. Cavity oscillations return around 600 mT and persist up to 900 mT where we stopped measuring in this dataset. The period remains similar at high $B_{\parallel,2}$.

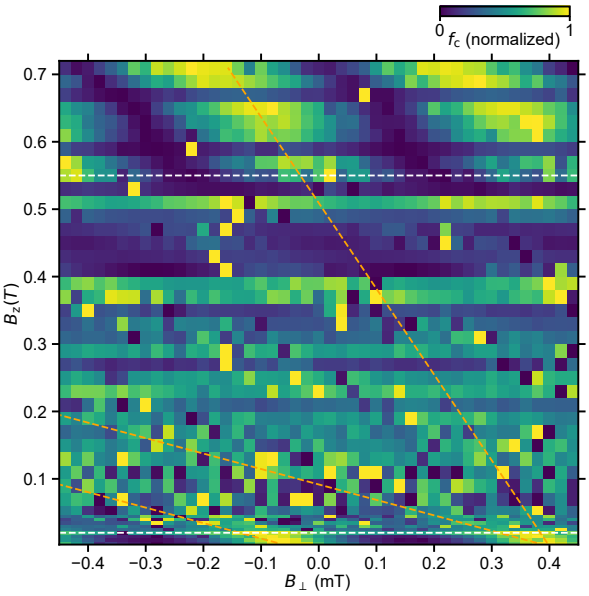

Figure 2.21: Cavity frequency as a function of $B_\perp$ and B_z (the physical magnet axis not aligned to the sample), which is largely the $B_{\parallel,2}$ direction. The data are normalized line-by-line to highlight the periodicity in $B_\perp$ due to the SQUID oscillations. Clear SQUID oscillations can only be made out up to $B_z = 0.02$ T (bottom white dashed line). At high fields they recommence clearly around 0.55 T (upper white dashed line). The linear dependence of the offset of the oscillation as a function of B_z is slightly different for the low-field and high-field regime (orange dashed lines).

3

QUASIPARTICLE EFFECTS IN MAGNETIC-FIELD-RESILIENT 3D TRANSMONS

As explained in Section 1.2.2, transmons can be used to sense charge dynamics in a circuit. This includes quasiparticle tunneling across the tranmon's JJ but also coupling to future Majorana qubits. For a Majorana qubit that is coupled to a transmon, incoherent tunneling of quasiparticles poisons the fermion parity of the topological qubits and thus limits their coherence. The research presented in this chapter therefore addresses two objectives in parallel: First, it quantifies the parity-switching time in magnetic-field-resilient 3D transmons based on Al/AlO$_x$/Al JJs as a function of in-plane magnetic fields $B_\parallel$ and temperature. With a comprehensive model, the data help to identify dominant parity-switching mechnisms and their dependence on the magnetic field thus providing the basis for improved setups and device designs that minimize quasiparticle poisoning in magnetic fields. Second, by demonstrating readout of the transmon parity in moderate magnetic fields up to 0.41 T *the work presented in this chapter realizes the protocol to readout the fermion-parity of future Majorana qubits in magnetic fields and establishes that Al/AlO$_x$/Al JJs can be used in architectures for the parity-readout and manipulation of topological qubits based on MZMs.*

This chapter has been published in Phys. Rev. Applied *with slight improvements based on the peer review process:*

J. Krause, G. Marchegiani, L.M. Janssen, G. Catelani, Y. Ando, C. Dickel, *Quasiparticle effects in magnetic-field-resilient three-dimensional transmons*, Phys. Rev. Applied **22** 044063 (2024).

Author contributions *The project was conceived by C.D. and Y.A.. J.K. and C.D. fabricated the device and took the measurements with help from L.M.J.. The data was analyzed by J.K. and C.D. with help from L.M.J.. The theoretical model was extended to the magnetic field by G.M. and G.C. and fit to the data by J.K. and G.M.. The manuscript was written by J.K., G.M., G.C., and C.D. with input from all coauthors.*

The data and analysis presented in this chapter enter yet another article, published in Nature Physics *[100]. As a byproduct to tuning up the parity measurements, we get precise measurements of various transmon transitions and their charge dispersions. Noticing that we cannot fit these data using the Cooper-pair-box Hamiltonian, Eq.* (1.9)*, with a sinusoidal current-phase relationship, we co-discover a slightly non-sinusoidal current-phase relationship in Al tunnel JJs leading to higher Josephson harmonics.*

Data availability *Datasets and analysis in the form of Jupyter notebooks that create the figures of this manuscript are available on Zenodo with doi 10.5281/zenodo.10728469.*

Recent research shows that quasiparticle-induced decoherence of superconducting qubits depends on the superconducting-gap asymmetry originating from the different thicknesses of the top and bottom films in Al/AlO_x/Al junctions. Magnetic field is a key tuning knob to investigate this dependence as it can change the superconducting gaps in situ. We present measurements of the parity-switching time of a field-resilient 3D transmon with in-plane field up to 0.41 T. At low fields, small parity splitting requires qutrit pulse sequences for parity measurements. We measure a non-monotonic evolution of the parity lifetime with in-plane magnetic field, increasing up to 0.2 T, followed by a decrease at higher fields. We demonstrate that the superconducting-gap asymmetry plays a crucial role in the observed behavior. At zero field, the qubit frequency is nearly resonant with the superconducting-gap difference, favoring the energy exchange with the quasiparticles and so enhancing the parity-switching rate. With a higher magnetic field, the qubit frequency decreases and gets detuned from the gap difference, causing the initial increase of the parity lifetime, while photon-assisted qubit transitions increase, producing the subsequent decrease at higher fields. Besides giving a deeper insight into the parity-switching mechanism in conventional transmon qubits, we establish that Al-AlO_x-Al JJs could be used in architectures for the parity-readout and manipulation of topological qubits based on Majorana zero modes.

3.1. INTRODUCTION

Superconducting quantum circuits such as qubits, sensors, and amplifiers have drastically improved over the last two decades [101], mostly thanks to the reduction and mitigation of charge noise, a recent example being the transmon qubit [16] based on tantalum capacitors [102]. Consequently, non-equilibrium quasiparticles are slowly becoming a dominant source of losses, in addition to already being a main cause of residual excitations [103]. Moreover, recent reports of chip-wide correlated decoherence due to quasiparticles [104] show that quasiparticle loss is a major obstacle to scaling up superconducting quantum processors. A wide range of solutions to quasiparticle loss is being explored: quasiparticle traps [105], pumping [106], gap engineering [107, 108], phonon downconversion [109, 110], optimizing device geometry [111], shielding and filtering [112] or even shielding the device from cosmic rays [113, 114]. Magnetic-field-resilient transmons made of thin-film Al/AlO_x/Al Josephson junctions (JJs) [115] provide yet another angle to tackle quasiparticle loss: the in-plane-magnetic field tunes in-situ both the transmon transition frequencies and the superconducting gaps of top and bottom aluminum electrodes, making these transmons an ideal system to study quasiparticle effects and optimize gap engineering.

In a parallel effort, magnetic-field-resilient transmons with aluminum tunnel JJs can be a key component for topological quantum-computation protocols based on precise readout and control of the fermion parity of Majorana zero modes (MZMs). Circuit QED measurements [13] of offset-charge-sensitive transmon circuits allow for robust and fast detection of charge-parity switching [116, 103], and hence transmons incorporating topological-superconductor nanowires provide an ideal platform to measure and manipulate MZMs [23, 24]. To host MZMs, the wires typically need to be threaded by large parallel magnetic fields on the order of at least 0.5 T, posing strong requirements on the magnetic-field resilience of the readout circuitry, too. In this context hybrid JJs for field compatible transmons have also been explored [39, 38, 40, 80]. With magnetic-field-resilient aluminum transmons, the advantages of highly coherent and reliable tunnel junctions can be exploited to achieve high-fidelity parity measurements even in large magnetic fields.

In this article, we present measurements of the quasiparticle-induced parity-switching rates in a 3D transmon [69] as a function of in-plane magnetic field up to 0.41 T, promoting thin-film aluminum transmons for the parity readout of future topological qubits. Using a comprehensive model, we distinguish the relevant mechanisms of parity switching, providing evidence for an interplay between Cooper-pair-breaking photons, the superconducting gaps in both sides of the JJs, and the Fraunhofer effect in the JJs. We report signatures of near-resonantly enhanced quasiparticle tunneling due to the superconducting-gap difference approaching the transmon frequency at low in-plane magnetic fields; this resonance condition is gradually lifted with increasing fields until photon-assisted parity switching dominates. Thus, counter-intuitively, the maximum parity lifetime is reached at a finite field of about 0.2 T.

Measurements of the temperature dependence of the parity-switching time for selected in-plane magnetic fields further support these findings. We use different transmon transitions in the parity measurements [117, 118], as the Josephson energy (E_J) changes with the magnetic field, mainly due to the Fraunhofer effect. Our results complement recent experimental [19, 119] and theoretical [120] works on the impact of gap asymmetry on the quasiparticle decoherence rate of transmons.

This article is organized as follows. In Sec. 3.2 we discuss the experiment design, while in Sec. 3.3 the magnetic-field dependent spectrum is shown and parameters of the transmon are determined by modeling it. Sec. 3.4 is devoted to the in-plane magnetic field dependence of the parity-switching time and Sec. 3.5 to its temperature dependence for selected in-plane magnetic fields. In the Conclusions [Sec.3.6], we summarize the results and give an outlook for future research.

3.2. EXPERIMENT DESIGN

The experiment is conceived to measure the effect of magnetic fields on the parity-switching time τ_p of an offset-charge-sensitive transmon [121]. For dispersive readout, the transmon is coupled to a 3D copper cavity [Fig. 3.1 (a)], which is unaffected even by large magnetic fields. We use a bias tee at one of the cavity pins to apply an offset voltage V_g to the two transmon islands (see Section 3.A for details of the setup and Section 3.B for the device fabrication and geometry). In this way, we can measure the charge dispersion, the dependence of the spectrum on the offset charge $n_g \propto V_g$.

The charge dispersion is $2e$-periodic, where e is the elementary charge (for transmon Hamiltonian see Section 3.C). We define the peak-to-peak variation of transmon level i as ϵ_i. However, the transmon energy spectrum splits into two separate manifolds that differ by one electron charge [see Fig. 3.1 (b)] and are labeled "even" and "odd". Microwave transitions are only possible within each manifold with frequencies f^e_{ij} and f^o_{ij} respectively, but not between them, as this would require a term in the Hamiltonian that connects them [26]. The two manifolds are incoherently connected by the tunneling of single quasiparticle excitations across the junction [20, 21, 22]. This is equivalent to a 1/2 shift in n_g (a shift by $1e$), which changes the transmon transition frequencies from f^e_{ij} to f^o_{ij} or vice versa and can be accompanied by qubit relaxation or excitation. We define the transmon parity as the parity of the number of single quasiparticles that have tunneled across the junction [19] and the parity-switching time τ_p as the mean dwell time between two such events. In addition to the discrete parity jumps caused by quasiparticles tunneling across the junction, the charge environment creates noise in n_g including slow drift, shifting by about $1e$ over a time scale of order 10 min. The transmon was introduced [122] as a qubit design less sensitive to noise in n_g, but charge noise in transmons continues to be a subject of research [123].

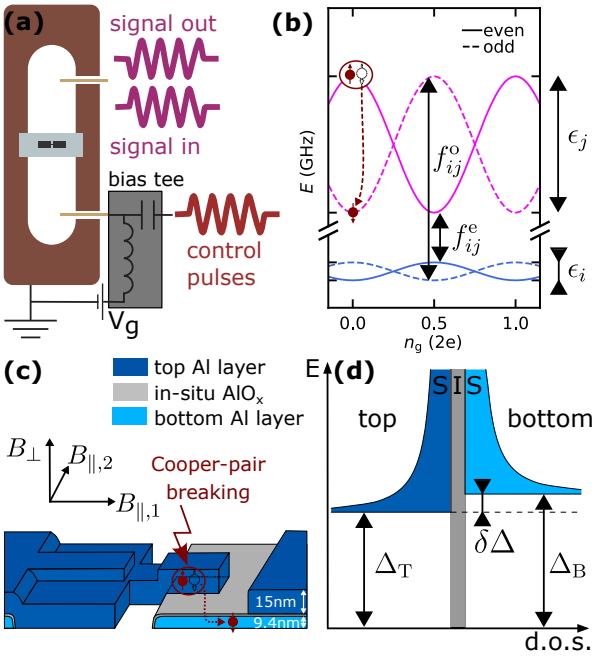

Figure 3.1: Schematic of the experiment design. **(a)** Sketch of the 3D copper cavity with the transmon. A bias-tee at one of the cavity pins enables voltage biasing of the transmon. **(b)** Successive transmon energy levels i and j as a function of n_g (proportional to V_g). There are two manifolds ("even" and "odd") connected by the incoherent tunneling of single quasiparticles. Energy levels have a charge dispersion with peak-to-peak value ϵ_i and transition frequencies f^e_{ij} and f^o_{ij}. **(c)** Sketch of a Dolan-bridge Josephson junction (JJ) relating the magnetic-field axes to the JJ geometry. A vector magnet is used to flux-bias the SQUID loop along $B_\perp$ and to apply in-plane magnetic fields along $B_{\parallel,1}$ and $B_{\parallel,2}$. Quasiparticles can be generated by Cooper-pair breaking photons; any event where single quasiparticles tunnel through the JJ changes the charge parity of both electrodes and makes the transmon transition frequencies jump from f^e_{ij} to f^o_{ij} or vice versa. The two electrodes in the JJ have different thicknesses for the top and bottom aluminum layers, leading to different superconducting gaps in the excitation spectrum. **(d)** Density of states (d.o.s.) and superconducting gap for the two electrodes.

Our transmon includes a Superconducting Quantum Interference Device (SQUID) comprising two Al/AlO$_x$/Al tunnel junctions. Thin aluminum films yield relatively high critical fields $B_c \sim 1$T for

magnetic fields applied in-plane [124, 125], and narrow superconducting electrodes minimize vortex losses. Previously, we showed that a device based on the same geometry can remain sufficiently coherent (with lifetimes of the order of 1µs) even at high magnetic fields [115]. The two superconducting electrodes composing each junction are characterized by different superconducting gaps, Δ_B and Δ_T, due to the different film thicknesses of the bottom (B) and top (T) aluminum layer [Fig. 3.1 (c) and (d)]. The gap asymmetry $\delta\Delta = \Delta_B - \Delta_T$ estimated with a phenomenological law [126, 127, 120] is on the order of the transmon transition energy hf_{01}, making it relevant for quasiparticle-tunneling processes [120]. A SQUID transmon was chosen such that at low fields, the bottom sweet spot has a sufficient charge dispersion for charge-parity measurements, while at higher fields eventually, the top sweet spot charge dispersion becomes sufficient. However, due to flux instabilities, we could not measure the spectrum for $B_{\parallel,1} > 0.41\,\mathrm{T}$ for reasons that are currently not understood. Coherence times start to drop sharply slightly below 0.40 T (see supplementary information [73] for details). Due to flux noise, the qubit coherence is severely reduced away from the top and bottom sweet spots of the SQUID, so measurements of the parity-switching time were mainly performed at the bottom sweet spot.

A vector magnet is used to flux-bias the SQUID loop with an out-of-plane field $B_\perp$ and to apply in-plane magnetic fields along $B_{\parallel,1}$ and $B_{\parallel,2}$ [see Fig. 3.1 (c)]. The frequency modulation due to the SQUID is highly sensitive to $B_\perp$ which enables precise alignment of the magnetic field to the sample plane to within ±0.05°. To measure the magnetic-field dependence of the parity-switching time, we apply the field along the $B_{\parallel,1}$ axis. Previously we saw that the magnetic-field dependence along the $B_{\parallel,2}$ axis was more erratic [115], which we hypothesize to be due to different spurious JJs in the two field directions. In the following, we will use $B_\parallel$ as a shorthand for $B_{\parallel,1}$.

3.3. IN-PLANE MAGNETIC FIELD DEPENDENCE OF THE TRANSMON SPECTRUM

First, we investigate the evolution of the transmon spectrum with the applied magnetic field to extract the parameters of our device, such as the Josephson energy (E_J) and the charging energy (E_C). The in-plane magnetic field $B_\parallel$ modulates E_J, while E_C remains unaffected. Consequently, the transmon spectrum changes as a function of $B_\parallel$; both the transition frequencies between different transmon levels and their respective charge dispersions are modified.

Two different mechanisms contribute to the suppression of the Josephson energy E_J in the presence of an in-plane magnetic field. First, the magnetic field weakens superconductivity in the two electrodes composing the SQUID [17]. Specifically, the superconducting gaps Δ_B, Δ_T, and so $E_J \propto \Delta_B\Delta_T/(\Delta_B+\Delta_T)$, decrease monotonically with increasing $B_\parallel$. Second, the magnetic field directly affects the Josephson coupling at the junction by laterally penetrating the JJ's oxide barrier. This causes a Fraunhofer-like pattern in the dependence of the junction's critical current I_c on $B_\parallel$ [17] (c.f. Fig. 3.8); this modulation is significant when the lateral flux associated with the field is of the order of the superconducting flux quantum $\Phi_0 = h/(2e)$. In our case, with JJs of width $l_2 \sim 200\,\mathrm{nm}$ and film thickness $t \sim 10\,\mathrm{nm}$ [1], this field is of order $B_{\Phi_0}(t, l_2) \sim \Phi_0/(l_2\, t) \sim 1\,\mathrm{T}$. We were able to explore this regime here due to the large in-plane critical field B_c of thin-film superconducting electrodes [125]. In typical JJs, the electrodes are thicker, usually 30 nm and above; as the critical field B_c decreases faster with thickness than B_{Φ_0} ($t^{-3/2}$ [125] vs t^{-1}), the Fraunhofer effect becomes less important as thickness increases.

To quantify both contributions to E_J, we measure the perpendicular flux dependence of the lowest energy transitions in a SQUID transmon for selected in-plane magnetic fields $B_\parallel$ [Fig. 3.2 (a)]. The SQUID is asymmetric; the two JJs have different dimensions, and hence different Josephson energies E_{Ja} and E_{Jb} proportional to the junction area. Therefore the flux arcs shown in Fig. 3.2 (a) display both a top and a bottom flux sweet spot, for which $E_J(\phi = 0) = E_{Ja} + E_{Jb}$ and $E_J(\phi = 0.5\Phi_0) = |E_{Ja} - E_{Jb}|$, respectively. The inset of Fig. 3.2 (a) shows the extracted Josephson energies as a function of $B_\parallel$. In general, the magnitude of gap suppression at a given field is determined by material properties and film thickness; since the two arms of the SQUID have been fabricated simultaneously, we take the two junctions to be equally affected

[1] More generally, given the penetration depths λ_T, λ_B and the film thicknesses of the two electrodes t_T, t_B, the effective thickness determining the Fraunhofer critical field amounts to $\lambda_T \tanh(t_T/2\lambda_T) + \lambda_B \tanh(t_B/2\lambda_B) + t_{AlOx}$, where t_{AlOx} is the thickness of the insulating oxide-barrier of the Josephson junction.

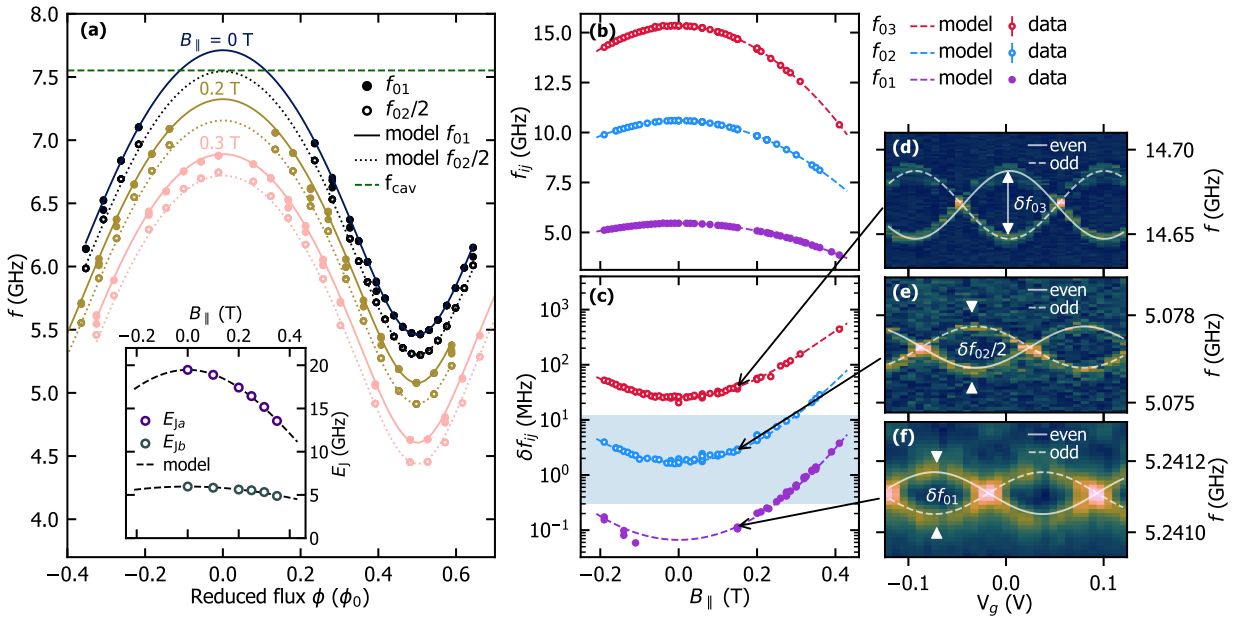

Figure 3.2: Transmon spectroscopy in a magnetic field. **(a)** Transmon frequencies f_{01}, $f_{02}/2$ as a function of $B_\perp$ (here expressed as the reduced flux Φ/Φ_0) for selected $B_\parallel$. The asymmetric SQUID oscillates between top and bottom flux sweet spots, corresponding to the sum and difference of the two junctions' Josephson energies E_{Ja} and E_{Jb}. For $B_\parallel \leq 0.2\,\mathrm{T}$ the top sweet spot is close to f_{cav} and therefore we do not perform dispersive two-tone spectroscopy for frequencies above 7.1 GHz. The inset shows E_{Ja} and E_{Jb} as a function of $B_\parallel$. Their monotonic decrease with $B_\parallel$ is mainly due to a Fraunhofer-like pattern in the junctions' critical currents $I_{c,a}$ and $I_{c,b}$; the magnetic field further decreases E_J by suppressing the superconducting gap. However, in the magnetic-field range covered by quasiparticle-parity measurements, the effect is small, less than 3% (see Section 3.D). **(b)** and **(c)** In-plane magnetic field dependence of the bottom-sweet spot transitions f_{01}, f_{02} and f_{03} and their respective parity-frequency splittings $\delta f_{ij} = \max_{n_g}(f^e_{ij} - f^o_{ij})$. As E_J decreases all f_{ij} decrease, while their δf_{ij} increase; we assume E_C to be unaffected by $B_\parallel$. We obtain the f_{ij} and δf_{ij} in voltage-gate scans as shown in panels **(d)**-**(f)**. For each transition, two separate frequency branches differ by one missing or extra quasiparticle in each of the transmon's electrodes, making it possible to turn the transmon into a quasiparticle parity meter. The blue-shaded area in panel (d) indicates where δf_{ij} is in a useful range for parity-state-mapping. For $B_\parallel \leq 0.3\,\mathrm{T}$ we employ the f_{12} transition, for $B_\parallel \geq 0.25\,\mathrm{T}$ we can also use the f_{01} transition. The joint fit to all f_{ij} and δf_{ij} shown in this figure requires higher harmonics $E_{J,m}\cos(m\phi)$ (with m integer) in the Josephson energy term of the transmon Hamiltonian, for details see Section 3.C. We find $E_C/h = 327.5\,\mathrm{MHz}$ and the zero-field Josephson energies $E^0_{Ja}/h = 19.47\,\mathrm{GHz}$ and $E^0_{Jb}/h = 5.97\,\mathrm{GHz}$.

by gap suppression. In contrast, the characteristic fields for the Fraunhofer contribution to I_c are different ($B_{\Phi_0,a} \neq B_{\Phi_0,b}$) due to the SQUID asymmetry. Consequently, the parameter characterizing the SQUID asymmetry $\alpha_{JJ} = |E_{Ja} - E_{Jb}|/(E_{Ja} + E_{Jb})$ changes with $B_\parallel$; this feature allows us to discriminate between the Fraunhofer contribution and the suppression of the superconducting gaps (for details see Section 3.D). In the magnetic-field range covered by quasiparticle-parity measurements, we estimate the contribution of the gap suppression to $E_J \propto \Delta_B\Delta_T/(\Delta_T + \Delta_B)$ to be less than 3%, so the decrease in E_J is mainly due to the Fraunhofer contribution.

Measuring the parity-switching time requires the transmon to be in an offset-charge sensitive regime. The charge dispersion's peak-to-peak values $\epsilon_i \propto E_C(E_J/E_C)^{i/2+3/4}\exp(-\sqrt{8E_J/E_C})$ [16] depend exponentially on the ratio of E_J/E_C and are larger for higher levels. Experimentally we measure the transition frequencies f_{ij} between two levels $|i\rangle$ and $|j\rangle$ and their parity-frequency splittings $\delta f_{ij} = \max_{n_g}(f^e_{ij} - f^o_{ij})$. Now, as E_J decreases with $B_\parallel$, the f_{ij} decrease and the δf_{ij} increase. Figure 3.2 (b) and (c) show f_{01}, f_{02} and f_{03} as well as the corresponding δf_{ij} measured at the bottom flux sweet spot as a function of $B_\parallel$. The data is determined from voltage-gate scans like the ones displayed in Fig. 3.2 (d)-(f); these examples were taken at $B_\parallel = 0.15\,\mathrm{T}$ (see also Section 3.E). We observe both frequency branches f^e_{ij} and f^o_{ij} in two-tone spectroscopy as the measurement is slow compared to the characteristic parity-switching time τ_p. In successive single-shot measurements, however, the transmon is either in the "odd" parity state or in the "even" parity state, and parity switches come with a measurable frequency jump. This jump is maximally resolved when the gate voltage V_g is set to the charge sweet spot, i.e., $n_g = 0, 1/2, 1\ldots$ in Fig. 3.1 **(b)**, and it enables a charge-parity meter based on

a frequency-dependent gate [116]. To measure the parity-switching rates we use different transmon transitions depending on the field range: For $B_\parallel \geq 0.25\,\mathrm{T}$, $\delta f_{01} \geq 0.2\,\mathrm{kHz}$, and we can use the f_{01} transition. For smaller fields, however, the $E_\mathrm{J}/E_\mathrm{C}$-ratio is on the order of 45 to 30 even for the bottom sweet spot, and δf_{01} is too small for charge parity measurements given our dephasing times. With δf_{02} being a factor 10 larger with comparable dephasing times, we employ the f_{12} transitions instead. That way, we can measure the transmon parity also for higher $E_\mathrm{J}/E_\mathrm{C}$-ratios and cover a wide range of magnetic fields.

Notably, a joint fit to all f_{ij} and δf_{ij} shown in Fig. 3.2 requires the inclusion of higher Josephson harmonics $E_{\mathrm{J,m}}\cos(m\phi)$ in the transmon Hamiltonian. The data we collected in the process of pursuing the quasiparticle physics shows good evidence for the Josephson harmonics; it has been combined with results from other groups to make the case for a more complex current-phase relationship in conventional Al/AlO_x/Al tunnel JJs that had previously been overlooked, see Ref. [100]. Here we explicitly consider the SQUID nature of the transmon in analyzing our data, see Section 3.C for details. The parameters we extract from the spectroscopic data, in particular the charging and Josephson energies, also enter into the estimates of the parity-switching time that we consider in the next Section.

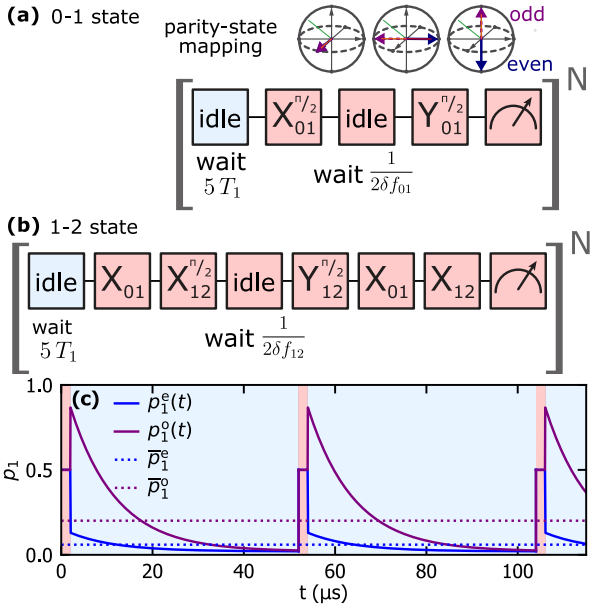

Figure 3.3: Parity-mapping scheme. **(a)** and **(b)** show the gate sequences for the parity measurements using superpositions $|0\rangle + |1\rangle$, and $|1\rangle + |2\rangle$ respectively. They are repeated $N = 2^{18}$ times. For an initial $|0\rangle$ state, we define "even" ("odd") parity as the parity that is ideally mapped on $|0\rangle$ ($|1\rangle$). During the parity measurement sequence, the transmon is out of equilibrium. **(c)** estimated excited-state population p_1 for "even" and "odd" parity as a function of time during the parity-measurement cycle. From the hidden-Markov model, we obtain measurement outcomes for declared "even" and "odd" parities, which give the initial populations after the measurement. Finite parity-measurement fidelity leads to slight deviations from the ideal $p_1 = 0$ for "even" parity. Taking the average over the cycle, we can estimate the mean populations $\overline{p}_1^\mathrm{e}$, $\overline{p}_1^\mathrm{o}$ for the "even" and "odd" parities, which are input parameters for modeling the switching-time data.

3.4. IN-PLANE MAGNETIC FIELD DEPENDENCE OF THE PARITY-SWITCHING TIME

We now turn to the characterization of the transmon's parity-switching time as a function of $B_\parallel$. Measurements are performed at the bottom sweet spot in $B_\perp$, see discussion in Sec. 3.2. We use a Ramsey-based parity measurement [116] with superpositions of $|0\rangle$ and $|1\rangle$ as well as $|1\rangle$ and $|2\rangle$, as illustrated in in Fig. 3.3. At a gate-voltage sweet spot ($n_\mathrm{g} = 0, 1/2, 1\ldots$), the parity-measurement protocol projects the lower frequency branch predominantly onto the transmon ground state $|0\rangle$, and the upper-frequency branch onto the first excited state $|1\rangle$. We henceforth call "even" the parity branch that is projected onto $|0\rangle$ and denote its mean dwell time by $\tau_\mathrm{p}^\mathrm{e}$. Similarly, "odd" is the parity branch that is projected onto $|1\rangle$, with a mean dwell time $\tau_\mathrm{p}^\mathrm{o}$. As we do not actively reset the qubit state after an individual single-shot parity measurement, we include a waiting time of $5T_1$ before taking the next single-shot parity measurement. As a result, the qubit's first-excited-state population p_1 is on average higher for "odd" than for "even" parity mapping, as the transmon relaxes from the excited state to the ground state during the waiting time, see Fig. 3.3 (c). At the base temperature of the cryostat, $T \sim 7\,\mathrm{mK}$, we estimate a mean excited-state population $\overline{p}_1^\mathrm{e} = 4.3\%$ for "even" parity and $\overline{p}_1^\mathrm{o} = 19.5\%$ for "odd" parity. More details on the parity-measurement sequence and its analysis in terms of a Hidden Markov Model can be found in Section 3.F.

Figure 3.4 (a) shows the two parity-switching times for "even" ($\tau_\mathrm{p}^\mathrm{e}$) and "odd" ($\tau_\mathrm{p}^\mathrm{o}$) parity as a function of $B_\parallel$. Most notably, the two parity-switching times evolve non-monotonically with $B_\parallel$: for both $\tau_\mathrm{p}^\mathrm{e}$ and $\tau_\mathrm{p}^\mathrm{o}$ we observe an initial increase with applied magnetic field, reaching a maximum at $B_\parallel \approx 0.2\,\mathrm{T}$, before decreasing again at higher fields. Besides, we generally observe $\tau_\mathrm{p}^\mathrm{e} \neq \tau_\mathrm{p}^\mathrm{o}$; in particular for $|B_\parallel| \leq 0.2\,\mathrm{T}$, $\tau_\mathrm{p}^\mathrm{o}$ is smaller than $\tau_\mathrm{p}^\mathrm{e}$. Theoretically, we expect $\tau_\mathrm{p}^\mathrm{e} \approx \tau_\mathrm{p}^\mathrm{o}$, since the asymme-

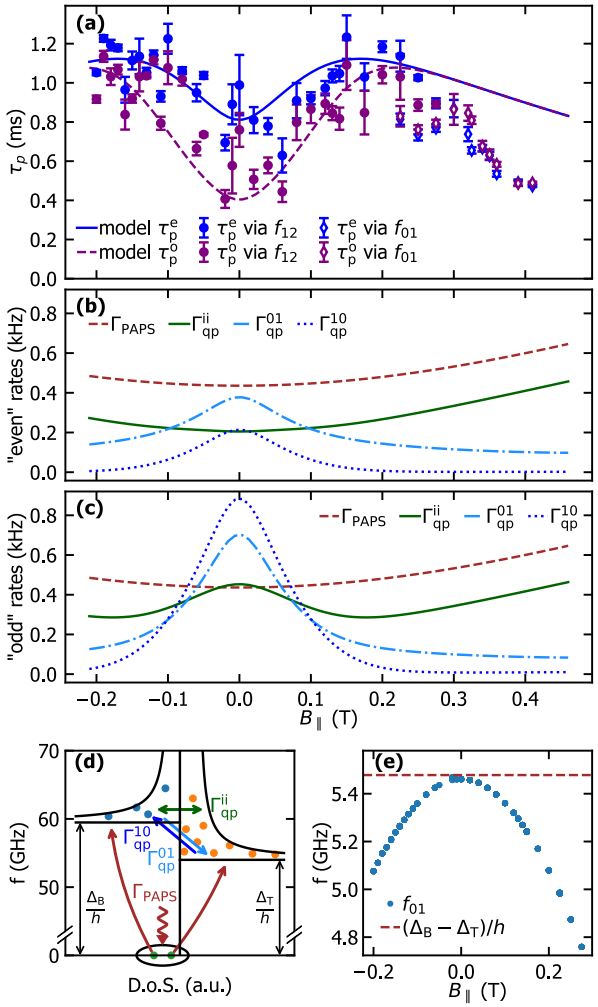

Figure 3.4: **(a)** Parity-switching times τ_p^e and τ_p^o for "even" and "odd" parity vs $B_\parallel$ measured at the flux bottom sweet spot. Model contributions to **(b)** $1/\tau_p^e$ and **(c)** $1/\tau_p^o$. Around $B_\parallel = 0$ T the population-weighted quasiparticle-tunneling rates Γ_{qp}^{01} and Γ_{qp}^{10} [Eqs. (3.5) and (3.6)] show a peak. These two processes excite or relax the transmon while bridging the superconducting-gap difference and are resonantly enhanced when $f_{01} \simeq \delta\Delta/h$, explaining the low-field dip in τ_p. A higher first-excited-state population p_1 further increases Γ_{qp}^{10} for the "odd" case, which is why $\tau_p^o < \tau_p^e$ in this region. Rate Γ_{qp}^{ii} accounts for quasiparticle tunneling not accompanied by qubit logical state change. Photon-assisted quasiparticle tunneling Γ_{PAPS} dominates for higher fields. **(d)** Schematic density of states for the quasiparticle excitation spectra in high- and low-gap (bottom and top) electrodes. The quasiparticles are generated by pair-breaking photons; they can tunnel at constant quasiparticle and transmon energy or by exchanging energy with the transmon. **(e)** Qubit frequency f_{01} and estimated superconducting-gap difference $\delta\Delta/h = (\Delta_B - \Delta_T)/h$ vs $B_\parallel$. While at zero field $f_{01} \simeq \delta\Delta/h$, the transmon is tuned further away from resonance for higher fields. Gaps used for the theoretical curves are $\Delta_T/h = 54$ GHz and $\delta\Delta/h = 5.48$ GHz. For the remaining model parameters see Section 3.G.

try between "even" and "odd" parity-switching rates is at most of order $e^{-h\delta f_{01}/k_B T}$ [128]. Even at the nominal base temperature of the cryostat $T_0 \approx 7$ mK, we have $k_B T_0 \approx 150\,\text{MHz} \gg \delta f_{01} \sim 0.1 - 10\,\text{MHz}$ [cf. Fig. 3.2 (c)]. As we will argue below, the difference between τ_p^e and τ_p^o is instead due to the measurement-induced $\overline{p}_1$.

3.4.1. MODELLING THE PARITY SWITCHING TIME

To understand the non-monotonic magnetic-field dependence of τ_p and the difference between "even" and "odd" parities we model different contributions to the parity-switching time. Adopting the notation of Ref. [19], we distinguish photon-assisted parity switching (PAPS) [129], from number-conserving parity switching (NUPS) events, expressing

$$\frac{1}{\tau_p} = \Gamma_{PAPS} + \Gamma_{NUPS}\,. \tag{3.1}$$

For PAPS events, pair-breaking photons with energy larger than the gap sum $\Delta_B + \Delta_T$ are absorbed right at the JJ, leading to the generation of quasiparticles in the bottom and top electrode at a total rate

$$\Gamma_{PAPS} = p_0(\Gamma_{00}^{ph} + \Gamma_{01}^{ph}) + p_1(\Gamma_{11}^{ph} + \Gamma_{10}^{ph})\,. \tag{3.2}$$

In Eq. (3.2), p_1 is the occupation probability of the first excited state of the qubit, $p_0 = 1 - p_1$ [we disregard the occupation of higher excitation levels, see discussion in Appendix 3.G], and the subscripts in Γ_{ij}^{ph} denote the initial and final transmon logical states i and j.

In NUPS events, quasiparticles tunnel from one side of the JJ to the other, conserving the total quasiparticle number. We distinguish three terms in the total rate of these events,

$$\Gamma_{NUPS} = \Gamma_{qp}^{ii} + \Gamma_{qp}^{01} + \Gamma_{qp}^{10} \tag{3.3}$$

In general, both quasiparticles in the bottom and top electrodes contribute to each term. For instance, for the "quasi-elastic" events modifying the qubit parity only but not its logical state (i.e., with exchanged energy $|\epsilon_i| \ll h f_{01}$) their rate takes the form

$$\begin{aligned}\Gamma_{qp}^{ii} &= p_0(\tilde{\Gamma}_{00}^{B} x_B + \tilde{\Gamma}_{00}^{T} x_T) + p_1(\tilde{\Gamma}_{11}^{B} x_B + \tilde{\Gamma}_{11}^{T} x_T) \\ &\approx \tilde{\Gamma}_{00}^{B} x_B + \tilde{\Gamma}_{00}^{T} x_T\end{aligned} \tag{3.4}$$

where x_B, x_T are the dimensionless quasiparticle densities in the top and bottom electrodes, respectively [$x_\alpha = N_\alpha / N_{Cp}^\alpha$, with N_α and N_{Cp}^α the numbers of quasi-

particle and the Cooper pairs in electrode α]. The rates $\tilde{\Gamma}^{\alpha}_{ij}$ denote tunneling of quasiparticles initially located in electrode α into the other electrode with initial and final transmon states i and j. The approximation in the last expression is valid at leading order in the ratio E_J/E_C for a transmon qubit. For the rates of events changing the transmon state by exchanging energy $\sim hf_{01}$ (weighted by the qubit state occupation probability) we consider

$$\Gamma^{01}_{qp} = p_0 \tilde{\Gamma}^{B}_{01} x_B \,, \tag{3.5}$$

$$\Gamma^{10}_{qp} = p_1 (\tilde{\Gamma}^{T}_{10} x_T + \tilde{\Gamma}^{B}_{10} x_B) \tag{3.6}$$

for events associated with qubit excitation and relaxation, respectively (see Appendix 3.G about the contribution to Γ^{01}_{qp} from the top electrode's quasiparticles). Note that the excited state population p_1 is in general determined not just by quasiparticles, but by all the mechanisms affecting the qubit, including measurement as explained above; since p_1 can be determined experimentally, we treat it as an input parameter in analyzing the parity-switching time.

The steady-state values of the quasiparticle densities in the two electrodes x_B and x_T are computed by solving a system of coupled rate equations. Physically, these densities are determined by the balance between processes keeping the quasiparticles away from the junctions, such as recombination and trapping, and quasiparticle generation, which in our model originates from pair breaking by high-frequency photons with rate $\propto \Gamma_{PAPS}$. Details on the approximate solution to the rate equations and on the temperature and parallel field dependencies of the rates $\tilde{\Gamma}^{\alpha}_{ij}$ and Γ^{ph}_{ij} are given in Appendix 3.G. The parallel magnetic field modulates these rates via three distinct effects: first, E_J changes due to a combination of gap suppression and Fraunhofer effect; this also changes the qubit frequency and influences the matrix elements for quasiparticle transitions. Second, similarly to the Fraunhofer modulation of the critical current, these matrix elements are also directly altered by phase-interference effects. Third, the two superconducting gaps get suppressed differently because the critical field depends on film thickness; in modeling the parity-switching time in the following section, we can neglect the field dependence of the superconducting gap as we only reach a small fraction of the critical field.

3.4.2. DISTINGUISHING PARITY SWITCHING MECHANISMS

Figure 3.4 (b) and (c) show the magnetic-field dependence of the estimated contributions Γ_{PAPS}, Γ^{01}_{qp}, Γ^{10}_{qp} and Γ^{ii}_{qp} to τ^{e}_{p} and τ^{o}_{p}, respectively. We first address the nonmonotonic behavior of τ_p, so we focus on the "odd" case, where this feature is more prominent. At zero field, the quasiparticle tunneling rates Γ^{01}_{qp} and Γ^{10}_{qp} are maximum, decreasing monotonically with $|B_\parallel|$. The transitions described by the rates Γ^{01}_{qp} and Γ^{10}_{qp} excite and relax the transmon, respectively, exchanging an energy $\sim hf_{01}$. This process is strongly enhanced when $\Delta_B - \Delta_T \simeq hf_{01}$ due to the large density of states in the quasiparticle spectrum near the gap edge [see Fig. 3.4 (d) and Ref. [120]]. At zero field, the gap difference estimated through fitting slightly exceeds the qubit frequency, i.e., $\delta\Delta \gtrsim f_{01}$. With increasing magnetic field, f_{01} decreases and is progressively detuned from the gap difference [Fig. 3.4 (e)], causing the initial increase of τ_p with applied magnetic field. In contrast, photon-assisted pair-breaking increases as E_J decreases, producing the subsequent decay of τ_p at higher fields. The competition between PAPS and NUPS is similar to the one reported in Ref. [19], where the authors distinguish the two contributions by exploiting the modulation of the frequency of a SQUID transmon with an out-of-plane magnetic field. Here, instead, the interplay of PAPS and NUPS is tuned by $B_\parallel$, causing the non-monotonic evolution of τ_p: while PAPS dominates for higher fields, NUPS dominates at low fields.

The difference between "even" and "odd" parity-switching times τ^{e}_{p} and τ^{o}_{p} is related to the dependence of the average excited-state population p_1 on the parity measurements: as discussed above, p_1 is higher for "odd" than for "even" parity, because the "odd" parity predominantly ends up in $|1\rangle$ at the end of the parity mapping and then relaxes during the idling, while the even parity predominantly ends up in $|0\rangle$ (see Fig. 3.3). Quasiparticle transitions with concomitant transmon relaxation at rate Γ^{10}_{qp} require the transmon to be in the excited state and are therefore proportional to p_1. Consequently, the contribution of Γ^{10}_{qp} is enhanced for "odd" parity compared to "even" parity. At the same time, quasiparticle transitions at rate Γ^{10}_{qp} are dominantly from the low-gap (top) electrode to the high-gap (bottom) electrode, since $x_T \gg x_B$ for $\delta\Delta > f_{01}$ [120]. These transitions further increase the quasiparticle density in the high-gap electrode. As a result, x_B is larger for "odd" parity, thus enhancing the contribu-

tion of $\Gamma_{\mathrm{qp}}^{01} \propto x_{\mathrm{B}}$, despite the lower occupation of the ground state $p_0 = 1 - p_1$. Plots of the estimated quasiparticle densities x_{B}, x_{T} can be found in the supplemental material [73].

At the highest fields, i.e., $0.3\,\mathrm{T} \lesssim B_{\parallel} \lesssim 0.41\,\mathrm{T}$, τ_{p} decays more strongly than the model predicts. This coincides with an overall deterioration of the transmon coherence: For $B_{\parallel} \gtrsim 0.3\,\mathrm{T}$, the cavity Q-factor starts to decrease and the transmon lifetime T_1 and Ramsey-coherence time T_2^* drop by an order of magnitude between $B_{\parallel} = 0.3\,\mathrm{T}$ and $0.41\,\mathrm{T}$ (see supplemental material [73]). Above $B_{\parallel} = 0.41\,\mathrm{T}$ we observe an extended magnetic-field range where the transmon frequency is very unstable in $B_{\perp}$ and in time and therefore largely not measurable. While generally recovering for $B_{\parallel} \geq 0.6\,\mathrm{T}$, the SQUID remains unstable around its top sweet spot hence thwarting our plan to use the top sweet spot for high-field measurements of τ_{p}. In Ref. [115] we also observed an unstable region between $B_{\parallel} = 0.4\,\mathrm{T}$ and $0.5\,\mathrm{T}$ with a similar device and suspected spurious JJs in the leads to cause it. Here, these effects may be connected to the reduction of τ_{p} in a way that we currently do not understand. It is also possible that the theory overestimates τ_{p} for higher magnetic fields as we disregard the field dependence of the gaps. As discussed in Section 3.3, we estimate the contribution of the gap suppression to E_{J} to be less than 3% and therefore only account for the Fraunhofer effect on the quasiparticle-tunneling rates. However, the model uses a simplified description of the pair-breaking photons in terms of a single frequency (monochromatic radiation, see Appendix 3.G). More generally, few or several modes can contribute to the photon-assisted pair-breaking rate, and considering for example blackbody radiation originating from higher-temperature stages of the refrigerator, the photon-assisted switching rates could increase more strongly than predicted by our model.

3.5. TEMPERATURE DEPENDENCE OF THE PARITY-SWITCHING TIME

To complement the data on the magnetic-field dependence of τ_{p}, we measured its temperature dependence for selected in-plane magnetic fields $B_{\parallel}$. Figure 3.5 (a) and (b) show the temperature dependence of "even" and "odd" parity-switching times $\tau_{\mathrm{p}}^{\mathrm{e}}$ and $\tau_{\mathrm{p}}^{\mathrm{o}}$ for $B_{\parallel} = 0\,\mathrm{T}$ and $B_{\parallel} = -0.13\,\mathrm{T}$ (which is close to the maximum observed τ_{p}; measurements performed at additional values of $B_{\parallel}$ can be found in Ref. [73]). Interestingly, we

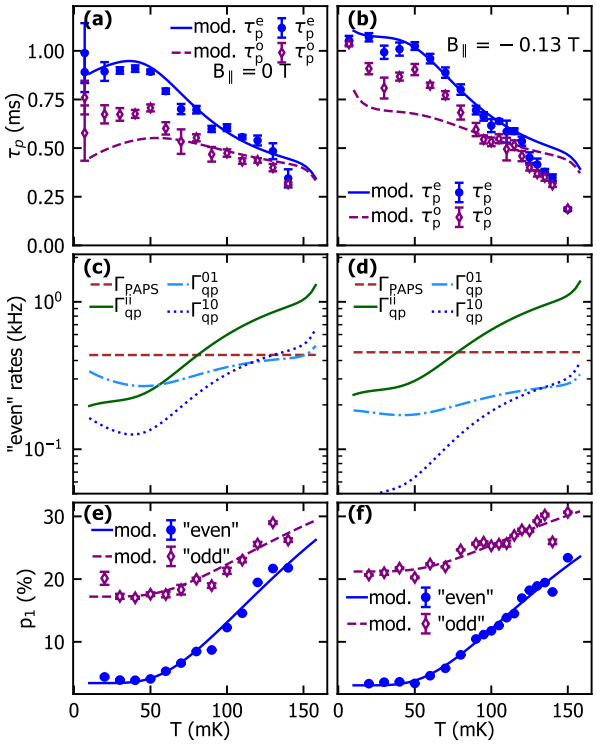

Figure 3.5: Temperature dependence of τ_{p} for **(a)** $B_{\parallel} = 0\,\mathrm{mT}$ and **(b)** $B_{\parallel} = -0.13\,\mathrm{T}$. A cascading decay starting already around $T \sim 50\,\mathrm{mK}$ cannot be explained by quasiparticle generation due to thermal phonons. **(c)** and **(d)**: Model contributions to $1/\tau_{\mathrm{p}}^{\mathrm{e}}$ for both fields. The increase in quasiparticle-tunneling with temperature is dominantly caused by enhanced "quasi-elastic" tunneling $\Gamma_{\mathrm{qp}}^{\mathrm{ii}}$ due to a change in the quasiparticle distributions. Two different processes contribute here: first, an increasing excited-state populations p_1 enhances $\Gamma_{\mathrm{qp}}^{10}$, resulting in an increasing high-gap quasiparticle density. Additionally, a thermal broadening of the quasiparticle energy distributions in bottom and top electrode yields more quasiparticles that can tunnel at a given energy. **(e)** and **(f)**: Temperature dependencies of p_1. The semi-phenomenological expression for the fits in these panels is discussed in Appendix 3.H.

observe a cascading decay of τ_{p} starting already at relatively low temperatures of order $T \sim 50\,\mathrm{mK}$. This behavior cannot be explained by quasiparticle generation due to thermal phonons alone; indeed, this contribution is exponentially suppressed as $\exp(-2\Delta_{\mathrm{T}}/T)$ and typically dominates over pair-breaking photons only at higher temperatures (see Section 3.I and Ref. [130]). A similar temperature dependence has been observed but not explained at finite field in a semiconducting nanowire-based transmon [80]. At zero field and in tunnel-junction-based transmons, a decrease in τ_{p} with temperature has been attributed to the excitation of quasiparticles out of superconducting traps by phonons [111] and more recently related to the gap asymmetry [119].

Our model can capture the cascading decay by tak-

ing into account, along with the gap asymmetry, two distinct effects: the thermal broadening of the quasiparticle energy distributions and an increase in the excited state population p_1. To illustrate these points, we consider the same contributions determining τ_p in our model as in the previous section, now additionally accounting for the temperature variation [Fig. 3.5 (c) and (d)]. The contribution Γ_{PAPS} from photon-assisted parity switching is temperature-independent in the measured range [2]. At base temperature $T \sim 7\,\mathrm{mK} \ll \delta\Delta/k_B$ quasiparticle tunneling rates that leave the transmon state unchanged are slower, $\Gamma^{\mathrm{ii}}_{\mathrm{qp}} < \Gamma_{\mathrm{PAPS}}$; quasiparticles are mainly located in the lower-gap electrode with energy $\sim \Delta_T$, and rates for events where they tunnel from the bottom to the top electrode without changing the qubit logical state are suppressed as $e^{-\delta\Delta/k_B T}$. Starting from $T \gtrsim 50\,\mathrm{mK}$, the excited state population p_1 increases [see Fig. 3.5 panels (e) and (f)], and so the (weighted) rate $\Gamma^{10}_{\mathrm{qp}}$ increases. Since this process leads to a larger quasiparticle density in the high-gap (bottom) electrode (see plots in [73]), the rates $\Gamma^{\mathrm{qp}}_{01}$ and $\Gamma^{\mathrm{qp}}_{ii}$ are enhanced, too. The increase of $\Gamma^{\mathrm{qp}}_{ii}$ is also assisted by the thermal broadening of the quasiparticles distributions [see Fig. 3.4(d)]. All these processes gradually suppress τ_p already for temperatures well below those at which quasiparticles generated by thermal phonons eventually become the limiting factor, $T \gtrsim 150\,\mathrm{mK}$.

The robustness of our modeling is demonstrated by the fact that a fixed set of (few) parameters captures both the magnetic field and the temperature dependencies of τ_p. Moreover, the estimated superconducting-gap difference $\delta\Delta = 5.48\,\mathrm{GHz}$ is in reasonable agreement with a simple estimate based on a phenomenological law for aluminum thin films [120]. Our estimate for the trapping rates $s_B = s_T = 3.39\,\mathrm{Hz}$ is smaller yet comparable to previously reported values for transmons of similar geometry, which are in the range 10 to 30 Hz [74, 19]; we note that when fitting the data, the photon-assisted rate Γ_{PAPS} weakly correlates with s. We independently quantify the gap Δ_T, and so the onset of thermal quasiparticles, by fitting the temperature dependence of T_1 measured for different in-plane magnetic fields $B_\parallel$ (Section 3.I). The resulting $\Delta_T/h = 54\,\mathrm{GHz}$ slightly overestimates the onset temperature for thermal quasiparticles to dominate the temperature dependence of τ_p; accounting for the temperature dependence of the trapping dynamics could perhaps reduce the mismatch. Moreover, the "even" case is generally better described than the "odd" case as the model considers a steady-state solution of coupled rate equations. Our pulse sequence, however, maps "odd" parity to the transmon state $|1\rangle$, repeatedly driving the system away from its steady state. Hence, possible deviations due to the dynamics of the qubit during the measurement of τ_p affect more significantly the "odd" assignment.

[2] The gap suppression with temperature can be safely neglected in this range, temperature being much smaller than the critical temperatures of the two electrodes.

3.6. CONCLUSIONS AND OUTLOOK

We have explored the magnetic-field dependence of parity switching times in a 3D SQUID transmon with thin-film Al/AlO_x/Al Josephson junctions. The magnetic field provides a tuning knob to explore the physics of quasiparticle dynamics in aluminum tunnel junctions; it suppresses the superconducting gaps Δ_B, Δ_T of both sides of the JJ and it introduces a Fraunhofer-like pattern in the junction's critical current. Both effects can influence the parity switching times. We observe a non-monotonic evolution of the "even" and "odd" parity-switching times τ^{e}_p and τ^{o}_p with $B_\parallel$: a dip around $B_\parallel = 0\,\mathrm{T}$ is followed by an initial increase reaching a maximum at $B_\parallel \sim 0.2\,\mathrm{T}$, before decaying again at higher fields. The observed maximum parity-switching time (τ_p) of 1.2 ms is below the current state of the art on the order of a minute [131, 110], but the shielding and filtering of our setup are not as advanced as those used in these works, and the 3D transmon has an antenna-like geometry that is more prone to absorption of pair-breaking photons [132, 133].

Modeling the quasiparticle dynamics between the two electrodes separated by the JJ with photon-induced pair-breaking as a generation mechanism, we explain this behavior by a changing dominant contribution to the parity-switching rate as the magnetic field increases: while photon-assisted parity switching (PAPS) dominates for higher fields, number-conserving parity switching (NUPS) dominates at lower fields. More precisely, NUPS processes $\Gamma^{01}_{\mathrm{qp}}$ and $\Gamma^{10}_{\mathrm{qp}}$ that excite or relax the transmon to bridge the superconducting-gap difference $\delta\Delta$ are resonantly enhanced around zero field as $hf_{01} \simeq \delta\Delta$. The effect is more pronounced for τ^{o}_p than for τ^{e}_p, which we attribute to the additional excited-state population p_1 introduced by our pulse sequence for "odd" parity, which further enhances $\Gamma^{10}_{\mathrm{qp}}$. While photon-assisted parity switches could likely be reduced by better

shielding and filtering, the superconducting-gap difference needs to be carefully engineered to avoid any resonance with transmon transition energies. As this work shows, the magnetic field lifts the resonance condition $hf_{01} \simeq \delta\Delta$ and can in principle be used post-fabrication as an analog to gap engineering.

To complement the magnetic-field data we also measured the temperature dependence of τ_p for selected $B_\parallel$. A cascading decay starting already at relatively low temperatures of $T \sim 50\,\mathrm{mK}$ is not due to quasiparticle generation by thermal phonons, as our model helps us understand. Instead, the "quasi-elastic" tunneling rate Γ_{qp}^{ii} rapidly increases above this temperature as the quasiparticle energy distributions in the bottom and top electrodes broaden, yielding more available quasiparticles for tunneling at constant energy. Additionally, Γ_{qp}^{10} increases with temperature due to an increasing excited-state population p_1. With the same model parameters, we consistently describe the magnetic-field and temperature dependencies of the measured parity-switching times. The model thus helps to identify the relevant tunneling mechanisms and provides insight into how they contribute to the total parity switching rate: Γ_{qp}^{01} and Γ_{qp}^{10} dominantly capture the low-field behavior, Γ_{PAPS} the high field behavior, and Γ_{qp}^{ii} the temperature dependence.

Our results suggest that Al/AlO_x/Al JJ circuits are a viable option for parity readout of topological qubits [24] and that the required magnetic fields do not necessarily cause quasiparticle tunneling to limit the coherence of Al/AlO_x/Al JJ circuits. The model we developed can help choose appropriate film thicknesses and junction geometries to approach operation up to 1 T. Moreover, magnetic fields can help in understanding and optimizing gap engineering, as they provide a way to in-situ change the superconducting gap without heating the sample. In samples with large gap asymmetry, the difference in critical fields will be more pronounced; hence, magnetic fields will strongly change the gap difference elucidating its impact on quasiparticle dynamics.

ACKNOWLEDGMENTS

We acknowledge Ioan Pop, Dennis Willsch, and the other authors of Ref. [100], for help in modeling and understanding the spectroscopic data. We also thank Dennis Willsch for his feedback on a draft of the manuscript. We would like to thank Philipp Janke for contributing to data analysis during a student internship. We thank Kelvin Loh, M. Adriaan Rol, and Garrelt Alberts from Orange Quantum Systems for developing software with us to compile the time-domain sequences to the Zürich Instruments hardware. We thank Michel Vielmetter for supporting the time-domain software development. We thank Jurek Frey and Felix Motzoi for discussions on improving the parity-to-state mapping sequences. We thank Lucie Hamdan and Timur Zent for their technical assistance. This project has received funding from the European Research Council (ERC) under the European Union's Horizon 2020 research and innovation program (grant agreement No 741121) and was also funded by the Deutsche Forschungsgemeinschaft (DFG, German Research Foundation) under CRC 1238 - 277146847 (Subproject B01) as well as under Germany's Excellence Strategy - Cluster of Excellence Matter and Light for Quantum Computing (ML4Q) EXC 2004/1 - 390534769. G.C. acknowledges support by the German Federal Ministry of Education and Research (BMBF), funding programme "Quantum technologies – from basic research to market", project QSolid (Grant No. 13N16149).

AUTHOR CONTRIBUTIONS

The project was conceived by C.D. and Y.A.. J.K. and C.D. fabricated the device and took the measurements with help from L.M.J.. The data was analyzed by J.K. and C.D. with help from L.M.J.. The theoretical model was extended to the magnetic field by G.M. and G.C. and fit to the data by J.K. and G.M.. The manuscript was written by J.K., G.M., G.C., and C.D. with input from all coauthors.

SOFTWARE

The setup was controlled based on QCoDeS drivers and logging [134], while the measurements were run using Quantify-core and the time-domain experiments were defined and compiled to hardware using Quantify-scheduler [135, 136]. In the data analysis, we used qutip for modeling a qutrit lindblad equation [137] and hmmlearn for fitting a Gaussian hidden-Markov model to analyze the parity-switching datasets [138].

DATA AVAILABILITY

Datasets and analysis in the form of Jupyter notebooks that create the figures of this manuscript are available on Zenodo with doi 10.5281/zenodo.10728469.

3.A. EXPERIMENTAL SETUP

The transmon is mounted in a 3D copper cavity which is loaded into a bottom-loading dilution refrigerator (Triton 500, Oxford Instruments) with a nominal base temperature of ~7 mK. The cavity was wrapped in Eccosorb LS-26 foam to improve the radiation shielding. This might be necessary because the outside of the puck sees the still plate environment, which is at about 1 K.

A detailed wiring diagram of the experiment can be found in Fig. 3.6. An Eccosorb filter on the input line filters high-frequency radiation. However, the output line remained unfiltered to avoid signal loss. Consequently, potential high energy photons coming from the LNF-LNC4_8C HEMT amplifier at the 4 K plate may leak back into the cavity to generate quasiparticles. Likely filtering of the output line is currently the easiest way to reduce the Cooper-pair breaking radiation in the setup.

To voltage-bias the device we use a bias-tee at one of the cavity pins. The voltage is applied relative to the ground of the dilution refrigerator, which is connected to the copper cavity, while the transmon islands are both floating. The cavity pin couples asymmetrically to the two islands enabling efficient charge-bias (see Section 3.E).

The temperature control is done via a PID loop using the Lakeshore resistance bridge of the dilution refrigerator. We took care to always stabilize for about 10 min at every temperature to make sure the transmon reaches equilibrium. All temperature readings are based on the mixing chamber RuO_x thermometer. To check the thermalization, we also looked at the transmon temperature based on ground-state occupancy measurements with the transmon nominally in the ground state (for details see Ref. [73]). At the base temperature the transmon temperature is about 50 mK.

The transmon is controlled with standard DRAG pulses [139, 140]. Predominantly the gate times for π and $\pi/2$ pulses were 20 ns. The pulse amplitude is optimized based on Rabi sequences, the frequency based on Ramsey sequences (including beating) and the DRAG parameter is optimized based on an XY sequence [141]. While the transmon control pulses and continuous-wave tones were routed to the input port of the cavity, we measured the cavity in reflection via the circulator. The transmon readout was performed without a parametric amplifier. Nonetheless, typical assignment fidelities of >90 % could be achieved for the qubit subspace with readout durations around 1 µs.

3.B. DEVICE FABRICATION, GEOMETRY AND FILM THICKNESS

The 3D transmon used in this experiment was fabricated in the same batch and with the same capacitor geometry as the device in Ref. [115]. The aluminum film thickness plays a crucial role in making the transmon magnetic field resilient, but in the thin-film limit, it also has a strong effect on the magnitude of the superconducting gap [126, 142, 127, 120]. In Ref. [115], the nominal film thicknesses for the two aluminum layers according to the Plassys MEB 550S evaporator used for the film deposition were reported to be 10 nm and 18 nm. The deposition rate was 0.2 nm s^{-1}. Between the two evaporations, the JJ barrier is formed by oxidation in 1 mbar of pure oxygen in a static setting for 6 min. After the second layer, another oxidation step was added to grow the initial oxide in a more controlled way with 1 mbar of oxygen for 10 min.

To measure the film thicknesses and JJ geometry, we perform Atomic force microscope imaging of the SQUID region of the device (Fig. 3.7). The height profile [see Fig. 3.7 **(c)**, **(d)** and **(e)**] shows three characteristic thicknesses at $t_1 = 15.5$ nm for the bottom layer, $t_2 = 21.4$ nm for the top layer, and $t_3 = 31.8$ nm for the double layer. Since these measurements include either one or two additional oxide layers, we estimate the thicknesses t_B and t_T of the bottom and top superconducting electrodes using the following equations:

$$t_1 = t_B + t_{AlO_x}^{ext} \tag{3.7}$$

$$t_2 = t_T + t_{AlO_x}^{ext} \tag{3.8}$$

$$t_3 = t_B + t_T + t_{AlO_x}^{ext} + t_{AlO_x}^{int} \tag{3.9}$$

where $t_{AlO_x}^{int}$ and $t_{AlO_x}^{ext}$ are the thicknesses of the inter-electrode and external AlO_x insulating barriers, respectively. We assume that, due to the exposure to ambient air and temperature, the oxide layers adding to t_1 and t_2 are the same, regardless of the extra-oxidation step that the bottom layer has faced during fabrication. Assuming that the thickness of the inter-layer barrier is approximately $t_{AlO_x}^{int} \approx 1$ nm, we obtain $t_B \approx 9.4$ nm, $t_T \approx 15.3$ nm and an outer insulating oxide layer of $t_{AlO_x}^{ext} \approx 6.1$ nm. Notably, the gaps estimated with the phenomenological model $\Delta_{B,T} \approx \Delta_{Al}^{bulk} + a/t_{B,T}$ (with $a = 600\,\mu$eV/nm and $\Delta_{Al}^{bulk} \approx 180\,\mu$eV, see Ref. [120] and references therein) are $\Delta_B = 59\,\text{GHz} \cdot h$ and $\Delta_T =$

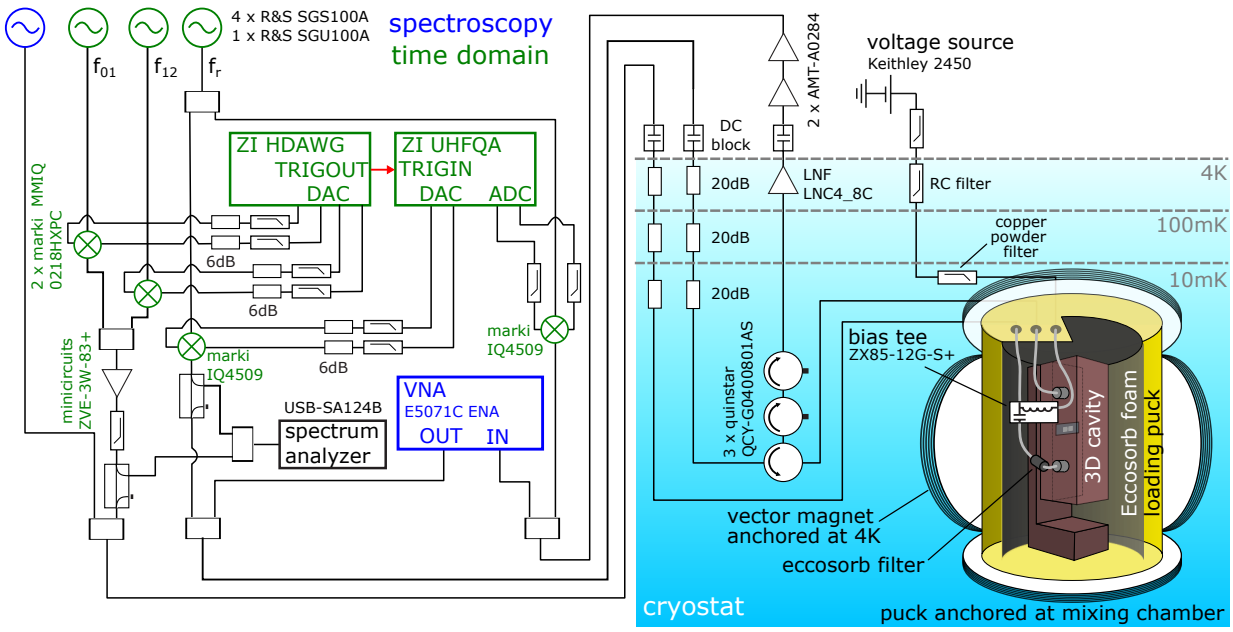

Figure 3.6: Wiring diagram of the experiment with the setup for spectroscopy using a two-port VNA and an additional microwave source and the time-domain setup using ADCs, DACs, and mixers. The transmon is inside a 3D cavity that is in the puck of the bottom loading dilution refrigerator.

53 GHz·h; these values differ by less than 2 % (and their difference by less than 10 %) from the gaps estimated in fitting the measured parity-switching and T_1 times. Figure 3.7 also clearly shows that the aluminum film is polycrystalline with typical grain sizes on the order of 50 nm and film thickness variations on the order of up to 2 nm.

Additional information on the device stability, coherence times, and transmon temperature is provided in the supplementary information [73].

3.C. JOSEPHSON HARMONICS

The measurements of the frequencies f_{ij} and their parity splittings δf_{ij} of the three lowest logical transmon states unexpectedly cannot be described by the standard Cooper-pair box Hamiltonian

$$H = 4E_C \sum_n (n-n_g)^2 |n\rangle\langle n| - \frac{1}{2}E_J \sum_n (|n\rangle\langle n+1| + |n+1\rangle\langle n|), \tag{3.10}$$

when trying to fit them simultaneously. Here $|n\rangle$ represents the charge basis state with excess charge $2en$. Related observations by other groups have been combined with our data from this device into a joint publication that reports evidence of deviations from the sinusoidal current-phase relationship for conventional Al/AlO_x/Al JJs [100]. A more accurate description of the spectrum requires introducing higher harmonics $E_{J2}\cos(2\phi)$, $E_{J3}\cos(3\phi)$, ... into the Hamiltonian. In the charge basis, the modified transmon Hamiltonian reads

$$H = 4E_C \sum_n (n-n_g)^2 |n\rangle\langle n| - \frac{1}{2}\sum_{m=1}^{\infty}\sum_n E_{Jm}\left(|n\rangle\langle n+m| + |n+m\rangle\langle n|\right) \tag{3.11}$$

where the index m identifies the order of the Josephson harmonic. Here we generalize this approach to a SQUID transmon with two junctions a and b; then Eq. (3.11) becomes

$$H = 4E_C \sum_n (n-n_g)^2 |n\rangle\langle n| - \frac{1}{2}\sum_{m=1}^{\infty}\left(E_{Ja,m} + E_{Jb,m}e^{im\phi}\right)\sum_n |n\rangle\langle n+m| - \frac{1}{2}\sum_{m=1}^{\infty}\left(E_{Ja,m} + E_{Jb,m}e^{-im\phi}\right)\sum_n |n+m\rangle\langle n| \tag{3.12}$$

where the phase factors multiplying $E_{Jb,m}$ account for the (reduced) flux ϕ piercing the SQUID.

To start with, we fit Eq. (3.12) to the zero-field data of Fig. 3.2, including both the perpendicular flux scan for $B_\parallel = 0$ and the f_{ij} and δf_{ij} obtained in voltage-gate scans at bottom sweet spots of the flux arc. We assume that JJs a and b have the same harmonics ratios $E_{Ja,m}/E_{Ja,1} = E_{Jb,m}/E_{Jb,1} \equiv c_m$. The voltage-gate scans of f_{01}, $f_{02}/2$, f_{12}, and f_{03} dominantly determine the Josephson energy at the bottom sweet spot, $E_J(\phi = 0.5) = E_{Ja,1} - E_{Jb,1}$, and the harmonics ratios at the bot-

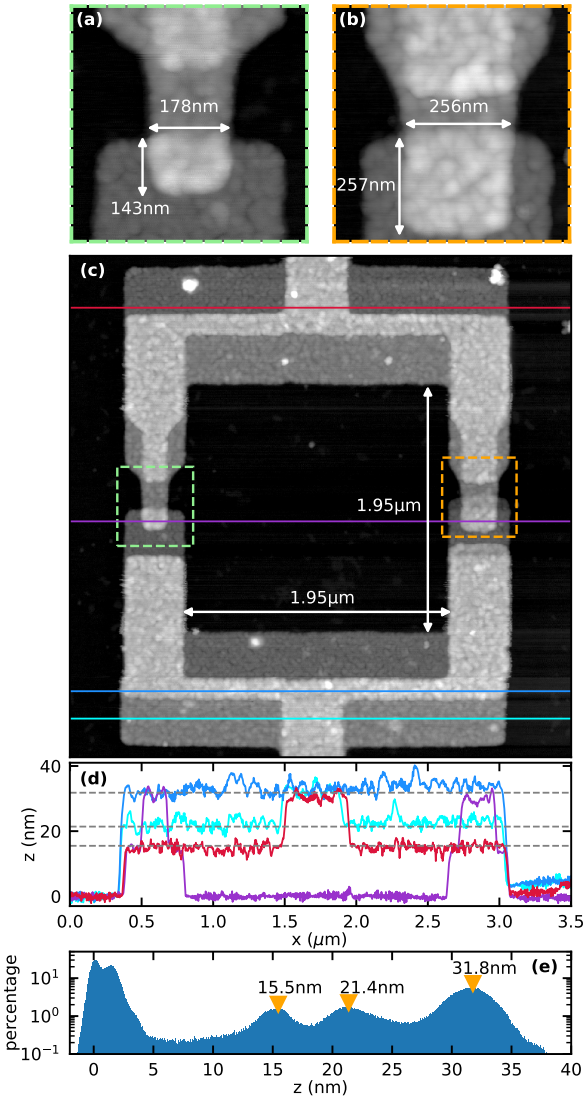

Figure 3.7: Atomic force microscope image showing in **(c)** the SQUID region of the transmon with the dimensions of the SQUID loop. The height is color-coded. Panels **(a)** and **(b)** are magnified images of the JJs and include their lateral dimensions. Aluminum grains with a typical size of 50 nm are visible. **(d)** Height profiles along the lines indicated in **(c)**. **(e)** Histogram of the heights in the image with indicated peaks. The three peaks at larger heights correspond to the bottom aluminum layer, the top layer, and the regions where they overlap.

tom sweet spot,

$$\frac{E_{Ja,m}+(-1)^m E_{Jb,m}}{E_{\mathrm{Ja},1}-E_{\mathrm{Jb},1}}=\begin{cases} c_m & \text{for } m \text{ odd} \\ c_m/\alpha_{\mathrm{JJ}} & \text{for } m \text{ even}. \end{cases} \tag{3.13}$$

The flux scan in turn determines the SQUID asymmetry α_{JJ}. As a result, we find the zero-field Josephson energies $E_{Ja}(0)/h = 19.47\,\mathrm{GHz}$, $E_{Jb}(0)/h = 5.97\,\mathrm{GHz}$ (corresponding to $\alpha_{\mathrm{JJ}}(0) = 0.53$), and the charging energy $E_C/h = 327.5\,\mathrm{MHz}$. We find that the higher harmonics decay rapidly with the index m, estimating $c_2 = -0.9\%$ and $c_3 = 0.03\%$. To avoid overfitting, we set the harmonics of order $m \geq 4$ to zero.

We note that our methodology is somewhat different from that employed in Ref. [100]: there, extensive scans of the sets $\{E_{Jm}\}$ of harmonics compatible with the data are performed and the interaction of the transmon with the readout resonator or cavity is taken into account; here we instead just perform a fit to the data using a limited number of harmonics and do not include the effect of the cavity. Thus, we find slightly different results based on the same data. For instance, for the charging energy we obtain a value about 1% lower than the estimate in Ref. [100]. As for the values of the Josephson harmonics, our estimates become smaller with increasing order m compared with those in that reference (by factors of order 1.4 and 13 for c_2 and c_3, respectively, when comparing to the model truncated to 4 rather than 3 harmonics).

Hereafter, we drop the label 1 to denote the first Josephson harmonic, i.e., $E_J \equiv E_{J1}$, and $E_{Ja(b)} \equiv E_{Ja(b),1}$, for notational simplicity.

3.D. ESTIMATING FRAUNHOFER AND CRITICAL FIELDS

The experimental data analysis of Appendix 3.C yields the zero-field Josephson energies $E_{Ja}(0)$ and $E_{Jb}(0)$ of the SQUID, and their harmonics. The Josephson energies vary as a function of the magnetic field. In this Appendix, we discuss a theoretical model for this dependence to quantify the relative contributions of i) field-suppression of the superconducting gaps Δ_B and Δ_T, ii) Fraunhofer-like modulation of the Josephson energy, quantified in terms of two characteristic fields $B_{\Phi_0,a}$ and $B_{\Phi_0,b}$ for JJ_a and JJ_b, respectively. We model the field evolution of $E_{Ja}(B_\parallel)$ and $E_{Jb}(B_\parallel)$ by the following expression, also used in Ref. [115]:

$$E_{Ja(b)}(B_\parallel) = E_{Ja(b)}(0)\sqrt{1-\left(\frac{B_\parallel}{B_c}\right)^2}\left|\mathrm{sinc}\left(\frac{B_\parallel}{B_{\Phi a(b)}}\right)\right|, \tag{3.14}$$

where $\mathrm{sinc}(x) \equiv \sin(\pi x)/(\pi x)$. The factor in the absolute value in the right-hand side of Eq. (3.14) accounts for the Fraunhofer modulation of the Josephson energy for a rectangular junction [143]. Even though thin aluminum films with different thicknesses and gaps display unequal critical fields ($B_c^{\mathrm{B}} \neq B_c^{\mathrm{T}}$) [124], we find that a single effective critical field B_c can be used to capture the impact of the gaps' suppression on E_J; the square root in the right-hand side of Eq. (3.14)

models the gap suppression with a Ginzburg-Landau type formula $\Delta(B_\parallel)/\Delta(0) = \sqrt{1-(B_\parallel/B_c)^2}$ [17] (see [35] for the applicability of this approach). The Josephson energy of a JJ with asymmetric gaps is proportional to the harmonic mean of the two gaps, i.e., $E_J \propto \Delta_B\Delta_T/(\Delta_T+\Delta_B)$, so at the leading order in $B_\parallel \ll B_c^B, B_c^T$, Eq. (3.14) approximates the expression obtained retaining separately B_c^B, B_c^T, if we set $B_c^{-2} = [\Delta_T(0)(B_c^B)^{-2} + \Delta_B(0)(B_c^T)^{-2}]/[\Delta_B(0)+\Delta_T(0)]$. The validity of this approach is also supported by the analysis of the cavity frequency shown below.

To start with, we estimate the Fraunhofer fields for the two JJs. While we could not systematically measure the transmon spectrum for $B_\parallel > 0.41\,\mathrm{T}$, we did measure the cavity resonance frequency f_{cav} up to 1 T, the limit of our magnet. Sweeping $B_\perp$ by a few hundreds of μT for every $B_\parallel$, we could clearly observe the SQUID oscillations in f_{cav} mediated by the dispersive shift up to 0.9 T [see Fig. 3.8(a) and (b)]. Around $B_\parallel \simeq 0.8\,\mathrm{T}$ the oscillation collapses, before reviving again for fields $0.82\,\mathrm{T} \le B_\parallel \le 0.9\,\mathrm{T}$. We attribute this behavior to one superconducting flux quantum ($\Phi_0 = h/(2e)$) threading the larger of the two JJs, turning the SQUID effectively into a single-JJ transmon [right arrow in panel (c) of Fig. 3.8]. Therefore, we estimate $B_{\Phi_0,a} = 0.8\,\mathrm{T}$. Moreover, we observe a local minimum in f_{cav} around 0.7 T. As indicated by the left arrow in panel (c) of Fig. 3.8 this minimum corresponds to the condition $E_{Ja} = E_{Jb}$, where the SQUID is symmetric. The resulting near-complete suppression of E_J for half a flux quantum through the SQUID leads to a reduction of the dispersive shift so that f_{cav} approaches the bare cavity frequency. The intersection of E_{Ja} and E_{Jb} depends only on the zero-field Josephson energies $E_{Ja}(0)$ and $E_{Jb}(0)$, and on the characteristic Fraunhofer fields $B_{\Phi_0,a}$ and $B_{\Phi_0,b}$, the latter being the only remaining unknown at this point. Requiring $E_{Ja}(0.7\,\mathrm{T}) = E_{Jb}(0.7\,\mathrm{T})$ we estimate $B_{\Phi_0,b} = 1.12\,\mathrm{T}$. As shown in Fig. 3.8 (d) the estimated Fraunhofer fields B_{Φ_0} of JJ$_a$ and JJ$_b$ are inversely proportional to the laterally penetrated junction width l_2, with a proportionality constant that agrees well with that for other devices from the same fabrication batch and that were measured in two-tone spectroscopy up to 1 T [115].

To determine the effective critical field B_c we substitute Eq. (3.14) into the Hamiltonian that includes the higher Josephson harmonics, Eq. (3.12), and fit the spectroscopic data for the qubit transitions and parity-frequency splittings in Fig. 3.2(b) and (c) [also reproduced in Fig. 3.9(a) and (e)]. For the higher harmonics, as in Appendix 3.C we keep only those with $m = 2$ and 3, and assume their ratios c_m to be independent of parallel field (see end of this Appendix about this assumption). Using this procedure, we estimate $B_c = 1.85\,\mathrm{T}$. The actual B_c is likely lower, given that we fit a Ginzburg-Landau dependence and for thin films at low temperatures one expects a faster suppression of Δ close to the critical field [35]. Indeed, we do not observe SQUID oscillations in f_{cav} for $B_\parallel \ge 0.92\,\mathrm{T}$, and the critical field estimated for similar devices is about 1 T [115]. We also note that the fitted value of the critical field might in part account for the field-dependent effects, not included in the model, that we discuss at the end of this Appendix; in this context, one can regard B_c as an effective critical field that makes possible a more accurate modeling of the spectroscopic data. Figure 3.9 shows the fit including the residuals. As in Section 3.C, the voltage-gate scans of f_{01}, $f_{02}/2$, f_{12}, and f_{03} dominantly determine the Josephson energy at the bot-

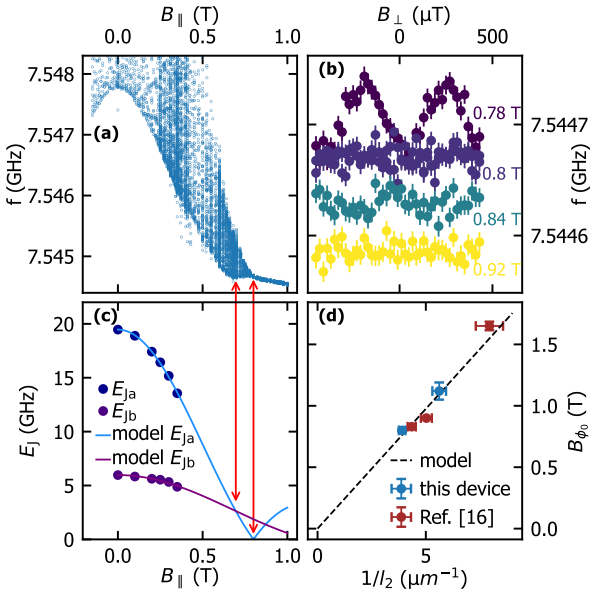

Figure 3.8: Estimation of the Fraunhofer modulation of the Josephson energy. **(a)**-**(b)** Measurements of the resonance frequency f_{cav} of the cavity for different values of the out-of-plane ($B_\perp$) and in-plane ($B_\parallel$) magnetic field plotted against **(a)** $B_\parallel$ and **(b)** $B_\perp$ for selected values of $B_\parallel$. The cavity is coupled to the transmon; the periodic oscillations of the transmon frequency with $B_\perp$ (due to the SQUID geometry) translate to oscillations in f_{cav} via the dispersive shift. Due to the Fraunhofer effect, the oscillation vanishes at $B_{\Phi_0,a} = 0.8\,\mathrm{T}$ (see the text for the explanation). **(c)** The estimated Josephson energies E_{Ja} and E_{Jb} of the two JJs intersect at $B_\parallel \simeq 0.7\,\mathrm{T}$, corresponding to the minimum f_{cav} in **(a)**. That way we can estimate $B_{\Phi_0,b} = 1.12\,\mathrm{T}$. **(d)** The estimated $B_{\Phi_0,a}, B_{\Phi_0,b}$ are inversely proportional to the JJ width l_2 that is penetrated by $B_\parallel$ (as expected for a rectangular junction [143]) and agree with more direct measurements performed in Ref. [115] on other devices from the same batch.

tom sweet spot, $E_J(B_\parallel, \phi = 0.5) = E_{Ja}(B_\parallel) - E_{Jb}(B_\parallel)$. Fitting the remaining perpendicular flux scans for fields $B_\parallel > 0$, we can further determine $\alpha_{JJ}(B_\parallel)$, and hence the data points for E_{Ja} and E_{Jb} shown in the inset of Fig. 3.2 (a) [also in Fig. 3.8 (c)]. We find their field dependence to be well described by Eq. (3.14) and the fit parameters obtained in the course of this section, showing the self-consistency of our modeling. We note that, for our purposes, it is sufficient to quantify the gap suppression in the magnetic-field range covered by measurements of the parity-switching time, $|B_\parallel| \leq 0.41\,\mathrm{T} \ll B_c$. In this field range the gaps are suppressed by less than 3% compared to the zero-field values, based on Eq. (3.14) and the estimated B_c. For this reason, we disregard the field-dependence of the gaps in modeling the parity-switching rates.

In closing this Appendix, we note that the assumption that the ratios E_{Jm}/E_{J1} are independent of parallel field [implying $E_{Jm} \propto \mathrm{sinc}(B_\parallel/B_\Phi)$] is strictly speaking incorrect, since for rectangular junctions the argument [143] leading to the sinc modulation in Eq. (3.14) gives $E_{Jm} \propto \mathrm{sinc}(mB_\parallel/B_\Phi)$. Similarly, a contribution to the second harmonic arising from an inductance in series to the junction would change as $[\mathrm{sinc}(B_\parallel/B_\Phi)]^2$ (at leading order in the ratio between Josephson and inductive energies, see supplementary to Ref. [100]). We disregard these effects for simplicity since an even more accurate modeling of the spectroscopic data is beyond the scope of the present work. Still, we note that the different dependencies of the junction harmonics and inductive corrections on the parallel field could in principle be used to distinguish these two contributions.

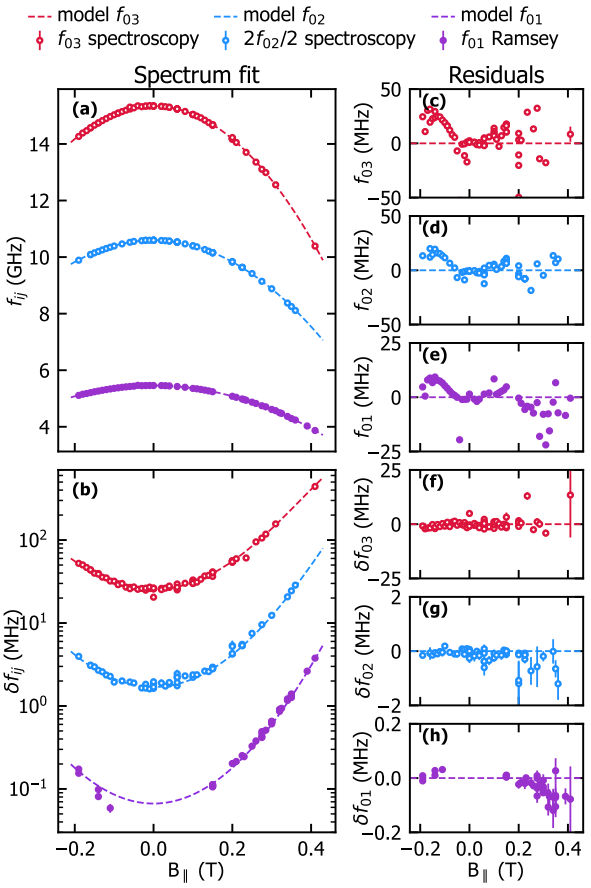

Figure 3.9: Transmon transitions frequencies f_{ij} **(a)** and parity-frequency splittings δf_{ij} **(b)** measured at the bottom sweet spot as a function of $B_\parallel$. The data is obtained from voltage-gate scans like the ones shown in Fig. 3.2. Substituting Eq. (3.14) into Eq. (3.12) we estimate $B_c = 1.85\,\mathrm{T}$ based on a fit to the data (see text). Fit residuals **(c)**-**(h)** are relatively flat for all f_{ij} and δf_{ij}.

3.E. GATING THE OFFSET VOLTAGE

In this Appendix, we show that we can control the charge bias of the transmon by applying a DC gate voltage V_g to the bias-tee on the cavity input port. Measuring the transmon transitions f_{01}, $f_{02}/2$, f_{12}, and f_{03} as a function of V_g, we observe clear signature of charge-parity splitting for all the transitions (Fig. 3.2). This feature allows for gate-tuning of the transmon to a point of maximum charge-parity splitting, which is the ideal situation to measure the parity-switching time.

Some of the transitions shown in Fig. 3.2 (d)-(f) were measured in time-domain, in a Ramsey-type measurement (see Fig. 3.10 for an example measurement using a superposition of $|1\rangle$ and $|2\rangle$). Depending on V_g, the Ramsey data shows a beating of two frequency contributions or just a single frequency [see Fig. 3.10 (b) and (c)]. A Fourier transform of the Ramsey data [Fig. 3.10 (d)] shows the detuning of the transition energies as plotted in Fig. 3.2 (d)-(f); here the microwave frequency was chosen at the midpoint between the "even" and "odd" transition frequencies. Accurately fitting the Ramsey data and tuning to this condition is essential for the subsequent parity measurements. The Ramsey pure-dephasing time $T^*_{\phi,12}$ as a function of V_g, Fig. 3.10 (e), is extracted from fitting the linecuts of Fig. 3.10 (a) using relaxation times from a preceding measurement of relaxation from the $|2\rangle$ state (see supplementary information [73] for an example). It shows an enhancement at the charge sweet spots but is not T_1 limited as e.g. flux noise also contributes to $T^*_{\phi,12}$. While Ramsey measurements are sensitive to V_g, measurements of T_1 and T_2^{echo} do not show a V_g dependence [73], suggesting that the dominant charge noise is slow.

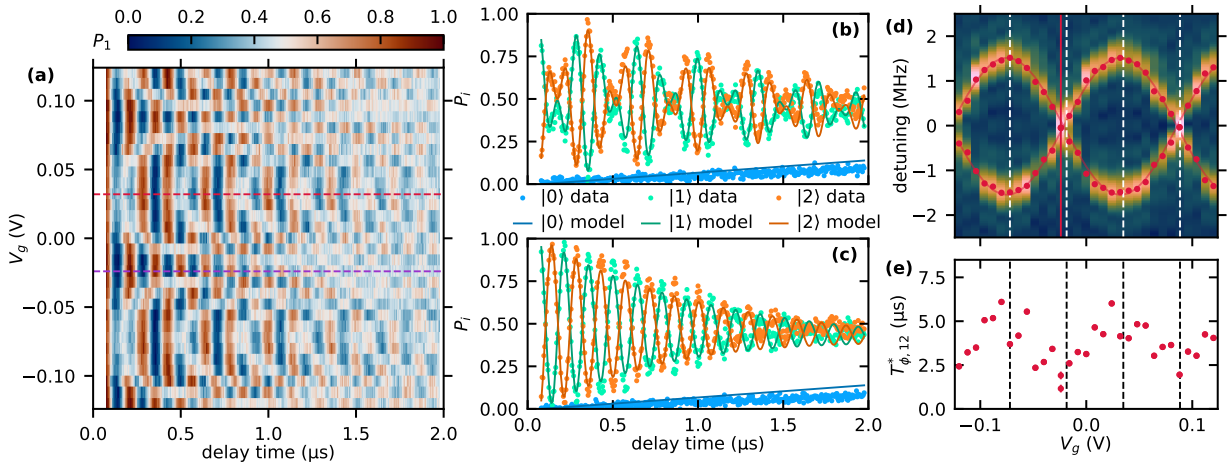

Figure 3.10: **(a)** Ramsey measurement for the 1-2 transition as a function of V_g. The color plot gives the population of $|1\rangle$ as a function of waiting time between the $\pi/2$ pulses and V_g. **(b)** and **(c)** linecuts of **(a)** close the charge sweet spot and anti sweet spot. In **(b)**, the characteristic beating for the two parities can be clearly seen. The three-state data is fitted with a qutip [137] simulation. **(d)** Fourier transform of the temporal data in **(a)**, revealing the charge dispersion directly. Data points are frequencies extracted from the fits to the linescans. **(e)** Ramsey pure dephasing time $T^*_{\phi,12}$ as a function of gate voltage. While charge noise is not the dominant dephasing process, a slight sweet spot enhancement can be observed.

We have also explored scanning V_g over many periods and see few jumps and no anomalies [73]. Generally, we find that the V_g scans show the expected double-sinusoidal dependence with few jumps and distortions, but we do find that V_g shows a slight hysteresis when reversing the scan direction. We observe drift in the charge offset at fixed V_g that can cover a period on a timescale of 10 min [123].

3.F. PARITY MEASUREMENT SCHEMES

A single parity measurement is realized by a parity-dependent gate on the transmon that flips the qubit state for "odd" parity and leaves it unchanged for "even" parity, followed by a measurement of the transmon state. The parity-dependent gate we use is Ramsey-based [144]; its basic scheme and illustration on the Bloch sphere can be found in Fig. 3.3 (a). The gate requires a careful tune-up: the carrier frequency of the qubit-control pulses needs to be well-centered between "even" and "odd" transmon frequencies f_e, f_o and the voltage gate on the bias-tee, V_g, is chosen such that $|f_e - f_o|$ is maximized. Generally, for $\delta f_{ij} <$ 10 MHz, our usual 20 ns control pulses are not parity selective, meaning a $\pi/2$ pulse will map both parities onto the same point on the Bloch sphere [see Fig. 3.3 (a)]. The microwave carrier defines a rotating frame, such that the detuning of each parity from the carrier gives the rotation frequency on the Bloch-sphere equator. The detunings have opposite signs, and the parities precess in opposite directions. After a waiting time $t_w = (2\delta f_{ij})^{-1}$, the two parities will have rotated to orthogonal states on the Bloch sphere that, with the right rotation, can be mapped to the ground and first-excited states $|0\rangle$ and $|1\rangle$, respectively. The same method can be used with a superposition of $|1\rangle$ and $|2\rangle$ [see Fig. 3.3 (b)]. As explained in Sec. 3.3 of the main text, we explore a range of E_J/E_C ratios while sweeping $B_\parallel$, such that the sequences involving higher transitions are useful when the charge dispersion for the 0-1 transition is too small: the charge dispersion increases roughly by a factor of 10 with the level index, while T_1 and T_2^* decrease for the higher levels typically by less than 50%.

In addition to the parity-selective gate, the transmon needs to start in a known state for each run, and a good single-shot readout fidelity for the transmon is required to resolve the parity dynamics. We generally achieve high single-shot fidelities > 90% that can distinguish $|0\rangle$, $|1\rangle$ and $|2\rangle$ [see Fig. 3.11 (b)]. We let the qubit relax by waiting $5T_1$ between individual runs; at temperatures $\lesssim$ 50 mK, our qubit has a residual excitation of up to 5 %. In principle, one can also initialize by measurement [116] or just look if the transmon state flips or stays the same compared to the previous measurement.

We then perform the parity-mapping sequence consisting of idling, parity gate, and readout $N = 2^{18}$ times. The measurement results form a sequence of N points in the IQ plane, from which the τ_p^e and τ_p^o are determined by fitting a Gaussian hidden-Markov model (HMM) [145]. The hidden parameter in our

Markov model is the "true" parity, while the measured parameters are the IQ Voltages which have different probability distributions for the $|0\rangle$, $|1\rangle$ and $|2\rangle$ states. Depending on the parity, there are different probabilities of the transmon being mapped on the states indicated by colored arrows in Fig. 3.11 (a), which we call emission probabilities. Between two consecutive runs, the hidden parity can change or stay the same with fixed probabilities $t_{\mathrm{rep}}\Gamma_{ij}$ where t_{rep} is the repetition time and Γ_{ij} [with i,j={"even" (e), "odd" (o)}] are the transition rates illustrated by black arrows in Fig. 3.11 (a). In the model, we allow for different Γ_{eo} and Γ_{oe}, which in turn fix Γ_{oo} and Γ_{ee}. The calibration points for the $|0\rangle$, $|1\rangle$ and $|2\rangle$ states are obtained by preparing those states followed by a measurement [see Fig. 3.11 (b)]. Each IQ histogram for the prepared states ($|0\rangle$, $|1\rangle$ and $|2\rangle$) is well described by sums of three Gaussian probability distributions (one of the three Gaussians clearly dominates for each state, but we consider that our calibration points are slightly mixed due to residual excitation as well as relaxation). The means and covariances of the dominant Gaussians corresponding to $|0\rangle$, $|1\rangle$ and $|2\rangle$, respectively, fix the probability distributions of the Gaussian HMM. The free parameters of the HMM are the emission probabilities of the "even" and "odd" parities (the probabilities to measure each state given a parity) as well as Γ_{eo} and Γ_{oe}. These parameters are determined by a likelihood fit of the HMM to the data using the *hmmlearn* package [138].

As outcomes of the HMM fit, we get the assigned parities for each run and the transition probabilities, from which $\tau_{\mathrm{p}}^{\mathrm{e}} = (\Gamma_{\mathrm{eo}})^{-1}$ and $\tau_{\mathrm{p}}^{\mathrm{o}} = (\Gamma_{\mathrm{oe}})^{-1}$ can be calculated with the known repetition time of the sequence. Fig. 3.11 (c) and (d) show the assigned parities as a function of time; here the assigned states are based on a Gaussian classifier yielding the most likely state for any point in the IQ plane [see colors in Fig. 3.11 (b)]. We find that generally the "even" ("odd") parity is associated with the $|0\rangle$ ($|1\rangle$) state. The histograms of the IQ data selected on the "even" and "odd" parity are shown in Fig. 3.11 (e) and (f). The overlap of the emission probability distributions of the two parities is $1-F_{\mathrm{p}}$ with F_{p} being the parity-measurement fidelity. To check the HMM methodology for consistency, we compared it with the results for the parity-switching time based on a fit to the power spectral density of the assigned states (see supplementary information [73]).

We filter our data based on Ramsey measurements before and after each parity measurement sequence: The splitting δf_{ij} between "even" and "odd" transmon frequencies has to match $t_w = (2\delta f_{ij})^{-1}$, and we reject data in which the transmon frequencies drifted during the time of the parity-measurement sequence. Moreover, we ensured that t_w is small compared to T_2^* and T_1.

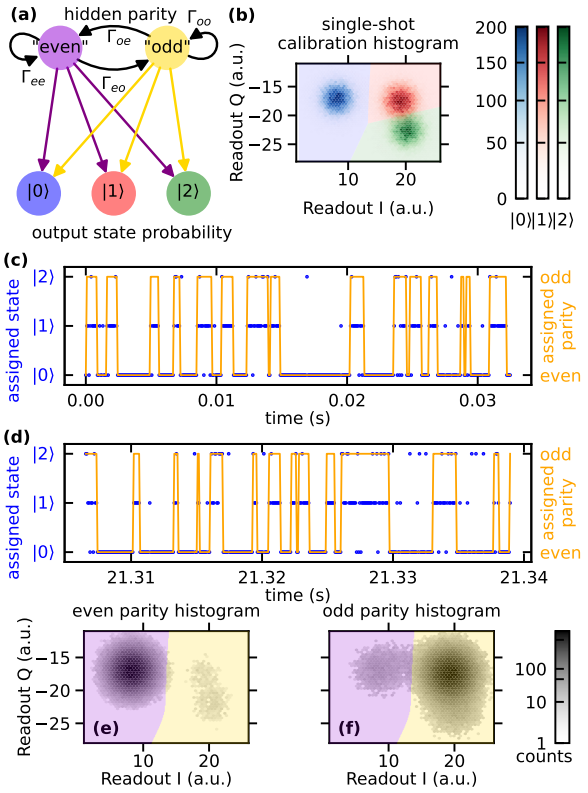

Figure 3.11: **(a)** Diagram illustrating the Gaussian mixture hidden Markov model. The parity state changes with certain (fixed) probabilities between runs. Both parities have different state probabilities, which correspond to different weights in a Gaussian mixture for the output probabilities. **(b)** Histogram of calibration points for the different prepared states directly preceding the parity measurement run. The colors show the most likely state in each region based on a Gaussian classifier. **(c)** and **(d)** Assigned states from the Gaussian classifier and assigned parities from the HMM fit for the first 400 measurements at the beginning and the end of the parity measurement run comprising 262144 measurements. **(e)** and **(f)** Histograms of the output voltages conditioned on the assigned parity. The colors show the most likely parity in each region based on a Gaussian classifier.

3.G. MODELING THE CONTRIBUTIONS TO THE PARITY-SWITCHING TIME

We discussed the theoretical model for the parity switching time in Sec. 3.4.1 of the main text. Here, we present explicit expressions for the rates associated with PAPS and NUPS contributions in Eqs. (3.2)-(3.6). The parity-switching time measurements have

been performed at the lower sweet spot of the split-transmon device ($\Phi = \Phi_0/2$), where the gap difference is larger than the qubit energy transition, *i.e.*, $f_{\delta\Delta} > f_{01}$ (denoted as case II in Ref. [120]) with $f_{\delta\Delta} = (\Delta_B - \Delta_T)/h$. In this situation, quasiparticles accumulate in the lower-gap electrode at energies close to its gap due to relaxation (via phonon emission) and suppressed tunneling into the higher-gap electrode (because of the energy difference $f_{\delta\Delta} - f_{01} > 0$), see Ref. [120].

As in the reference, we describe the quasiparticle dynamics in each superconducting electrode via rate equations for their density, see also Appendix E of Ref. [19] and Sec. III.D of the supplement to Ref. [119]. The equations are written in terms of the dimensionless quantities x_B and x_T, obtained normalizing the quasiparticle density in electrode $\alpha = \{T, B\}$ by the Cooper pair density $n_{Cp}^{\alpha} = 2\nu_0\Delta_\alpha$ (with $\nu_0 \approx 0.73 \times 10^{47} J^{-1}m^{-3}$ the single spin density of states of aluminum at the Fermi level and Δ_α the superconducting gap),

$$\frac{dx_B}{dt} = g^B - s_B x_B - r^B x_B^2 + \delta\bar{\Gamma}^T x_T - \delta\bar{\Gamma}^B x_B\,, \tag{3.15}$$

$$\frac{dx_T}{dt} = g^T - s_T x_T - r^T x_T^2 - \bar{\Gamma}^T x_T + \bar{\Gamma}^B x_B\,. \tag{3.16}$$

where $\delta = \Delta_T/\Delta_B$. In the right-hand sides of Eqs. (3.15) and (3.16), g^α, $\alpha = \{T, B\}$, describe quasiparticle generation, and the terms proportional to s_α and r^α account for quasiparticle trapping and recombination, respectively; for the recombination rate, we use the values $r^T = r^B = 1/(160\,ns)$ [74, 120]. Finally, the terms proportional to

$$\bar{\Gamma}^\alpha = (1-p_1)(\bar{\Gamma}_{00}^\alpha + \bar{\Gamma}_{01}^\alpha) + p_1(\bar{\Gamma}_{11}^\alpha + \bar{\Gamma}_{10}^\alpha) \tag{3.17}$$

account for the tunneling of quasiparticles initially located in electrode α ($\alpha = \{T, B\}$) into the other electrode, where p_1 is the occupation probability of the excited state of the qubit. Note that in writing the first factor on the right-hand side in the form $(1 - p_1) = p_0$ we implicitly assume that the occupations of higher levels can be ignored; it was estimated in the supplement to Ref. [119] that for high p_1 taking the occupation of second excited state into consideration could lead to corrections of the order of several percent, so we neglect this possibility here. In our notation for NUPS [see, for instance, Eqs. (3.4)-(3.6) in the main text], $\tilde{\Gamma}_{ij}^\alpha x_\alpha$ represents the quasiparticle-tunneling induced transition rate for the qubit from the initial logical state i to the final state f ($i, f = \{0, 1\}$). The barred rates $\bar{\Gamma}_{ij}$ are obtained dividing $\tilde{\Gamma}_{ij}$ by the Cooper pair number in the low-gap electrode, *i.e.*, $\bar{\Gamma}^\alpha = \tilde{\Gamma}^\alpha/(n_{Cp}^T \mathcal{V}_T)$, where $\mathcal{V}_T \simeq 3400\,\mu m^3$ is the volume of the low-gap electrode; this normalization is at the origin of the factors δ appearing in Eq. (3.15). In comparing Eqs. (3.15) and (3.16) to the model of Ref. [120] [see Eqs. (11)-(13) there], we note that here the terms $-s_\alpha x_\alpha$ in the right-hand side account for trapping (cf. Sec. IV.D in Ref. [120]) and we additionally assume quasi-equilibrium quasiparticle distributions in both electrodes, having temperature coinciding with the fridge temperature, but allowing for different effective chemical potentials in the two electrodes. This assumption enables us to use a single equation for $x_T = x_{T<} + x_{T>}$ obtained by summing Eqs. (12) and (13) of Ref. [120] (the rates from the top electrode are defined so to obtain $\bar{\Gamma}_{ij}^T x_T = \bar{\Gamma}_{ij}^{T<} x_{T<} + \bar{\Gamma}_{ij}^{T>} x_{T>}$).

For the modeling of the parity-switching time, we are interested in the steady-state values of the quasiparticle densities in the two electrodes ($dx_B/dt = dx_T/dt = 0$). Assuming $\delta\bar{\Gamma}^B + s_B \gg r^B x_B$, we can neglect recombination in the bottom electrode in Eq. (3.15), and then we can express the steady-state value of x_B in terms of x_T,

$$\begin{aligned} x_B &= \frac{g^B/\delta + [p_0(\bar{\Gamma}_{00}^T + \bar{\Gamma}_{01}^T) + p_1(\bar{\Gamma}_{11}^T + \bar{\Gamma}_{10}^T)]x_T}{p_0(\bar{\Gamma}_{00}^B + \bar{\Gamma}_{01}^B) + p_1(\bar{\Gamma}_{11}^B + \bar{\Gamma}_{10}^B) + s_B/\delta} \\ &\approx \frac{g^B/\delta + (\bar{\Gamma}_{00}^T + p_1\bar{\Gamma}_{10}^T)x_T}{\bar{\Gamma}_{00}^B + p_0\bar{\Gamma}_{01}^B + p_1\bar{\Gamma}_{10}^B + s_B/\delta}\,. \end{aligned} \tag{3.18}$$

The approximate expression in the second line of Eq. (3.18) is obtained noticing that parity switching rates for a transmon qubit are independent of the logical state of the qubit at the leading order in E_J/E_C [146, 120], *i.e.*, $\bar{\Gamma}_{00}^\alpha \approx \bar{\Gamma}_{11}^\alpha$, and neglecting the contribution of transitions exciting the qubit for quasiparticles initially located in the low-gap (top) electrode, since $\bar{\Gamma}_{01}^T \ll \bar{\Gamma}_{00}^T, \bar{\Gamma}_{10}^T$ (the rates are discussed in more detail later in this Appendix). This strong inequality also justifies neglecting terms proportional to x_T in qubit's excitation rates [see Eq. (3.5) in the main text]. Substituting Eq. (3.18) into Eq. (3.16), the steady-state density in the top electrode x_T is obtained by solving a quadratic equation, yielding the result

$$x_T = \frac{\sqrt{\tilde{s}^2 + 4\tilde{g}r^T} - \tilde{s}}{2r^T}\,, \tag{3.19}$$

where for notational convenience, we introduced an

effective trapping rate $\tilde{s}$

$$\tilde{s} = s_T + s_B \frac{p_0(\bar{\Gamma}^T_{00}+\bar{\Gamma}^T_{01}) + p_1(\bar{\Gamma}^T_{11}+\bar{\Gamma}^T_{10})}{s_B + \delta[p_0(\bar{\Gamma}^B_{00}+\bar{\Gamma}^B_{01}) + p_1(\bar{\Gamma}^B_{11}+\bar{\Gamma}^B_{10})]}$$
$$\approx s_T + s_B \frac{\bar{\Gamma}^T_{00} + p_1\bar{\Gamma}^T_{10}}{s_B + \delta[\bar{\Gamma}^B_{00} + p_0\bar{\Gamma}^B_{01} + p_1\bar{\Gamma}^B_{10}]}, \quad (3.20)$$

and generation rate $\tilde{g}$

$$\tilde{g} = g^T + \frac{g^B}{\delta}\left(1 - \frac{s_B}{\delta[p_0(\bar{\Gamma}^B_{00}+\bar{\Gamma}^B_{01}) + p_1(\bar{\Gamma}^B_{11}+\bar{\Gamma}^B_{10})] + s_B}\right)$$
$$\approx g^T + \frac{g^B}{\delta}\left(1 - \frac{s_B}{\delta[\bar{\Gamma}^B_{00} + p_0\bar{\Gamma}^B_{01} + p_1\bar{\Gamma}^B_{10}] + s_B}\right). \quad (3.21)$$

The generation rates in the two electrodes originate from pair breaking by high-frequency photons with rate g^{PAPS} and by thermal phonons,

$$g^B/\delta = g^{PAPS},\ g_T = g^{PAPS} + 2\pi r^T \frac{k_B T}{\Delta_T} e^{-2\Delta_T/k_B T} \quad (3.22)$$

where thermal phonons generation in the high-gap (bottom) electrode is neglected for consistency with the approximation ignoring recombination there (alternatively, once the parameters are determined from the experimental data, one can check if the thermal phonon generation term is small compared the the photon pair-breaking one, which independently justifies ignoring the former). The photon-assisted generation rate is computed by dividing the photon-assisted tunneling rates Γ^{PAPS} [129, 120] by the Cooper pair number in the low-gap electrode,

$$g^{PAPS} = \frac{\Gamma^{PAPS}}{n^T_{Cp}\mathcal{V}_T} \approx \frac{\Gamma^{ph}_{00} + p_0\Gamma^{ph}_{01} + p_1\Gamma^{ph}_{10}}{2\nu_0\mathcal{V}_T\Delta_T}. \quad (3.23)$$

The (inverse) parity-switching time can be expressed summing all the rates associated with quasiparticle tunneling, reading

$$\tau_P^{-1} = \Gamma^{PAPS} + [p_0(\tilde{\Gamma}^B_{00}+\tilde{\Gamma}^B_{01}) + p_1(\tilde{\Gamma}^B_{11}+\tilde{\Gamma}^B_{10})]x_B +$$
$$[p_0(\tilde{\Gamma}^T_{00}+\tilde{\Gamma}^T_{01}) + p_1(\tilde{\Gamma}^T_{11}+\tilde{\Gamma}^T_{10})]x_T$$
$$\approx \Gamma^{PAPS} + (\tilde{\Gamma}^B_{00} + p_1\tilde{\Gamma}^B_{10} + p_0\tilde{\Gamma}^B_{01})x_B + (\tilde{\Gamma}^T_{00} + p_1\tilde{\Gamma}^T_{10})x_T$$
$$= \left(2 - \frac{s_B}{\delta[\bar{\Gamma}^B_{00} + p_0\bar{\Gamma}^B_{01} + p_1\bar{\Gamma}^B_{10}] + s_B}\right)$$
$$\times [\Gamma^{PAPS} + (\tilde{\Gamma}^T_{00} + p_1\tilde{\Gamma}^T_{10})x_T]. \quad (3.24)$$

The calculation of the quasiparticle rates $\tilde{\Gamma}^{\alpha}_{ij}$ and Γ^{ph}_{ij} can be performed using Fermi's Golden rule, as extensively discussed in the literature, see, for instance, Refs. [91, 146, 120, 119]. Below, we report the results for the rates entering τ_P^{-1} under the assumption of quasiequilibrium distributions in the two electrodes; the detailed derivation of the quasiparticle rates in the presence of Fraunhofer effect will be given elsewhere. First, we consider the relaxation and parity switching tunneling rates for quasiparticles initially located in the top electrode:

$$\tilde{\Gamma}^T_{10} = \frac{8E^0_{J\Sigma}}{h}\sqrt{\frac{E_C}{8E_J}}\sqrt{\frac{2\Delta_T}{\pi k_B T}}\,\mathrm{Exp}\left[-\frac{h(f_{\delta\Delta}-f_{01})}{2k_B T}\right]$$
$$\left\{\gamma_+ K_0\left[\frac{h|f_{\delta\Delta}-f_{01}|}{2k_B T}\right]\right.$$
$$\left. + \left(\gamma_- + \frac{\gamma_+}{2}\right)\frac{h|f_{\delta\Delta}-f_{01}|}{2\bar{\Delta}} K_1\left[\frac{h|f_{\delta\Delta}-f_{01}|}{2k_B T}\right]\right\}, \quad (3.25)$$
$$\tilde{\Gamma}^T_{00} = \frac{8E^0_{J\Sigma}}{h}\sqrt{\frac{2\Delta_T}{\pi k_B T}}\,\mathrm{Exp}\left[-\frac{hf_{\delta\Delta}}{2k_B T}\right]$$
$$\left\{\gamma_- K_0\left[\frac{h|f_{\delta\Delta}|}{2k_B T}\right] + \left(\gamma_+ + \frac{\gamma_-}{2}\right)\frac{h|f_{\delta\Delta}|}{2\bar{\Delta}} K_1\left[\frac{h|f_{\delta\Delta}|}{2k_B T}\right]\right\}, \quad (3.26)$$

where E_J and f_{01} are the Josephson energy and the frequency of the qubit at the lower sweet spot in the presence of the parallel field, K_n are modified Bessel functions of the second kind, and $E^0_{J\Sigma} = E_{Ja}(B_\parallel = 0) + E_{Jb}(B_\parallel = 0)$. The remaining rates are obtained from the ones given in Eqs. (3.25) and (3.26) with the following substitutions:

$$\tilde{\Gamma}^T_{01} = \tilde{\Gamma}^T_{10}(f_{01} \to -f_{01}) \quad (3.27)$$
$$\tilde{\Gamma}^B_{10} = \sqrt{\frac{\Delta_B}{\Delta_T}}\tilde{\Gamma}^T_{10}(f_{\delta\Delta} \to -f_{\delta\Delta}), \quad (3.28)$$
$$\tilde{\Gamma}^B_{00} = \sqrt{\frac{\Delta_B}{\Delta_T}}\mathrm{Exp}\left[\frac{hf_{\delta\Delta}}{k_B T}\right]\tilde{\Gamma}^T_{00}, \quad (3.29)$$
$$\tilde{\Gamma}^B_{01} = \sqrt{\frac{\Delta_B}{\Delta_T}}\mathrm{Exp}\left[\frac{-h(f_{01}-f_{\delta\Delta})}{k_B T}\right]\tilde{\Gamma}^T_{10}. \quad (3.30)$$

The transformations in Eqs. (3.28) and (3.29) exploit the symmetry of the rates and are equivalent to exchanging the role of the two electrodes $B \leftrightarrow T$, while (3.30) follows from the detailed balance principle. The weights in the curly brackets of Eqs. (3.25) and (3.26)

$$\gamma_\pm = \frac{2 \pm (z_- + \alpha_{JJ,0} z_+)}{4}. \quad (3.31)$$

accounts for the interference effects related to the SQUID interferometer as well as the Fraunhofer effect: $\alpha_{JJ,0} = \alpha_{JJ}(B_\parallel = 0) = (E_{Ja} - E_{Jb})/(E_{Ja} + E_{Jb})$ is the split-transmon asymmetry parameter at zero parallel field, while $z_\pm = \mathrm{Sinc}(B_\parallel/B_{\Phi a}) \pm \mathrm{Sinc}(B_\parallel/B_{\Phi b})$. For comparison, the rates for a single-junction transmon

correspond to the case $\alpha_{\mathrm{JJ},0} = 1$; if we further consider zero parallel magnetic field, we have $\{\gamma_+, \gamma_-\} = \{1, 0\}$.

We can present the photon-assisted tunneling rates $\Gamma_{ij}^{\mathrm{ph}}$ in a similar way. For simplicity, we consider monochromatic radiation with frequency $f_\nu > (\Delta_\mathrm{B} + \Delta_\mathrm{T})/h$ to allow for Cooper-pair breaking. The rates can be expressed as

$$\Gamma_{00}^{\mathrm{ph}} = \Gamma_\nu \frac{g_\Sigma \Delta_\mathrm{B}}{8e^2}\left[\gamma_- S_{\mathrm{ph}}^{+}\left(\frac{hf_\nu}{\Delta_\mathrm{B}}, \delta\right) + \gamma_+ S_{\mathrm{ph}}^{-}\left(\frac{hf_\nu}{\Delta_\mathrm{B}}, \delta\right)\right] \tag{3.32}$$

$$\Gamma_{10}^{\mathrm{ph}} = \Gamma_\nu \frac{g_\Sigma \Delta_\mathrm{B}}{8e^2}\sqrt{\frac{E_\mathrm{C}}{8E_\mathrm{J}}}\left[\gamma_+ S_{\mathrm{ph}}^{+}\left(\frac{f_\nu + f_{01}}{\Delta_\mathrm{B}/h}, \delta\right) + \gamma_- S_{\mathrm{ph}}^{-}\left(\frac{f_\nu + f_{01}}{\Delta_\mathrm{B}/h}, \delta\right)\right] \tag{3.33}$$

$$\Gamma_{01}^{\mathrm{ph}} = \Gamma_\nu \frac{g_\Sigma \Delta_\mathrm{B}}{8e^2}\sqrt{\frac{E_\mathrm{C}}{8E_\mathrm{J}}}\left[\gamma_+ S_{\mathrm{ph}}^{+}\left(\frac{f_\nu - f_{01}}{\Delta_\mathrm{B}/h}, \delta\right) + \gamma_- S_{\mathrm{ph}}^{-}\left(\frac{f_\nu - f_{01}}{\Delta_\mathrm{B}/h}, \delta\right)\right] \tag{3.34}$$

where $g_\Sigma \approx 8 g_k E_{\mathrm{J}\Sigma}^0 (\Delta_\mathrm{B} + \Delta_\mathrm{T})/(2\Delta_\mathrm{B}\Delta_\mathrm{T})$ is the total tunnel conductance of the SQUID in the normal state, Γ_ν is the dimensionless photon rate that accounts for the coupling strength between transmon and pair-breaking photons, and the photon spectral densities read [120]

$$\begin{aligned} S_{\mathrm{ph}}^{\pm}(x,z) &= \theta(x-1-z)\int_1^{x-z} dy \frac{y(x-y)\pm z}{\sqrt{y^2-1}\sqrt{(x-y)^2-z^2}} \\ &= \theta(x-1-z)\left\{\sqrt{x^2-(z-1)^2}\,E\left[\sqrt{\frac{x^2-(z+1)^2}{x^2-(z-1)^2}}\right]\right. \\ &\left. - 2z\frac{1\mp 1}{\sqrt{x^2-(z-1)^2}}K\left[\sqrt{\frac{x^2-(z+1)^2}{x^2-(z-1)^2}}\right]\right\} \end{aligned} \tag{3.35}$$

with E and K complete elliptic integrals of the second and first kind, respectively.

We note that all the rates, being expressed in terms of the conductance g_Σ, are calculated at leading order in the tunneling transmission probability. This means in particular that we are ignoring effects comparable in magnitude to those of the Josephson harmonics, which can introduce corrections at most at the percent level, see Appendix 3.C and Ref. [100]. Given the limited accuracy of time-domain measurements, this approach is sufficient for our purposes.

Finally, let us comment on the data fitting procedure. We base values for E_J, E_C and f_{01} on the fitting of the spectroscopic data (Appendices 3.C and 3.D); the occupation probability p_1 are estimated based on the single-shot parity outcomes and the measured relaxation times (see Fig. 3.3 and Section 3.H). We estimate the smaller gap Δ_T based on modeling the temperature dependence of T_1 (see Section 3.I). That leaves as unknown parameters the gap difference, the photon frequency, the trapping rates, and the dimensionless photon rate. The values used in calculating the theoretical curves in Figs. 3.4 and 3.5 are $\delta\Delta/h = 5.48\,\mathrm{GHz}$, $f_\nu = 119\,\mathrm{GHz}$, $s_\mathrm{B} = s_\mathrm{T} = 3.39\,\mathrm{Hz}$, and $\Gamma_\nu = 1.71 \times 10^{-8}$.

3.H. MODELING THE TEMPERATURE DEPENDENCE OF THE EXCITED STATE POPULATION

In our model, the parity switching time is parametrically expressed in terms of the populations of the ground and first excited state of the qubit (see Section 3.G). The population of the excited state of the qubit is given by

$$p_1 = \frac{\Gamma_{01}^{\mathrm{ee}} + \Gamma_{01}^{\mathrm{eo}}}{\Gamma_{01}^{\mathrm{ee}} + \Gamma_{01}^{\mathrm{eo}} + \Gamma_{10}^{\mathrm{ee}} + \Gamma_{10}^{\mathrm{eo}}} = (\Gamma_{01}^{\mathrm{ee}} + \Gamma_{01}^{\mathrm{eo}})\, T_1 \tag{3.36}$$

where $\Gamma_{10}^{\mathrm{ee}}$, and $\Gamma_{01}^{\mathrm{ee}}$ are the parity-preserving (thus not associated with quasiparticles) qubit' relaxation and excitation rates, respectively. For terms changing the parity, we identity the rates adding NUPS and PAPS contributions, i.e., $\Gamma_{10}^{\mathrm{eo}} = \Gamma_{10}^{\mathrm{ph}} + \Gamma_{10}^{\mathrm{qp}}/p_1$ and $\Gamma_{01}^{\mathrm{eo}} = \Gamma_{01}^{\mathrm{ph}} + \Gamma_{01}^{\mathrm{qp}}/p_0$ [cf. Eqs. (3.5) and (3.6)]. In the temperature regime for the parity-switching time measurements, the lifetime of the qubit is mainly limited by dielectric losses $T_1 \approx 1/(\Gamma_{10}^{\mathrm{ee}} + \Gamma_{01}^{\mathrm{ee}})$. Indeed, the maximum qubit's lifetime is of the order of 10 μs (see Appendix 3.I), which is more than an order of magnitude shorter than the parity lifetime. Assuming that the parity-preserving rates satisfy the detailed balance principle, i.e., $\Gamma_{01}^{\mathrm{ee}} = \Gamma_{10}^{\mathrm{ee}} e^{-hf_{01}/k_B T}$, we can write

$$p_1 \approx T_1 \Gamma_{01}^{\mathrm{eo}} + \frac{\exp(-hf_{01}/k_B T)}{1 + \exp(-hf_{01}/k_B T)}\,. \tag{3.37}$$

In the experimental protocol for determining the parity-switching time, the qubit's parity is mapped onto the qubit's logical state, with the convention e $\to$ 0 and o $\to$ 1. After the mapping, the qubit's state is not reset to zero, rather there is a waiting time equal to five times T_1. As a result, the qubit's excited state population relaxes exponentially from $p_1 = 0$ (for even assignment) or $p_1 = 1$ (for odd assignment) to the steady-state value p_1 of Eq. (3.36). Integrating the rate equation for the qubit's excited state population over the waiting time $5T_1$, we obtain the average excited

state population for the two parity assignments

$$\overline{p}_1^{\mathrm{e}} \approx 0.8\, p_1\ ,\ \overline{p}_1^{\mathrm{o}} \approx 0.2 + 0.8\, p_1\ . \tag{3.38}$$

The analysis of the hidden Markov model, combined with the considerations on the parity assignment, allows us to determine an average population of the excited state during the measurements of the parity-switching rates [points in Figs. 3.5(e) and 3.5(f)]. Motivated by the considerations made above, we use the following semi-phenomenological expression

$$p_1^{\mathrm{fit}} = \frac{a}{1+\mathrm{Exp}[-hf_{01}/k_BT]} + b\,\frac{\mathrm{Exp}[-hf_{01}/k_BT]}{1+\mathrm{Exp}[-hf_{01}/k_BT]} \tag{3.39}$$

and we perform a two-parameter fit (a, b) to the data [solid curves in Figs. 3.5(e) and 3.5(f)] The parameter a quantifies the average excited's state population at low temperatures $T \ll hf_{01}/k_B$; for even assignment, it is in the range of a few percent while for odd assignment is around 20% [see the considerations leading to Eq. (3.38)]. The prefactor of the last term in Eq. (3.39) turns out to be in the range of 0.8 to 1.3, in reasonable agreement with our interpretation.

3.I. TEMPERATURE DEPENDENCE OF THE QUBIT RELAXATION TIME

As mentioned in Appendix 3.H, the qubit relaxation time T_1 is much shorter than the parity-switching time at the base temperature of the dilution refrigerator, suggesting that T_1 is limited by decay processes unrelated to quasiparticle tunneling, such as dielectric losses; we model the latter as a two-level-system bath. At low temperatures, $T \ll hf_{01}/k_B$, the qubit's relaxation time is approximately the inverse of the parity-conserving relaxation rate, $T_1 \approx 1/\Gamma_{10}^{\mathrm{ee}}$, see Appendix 3.H; this quantity is an unknown function of the parallel magnetic field. Upon increasing the temperature $T \lesssim hf_{01}/k_B$, the qubit lifetime decreases due to the non-negligible qubit excitation rate caused by the TLS bath. Moreover, the quasiparticle density increases exponentially with the phonon temperature; thus, the qubit's relaxation time is eventually limited by quasiparticle tunneling above a crossover temperature; we assume this temperature to be sufficiently high so that deviations of the quasiparticle distribution from thermal equilibrium due to *e.g.* photon pair-breaking can be ignored (see the discussion at the end of this Appendix).

As in previous works [91, 146], to capture the temperature evolution of the qubit's relaxation time we

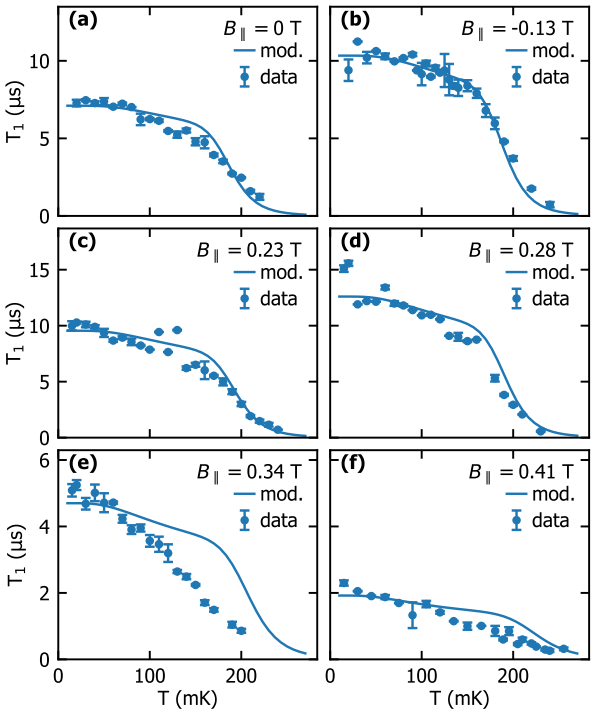

Figure 3.12: Qubit lifetime vs. temperature for different values of the in-plane magnetic field. Points are the experimental data, continuous curves are given by Eq. (3.40) and are obtained using $\Delta_B/h = 59.48$ GHz, $\Delta_T/h = 54$ GHz, and the spectroscopic parameters estimated in Appendices 3.C and 3.D. The parity preserving relaxation rate used in the plot is $\Gamma_{10}^{\mathrm{ee}}$ = **(a)** 141 kHz, **(b)** 97 kHz, **(c)** 105 kHz, **(d)** 79 kHz, **(e)** 213 kHz, **(f)** 521 kHz. The dependence of the superconducting gaps on the magnetic field has not been included.

sum the thermal quasiparticle decoherence rate $(T_{1,\mathrm{qp}}^{-1})$ and the contribution of the dielectric losses,

$$T_1(T) = \left\{\Gamma_{10}^{\mathrm{ee}}\left[1+\exp\left(-\frac{hf_{01}}{k_BT}\right)\right] + T_{1,\mathrm{qp}}^{-1}(T)\right\}^{-1}. \tag{3.40}$$

The relaxation rate due to thermal quasiparticles alone is

$$T_{1,\mathrm{qp}}^{-1} = (\tilde{\Gamma}_{10}^{\mathrm{B}} x_{\mathrm{B}}^{\mathrm{th}} + \tilde{\Gamma}_{10}^{\mathrm{T}} x_{\mathrm{T}}^{\mathrm{th}})[1+\exp(-hf_{01}/k_BT)] \tag{3.41}$$

where

$$x_\alpha^{\mathrm{th}} = \sqrt{\frac{2\pi k_B T}{\Delta_\alpha}}\exp\left[-\frac{\Delta_\alpha}{k_BT}\right] \tag{3.42}$$

is the thermal quasiparticle density in the electrode $\alpha = \{\mathrm{T},\mathrm{B}\}$. In Eq. (3.41), the relaxation rate for quasiparticles tunneling from the top to the bottom electrode $\tilde{\Gamma}_{10}^{\mathrm{T}}$ is given by Eq. (3.25), the corresponding rate for quasiparticles initially located in the bottom electrode is simply obtained exchanging $\Delta_B \leftrightarrow \Delta_T$ in Eq. (3.25). The exponential factor in the square bracket of Eq. (3.41) accounts for qubit's excitation rates, according to the detailed balance principle.

To check that the thermal equilibrium assumption for quasiparticles is justified in fitting the T_1 data, we proceed as follows: we start by noticing that the thermal quasiparticle contribution becomes relevant at temperature $\sim 170\,\mathrm{mK}$ above which T_1 decreases markedly faster with temperature. At that temperature, the thermal phonon generation rate is given by $r^{\alpha}(x_{\alpha}^{\mathrm{th}})^2$, cf. the last term in Eq. (3.22); for the low-gap (top) electrode, this rate is about $1.5\times10^{-7}\,\mathrm{Hz}$. The thermal phonon generation rate should be compared with g^{PAPS} of Eq. (3.23), which we estimate to be at most of order $3.7\times10^{-8}\,\mathrm{Hz}$ (cf. Fig. 3.4); therefore, non-equilibrium generation by pair-breaking photons can be ignored when analyzing the T_1 data. Conversely, we conclude that in our experiment at temperatures below about 150 mK the generation by thermal phonons plays essentially no role in the temperature dependence of τ_p; in fact, in Fig. 3.5 (a) and (b) we see a steeper decline in τ_p beginning at that temperature.

Supplementary Information for
"Quasiparticle effects in magnetic-field-resilient 3D transmons"

This supplement provides experimental details and additional data supporting the claims in the main text. Supplementary 3.J contains plots of the qubit lifetime, estimated mean excited-state populations for the "even" and "odd" parity outcomes, and parity lifetimes with corresponding model contributions for all temperature dependence datasets that were measured. Supplementary 3.K gives the estimated single-shot fidelities of the parity measurements as a function of the parallel field $B_\parallel$ and the temperature T. Supplementary 3.L contains data on the gate voltage V_g control of the offset charge of the transmon over a wider range compared to the main text [cf. Fig.3.2 (d)-(f) in Sec.3.3]; moreover we show that V_g has no influence on qutrit measurements for T_1 and T_2^{echo}. The coherence times as a function of $B_\parallel$ are presented in Supplementary 3.M. They show a clear decrease towards the edge of our measurement range $|B_\parallel| > 0.4\,\text{T}$ that also can be seen in the cavity quality factor. Supplementary 3.N contains additional information on the extraction of the parity lifetimes from the data comparing the fit to the power spectral density [116] to the hidden-Markov model. Supplementary 3.O shows the transmon temperature extracted from single-shot measurements as a function of fridge temperature at different fields. Supplementary 3.P contains details on the SQUID instability at high fields.

3.J. FULL TEMPERATURE DEPENDENCE DATASETS

In the main text, we report the temperature evolution of the parity switching time only for a few in-plane magnetic fields, for the sake of brevity. Figures 3.13 and 3.14 display the parity switching times τ_p^e and τ_p^o, and the corresponding model contributions obtained through fitting for all the measured temperature-dependent datasets using the first-to-second excited (cf. Fig. 3.4b) and the ground to-first excited protocol (cf. Fig. 3.4a), respectively. Moreover, for each $B_\parallel$, we conveniently compare with the corresponding temperature evolution of T_1 already shown in Appendix 3.I.

The model describes the τ_p^e data quite accurately up to 0.23 T, while a noticeable mismatch can be observed at larger fields. For the highest field values, $B_\parallel = 0.34$ T and $B_\parallel = 0.41$ T, the τ_p is shorter (roughly half the value at the base temperature of the cryostat) than expected from the model, suggesting that there may be additional mechanisms that we do not account for; another possibility is that our model parameters depend more drastically on the magnetic field, even though we do not believe that $\delta\Delta$ change significantly in the measured range, as the estimated critical field is above 1T. The most puzzling behavior, which we currently cannot explain, concerns the 0.28 T dataset, where the model notably overestimates the decay of τ_p^e and τ_p^o with the temperature. Furthermore, we note that for this particular field, we measured the parity switching time using both the protocols (cf. Figs.3.4a and b) reporting similar values; however we point out that the protocol involving the ground-to-first excited transition is less trustworthy than the other (cf. Supplementary 3.K), given the small charge dispersion of f_{01} transition, which implies that the waiting times of the Ramsey protocol are of the order of the coherence time of the transmon T_2^*.

$B_\parallel$ [T]	0.	-0.13	0.23	0.28 (f_{12})	0.28 (f_{01})	0.34	0.41
$\bar{p}_1^e$ vs T	$a = 0.034$	$a = 0.031$	$a = 0.014$	$a = 0.052$	$a = 0.061$	$a = 0.094$	$a = 0.064$
parameters	$b = 1.461$	$b = 1.261$	$b = 1.280$	$b = 1.806$	$b = 1.859$	$b = 0.712$	$b = 0.649$
$\bar{p}_1^o$ vs T	$a = 0.172$	$a = 0.212$	$a = 0.172$	$a = 0.180$	$a = 0.173$	$a = 0.183$	$a = 0.167$
parameters	$b = 0.932$	$b = 0.788$	$b = 0.788$	$b = 1.382$	$b = 1.448$	$b = 0.523$	$b = 0.407$

Table 3.1: Fit Parameters for the temperature dependence of the excited state population of the qubit.

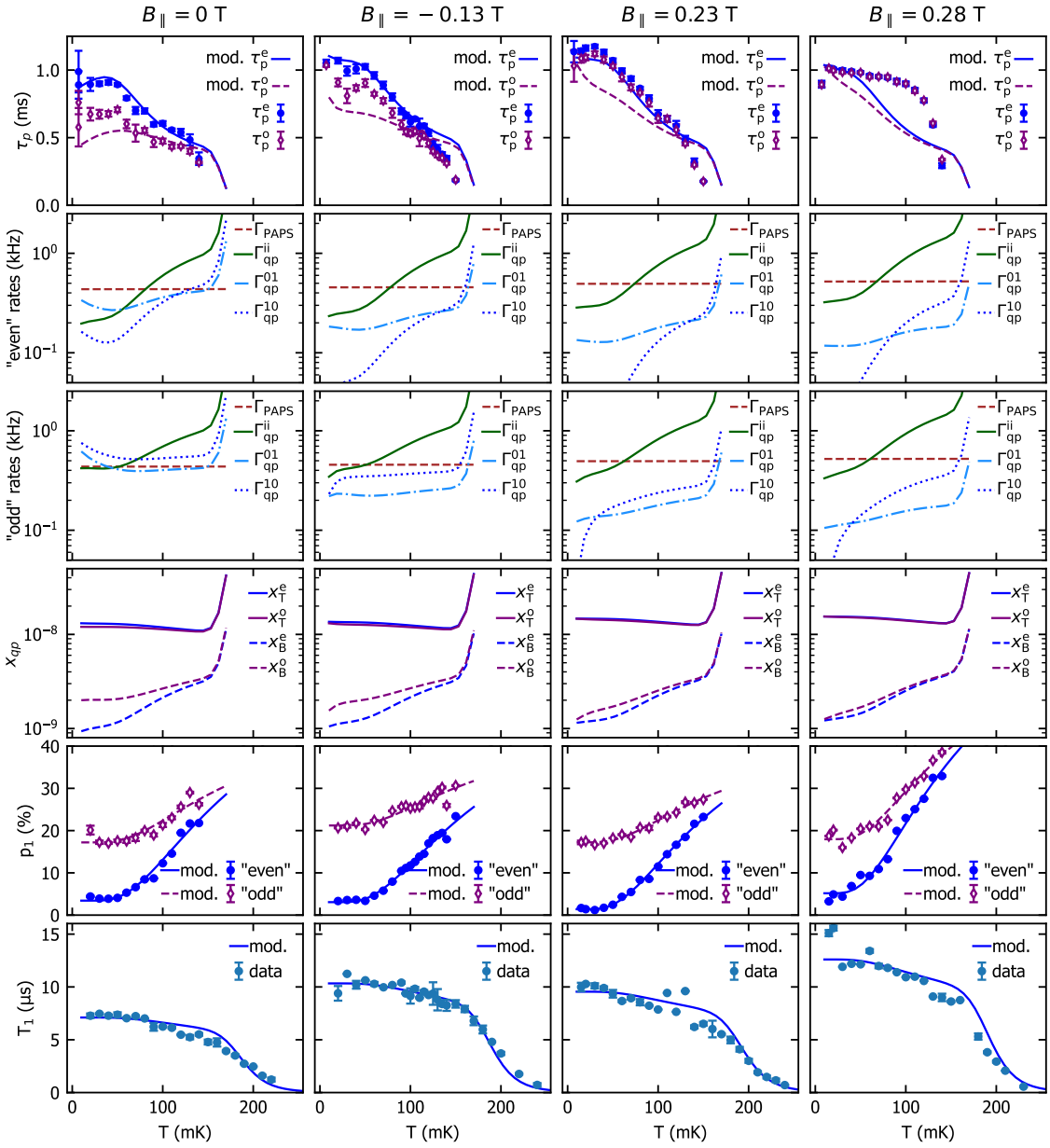

Figure 3.13: Temperature dependence of τ_p, p_1 and T_1 for different in-plane magnetic fields $B_\parallel$. Here, the entangled transition during parity measurements is f_{12}. Columns one and two have been discussed extensively in the main text. For the "even" and "odd" parity-switching times τ_p^e and τ_p^o, the agreement with model decreases with increasing magnetic field. For the highest field, $B_\parallel = 0.28$ T, the predicted waterfall-like decay of τ_p is not observed, possibly due to a neglected evolution of the superconducting-gap difference $\delta\Delta$ and/or altered quasiparticle-trapping dynamics. Parameters for the fit of the excited state population are given in Table 3.1, Γ_{10}^{ee} for the different fields are the same as in Fig. 3.12. The remaining parameters are given in the main text.

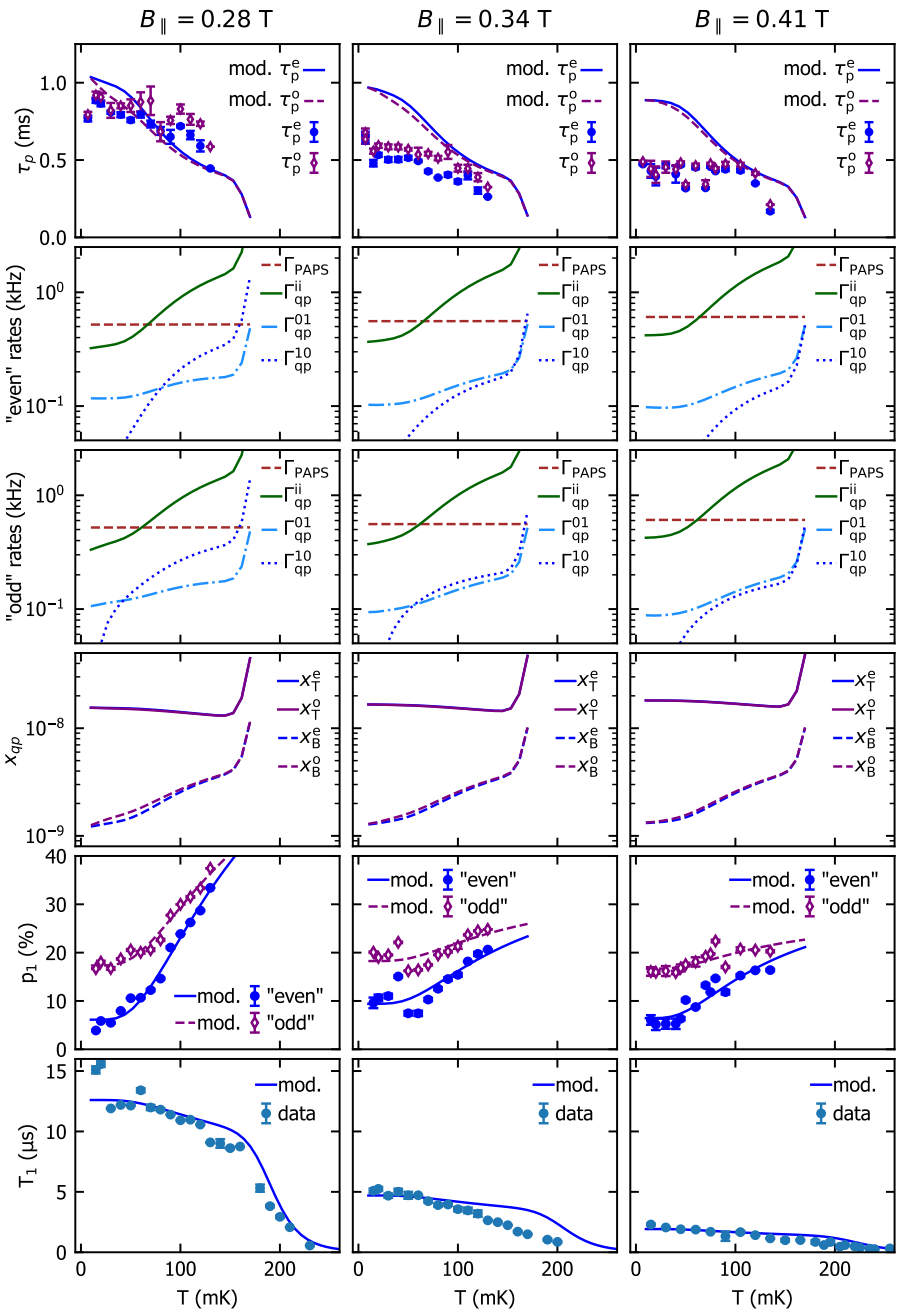

Figure 3.14: Temperature dependence of τ_p, p_1 and T_1 for different in-plane magnetic fields $B_\parallel$. Here, the entangled transition during parity measurements is f_{01}. The increasing mismatch with $B_\parallel$ for low temperatures is the same as in Fig. 3.4; its origin is unclear. Notably, some of the data suggests $\tau_p^e < \tau_p^o$ unlike for lower fields. However, the single-shot parity fidelity is significantly reduced in these measurements, $0.2 \leq F_{p,01} \leq 0.7$ (with fidelity generally decreasing with increasing temperature), compared to the parity measurements using the f_{12} transition shown above, where $0.5 \leq F_{p,12} \leq 0.9$. Parameters for the fit of the excited state population are given in Table 3.1, Γ_{10}^{ee} for the different fields are the same as in Fig. 3.12. The remaining parameters are given in the main text.

3.K. PARITY MEASUREMENT FIDELITIES

As shown in Section 3.F, we can estimate a single-shot parity measurement fidelity based on the assigned parity histograms. In Fig. 3.15 we show the fidelities as a function of $B_\parallel$ [panel (a)] and T [panel (b)]. Generally, the fidelities of the parity mapping based on the first and the second excited states of the transmon are higher, because $\delta f_{12} > \delta f_{01}$, while the coherence times are comparable. Moreover, the measurements based on the ground-to-first-excited state transition are performed at higher fields, where T_2^* is typically lower [see Fig. 3.18].

Fidelities decrease monotonically with T mainly due to three distinct effects: firstly, the coherence time T_2^* is reduced due to thermally populated photons in the cavity; secondly, parity switching becomes faster, which makes it harder to measure, in turn making the assignment less accurate, which reduces the fidelity (it also reduces T_2^* as well); thirdly, the transmon becomes hotter which also leads to assignment errors.

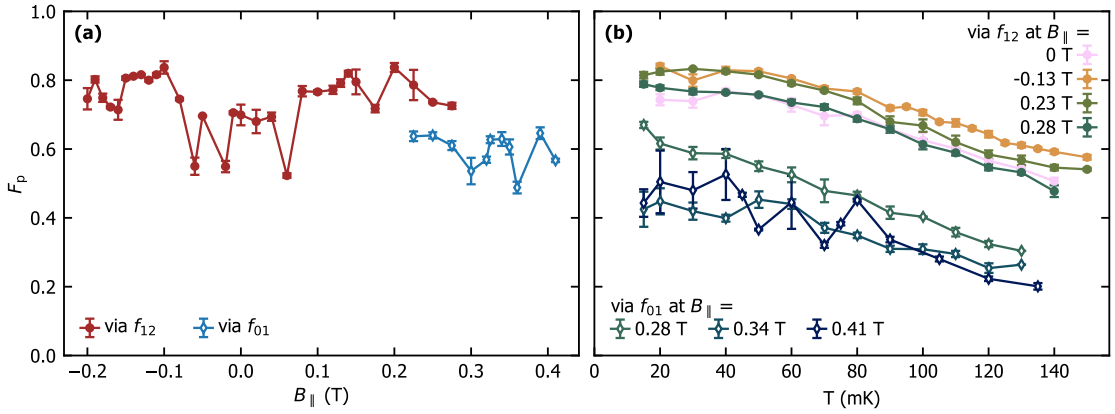

Figure 3.15: Single-shot parity measurement fidelities F_p based on the HMM as a function of **(a)** $B_\parallel$ and **(b)** temperature.

3.L. GATE-VOLTAGE CONTROL OF THE EXCESS CHARGE OF THE TRANSMON AND POTENTIAL EFFECTS ON THE TRANSMON'S LIFETIME AND COHERENCE TIME.

We explored scanning the gate voltage V_g over a wide range of many of the charge dispersion periods to verify that the transmon levels follow the expected periodicity [see Fig. 3.16 for the two-photon ground to second excited transition]. Overall, we observe the expected periodicity with one jump around $V_g = -0.5\,\mathrm{V}$. Our measurements suggest that charge jumps are relatively rare but we do observe drift in V_g that can cover up to a period on a 10 min timescale. For this reason, we usually sandwich the parity measurement sequences between two Ramsey measurements to be able to post-select on runs where the drift was not severe.

We have also investigated if the gate voltage has measurable effects on transmon T_1 and T_2^{echo}, concluding that they are not strongly affected by V_g [see Fig. 3.17 (a) and (c)]. As the majority of our measurements are done with qutrit pulse sequences, we also measured the relaxation of the transmon after preparing the state $|2\rangle$ and show an example of the estimated populations P_i as a function of time [see Fig. 3.17(b)]. We model the dynamics of the populations using standard rate equations, and we disregard transmon excitation processes, since at low temperatures we expect $\Gamma_{01}, \Gamma_{12}, \Gamma_{02} \ll \Gamma_{10}, \Gamma_{21}, \Gamma_{20}$.

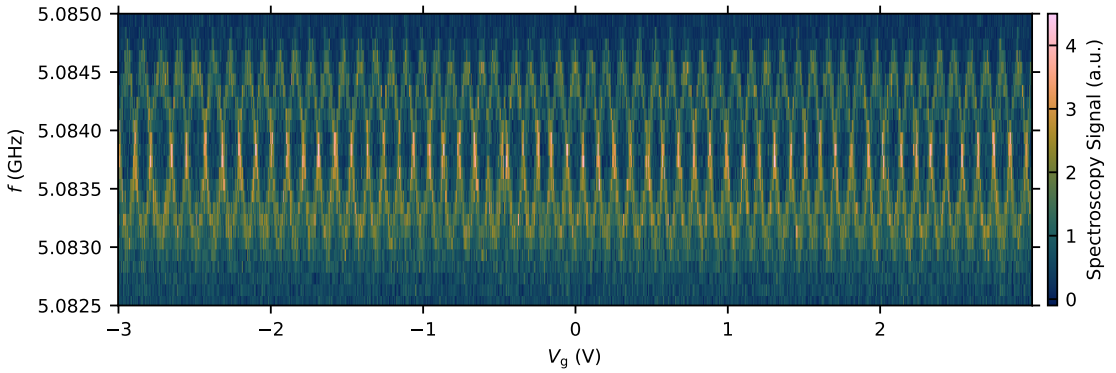

Figure 3.16: Wide range scan of the charge dispersion for $f_{02}/2$ as a function of V_g. More than 25 periods can be observed with one jump around −0.5 V. The data was taken at the bottom sweet spot at $B_{\parallel} = 150\,\mathrm{mT}$.

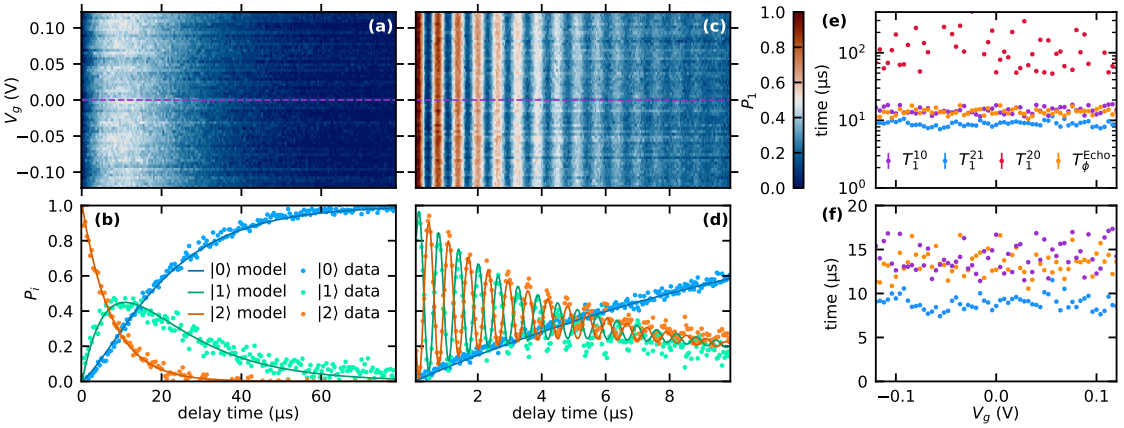

Figure 3.17: Transmon qutrit lifetimes and echo coherence time T_2^{echo} as a function of the gate voltage V_g. Color plots of the $|1\rangle$ state population P_1 vs delay time and V_g for (a) a T_1 sequence where the transmon is initialized in the $|2\rangle$ state and left to relax to the steady state, and (c) for an echo coherence time experiment where the qubit is initialized in the superposition of $|1\rangle$, and $|2\rangle$. The cuts at $V_g = 0$ show the dynamics of the population of $|0\rangle$, $|1\rangle$, and $|2\rangle$ states (points) for (b) the T_1 sequence and (d) the echo experiment. Experimental data are compared with a fitted model (solid) based on Eqs. (3.43)-(3.45) for panel (b) and a master equation for panel (d) [see text]. (e)-(f) Decay time and echo coherence times for the first two excitations of the transmon, as obtained from the fitted models, vs gate voltage.

Within this approximation, the time evolution of the populations can be readily obtained by solving the linear system of rate equations [with initial condition $P_0(0) = P_1(0) = 1 - P_2(0) = 0$], yielding

$$P_0(t) = 1 - \frac{\Gamma_{21}}{\Gamma_{21}+\Gamma_{20}-\Gamma_{10}}\mathrm{Exp}[-\Gamma_{10}t]\{1-\mathrm{Exp}[-(\Gamma_{21}+\Gamma_{20}-\Gamma_{10})t]\} - \mathrm{Exp}[-(\Gamma_{21}+\Gamma_{20})t]\,, \tag{3.43}$$

$$P_1(t) = \frac{\Gamma_{21}}{\Gamma_{21}+\Gamma_{20}-\Gamma_{10}}\mathrm{Exp}[-\Gamma_{10}t]\{1-\mathrm{Exp}[-(\Gamma_{21}+\Gamma_{20}-\Gamma_{10})t]\}\,, \tag{3.44}$$

$$P_2(t) = \mathrm{Exp}[-(\Gamma_{21}+\Gamma_{20})t]\,. \tag{3.45}$$

The relaxation somehow cannot be accurately modeled by including only sequential decay $T_1^{21} = \Gamma_{21}^{-1}$ and $T_1^{10} = \Gamma_{10}^{-1}$, but we also need to take into account the non-sequential decay time $T_1^{20} = \Gamma_{20}^{-1}$ which should have a small transition matrix element in the transmon but has also been previously observed [147].

We also show an example of a T_2^{echo} experiment for a superposition of $|1\rangle$ and $|2\rangle$ [see Fig. 3.17 **(c)** and **(d)**]. In this case, the populations are modeled using a standard master equation for the density matrix to account for dephasing processes (see, for instance, Ref. [148]). In the modeling of the Echo experiment, we fix the relaxation rates based on a preceding relaxation experiment from the $|2\rangle$ state.

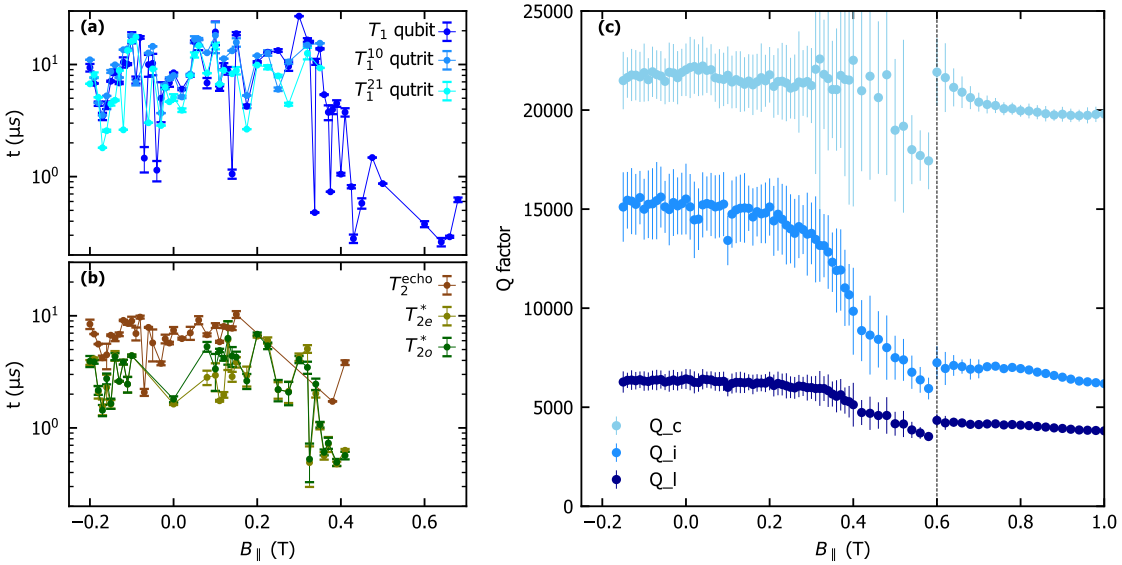

Figure 3.18: **(a)** relaxation times vs $B_\parallel$. There are two curves for the lifetime T_1, one for qubit and one for qutrit measurements of relaxation from $|2\rangle$. With the latter approach, also the decay rate from second to first excited states has been measured. **(b)** coherence times vs $B_\parallel$. The two curves for T_2^*, in contrast, are obtained in a single measurement and correspond to the two frequency branches of "even" and "odd" parity (T_{2e}^* and T_{2o}^*). Notably, the coherence times drop by an order of magnitude when approaching the region of SQUID instability (see Supplementary 3.P). **(c)** Loaded (Q_l), internal (Q_i), and coupling (Q_c) quality factors of the cavity vs $B_\parallel$. There is a drop in cavity Q_i setting in from 0.2 T, which was also reported in Ref. [115], described there as a step-like drop around 0.45 T, as only Q_l was extracted there. At 0.6 T, there is a jump in the data, as the power was slightly increased due to reduced non-linearity in the cavity.

The echo pure-dephasing rate T_ϕ^{Echo} is fitted using a qutrit lindblad-master equation that includes the wait-time-dependent phase in the second $\pi/2$ pulse responsible for the oscillations. The estimated T_1^{10}, T_1^{21}, T_1^{20} and T_ϕ^{Echo} as a function of V_g are shown in Fig. 3.17 **(e)** and **(f)**, showing no clear dependence on V_g. As the period of V_g is known to be 0.206 V, one could take T_1 vs V_g datasets over many periods and look for small effects in principle. Combined with SQUID or Fraunhofer tunability, one could try to identify effects of stable two-level fluctuators and understand their dependence on V_g but this is beyond the scope of this work.

3.M. QUTRIT COHERENCE TIMES AS A FUNCTION OF THE IN-PLANE MAGNETIC FIELD

We generally find that the transmon lifetime T_1 fluctuates with $B_\parallel$ and small changes in $B_\perp$ (for strong $B_\perp$ it is of course strongly suppressed as seen in Ref. [115]); nevertheless, for a given $B_\parallel$ one can find a high-coherence range in $B_\perp$. However, the T_1 times of the transmon show a sharp drop for in-plane fields above $B_\parallel = 0.4$ T [see Fig. 3.18 **(a)**], a similar behavior was observed in Ref. [115]. While in Ref. [115] the coherence times show a revival, reaching values above 10 μs around $B_\parallel = 0.5$ T, in this device, above $B_\parallel = 0.4$ T we did not find coherence times exceeding 2 μs. The decoherence mechanism causing this behavior is presently not understood, although we observe a strong drop of the cavity Q-factor in the same range of $B_\parallel$ [see Fig. 3.18 **(c)**].

For completeness, we also investigate the relaxation (T_1^{10}, T_1^{21}) of the first and second excited states of the transmon as well as the Ramsey and Echo coherence times for the qubit transition T_2^* and T_2^{echo}, respectively [examples of qutrit coherence-time measurements can be found in Fig. 3.10 and Fig. 3.17]. We find that the T_1 measurements based on measurements preparing the $|1\rangle$ and $|2\rangle$ states generally

give consistent results for T_1^{10}. T_2^{echo} is generally on the order of T_1, while T_2^* is typically around $T_1/2$ [see Fig. 3.18 **(b)**]. We fit the T_2^* Ramsey data with a model with two frequencies due to the two parities, but find that they generally have similar decay time constants, the difference is generally within the fit uncertainty. Our data for the ratio of T_1^{10}/T_1^{21} scatters significantly; typically $T_1^{10} > T_1^{21}$ (theory expectation would be $T_1^{10} = 2T_1^{21}$ [147]) but there are outliers for which $T_1^{10} < T_1^{21}$. This observation shows that losses are possibly due to a complicated environment with resonant two-level fluctuators, higher cavity modes, and the nearly-resonant quasiparticle tunneling.

3.N. HIDDEN MARKOV MODEL VS POWER-SPECTRAL-DENSITY BASED PARITY EXTRACTION

In early experiments using transmons to detect quasiparticle tunneling, the parity lifetime estimation from the Ramsey-based parity meter was done by assigning qubit states to the measurement outcomes and taking the power spectral density (*PSD*) of the resulting bitstrings [116], while hidden-Markov model (HMM) methods were introduced slightly later [145]. The advantage of the Gaussian HMM method we use is that it explicitly takes into account the Gaussian distributions of the single-shot measurement outcomes instead of thresholding the data. Moreover, the HMM method makes it possible to extract separate switching times τ_p^e and τ_p^o for the two parities in a straightforward way. In the following, we confirm that both methods of data analysis give roughly consistent results: the HMM method is presented in Section 3.F, while here we describe the *PSD* method and compare the results.

To extract τ_p and a parity fidelity from the raw IQ data using the *PSD* method, there are several steps:

1. assign the transmon states to the IQ measurement outcomes
2. assign a parity to each possible state
3. compute the *PSD* of the parity-vs-time bitstring
4. fit a Lorentzian-switching model to the *PSD* to get τ_p as well as the parity-measurement fidelity

The different steps are illustrated in Fig. 3.19. We use our Gaussian classifier trained on calibration points to assign a state to each IQ value [Fig. 3.19 **(b)**]. Based on this calibration, different regions of the IQ plane are colored in according to the most likely state. The raw IQ data of a calibration run and of a subsequent parity measurement is reported in Fig. 3.19 **(b)**. For this particular measurement, the parity outcomes are mostly $|0\rangle$ and $|1\rangle$ and any outcomes classified as $|2\rangle$ are likely due to the finite overlap between $|1\rangle$ and $|2\rangle$. We therefore identify the "even" parity for the $|0\rangle$ outcomes and "odd" for $|1\rangle$ or $|2\rangle$. In Fig. 3.19 **(c)** and **(d)**, we display the initial and the final section of the resulting parity-vs-time and state-vs-time sequences with a total duration of 21 s. We model the parity sequence as a random telegraph signal, characterized by a Lorentzian *PSD* [116]

$$PSD(f) = F^2 \frac{4\tau_p^{-1}}{(2\tau_p^{-1})^2 + (2\pi f)^2} + (1-F^2)\Delta t_{\text{exp}}, \tag{3.46}$$

where τ_p and the parity-measurement fidelity F are free parameters and Δt_{exp} is the repetition time of the runs. The experimental *PSD* and a fit are shown in Fig. 3.19 **(e)**. Notably, with this specific method, one can only get a mean τ_p, as one would have to modify the model for an asymmetric dwell time to extract τ_p^e and τ_p^o. This particular dataset is the same that was shown in Fig. 3.11 to illustrate

the HMM method. When comparing the assigned parities as a function of time for both figures, the HMM fit already filters out some wrong parity assignments due to "readout" errors (e.g. cases where there are relaxation events during the sequence or trivial readout errors). For this example, the fit yields $\tau_p = 1.36\,\text{ms}$ and $F = 0.88$, while the HMM gives $\tau_p^e = 1.21\,\text{ms}$ and $\tau_p^o = 1.09\,\text{ms}$ and $F = 0.89$. Alternatively, as done in Ref. [116] or Ref. [103], one can initialize the transmon as well as the parity by measurements and with post-selection extract the different individual rates; since we did not use a parametric amplifier, the measurements are not quantum non-demolition strictly-speaking, such that this was not attempted.

We now compare the outcomes for the HMM and *PSD*-fit extraction of τ_p and F for more datasets. We checked the results for all of our data and generally find the deviations to be within 20%. Only around zero field, where we observe a notable difference between τ_p^e and τ_p^o due to different p_1, $\tau_p^o \sim 0.5\,\tau_p^{PSD}$. Here we compare the two approaches for a set of data where we performed the Ramsey-based parity measurement using the superposition of $|1\rangle$ and $|2\rangle$ for different wait times. Sweeping the wait time ideally would see F oscillate between 0 and 1, as the azimuthal angles for the even and odd parities would generally not be separated by 180 degrees on the Bloch sphere when the measurement is performed. For the optimum wait time and at odd integer multiples of it, the parities reach orthogonal states on the Bloch sphere but they periodically converge as well. The results are shown in Fig. 3.20 **(a)**. We see the expected oscillations in F and a decay for long wait time, as the parity meter becomes limited by the coherence time. The fidelity estimate for the two methods only differs slightly and follows the same trend. Around the minimum F, the extracted τ_p do not reflect parity dynamics but other low-frequency noise processes in the setup [see outliers in Fig. 3.20 **(b)**]. This is likely the reason why F does not drop to zero and that F actually increases for the higher multiples of the wait times for the minimum. However, in the high-fidelity region we find that the extracted τ_p are generally similar and are not too sensitive to imperfect tune-up of the parity measurement [see Fig. 3.20 **(c)**]. At low fidelity, the HMM can not find a stable difference between τ_p^e and τ_p^o. The results presented in the main text are always measured around the first fidelity maximum.

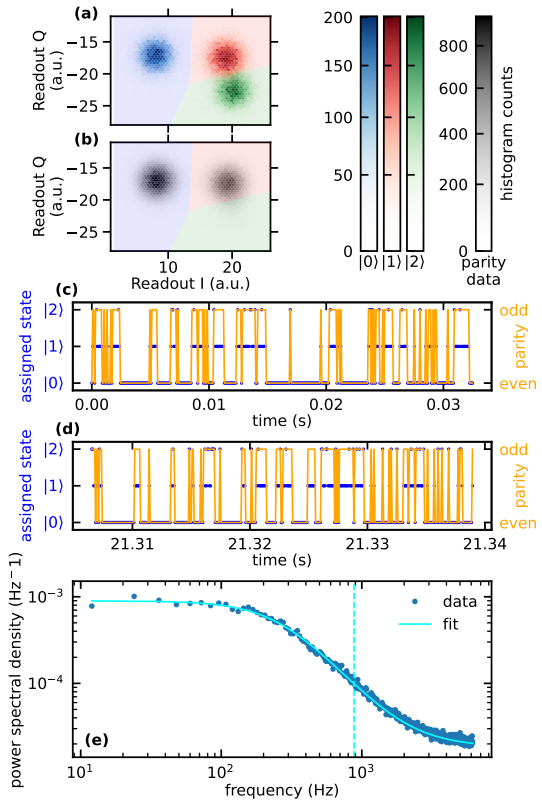

Figure 3.19: **(a)** Calibration points for the classifier. The transmon is prepared in the $|0\rangle$, $|1\rangle$ and $|2\rangle$ state and measured. Histograms for the readout voltage in I and Q are shown. The raw shots are fitted with Gaussian probability distributions. Thus a classifier can be constructed that assigns a most-likely state to every point in the IQ plane (overlayed colors). **(b)** Histogram of the data points from the parity measurements. States can be assigned based on the classifier. As expected from the sequence, the main outcomes are $|0\rangle$ and $|1\rangle$. **(c)** and **(d)** assigned state as a function of time for the beginning and end of the parity run. As the $|2\rangle$ outcomes are most likely due to the finite overlap with the $|1\rangle$ state, even parity is assigned to the $|0\rangle$ state, while odd parity is assigned to $|1\rangle$ and $|2\rangle$ outcomes. (d) Power spectral density calculated from the parity outcomes as a function of time. A fit of a "noisy" Lorentzian, Eq. (3.46), is used to determine the parity-switching time τ_p and fidelity F.

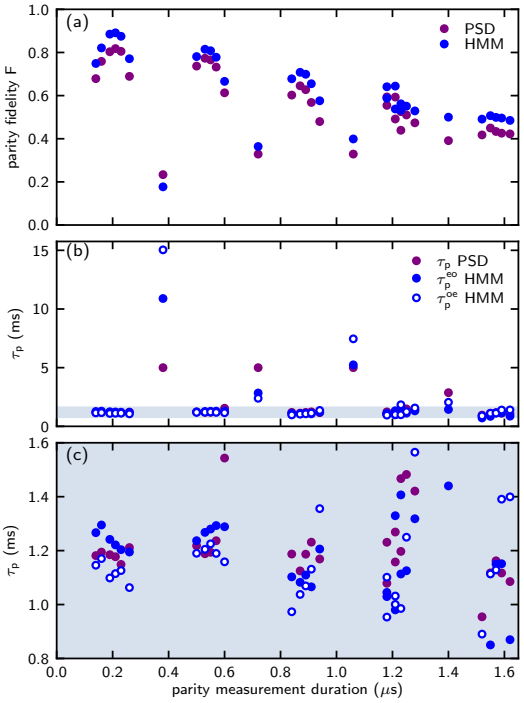

Figure 3.20: **(a)** Parity measurement fidelity F extracted from the PSD fit and the HMM fit as a function of parity measurement duration. The duration comprises the 20 ns pulses as well as the Ramsey wait time. Oscillations in F are expected and similar fidelities are extracted for both methods. **(b)** and **(c)** (zoomed in) τ_p extracted from the PSD fit and τ_p^e and τ_p^o extracted from the HMM fit. PSD and HMM fit generally give similar τ_p for a range of fidelities, showing that the measurements are relatively robust and that the two methods don't contradict each other. For long parity-measurement times, decoherence leads to very noisy τ_p. At the parity-insensitive wait time, the extracted τ_p and F are dominated by other low-frequency noise processes.

3.O. PRIMARY THERMOMETRY WITH THE TRANSMON

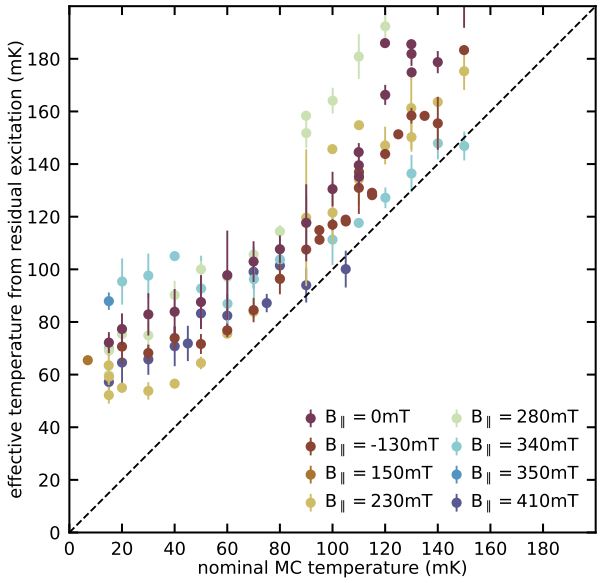

Figure 3.21: Transmon effective temperature extracted from the ground-state population as a function of mixing chamber (MC) temperature (see text). Data suggest a saturation of effective temperature taking place between a mixing chamber temperature of 50 mK and 60 mK.

As we measure the parity-switching time as a function of the nominal mixing-chamber temperature, it is instructive to compare the latter with the effective transmon temperature. If we assume that the transmon populations are Boltzmann distributed, we can approximately infer an effective temperature from the $|0\rangle$ state population P_0 and transition frequencies. The ground-state population can be extracted from a Gaussian fit to the single-shot measurement data for the nominal $|0\rangle$ state - we can extract the fraction of the single-shot IQ values that are assigned as zero. In principle, we can also extract P_1 and P_2 from the single-shot measurements to test and corroborate the hypothesis of the Boltzmann distribution (see for example Ref. [149]); for the sake of simplicity, here we just consider the ground state population. We have explicitly measured the first 3 transition frequencies and populations in the higher levels can be neglected, since we estimate that even at the highest field and temperature we consider, their inclusion would alter the results at most by a few percent. Then, treating the transmon as a ququart we can infer a temperature from P_0 by finding the root of the equation

$$P_0 = \frac{1}{1+\exp(-\frac{hf_{01}}{k_B T})+\exp(-\frac{hf_{02}}{k_B T})+\exp(-\frac{hf_{03}}{k_B T})}. \tag{3.47}$$

Alternatively, one could use the temperature estimation method described in Ref. [150], which does not rely on single-shot readout but rather on the contrast of Rabi oscillations between different states.

The estimated transmon temperature as a function of mixing-chamber temperature at different in-plane fields is shown in Fig. 3.21. Generally, there is a roughly linear dependence between fridge and transmon temperature starting from about 60 mK, in line with values reported in literature [150]. Below 60 mK of mixing chamber temperature the transmon temperature decouples from the fridge temperature and has different saturation values at different magnetic fields. Parity-switching qubit transitions are likely a main source of heating in this regime [cf. first term in the right-hand-side of Eq. (3.37)]. We find that the transmon temperature at the base temperature of the fridge depends on $B_\parallel$,

with estimated values in the range 50 mK-80 mK.

3.P. SQUID OSCILLATION STABILITY AND ANOMALIES AT HIGH FIELD

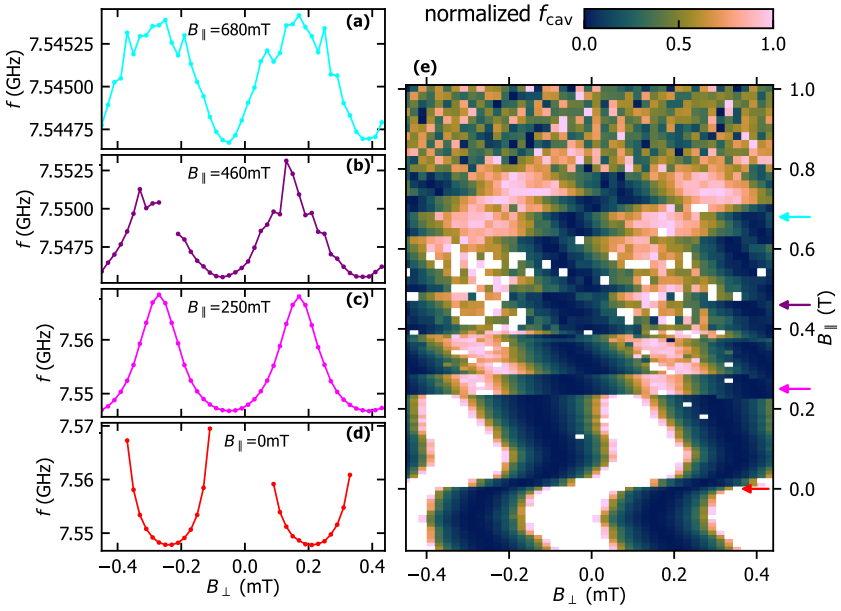

Figure 3.22: Flux instability at high in-plane magnetic fields. **(a)**, **(b)**, **(c)** and **(d)** SQUID oscillations in the cavity frequency as a function of $B_\perp$. At zero field in **(d)**, the top sweet spot is very close to the cavity such that the top sweet spot is missing but at medium field in **(c)** we see a smooth dependence with well-defined top and bottom sweet spot. However, at higher fields, the cavity frequency shows strange jumps around the top sweet spot [see **(a)** and **(b)**]. **(d)** Normalized f_{cav} as a function of $B_\perp$ and $B_\parallel$. The fact that the offset of the oscillations does not shift much shows that $B_\parallel$ is aligned well in the SQUID plane. However, around $B_\parallel = 0$, the offset shows a non-monotonous behavior possibly a magnet-inherent problem. At $B_\parallel$ between 0.4 T and 0.6 T, there is a mix of jumps and missing data points (white spots) where there is no cavity resonance in the measured range - which could be due to jumps. We also generally found flux jumps in this range when measuring at the same field multiple times.

As in Ref. [115], we observe that the SQUID oscillations with $B_\perp$ can become unstable at certain $B_\parallel$. This instability is the main reason why we can not measure the parity lifetime for $B_\parallel > 0.41$ T. Parity measurements require stability for several minutes for tuning-up the protocol. However, the reduced coherence at high field would also have made measurements more challenging. The SQUID instability is marked by frequency jumps in the flux dependence as well as instability in time, with jumps occurring so often that in unstable regions even quick time-domain measurements such as a T_1 measurement are challenging. In Ref. [115] measurements of the SQUID device were impossible between 0.4 T and 0.5 T, but the SQUID became stable again at higher fields and we could take more data up to 0.8 T. Here, we did not find another region where the SQUID does not suffer from rapid flux jumps above 0.5 T. The cavity frequency as a function of $B_\perp$ is displayed in Fig. 3.22, showing that cavity oscillations are clearly visible up to 0.8 T, where the transmon is effectively single-junction (cf. Section 3.D), and significantly weaker above. There is more noise especially between 0.4 T and 0.6 T. We also see a decline in the cavity quality factor setting in around 0.2 T and showing a kink around 0.4 T [see Fig. 3.18 **(c)**]. Currently, we do not have a good explanation for this phenomenology; possible culprits are spurious JJs, as already suggested in Ref. [115].

4

TRANSMONS BASED ON TOPOLOGICAL-INSULATOR JOSEPHSON JUNCTIONS

As elaborated in Section 1.2.4 the energy spectrum of transmons with Josephson junctions (JJs) made from topological superconductor nanowires is predicted to change drastically in the presence of MZMs. Due to a finite overlap the MZMs hybridize across the JJ, which introduces coherent electron tunneling to the Hamiltonian and couples the formerly disconnected "even" and "odd" transmon-parity sectors. This chapter presents the current status of our efforts to integrate topological-insulator nanowire JJs to transmon circuits. The ultimate objective of this research effort is to investigate the magnetic-field dependence of transmon spectrum and parity-switching rates in order to identify a topological regime.

Data availability *The raw data and Jupyter notebooks for their analysis are stored on the institute network servers.*

After showing that magnetic-field-resilient transmon circuits based on Al/AlO_x/Al JJs are a viable option for parity readout of future topological qubits we now turn to the integration of topological superconductor nanowires (TSCNW) to the transmon circuits. A building block of particular interest are Josephson junctions made of TSCNW. As discussed in Chapter 1 they are predicted to host hybridized MZMs in the junction area, imparting unique signatures to the transmon spectrum and its parity evolution. In the course of this PhD project we fabricated and measured transmon devices comprising Josephson junctions made of topological-insulator (TI) nanowires. The JJs form when two segments of the wire are proximitized by a superconductor (S), leaving an unproximitized normal (N) region in between. The system forms an SNS (or, further differentiating the original superconductor S from the proximitized region S' an $SS'NS'S$) junction. Here, supercurrent is carried across the unproximitized region by Andreev bound states [151]. For superconductors we used niobium or a bilayer of titanium and aluminum, where the titanium serves as a buffer layer to prevent diffusion of aluminum into the TI. For TIs we tested $(Bi_{1-x}Sb_x)_2Te_3$ (BST), $(Bi_{1-x}Sb_x)_2Se_3$ (SBS) and $BiSbTeSe_2$ (BSTS). The devices characterized in the course of this project span different platforms such as vapour-liquid-solid (VLS) grown nanowires (BST and SBS), devices based on exfoliated flakes (BSTS), as well as devices based on BST-films grown in molecular beam epitaxy [152, 153, 154]. For all these different platforms it is a formidable task on its own to optimize the growth and etching of the TI and its interface to the superconductor such that a bulk-insulating wire with good proximitization of the surface states is obtained. To fabricate the TI-based transmons I therefore collaborated intensly with other members of our group, asking them to fabricate devices based on my design or drawing heavily on their recipes and experience for my own fabrication. The subsequent section presents two example datasets, with one device being based on a VLS-grown BST nanowire and one device based on an exfoliated BSTS crystal flake, etched into a nanowire structure. In both cases the superconductor is niobium.

4.1. DEVICE FABRICATION

To start with I briefly sketch the fabrication process for each device. For the VLS device nanowires are grown on a silicon substrate in a vapour-liquid-solid growth process using gold nanoparticles as growth catalysts. The wires are subsequently transferred into pre-defined 100 µm × 100 µm-sized resist windows on the transmon chip by pressing the growth substrate onto the transmon chip. The transfer into resist windows works because the wires stick out of the growth substrate in random orientations and can reach several µm in length, such that some of them attach to the transmon chip. After stripping the resist off the transmon chip, nanowires of different sizes and random orientation remain in well defined areas. Using optical microscope images we can select nanowires with diameters of a few tens of nm based on their brightness in the image. In a single electron-beam-lithography (EBL) step the transmon islands and leads to the wires are defined. After a gentle interface cleaning process consisting of a diluted HCl dip and in-situ argon cleaning niobium is sputtered onto the sample. The final liftoff yields transmon devices based on proximitized VLS nanowire JJs (see Fig. 4.1 **(a)** and **(b)**). Both single-JJ devices and SQUIDs can be made, the device we show data on here is a SQUID. I fabricated the device myself with guidance by Oliver Breunig. The BST wires were grown by Felix Münning.

For the etched-flake-nanowire transmon the device fabrication starts from a single crystal of BSTS, of which flakes are exfoliated using a scotch tape. Subsequently, single suitable flakes of ~ 15 nm thickness are transferred deterministically to the sapphire transmon chip. In a dry etching process using Argon the flakes are patterned into nanowires and subsequently contacted by niobium transmon islands

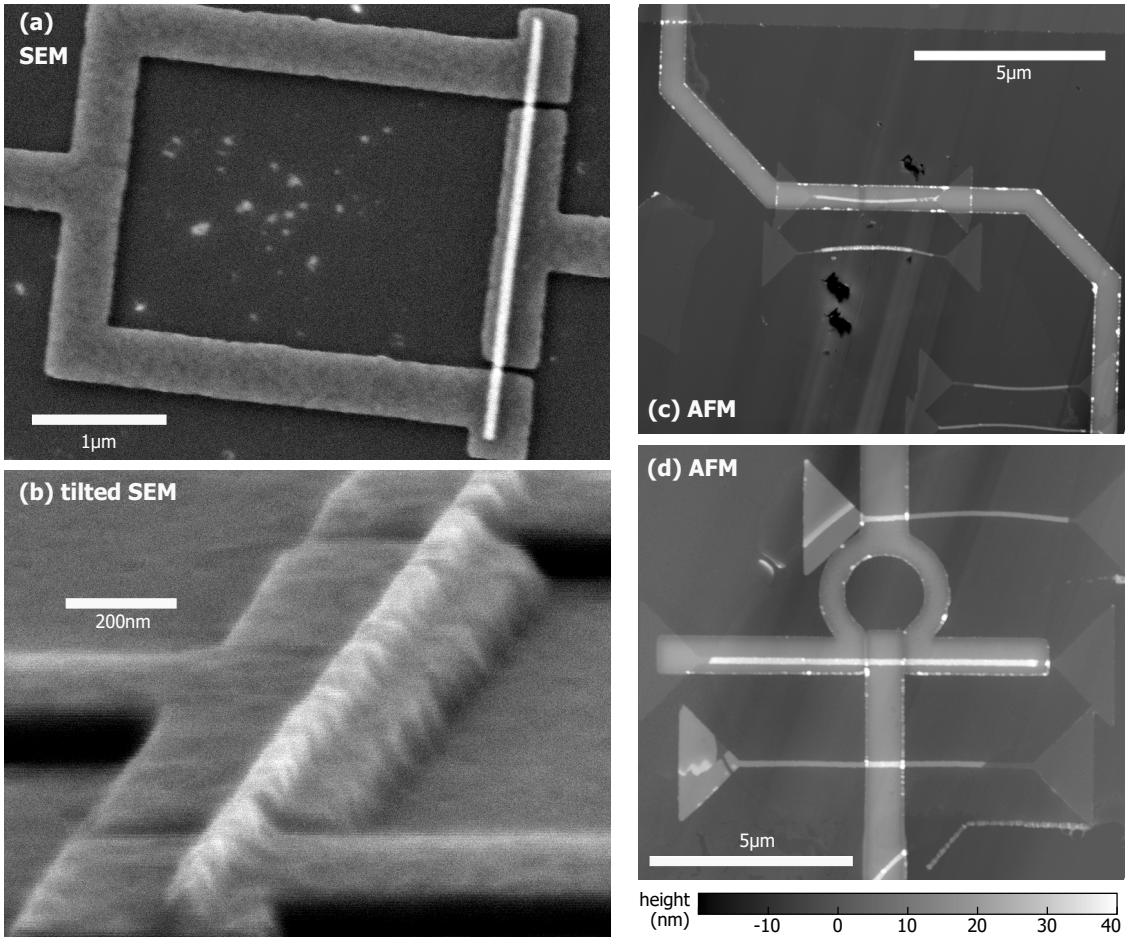

Figure 4.1: **(a)** and **(b)** Scanning electron micrographs of the SQUID loop of a VLS-nanowire transmon. The device is similar to the one being discussed in the main text. Atomic force micrographs of **(c)** the single-JJ and **(d)** the SQUID etched-flake-nanowire transmons. Niobium sidewalls form during sputtering.

and leads, similarly to the VLS-nanowire chip. The specific sample I present data on contains both a single-JJ transmon and a SQUID transmon. Figure 4.1 **(c)** and **(d)** show AFM images of the devices. The devices were fabricated by Junya Feng using BSTS grown by Zhiwei Wang.

4.2. SPECTROSCOPIC MEASUREMENTS

All TI-based transmon devices tested so far suffered from heavy microwave losses and did not achieve the strong coupling limit. In this situation the transmon can be so incoherent that it acts as a dominant loss channel for cavity photons and decreases the cavity Q-factor when the transmon frequency approaches the cavity resonance frequency. A dispersive shift of the cavity can still be observed, but it may be impossible to resolve the qubit frequency in two-tone spectroscopy, due to a bad SNR and a transition linewidth on the order of hundreds of MHz which requires spectroscopy powers orders of magnitude higher than for conventional transmons. Our Nb-BST VLS-NW transmon is a paradigmatic example of this scenario: Being unable to observe the transmon directly in two-tone spectroscopy we were left with measurements of the cavity resonance frequency f_{cav} and its Q-factor.

4.2.1. NB-BST VLS-NW TRANSMON

Figure 4.2 shows measurements of f_{cav} and Q_{load} as a function of temperature and as a function of perpendicular magnetic flux through the SQUID loop. During the cooldown, the cavity resonance

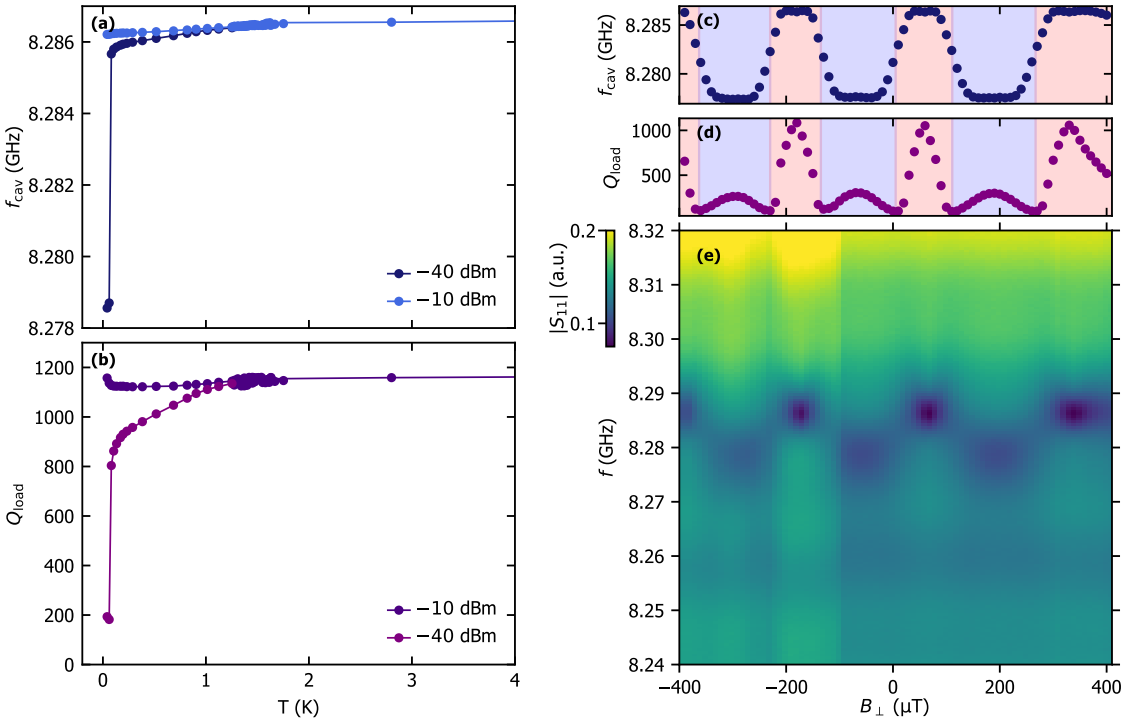

Figure 4.2: Spectroscopic measurements of a Nb-BST-VLS-nanowire SQUID transmon. Resonator frequency f_{cav} **(a)** and quality factor Q_{load} **(b)** as a function of fridge temperature. A gradual change in both f_{cav} and Q_{load} around 1.5 K suggests a superconducting transition of the JJ with an induced gap much smaller than that of Nb. **(c)** and **(d)** show the dependence of f_{cav} and Q_{load} on out-of-plane magnetic fields $B_\perp$. The SQUID transmon f_{01} repeatedly crosses f_{cav}, imparting a meandering dispersive shift to f_{cav}: Regions for which $f_{01} > f_{cav}$ are shaded in blue, regions for which $f_{01} < f_{cav}$ are shaded in red. Instead of an expected avoided crossing f_{cav} varies smoothly and Q_{load} becomes minimal for $f_{01} \simeq f_{cav}$ due to an inverse Purcell decay of resonator photons to the lossy transmon. **(e)** In a line-by-line colorplot of the reflected amplitude of the resonator response $|S_{11}|$ as a function $B_\perp$ the hint of an avoided crossing is visible.

peak is probed at two different VNA output powers, −10 dBm and −40 dBm. A gradual signal change in both f_{cav} and Q_{load} around 1.5 K point to a superconducting transition in the transmon device. The induced gap in the topological-insulator wire seems to be significantly reduced compared to that of Niobium, which has a critical temperature of about 8 K. Notably, the cavity resonance frequencies for high and low VNA output power increasingly diverge with decreasing temperature, stabilizing at a high-power low-power dispersive shift $\chi = 8$ MHz. As the dressed f_{cav} is being pushed downwards compared to its bare frequency the transmon f_{01} is expected to be above f_{cav}. In a simple estimate, $\chi \simeq g^2/\Delta$ with $\Delta = f_{01} - f_{cav}$ and a resonator-qubit coupling constant $g/2\pi \simeq 90$ MHz as found in the aluminum transmon measured in Chapter 3 sharing a similar design. Then, $f_{01} \sim 9.3$ GHz, which is in principle a good regime for dispersive qubit readout. Crucially, however, the low-power Q_{load} is very low, about 200 at base temperature, which is more than an order of magnitude lower than what we typically find for a cavity loaded with aluminum transmons (cf. Chapters 2 and 3). We interpret the low Q-factor to be due to an inverse Purcell-decay of cavity photons to a very lossy transmon.

This hypothesis is further supported by the flux dependence of f_{cav} and Q_{load}. Here, we see a regular pattern with a periodicity in $B_\perp$ matching the dimensions of the SQUID loop. This indicates, that both JJs of the transmon are working. As expected for a near-symmetric SQUID transmon, the perpendicular flux tunes the transmon frequency f_{01} periodically from its top sweetspot above f_{cav} to frequencies far below f_{cav} and back again. Usually, for a transmon in the strong coupling regime, this would result in a clear avoided crossing of magnitude $2g$ between resonator and transmon frequency. Instead, we

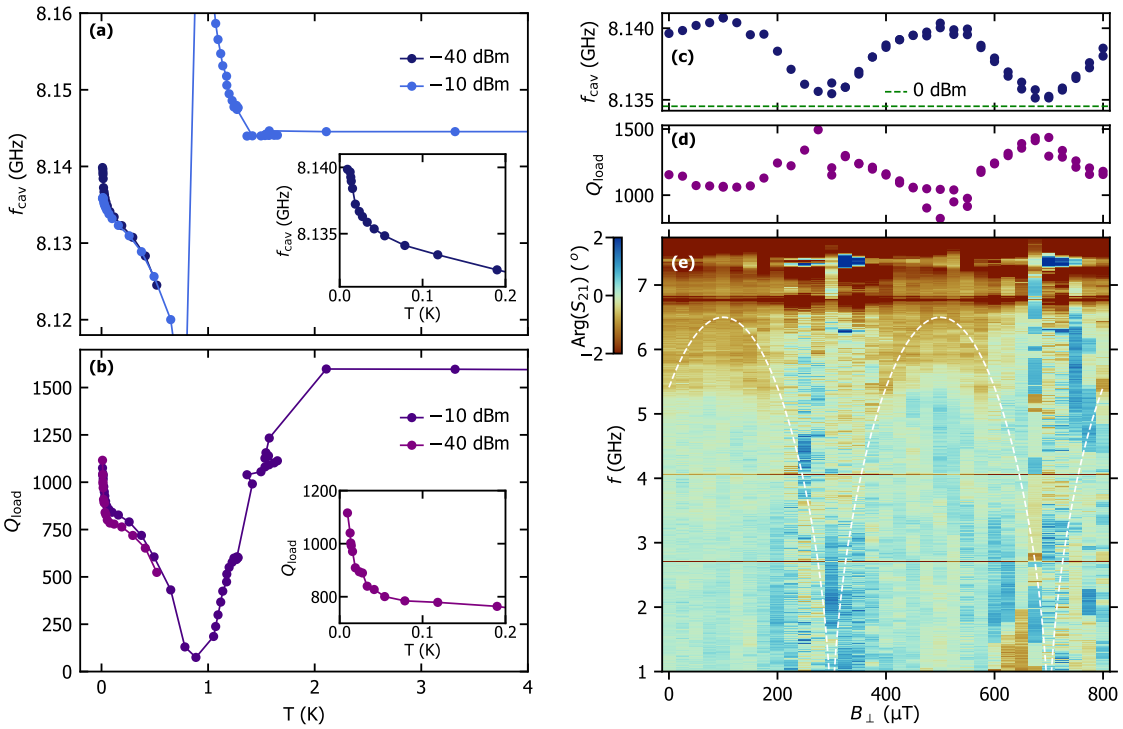

Figure 4.3: Spectroscopic measurements of a sample containing two Nb-BSTS-etched-flake-nanowire transmons, one single-JJ device and a SQUID device. Resonator frequency f_{cav} **(a)** and quality factor Q_{load} **(b)** as a function of fridge temperature. A clear change in both f_{cav} and Q_{load} around 1.5 K to 2 K suggests a superconducting transition of the JJs with an induced gap much smaller than that of Nb. For $T \leq 50$ mK, parallel resistive channels are partially being gapped out (see insets). **(c)** and **(d)** show the dependence of f_{cav} and Q_{load} on out-of-plane magnetic fields $B_\perp$. The SQUID transmon, for which $f_{01} < f_{cav}$ for all $B_\perp$, imparts an oscillating dispersive shift to f_{cav}. When f_{01} approaches f_{cav}, the dspersive shift on $fcav$ becomes maximal and Q_{load} becomes minimal due to an inverse Purcell decay of resonator photons to the lossy transmon. **(e)** Two-tone spectroscopy as a function of $B_\perp$ for frequencies below f_{cav}. Parts of the SQUID flux arcs are faintly visibe, in particular around its top sweetspot. Dashed white lines serve as a guide to the eye.

observe a gradual transition of f_{cav} between a bottom limit at 8.278 GHz, when $f_{01} > f_{cav}$, and a top limit at 8.286 GHz, when $f_{01} \ll f_{cav}$ (see Fig. 4.2 **(c)**). Right at the crossing between f_{01} and f_{cav} the cavity Q-factor becomes minimal (see Fig. 4.2 **(d)**). Assuming it is dominated by losses to the transmon the measured $\min Q_{load} = 100$ corresponds to a transmon linewidth of more than 83 MHz, which is the estimate for inifinite coupling g. In contrast, the Q-factor is maximal when f_{01} reaches its bottom sweetspot where it is is maximally detuned from the resonator frequency and it also shows a local maximum when f_{01} reaches its top sweetspot.

Figure 4.2 **(e)** shows the real part of the underlying raw data to the preceding discussion: a line-by-line colorplot of the reflected amplitude of the resonator response $|S_{11}|$ as a function $B_\perp$ and frequency. The meandering cavity resonance dip is visible in shades of blue and more pronounced for regions of high Q_{load} than for regions of low Q_{load}. Interestingly, the hint of an avoided crossing can be vaguely discerned in particular in the top half of the plot.

4.2.2. NB-BSTS ETCHED-FLAKE-NW TRANSMON

For the etched-flake-nanowire transmon figure 4.3 **(a)** and **(b)** show again measurements of f_{cav} and Q_{load} as a function of temperature. As before, the data suggest a superconducting transition of the junctions around 1.5 K to 2 K. A large avoided crossing around 1 K is seen in the raw data (not shown here), which is at present not understood. A dispersive high-power low-power shift of 6 MHz shows up

for low temperatures. However, this time the dispersive shift does not readily translate into a transmon frequency as it is the sum of two unknown dispersive shifts, one per transmon on the chip.

A striking feature of the cooldown data is a sharp increase in Q_{load} (and f_{cav}) towards the lowest temperatures, the insets of panels **(a)** and **(b)** show zoom-ins. It suggests a sudden increase of transmon coherence which was not observed in other devices, and points to resistive channels partially being gapped out for $T \leq 50\,\text{mK}$. This illustrates at the same time problem and hope for TI-based transmons: As further supported by tunneling spectroscopy measurements of TI-JJs within our group [155] we believe to have a soft induced gap in the JJ, i.e. the local density of states in the JJ is not fully gapped out but remains finite. Quasiparticles may then occupy these low-lying subgap states in the JJ, leading to a resistive shunt in parallel to the lossless superconducting channels. While invisible to DC measurements of the JJ's current-voltage characteristics, the resistive shunt introduces losses in alternating microwave potentials. A hard induced superconducting gap is thus crucial for better microwave performance, and this particular sample seems to at least have an additional reduction in the DoS for $T \leq 50\,\text{mK}$. This is still a far cry from a true hard gap as e.g. in Al/AlO_x/Al JJs, however: In stark contrast to the here presented low-temperature increase in transmon coherence, the temperature dependence of T_1 of aluminum transmons shown in Fig. 3.12 shows a clear plateau for $T \leq 150\,\text{mK}$, meaning that quasiparticle excitations are irrelvant for the low-temperature coherence. Ideas how to obtain a true hard gap also in TI-based JJs are being discussed in the outlook of this thesis, Chapter 6.

Turning towards the flux dependence of the etched-flake-nanowire transmons Fig. 4.3 **(c)** and **(d)** show f_{cav} and Q_{load} versus $B_\perp$. Clearly, the SQUID transmon oscillates again in frequency and imparts an oscillating dispersive shift to f_{cav}. However, this time $f_{01} < f_{\text{cav}}$ for all $B_\perp$, as the evolution of f_{cav} and Q_{load} tell: The minima of Q_{load}, i.e. the fluxes for which f_{01} is closest to f_{cav}, correspond to maxima of f_{cav}. Here, the dispersive shift on f_{cav} due to the SQUID transmon is largest, and its sign implies that $f_{01} < f_{\text{cav}}$ for the SQUID device. Comparing the minima of f_{cav} to its high-power value (dashed green line), a dispersive shift of about 1 GHz remains when the SQUID transmon is at its minimum frequency. This remaining dispersive shift could be due to the single-JJ device and would suggest $f_{01} \leq 4\,\text{GHz}$ for the single-JJ transmon.

In attempt to observe direct signatures of the two etched-flake transmons we also perform two-tone spectroscopy over a wide frequency range below f_{cav}. Figure 4.3 **(e)** shows a colorplot of the phase of the resonator response. Parts of the SQUID flux arcs are faintly visibe, in particular around its top sweetspot. Dashed white lines serve as a guide to the eye. Expecting a low SNR and a broad linewidth, the microwave source is set to its maximum output power of 25 dBm, which is why $f_{\text{cav}}/2$ and $f_{\text{cav}}/3$ show up as constant spectral lines at 4.07 GHz and 2.71 GHz, respectively.

The single-JJ transmon does not immediately show up in this colorplot. However, we measured more flux scans like the one shown in Fig. 4.3 **(c)**-**(e)** for various in-plane magnetic fields $B_\parallel$, and averaging them line-by-line for every $B_\parallel$ we find a signal at 3.7 GHz for $B_\parallel = 0$ and decreasing monotonically with $B_\parallel$ (see Fig. 4.4). We speculate this peak corresponds to the single-JJ f_{01} but cannot resolve the characteristic $f_{02}/2$ transition to further support this claim. The broad linewidth $\gtrsim 100\,\text{MHz}$ suggests again poor coherence and we may be lacking microwave power to drive $f_{02}/2$. Solving the transmon Hamiltonian for $n_g = 0$ and $n_g = 0.5$ gives the solid and dashed white lines for f_{01}, respectively, assuming a simple Fraunhofer-like $B_\parallel$-dependence of the JJs Josephson energy,

$$E_J(B_\parallel) = E_{J0}\left|\text{sinc}(B/B_{\Phi_0})\right|. \tag{4.1}$$

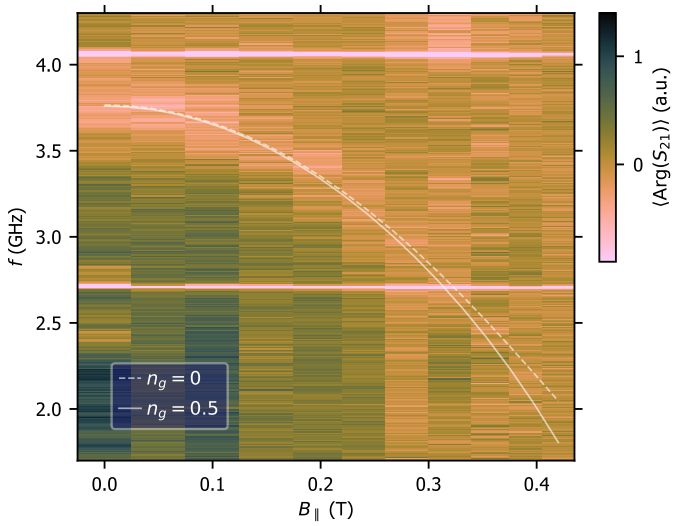

Figure 4.4: Two-tone spectroscopy as a function of magnetic field $B_\parallel$ parallel to the TI nanowire. A spectroscopic signal starting at 3.7 GHz for $B_\parallel = 0$ and decreasing monotonically with $B_\parallel$ may be attributed to the f_{01}-transition of the single-JJ transmon. Solid and dashed white lines represent model curves for $n_g = 0$ and $n_g = 0.5$ using a Fraunhofer-like $B_\parallel$-dependence of the JJs Josephson energy.

Here, E_{J0} denotes the Josephson energy at zero field, and we estimate $B_{\Phi_0} = 0.57\,\mathrm{T}$. B_{Φ_0} in this case is the in-plane field for which a fractionalized superconducting flux quantum ($= h/ne$) threads the JJ, with $n \in \mathbb{N}$. In theory, the critical current of a TI-nanowire JJ is expected to oscillate with increasing parallel magnetic field due to a number of different effects: For a periodical modulation of the topological subband structure one would expect $n = 1$ [10], for a little-Parks-like effect or Andreev-interference effects wrapping around the wire surface one would expect $n = 2$ [156, 157]. In our case, we do not see an oscillation in E_J but at best the onset of a first arc. Using the AFM data shown in Fig. 4.1 (d) we estimate the wire to be 17 nm thick and roughly 140 nm wide. Clearly then, the observed monotonic decrease of the presumed single-JJ-transmon signal is inconsistent with $n = 1$ or $n = 2$. Given that the critical field of niobium thin films typically is around 2 T to 3 T it is furthermore unlikely that the decrease is due to a decreasing superconducting gap. Higher values of n have been reported in Ref. [156] and setting $n = 3$ we obtain $B_{\Phi_0}(n = 3) \simeq 0.57\,\mathrm{T}$. It should be emphasized, however, that the presented data is not good enough to allow for more robust claims.

The two example devices shown here represent the current status of our efforts to integrate topological-insulator JJs to transmon circuits. We cooled down several more devices, experimenting with different material combinations using niobium or a bilayer of titanium/aluminum for the superconductor and BST (MBE-grown films and VLS-grown nanowires), SBS (VLS nanowires) or BSTS (exfoliated fakes) for the topological insulator. So far, the coherence of all our devices seems to be lower than what has been reported in more succesful experiments by Schmitt et al. [158] and Sun et al. [159]. The devices presented in these references are measureable both in spectroscopy and time domain and show T_1-times on the order of tens to hundreds of ns, however in the absence of any magnetic field. Measuring TI transmons in a magnetic field yet seems to pose a challenge. The device by Sun et al. for instance uses relatively thick layers of titanium and aluminum as a superconductor, which will restrict the magnetic field range severely. The TI nanowires used in [158] and [159] are moreover likely to be rather bulk-conducting, which may prevent the realization of stable MZMs. So, while these demonstrator devices generally give hope that microwave losses in TI materials can be handled, reproducible, high-coherence transmons that are resilient to magnetic fields and show signatures of

topolgical superconductivity are still lacking.

5

CONCLUSION

This study aimed to investigate to what extent transmons based on aluminum tunnel JJs can serve for readout and control of Majorana qubits. To this end, the magnetic-field dependence of spectrum and coherence times as well as the parity-switching time of aluminum transmons was measured. The measured devices were designed for enhanced magnetic field compatibility: Thin bottom and top aluminum layers of nominally 10 nm and 18 nm, respectively, gave critical fields high enough to operate the transmons in parallel magnetic fields approaching 1 T. Narrow leads to the JJ were chosen to minimize vortex losses and the transmons were placed in a three-dimensional copper cavity resonator, which is unaffected even by strong magnetic fields.

Chapter 2 focusses on measurement and analysis of the spectrum and coherence times of two devices, a single-JJ transmon and an asymmetric SQUID transmon, as a function of parallel and perpendicular magnetic fields. The results indicate that thin-film aluminum transmons can remain sufficiently coherent for qubit operation at considerable magnetic fields on the order of 1 T. To preserve coherence, accurate in-plane alignment of the magnetic field is paramount. A combination of gap suppression and a Fraunhofer-like modulation of the junction's critical current lead to a decrease in E_J, which eventually limits the experiment in two ways: First, the transmon frequency f_{01} is eventually far detuned from the cavity resonance frequency, by more than 5 GHz at the highest magnetic fields. The remaining dispersive shift on the cavity resonance frequency is tiny then, resulting in a poor SNR. Second, with decreasing $E_\mathrm{J}/E_\mathrm{C}$-ratio the transmons become more and more offset-charge sensitive, ultimately approaching the Cooper-pair-box regime. This comes with a loss in coherence as charge noise increasingly dephases the transmons. The resulting linewdith broadening further decreases the SNR and requires excessive averaging at the highest magnetic fields and broad (and hence short and high-power) microwave pulses for timedomain measurements. The situation is aggravated by the fact that we did not yet have offset-charge control via a voltage gate in Chapter 2, and slow charge drift changes f_{01} on the order of 100 MHz at the highest fields.

Clearly, these limitations can easily be overcome by improved experiment design. On the one hand, the modulation of E_J by the magnetic field can be optimized: Smaller JJ dimensions would push the characteristic field B_{Φ_0} to fields above 1 T making the Fraunhofer-like contribution to I_c less relevant. Even thinner aluminum films could moreover be used to further enhance the critical in-plane magnetic field. On the other hand, the zero-field $E_{\mathrm{J}0}$ could be chosen sufficiently high, such that f_{01} ends up

closer to the cavity resonance frequency at the target magnetic field and the device remains well in the transmon regime. One should keep in mind however, that this might result in an extended in-plane magnetic field range where the transmon f_{01} tunes through the resonator frequency.

The experimental study in Chapter 2 also demonstrates, that the operation of a SQUID transmon remains possible even in large in-plane magnetic fields. This is relevant for the Hassler and Hyart proposals introduced in Chapter 1. However, our findings suggest that vibrations of the magnet relative to the sample and noise from magnet current sources could become a limiting factor, when operating the SQUID transmon away from its top or bottom flux sweetspot. These challenges seem solvable with better vibrational damping of the dilution refrigerator and the use of persistent current magnets. Magnetic-field-resilient SQUID transmons can be used to elucidate the microscopic origins of on-chip flux noise in superconducting circuits, too. Performing a sensitivity analysis of the pure echo dephasing $\Gamma_{\phi}^{\mathrm{echo}}$ on the transmon frequency we had to discover, however, that our data is agnostic to this matter, likely because T_2^{echo} is limited by photon shot noise in the resonator.

An open question that remains to be addressed are extended magnetic-field regions of incoherence in which the transmon devices appear to be very jumpy and hard to measure. Along the $B_{\parallel,1}$ axis we observe this effect only in a limited field range from 0.4 T to 0.5 T, but along $B_{\parallel,2}$ the entire field range seems to be affected. Our current hypothesis is that the regions of incoherence are caused by large and ill-defined spurious JJs that form during shadow evaporation in the transmon leads and pads. Manhattan-style JJs [78] may therefore help to overcome this issue.

Chapter 3 shows measurements of the parity-switching time of an asymmetric SQUID transmon as a function of magnetic field and temperature. A comprehensive model consistently describes both the field and temperature dependence and helps to distinguish relevant parity-switching mechanisms. The model assumes Cooper-pair-breaking photons as a generation mechanism for quasiparticles and accounts for different superconducting gaps to both sides of the JJs and the Fraunhofer effect in the JJs to modulate the quasiparticle tunneling rates with $B_{\parallel}$. The results provide evidence for a changing dominant contribution to the parity-switching rate as the magnetic field increases: While photon-assisted parity switching (PAPS) dominates for higher fields, number-conserving parity switching (NUPS) processes $\Gamma_{\mathrm{qp}}^{01}$ and $\Gamma_{\mathrm{qp}}^{10}$ that excite or relax the transmon to bridge the superconducting-gap difference $\delta\Delta$ are resonantly enhanced around zero field as $hf_{01} \simeq \delta\Delta$. The top aluminum layer being about twice as thick as the bottom aluminum layer implies different superconducting gaps in the two layers, and hence to both sides of the JJs. Having chosen thin aluminum layers for magnetic field resilience this difference is comparable to the transmon transition energy hf_{01} introduces enhanced quasiparticle tunneling. The magnetic field gradually lifts this resonance condition and hence increases the parity-switching time until for fields $B_{\parallel} > 0.2\,\mathrm{T}$ photon-assisted parity switching starts to dominate, with rates modulated by the Fraunhofer effect.

The improved understanding of what is limiting our parity-switching times and how these processes evolve with an applied magnetic field paves the way for robust parity readout of topological MZM-based qubits using Al/AlO_x/Al JJ circuits. Already now, the required magnetic fields do not cause quasiparticle tunneling to limit the coherence of the Al/AlO_x/Al JJ circuits themselves. However, with the quasiparticle poisoning time setting the ultimate limit on the lifetime of a topological MZM-based qubit it is still worth to increase τ_{p}. Both PAPS and NUPS contributions to quasiparticle tunneling can be reduced by optimizing the device design and improving on the setup. For NUPS, the resonance condition $f_{01} \simeq \delta\Delta$ can be avoided by using even more asymmtric gaps, i.e. making the bottom film even thinner, or

by targeting f_{01} for a given field range. For PAPS, pair-breaking radiation can be reduced with better filtering of our microwave lines. In the experiment presented in Chapter 3, while filtering the input line with an Eccosorb filter we did not install a filter on the output line to not decrease the signal level. However, newly-available lowpass filters can cut signals above 80 GHz by more than 60 dB, leaving the signal level at the cavity frequency unchanged. Consequently, the PAPS contribution to parity switching should be orders of magnitude lower upon installation of such a filter. With a reduction of both PAPS and NUPS we expect an increase of τ_{p} by orders of magnitude.

Concluding on the outset question, whether transmons based on aluminum tunnel JJs can serve for readout and control of future Majorana qubits, the answer is hence affirmative. Al/AlO_x/Al JJ circuits are a viable option for parity readout of topological qubits. The required magnetic fields do not inhibit the coherent transmon operation, enabling single-shot measurements of the transmon parity at considerable magnetic fields. The parity lifetime in the devices presented here would be sufficiently high to allow for a demonstration of braiding operations, e.g. in a device as proposed by Hyart et al. [24].

Clearly then, the long-term goal is to integrate the here explored magnetic-field-resilient transmon circuits with topological-superconductor nanowires hosting MZMs. In particular, Josephson junctions made from such nanowires may form an important building block for topological quantum computing, and given the expertise in topological-insulator materials within our group, we focus on TI-based JJs here. Chapter 4 shows the current status of our parallel research effort to integrate TI-based JJs to transmon circuits. We experimented with different material combinations using niobium or a bilayer of titanium/aluminum for the superconductor and BST (MBE-grown films and VLS-grown nanowires), SBS (VLS nanowires) or BSTS (exfoliated fakes) for the topological insulator. None of the devices we measured so far was coherent enough to be well within the strong-coupling regime. Notably, in our case the TI-based transmons act as a sink for resonator photons leading to a drastic reduction of the cavity Q-factor upon resonance via the inverse Purcell decay. This prevents unambiguous spectroscopic measurements of the transmon frequencies, let alone time-domain measurements of the transmon coherence times.

To illustrate this effect, Chapter 4 shows data on two specific device chips, one containing a single Nb/BST VLS nanowire SQUID transmon and the other one containing two NB/BSTS etched-flake nanowire transmon at once. Of the latter, one is a single-JJ transmon and one is a SQUID transmon. The VLS nanowire transmon crosses the cavity resonance frequency, when tuning the perpendicular flux through the SQUID loop. However, the data do not show a clear avoided crossing which would be characteristic for the stong-coupling regime. Instead, the dispersive shift on f_{cav} due to the transmon mode gradually changes sign and f_{cav} evolves smoothly from a negatively-shifted to a positively-shifted frequency, with a reduction of Q_{load} by one order of magnitude right at the crossing. The remaining $Q_{\mathrm{load}} \simeq 100$ suggests a transmon linewidth of more than 83 MHz, which is the estimate for infinite coupling g. For the etched-flake transmons $f_{01} < f_{\mathrm{cav}}$ for both devices, but also here Q_{load} decreases when the SQUID f_{01} is close to f_{cav}. However, the devices may be slightly more coherent than the VLS device: A low-temperature increase in Q_{load} suggests that parallel resistive channels due to a soft induced gap are gradually being gapped out. Also, attempts to observe the f_{01}-transition of both devices in two-tone spectroscopy may have seen success but remain somewhat speculative.

6

OUTLOOK

Future plans encompass improvements of setup and aluminum JJs on the one hand and the succesful, low-loss integration of topological-superconductor nanowires on the other hand.

For the setup, we have already taken measures to further improve on our overall SNR and the level of pair-breaking radiation since completing the measurements for this thesis: We installed and tested a magnetic-field-compatible traveling wave parametric amplifier [35] and we added newly-available HERD-1 lowpass filters from Sweden Quantum to both our input and output line which cut signals above 80 GHz by more than 60 dB. Previously, we only had one Eccosorb filter on the input line but left the output line unfiltered to not decrease the signal level. As our findings in Chapter 3 suggest that our parity-switching time for $B_\parallel \geq 0.2\,\mathrm{T}$ is limited by Cooper-pair breaking radiation we expect a drastic improvement in the parity switching time.

To further improve on aluminum JJs, we plan to use even thinner aluminum films and smaller geometric footprints of the JJs. The former will increase B_c and the latter will push B_{Φ_0} to higher magnetic fields. As mentioned in Chapter 2 we suspect the large spurious JJs that form in the shadow evaporation process in transmon leads and pads to cause the transmon incoherence for fields along the $B_{\parallel,2}$-axis as well as in the $B_{\parallel,1}$-range from 0.4 T to 0.5 T. To avoid large and ill-defined spurious JJs due to shadow evaporation we are transitioning to Manhattan-style JJs [78], and fabricate leads and pads of a single layer of Niobium or Aluminum. It is yet to be confirmed, whether this solves the problem of incoherent field regions.

More interesting and at the same time more challenging is the integration of topological-superconductor nanowires to magnetic-field-resilient transmons to find signatures of MZMs. The remainder of this chapter discusses ideas to reduce losses in topological-insulator nanowire JJs on the one hand. On the other hand, it proposes devices that make use of Al/AlO_x/Al-JJs as much as they can, and may still show signatures of MZMs in spectrum and time-domain measurements.

The key challenge in integrating JJs based on TI nanowires to transmon circuits is to reduce and mitigate microwave losses. The origins of a finite sub-gap resistance in SNS JJs are not fully understood. Possible culprits are contact transparency, charge disorder and anti-proximity effects [160].

A systematic approach to optimizing the fabrication recipes for TI JJs with respect to their microwave properties comprises both an assessment of the material combinations and the involved fabrication steps. In our previous attempts to fabricate and measure transmons comprising TI JJs we already

experimented with different material combinations (Nb/BST, Nb/SBS, Nb/BSTS, Al/Ti/BST, Al/Ti/BSTS) and growth platforms (MBE-grown film, VLS nanowire, exfoliated (etched) flake). However, due to the numerous possible combinations we usually measured only one or few batches of samples of the same type. While we usually find a superconducting transition in most of these combinations in DC measurements, it is not clear yet how the fabrication steps can be optimized to reduce microwave losses. Contrary to RF measurements, DC measurements are blind to parallel resistive channels in the JJ. The minimum level of coherence required to quantify losses in transmon measurements meaningfully is rather high, however, and as shown in Chapter 4 our device quality is not yet sufficient to rigorously quantify their coherence. To systematically optimize fabrication recipes for microwave coherence, therefore, measurements of a 2D superconducting resonator shorted to ground via a TI JJ may be better suited. An experiment design similar to the one shown in Ref. [160] offers simultaneous DC and RF access and allows to quantify the sub-gap resistance in a JJ.

Possibly, in-situ interfaces between superconductor and topological insulator could provide a boost in coherence. For semiconductor nanowires, hard gaps were achieved by epitaxial in-situ growth of the superconductor on top of the semiconductor nanowire [161] pushing transmon coherence times to microsecond level [39]. In our lab, two promising in-situ interfaces can be realized, both of which have not been tested in microwave measurements yet: One is a self-epitaxy technique discovered when contacting BST thin films with Pd, resulting in a self-formation of the $PdTe_2$ superconductor by diffusion [162, 163]. The other one is an in-situ Argon etch of a BSTS flake with subsequent deposition of the superconductor into the etched features [164]. The latter can be done in our Plassys E-beam evaporator to create an Al/Ti/BSTS interface without breaking the vacuum. Both platforms offer another advantage, they both form a sandwich SNS JJ instead of more indirect SS'NS'S JJ. Andreev reflections then happen directly between the native superconductor leads, which might help to induce a hard gap in the JJ.

A concrete device proposal building on the technique to etch and laterally contact a BSTS flake in-situ is shown in Fig. 6.1. First, a laterally contacted flake nanowire is defined by etching and in-situ depositing superconductor (top-view in Fig. 6.1 **(a)**). Next, the part of the flake that is outside the superconducting electrodes is being etched, and the laterally-contacted nanowire is patterned into two segments connected by a constriction junction of remaining BSTS (Fig. 6.1 **(b)**). In a third step, a Manhattan-style Al/AlO_x/Al JJ is fabricated in parallel to the constriction junction. Together, the constriction and the Manhattan-style Al/AlO_x/Al JJ form the transmon's Josephson inductance (Fig. 6.1 **(c)**). Intriguingly, the technique to etch and laterally contact the flake is not used to define the transmon's Josephson junction. Rather, it is used to form nanowires that are being well-proximitized from two sides and moreover allow to phase-bias the nanowire with out-of-plane magnetic fields via an RF-SQUID geometry. The latter gives an additional tuning knob to tune the wire into a topological regime, next to applying magnetic field in parallel to the wire. In the topological regime, MZMs form at the ends of the topological-superconductor nanowire. The two center-most MZMs may interact via the constriction junction, giving rise to coherent tunneling of single electrons, as discussed in Chapter 1.

The device offers a number of advantages over the TI-based transmon devices presented in Chapter 4. In-situ interfaces between TI and superconductor hopefully lead to a hard induced gap in the TI nanowire. The more coherent device by Schmitt et al. for instance is fabricated in an all-in-situ process [158], which may enable higher interface quality between superconductor and TI. The constriction JJ can be made very narrow, and assuming that the microwave losses scale with the size of an SNS JJ

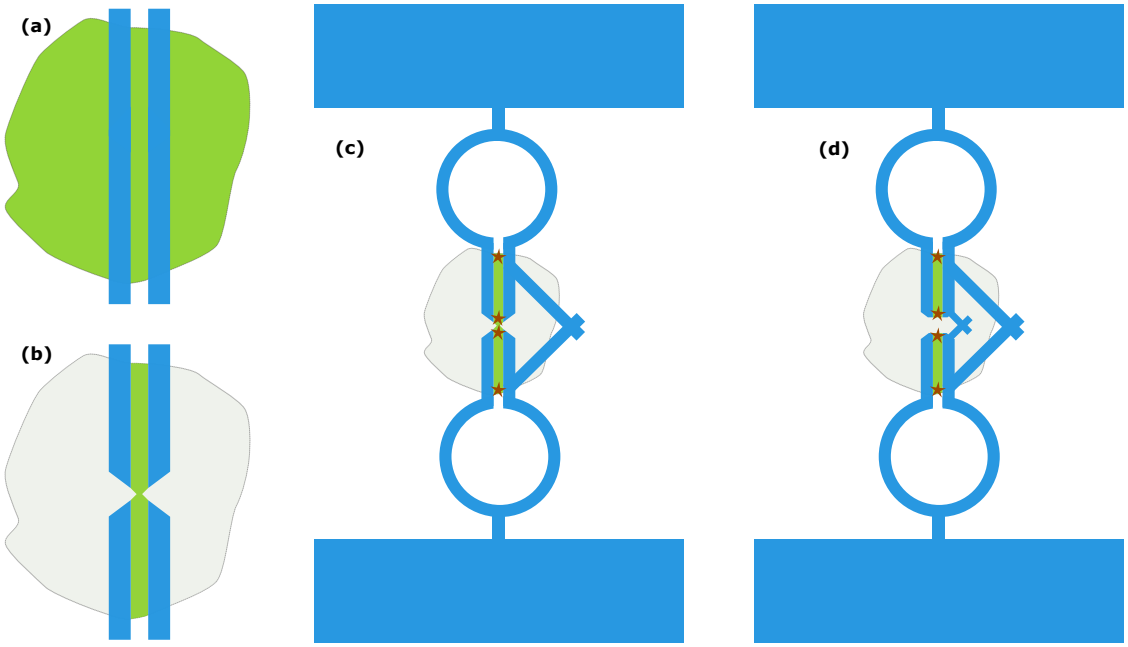

Figure 6.1: Proposal of a laterally contacted etched-flake-nanowire transmon. **(a)** Top view of a BSTS flake (green). In a single in-situ step trenches are etched into the flake and the trenches are filled with superconductor (blue). **(b)** In a next step, the outer parts of the flake are removed and a constriction junction is defined. **(c)** In a third step, a Manhattan-style Al/AlO_x/Al JJ is fabricated in parallel to the constriction junction. Together, constriction junction and Al/AlO_x/Al JJ form the flux-tuneable Josephson inductance of a transmon. An RF-SQUID geometry on the flake contacts furthermore enables phase-biasing the nanowires. Consequently, they can be tuned to a topological regime using both out-of-plane magnetic fields $B_\perp$ and magnetic fields $B_\parallel$ parallel to the wire. In the topological regime, the wire ends host MZMs (brown stars), of which the innermost may couple via the constriction junction. **(d)** The constriction junction is replaced by another Al/AlO_x/Al JJ very close to MZMs. The expected coupling of the innermost MZMs is tiny, but may be detectable in time-resolved measurements of the transmon parity (see Fig. 6.2).

this should further reduce microwave losses. Also the critical current accross the constriction junction should scale with the size of the constriction (although it may still vary wildly from sample to sample at a given constriction size). Hence, I_c is expected to be rather small across the constriction junction. Labeling E_{Ja} the Josephson energy of the constriction junction and E_{Jb} that of the aluminum JJ, we then have $E_{Ja} \ll E_{Jb}$. The parallel Al/AlO_x/Al JJ will then give the dominant contribution to the total transmon $E_J = E_{Ja} + E_{Jb}$ and can hence be used to target E_J reliably. Moreover, for $E_{Ja} \ll E_{Jb}$ the flux-dependence of E_J is dominated by the current-phase relationship of E_{Ja} [165], which is an interesting property to study even in the absence of MZMs. Controlling the topological regime by both the parallel magnetic field and a perpendicular magnetic flux through the phase-bias loops should furthermore help to unambiguously identify a topological regime. Clearly, any signal pointing to a topological phase for a given $B_\parallel$ should be periodic as a function of flux through the phase-bias loops. Ideally, the two phase-bias loops and the SQUID loop can all be controlled by separate flux lines. Concluding the list of merits, the proposed device is relatively easy to fabricate with established recipes for all individual components.

The idea of minimizing the constriction can be taken to its extreme, i.e. a disconnect. Then, a second Al/AlO_x/Al JJ may be fabricated as close by as possible, as shown in Fig. 6.1 **(d)**. In this situation, a small overlap of the two MZMs that are closest to the JJ may remain: In a superconductor, the quasiparticle wavefunctions of MZMs decay exponentially with a decay length $s_0 \sim \hbar/\sqrt{2 * m_{\text{eff}} * \Delta}$,

$$E_M(s) = E_M(0) exp(-s/s_0). \tag{6.1}$$

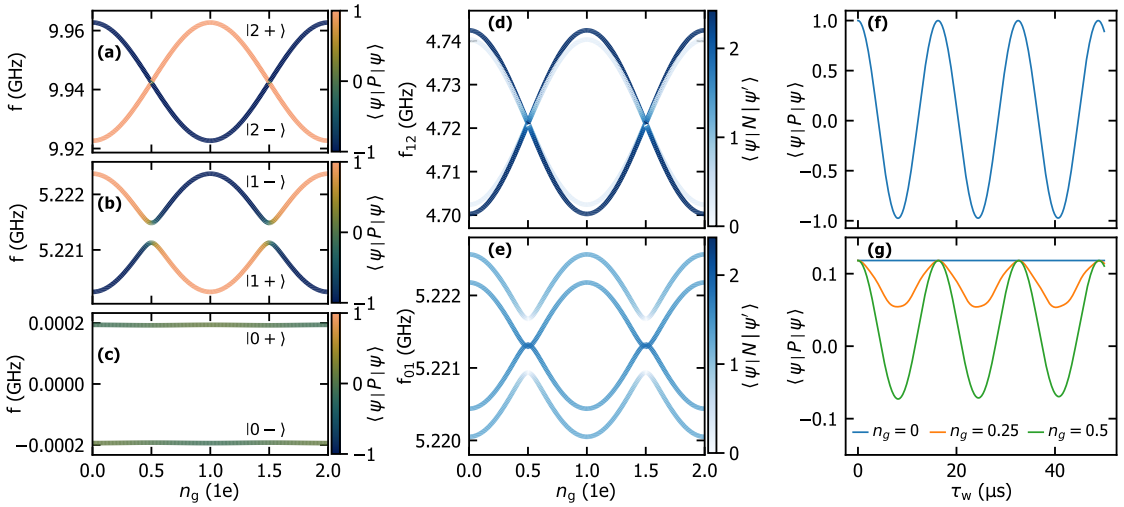

Figure 6.2: Simulation of Rabi-like oscillations in the transmon parity. **(a)**-**(c)** Hybridized levels $E_2^{\pm}/h$, $E_1^{\pm}/h$ and $E_0^{\pm}/h$ as a function of n_g for $E_J = 10\,\text{GHz}$, $E_C = 0.4\,\text{GHz}$ and $E_M = 200\,\text{kHz}$. The ground states $E_0^{\pm}$ are strongly parity-hybridized but higher levels are barely parity-hybridized and can therefore form a transmon-parity meter. The respective energy transition frequencies **(d)** f_{12} and **(e)** f_{01} as a function of n_g are colored by their spectral weight. The expected splittings of $E_M \leq 200\,\text{kHz}$ will be barely resolveable in two-tone spectroscopy. However, oscillations of the transmon parity are then slow enough to be detectable in subsequent parity measurements separated by a waiting time τ_w **(f)**. Depending on the specific groundstate that is attained after the initial parity projection at $\tau_w = 0$, a variant of the experiment is proposed, where n_g is pulsed to $0.5e$ during the waiting time (see text).

Here, s is the distance between the end of a topological-superconductor nanowire and the Al/AlO_x/Al JJ. $E_M(0)$ is the coupling of a fully hybridized pair of MZMs in the short-junction limit, and it is expected to be of the order of the proximity-induced gap in the TI wire [166], i.e. $E_M(0)/h \sim 30\,\text{GHz}$ [155]. The estimate further assumes the superconducting gap to be similar to the ones reported in Chapter 3, $\Delta/\hbar = 54\,\text{GHz}$, and the effective mass of quasiparticles to be similar to that of metallic Al, which is roughly the mass of an electron, $m_{\text{eff}} \sim m_e$ [167]. For a feasible distance s of 150 nm to 200 nm we can then estimate $E_M(s)$ to be on the order of tens to hundreds of kHz.This is likely not enough to be resolvable in transmon spectroscopy, assuming similar transmon coherence to the data shown in Chapters 2 and 3. However, the small but finite overlap still introduces coherent tunneling of single electrons from one transmon island to the other at a rate $\propto E_M(s)$. This should introduce Rabi-like oscillations in the transmon parity which may be detectable in time-resolved measurements of the transmon parity. The idea here is, to measure the transmon parity at a time t_0, wait a time τ_w and then measure again. Post-selecting the data on the initial parity-measurement at t_0 the expectation value of the parity operator should oscillate with τ_w.

Figure 6.2 simulates the proposed measurement. Here, $E_J = 10\,\text{GHz}$, $E_C = 0.4\,\text{GHz}$ and $E_M = 200\,\text{kHz}$. The value of E_M is chosen such that it is barely resolvable in spectroscopy, but the sampling rate of successive parity measurements, which is on the order of 1 μs, is just sufficient to resolve an oscillation of the transmon parity. In that sense, it describes a transition regime from spectroscopic measurements to time-resolved measurements of the transmon parity: If E_M is larger, spectroscopic measurements can directly resolve E_M. If E_M is smaller, time-resolved transmon-parity measurements should provide robust information on E_M down to a rate bounded by the quasiparticle poisoning rate. The latter is on the order of kHz in our measurements presented in Chapter 3, but may be reduced down to Hz-level with improved filtering and device design. Figure 6.2 **(a)**-**(c)** show the hybridized levels $E_2^{\pm}/h$, $E_1^{\pm}/h$ and $E_0^{\pm}/h$ for the given values of E_J, E_C and E_M. As in the introductory Chapter 1, the levels are

color-coded by the expectation value of the transmon-parity operator, $-1 \leq \langle\Psi|\,\hat{P}\,|\Psi\rangle \leq +1$, where -1 corresponds to "odd" transmon parity and $+1$ to "even" transmon parity. While the ground states $E_0^{\pm}$ are strongly parity-hybridized, the transmon parity is well-defined for higher levels. Similar to the parity measurements presented in Chapter 3 one could therefore use the $(E_2^{\pm} - E_1^{\pm})/h$-transitions (Fig. 6.2 **(d)**) to build a transmon-parity meter, at $n_g = 0$. There is however a subtlety to consider: After an initial projective measurement of the transmon parity using the higher levels, the transmon needs to be pulsed back to the ground states for the free evolution time τ_w to prevent transmon relaxation during τ_w. Alas, it is not immediately straightforward if the Majorana transmon can be pulsed to a parity-conserving groundstate level, i.e. an "even" superposition $|0,e\rangle = \alpha_e\,|0+\rangle + \beta_e\,|0-\rangle$ or an "odd" superposition $|0,o\rangle = \alpha_o\,|0+\rangle + \beta_o\,|0-\rangle$. Suppose the initial parity measurement projects the Majorana transmon state onto $|1,e\rangle \simeq |1-\rangle\,(n_g = 0)$. Calculating the transition dipole moments $d_1 = \langle 1,e||\hat{D}||0,e\rangle$, $d_2 = \langle 1,e||\hat{D}||0-\rangle$, $d_2 = \langle 1,e||\hat{D}||0+\rangle$ and $d_4 = \langle 1,e||\hat{D}||0,o\rangle$ we find $d_1 > d_2 > d_3 > 3 \gg d_4$, motivating two variants of the measurement: Driving the the Majorana transmon from $|1,e\rangle$ to $|0,e\rangle$ after the initial projective parity measurement we can simply let the system evolve freely for a time τ_w, pulse back and project again. The expectation value of the parity operator should show clear Rabi-like oscillations, as illustrated in Fig. 6.2 **(f)**. Here, an expected dampening of the oscillation amplitude, e.g. due to quasiparticle poisoning, is neglected. If instead the Majorana transmon is driven to $|0,\pm\rangle$ after the initial projective parity measurement parity oscillations may still be detectable setting $n_g = 0.5e$ during τ_w. The degree of parity hybridization varies with n_g and hence an adiabatic pulsing to the point of maximum hybridization with subsequent projective parity measurement results in an oscillation of the expectation value of the parity operator, too. Figure 6.2 **(g)** shows expected oscillations for different set points of n_g during τ_w. The contrast of the oscillation depends on the ratio E_M/E_C: if $E_M \ll E_C$ the parity hybridization varies more strongly with n_g due to a more pronounced charge dispersion.

Exciting prospects hence lie ahead. Magnetic-field resilient transmons based on thin-film aluminum JJs do not only provide useful control JJs to circuits designed for the detection and manipulation of MZMs. The idea to avoid TI-based JJs at all and instead build on a tiny E_M that is mediated by a near-by Al/AlO_x/Al-JJ and leads to detecteable oscillations of the transmon parity is the most direct continuation of this thesis and it may help tracking down the elusive Majorana fermion even if the bad coherence properties of TI-based JJs persist.

ACKNOWLEDGEMENTS

I would like to thank:

Chris, for teaching me all the practical knowledge about cQED, and for spending long day and night shifts together in an always patient and enjoyable atmosphere.

Yoichi for giving me the chance to do my PhD in a very exciting field of physics using state-of-the-art technologies and lab facilities.

Luc, for being a great team player and helping me out on various occasions, for sharing device-fabrication skills and for enjoying nice bike rides together.

Junya, **Oliver**, and **Jakob** for very helpful physics and nanofabrication discussions and (joint) device fabrication of TI transmons.

My further AG Ando fellows **Linh**, **Roozbeh**, **Matthias**, **Gertjan**, **Anjana**, **Ella**, **Priya**, **Felix**, **Elmore**, **Michel**, **Adrian**, **Alexey**, **Jens**, **Andrea**, **Cornelius**, **Manushi**, **Bibek**, **Esteban**, **Yongjian**, **Sweta**, and **Poojitha** for exchanging helpful insights and growing together as a team, for keeping up the team spirit in long meetings with good memes, for board game nights, bouldering and a lot of fun at conferences and retreats.

The **football all-star teams** of AG Ando and AG Bocquillon for great matches—I hope I am still entitled to join in frequently in future matches?

Harald and **Carmen** for helping with any organization-related issues and **Timur** for uncomplicated and quick help help with machined parts and technical issues.

My band **RasgaRasga**: **Luki**, **Felix**, **Gregor**, **Daria**, **Dung**, **Benni**, **Wolfi**, and **Julian**—touring with you and working together creatively on new songs is a wonderful balance to my scientific work.

Marina, I would like to thank you for your ever solidary support through all the ups and downs of my PhD. Sharing this special period of our lives together is unforgettable.

REFERENCES

[1] A.Yu. Kitaev. "Fault-tolerant quantum computation by anyons". In: *Annals of Physics* 303.1 (2003), pp. 2–30. ISSN: 0003-4916. DOI: https://doi.org/10.1016/S0003-4916(02)00018-0. URL: https://www.sciencedirect.com/science/article/pii/S0003491602000180.

[2] Chetan Nayak, Steven H Simon, Ady Stern, Michael Freedman, and Sankar Das Sarma. "Non-Abelian anyons and topological quantum computation". In: *Rev. Mod. Phys.* 80.3 (2008), p. 1083.

[3] Jason Alicea. "New directions in the pursuit of Majorana fermions in solid state systems." In: *Rep. Prog. Phys.* 75.7 (July 2012), p. 076501. ISSN: 1361-6633.

[4] Liang Fu and C. L. Kane. "Superconducting Proximity Effect and Majorana Fermions at the Surface of a Topological Insulator". In: *Phys. Rev. Lett.* 100 (9 Mar. 2008), p. 096407. DOI: 10.1103/PhysRevLett.100.096407. URL: https://link.aps.org/doi/10.1103/PhysRevLett.100.096407.

[5] Jay D. Sau, Roman M. Lutchyn, Sumanta Tewari, and S. Das Sarma. "Generic New Platform for Topological Quantum Computation Using Semiconductor Heterostructures". In: *Phys. Rev. Lett.* 104 (4 Jan. 2010), p. 040502. DOI: 10.1103/PhysRevLett.104.040502. URL: https://link.aps.org/doi/10.1103/PhysRevLett.104.040502.

[6] Jason Alicea. "Majorana fermions in a tunable semiconductor device". In: *Physical Review B* 81.12 (Mar. 2010). ISSN: 1550-235X. DOI: 10.1103/physrevb.81.125318. URL: http://dx.doi.org/10.1103/PhysRevB.81.125318.

[7] Yuval Oreg, Gil Refael, and Felix von Oppen. "Helical Liquids and Majorana Bound States in Quantum Wires". In: *Phys. Rev. Lett.* 105 (17 Oct. 2010), p. 177002. DOI: 10.1103/PhysRevLett.105.177002. URL: https://link.aps.org/doi/10.1103/PhysRevLett.105.177002.

[8] Roman M. Lutchyn, Jay D. Sau, and S. Das Sarma. "Majorana Fermions and a Topological Phase Transition in Semiconductor-Superconductor Heterostructures". In: *Phys. Rev. Lett.* 105 (7 Aug. 2010), p. 077001. DOI: 10.1103/PhysRevLett.105.077001. URL: https://link.aps.org/doi/10.1103/PhysRevLett.105.077001.

[9] A Yu Kitaev. "Unpaired Majorana fermions in quantum wires". In: *Physics-Uspekhi* 44.10S (Oct. 2001), p. 131. DOI: 10.1070/1063-7869/44/10S/S29. URL: https://dx.doi.org/10.1070/1063-7869/44/10S/S29.

[10] A. Cook and M. Franz. "Majorana fermions in a topological-insulator nanowire proximity-coupled to an *s*-wave superconductor". In: *Phys. Rev. B* 84 (20 Nov. 2011), 201105(R). URL: https://link.aps.org/doi/10.1103/PhysRevB.84.201105.

[11] Martin Leijnse and Karsten Flensberg. "Introduction to topological superconductivity and Majorana fermions". In: *Semiconductor Science and Technology* 27.12 (Nov. 2012), p. 124003. ISSN: 1361-6641. DOI: 10.1088/0268-1242/27/12/124003. URL: http://dx.doi.org/10.1088/0268-1242/27/12/124003.

[12] D. A. Ivanov. "Non-Abelian Statistics of Half-Quantum Vortices in *p*-Wave Superconductors". In: *Phys. Rev. Lett.* 86 (2 Jan. 2001), pp. 268–271. DOI: 10.1103/PhysRevLett.86.268. URL: https://link.aps.org/doi/10.1103/PhysRevLett.86.268.

[13] Alexandre Blais, Ren-Shou Huang, Andreas Wallraff, S. M. Girvin, and R. J. Schoelkopf. "Cavity quantum electrodynamics for superconducting electrical circuits: An architecture for quantum computation". In: *Phys. Rev. A* 69 (6 June 2004), p. 062320. DOI: 10.1103/PhysRevA.69.062320. URL: http://link.aps.org/doi/10.1103/PhysRevA.69.062320.

[14] Serge Haroche and Jean-Michel Raimond. *Exploring the Quantum: Atoms, Cavities, and Photons*. Oxford University Press, Aug. 2006. ISBN: 9780198509141. DOI: 10.1093/acprof:oso/9780198509141.001.0001. URL: https://doi.org/10.1093/acprof:oso/9780198509141.001.0001.

[15] Alexandre Blais, Arne L. Grimsmo, S. M. Girvin, and Andreas Wallraff. "Circuit quantum electrodynamics". In: *Rev. Mod. Phys.* 93 (2 May 2021), p. 025005. DOI: 10.1103/RevModPhys.93.025005. URL: https://link.aps.org/doi/10.1103/RevModPhys.93.025005.

[16] Jens Koch et al. "Charge-insensitive qubit design derived from the Cooper pair box". In: *Phys. Rev. A* 76 (4 Oct. 2007), p. 042319. DOI: 10.1103/PhysRevA.76.042319. URL: https://link.aps.org/doi/10.1103/PhysRevA.76.042319.

[17] M. Tinkham. *Introduction to Superconductivity*. 2nd. Dover Publications, 2004.

[18] J. Krause, G. Marchegiani, L.M. Janssen, G. Catelani, Yoichi Ando, and C. Dickel. "Quasiparticle effects in magnetic-field-resilient three-dimensional transmons". In: *Phys. Rev. Appl.* 22 (4 Oct. 2024), p. 044063. DOI: 10.1103/PhysRevApplied.22.044063. URL: https://link.aps.org/doi/10.1103/PhysRevApplied.22.044063.

[19] S. Diamond et al. "Distinguishing Parity-Switching Mechanisms in a Superconducting Qubit". In: *PRX Quantum* 3 (4 Oct. 2022), p. 040304. DOI: 10.1103/PRXQuantum.3.040304. URL: https://link.aps.org/doi/10.1103/PRXQuantum.3.040304.

[20] P. Joyez, P. Lafarge, A. Filipe, D. Esteve, and M. H. Devoret. "Observation of parity-induced suppression of Josephson tunneling in the superconducting single electron transistor". In: *Phys. Rev. Lett.* 72 (15 Apr. 1994), pp. 2458–2461. DOI: 10.1103/PhysRevLett.72.2458.

[21] J. Aumentado, Mark W. Keller, John M. Martinis, and M. H. Devoret. "Nonequilibrium Quasiparticles and 2*e* Periodicity in Single-Cooper-Pair Transistors". In: *Phys. Rev. Lett.* 92 (6 Feb. 2004), p. 066802. DOI: 10.1103/PhysRevLett.92.066802.

[22] R. M. Lutchyn, L. I. Glazman, and A. I. Larkin. "Kinetics of the superconducting charge qubit in the presence of a quasiparticle". In: *Phys. Rev. B* 74 (6 Aug. 2006), p. 064515. DOI: 10.1103/PhysRevB.74.064515.

[23] F Hassler, A R Akhmerov, and C W J Beenakker. "The top-transmon: a hybrid superconducting qubit for parity-protected quantum computation". In: *New J. Phys.* 13.9 (Sept. 2011), p. 095004. ISSN: 1367-2630. URL: https://doi.org/10.1088/1367-2630/13/9/095004.

[24] T. Hyart, B. van Heck, I. C. Fulga, M. Burrello, A. R. Akhmerov, and C. W. J. Beenakker. "Flux-controlled quantum computation with Majorana fermions". In: *Phys. Rev. B* 88 (3 July 2013), p. 035121. DOI: 10.1103/PhysRevB.88.035121. URL: http://link.aps.org/doi/10.1103/PhysRevB.88.035121.

[25] F Hassler, A R Akhmerov, C-Y Hou, and C W J Beenakker. "Anyonic interferometry without anyons: how a flux qubit can read out a topological qubit". In: *New Journal of Physics* 12.12 (Dec. 2010), p. 125002. DOI: 10.1088/1367-2630/12/12/125002. URL: https://dx.doi.org/10.1088/1367-2630/12/12/125002.

[26] Eran Ginossar and Eytan Grosfeld. "Microwave transitions as a signature of coherent parity mixing effects in the Majorana-transmon qubit". In: *Nat. Commun.* 5 (Sept. 2014), p. 4772. DOI: 10.1038/ncomms5772.

[27] Konstantin Yavilberg, Eran Ginossar, and Eytan Grosfeld. "Fermion parity measurement and control in Majorana circuit quantum electrodynamics". In: *Phys. Rev. B* 92 (7 Aug. 2015), p. 075143. DOI: 10.1103/PhysRevB.92.075143. URL: https://link.aps.org/doi/10.1103/PhysRevB.92.075143.

[28] J. Ávila, E. Prada, P. San-Jose, and R. Aguado. "Superconducting islands with topological Josephson junctions based on semiconductor nanowires". In: *Phys. Rev. B* 102 (9 Sept. 2020), p. 094518. DOI: 10.1103/PhysRevB.102.094518. URL: https://link.aps.org/doi/10.1103/PhysRevB.102.094518.

[29] J. Ávila, E. Prada, P. San-Jose, and R. Aguado. "Majorana oscillations and parity crossings in semiconductor nanowire-based transmon qubits". In: *Phys. Rev. Res.* 2 (3 Sept. 2020), p. 033493. DOI: 10.1103/PhysRevResearch.2.033493. URL: https://link.aps.org/doi/10.1103/PhysRevResearch.2.033493.

[30] C. W. J. Beenakker. "Universal limit of critical-current fluctuations in mesoscopic Josephson junctions". In: *Phys. Rev. Lett.* 67.27 (Dec. 1991), pp. 3836–3839. DOI: 10.1103/PhysRevLett.67.3836. URL: http://link.aps.org/doi/10.1103/PhysRevLett.67.3836 (visited on 11/22/2013).

[31] Rolf Landauer. "Information is Physical". In: *Physics Today* 44.5 (May 1991), pp. 23–29. ISSN: 0031-9228. DOI: 10.1063/1.881299. eprint: https://pubs.aip.org/physicstoday/article-pdf/44/5/23/8304036/23_1_online.pdf. URL: https://doi.org/10.1063/1.881299.

[32] François Mallet, Florian R. Ong, Agustin Palacios-Laloy, François Nguyen, Patrice Bertet, Denis Vion, and Daniel Esteve. "Single-shot qubit readout in circuit quantum electrodynamics". In: *Nat. Phys.* 5 (2009), pp. 791–795.

[33] R. Vijay, D. H. Slichter, and I. Siddiqi. "Observation of quantum jumps in a superconducting artificial atom". In: *Phys. Rev. Lett.* 106 (2011), p. 110502. ISSN: 0031-9007.

[34] T. Walter et al. “Rapid High-Fidelity Single-Shot Dispersive Readout of Superconducting Qubits”. In: *Phys. Rev. Appl.* 7 (5 May 2017), p. 054020. DOI: 10.1103/PhysRevApplied.7.054020. URL: https://link.aps.org/doi/10.1103/PhysRevApplied.7.054020.

[35] L.M. Janssen et al. “Magnetic field dependence of a Josephson traveling-wave parametric amplifier and integration into a high-field setup”. In: *Phys. Rev. Appl.* 22 (5 Nov. 2024), p. 054018. DOI: 10.1103/PhysRevApplied.22.054018. URL: https://link.aps.org/doi/10.1103/PhysRevApplied.22.054018.

[36] Morteza Aghaee et al. *Interferometric Single-Shot Parity Measurement in an InAs-Al Hybrid Device*. 2024. arXiv: 2401.09549 [cond-mat.mes-hall].

[37] A. Wallraff et al. “Strong coupling of a single photon to a superconducting qubit using circuit quantum electrodynamics”. In: *Nature* 431 (2004), pp. 162–167.

[38] J. G. Kroll et al. “Magnetic field compatible circuit quantum electrodynamics with graphene Josephson junctions”. In: *Nat Commun* 9.1 (2018), p. 4615. URL: https://www.nature.com/articles/s41467-018-07124-x.

[39] F. Luthi et al. “Evolution of Nanowire Transmon Qubits and Their Coherence in a Magnetic Field”. In: *Phys. Rev. Lett.* 120 (10 Mar. 2018), p. 100502. DOI: 10.1103/PhysRevLett.120.100502. URL: https://link.aps.org/doi/10.1103/PhysRevLett.120.100502.

[40] A. Kringhøj et al. “Magnetic-Field-Compatible Superconducting Transmon Qubit”. In: *Phys. Rev. Applied* 15 (5 May 2021), p. 054001. DOI: 10.1103/PhysRevApplied.15.054001. URL: https://link.aps.org/doi/10.1103/PhysRevApplied.15.054001.

[41] Vinay Ambegaokar and Alexis Baratoff. “Tunneling Between Superconductors”. In: *Phys. Rev. Lett.* 10 (11 June 1963), pp. 486–489. DOI: 10.1103/PhysRevLett.10.486.

[42] J M Kreikebaum, K P O’Brien, A Morvan, and I Siddiqi. “Improving wafer-scale Josephson junction resistance variation in superconducting quantum coherent circuits”. In: *Superconductor Science and Technology* 33.6 (May 2020), 06LT02. DOI: 10.1088/1361-6668/ab8617. URL: https://doi.org/10.1088/1361-6668/ab8617.

[43] Nandini Muthusubramanian, Alessandro Bruno, Brian Tarasinski, Andreas Fognini, Ronald Hagen, Leonardo Dicarlo, and Nandini Muthusubramanian Team. “Local trimming of transmon qubit frequency by laser annealing of Josephson junctions”. In: *APS March Meeting Abstracts*. Vol. 2019. 2019, B29–015. URL: https://meetings.aps.org/Meeting/MAR19/Session/B29.15.

[44] Jared B Hertzberg et al. “Laser-annealing Josephson junctions for yielding scaled-up superconducting quantum processors”. In: *npj Quantum Inf* 7.1 (2021), pp. 1–8. URL: https://rdcu.be/cF5hJ.

[45] Frank Arute et al. “Quantum supremacy using a programmable superconducting processor”. In: *Nature* 574.7779 (2019), pp. 505–510. DOI: https://doi.org/10.1038/s41586-019-1666-5. URL: https://www.nature.com/articles/s41586-019-1666-5.

[46] C. Macklin et al. “A near–quantum-limited Josephson traveling-wave parametric amplifier”. In: *Science* 350.6258 (2015), pp. 307–310. URL: https://science.sciencemag.org/content/350/6258/307.

[47] AA Clerk, KW Lehnert, P Bertet, JR Petta, and Y Nakamura. “Hybrid quantum systems with circuit quantum electrodynamics”. In: *Nat. Phys.* 16.3 (2020), pp. 257–267. URL: https://www.nature.com/articles/s41567-020-0797-9.

[48] John Clarke and Alex I Braginski. *The SQUID handbook: Applications of SQUIDs and SQUID systems*. John Wiley & Sons, 2006.

[49] L. DiCarlo et al. “Demonstration of two-qubit algorithms with a superconducting quantum processor”. In: *Nature* 460 (2009), p. 240. URL: https://www.nature.com/articles/nature08121.

[50] Yu Chen et al. “Qubit Architecture with High Coherence and Fast Tunable Coupling”. In: *Phys. Rev. Lett.* 113 (22 Nov. 2014), p. 220502. DOI: 10.1103/PhysRevLett.113.220502. URL: https://link.aps.org/doi/10.1103/PhysRevLett.113.220502.

[51] Matthew Reagor et al. “Demonstration of universal parametric entangling gates on a multi-qubit lattice”. In: *Science Advances* 4.2 (2018). URL: https://advances.sciencemag.org/content/4/2/eaao3603.

[52] Lei Chen, Wolfgang Wernsdorfer, Christos Lampropoulos, George Christou, and Irinel Chiorescu. “On-chip SQUID measurements in the presence of high magnetic fields”. In: *Nanotechnology* 21.40 (2010), p. 405504.

[53] BH Schneider, S Etaki, HSJ Van Der Zant, and GA Steele. “Coupling carbon nanotube mechanics to a superconducting circuit”. In: *Scientific reports* 2.1 (2012), pp. 1–5. URL: https://www.nature.com/articles/srep00599.

[54] K. E. Khosla, M. R. Vanner, N. Ares, and E. A. Laird. “Displacemon Electromechanics: How to Detect Quantum Interference in a Nanomechanical Resonator”. In: *Phys. Rev. X* 8 (2 May 2018), p. 021052. DOI: 10.1103/PhysRevX.8.021052. URL: https://link.aps.org/doi/10.1103/PhysRevX.8.021052.

[55] IC Rodrigues, D Bothner, and GA Steele. “Coupling microwave photons to a mechanical resonator using quantum interference”. In: *Nat Commun* 10.1 (2019), pp. 1–7. URL: https://doi.org/10.1038/s41467-019-12964-2.

[56] Marios Kounalakis, Yaroslav M Blanter, and Gary A Steele. “Synthesizing multi-phonon quantum superposition states using flux-mediated three-body interactions with superconducting qubits”. In: *npj Quantum Inf* 5.1 (2019), pp. 1–7. URL: https://www.nature.com/articles/s41534-019-0219-y.

[57] Philip Schmidt, Mohammad T Amawi, Stefan Pogorzalek, Frank Deppe, Achim Marx, Rudolf Gross, and Hans Huebl. “Sideband-resolved resonator electromechanics based on a nonlinear Josephson inductance probed on the single-photon level”. In: *Communications Physics* 3.1 (2020), pp. 1–7. URL: https://www.nature.com/articles/s42005-020-00501-3.

[58] Tanmoy Bera, Sourav Majumder, Sudhir Kumar Sahu, and Vibhor Singh. “Large flux-mediated coupling in hybrid electromechanical system with a transmon qubit”. In: *Communications Physics* 4.1 (2021), pp. 1–7. URL: https://www.nature.com/articles/s42005-020-00514-y.

[59] Thomas Luschmann, Philip Schmidt, Frank Deppe, Achim Marx, Alvaro Sanchez, Rudolf Gross, and Hans Huebl. “Mechanical frequency control in inductively coupled electromechanical systems”. In: *Scientific Reports* 12.1 (Jan. 2022), p. 1608. URL: https://doi.org/10.1038/s41598-022-05438-x.

[60] N. Samkharadze et al. “Strong spin-photon coupling in silicon”. In: *Science* 359.6380 (2018), pp. 1123–1127. DOI: 10.1126/science.aar4054. URL: https://science.sciencemag.org/content/359/6380/1123.

[61] Xiao Mi, Mónica Benito, Stefan Putz, David M Zajac, Jacob M Taylor, Guido Burkard, and Jason R Petta. “A coherent spin–photon interface in silicon”. In: *Nature* 555.7698 (2018), pp. 599–603. URL: https://www.nature.com/articles/nature25769.

[62] N. Samkharadze, A. Bruno, P. Scarlino, G. Zheng, D. P. DiVincenzo, L. DiCarlo, and L. M. K. Vandersypen. “High-Kinetic-Inductance Superconducting Nanowire Resonators for Circuit QED in a Magnetic Field”. In: *Phys. Rev. Applied* 5 (4 Apr. 2016), p. 044004. DOI: 10.1103/PhysRevApplied.5.044004. URL: https://link.aps.org/doi/10.1103/PhysRevApplied.5.044004.

[63] J. G. Kroll et al. “Magnetic-Field-Resilient Superconducting Coplanar-Waveguide Resonators for Hybrid Circuit Quantum Electrodynamics Experiments”. In: *Phys. Rev. Applied* 11 (6 June 2019), p. 064053. URL: https://link.aps.org/doi/10.1103/PhysRevApplied.11.064053.

[64] K Borisov et al. “Superconducting granular aluminum resonators resilient to magnetic fields up to 1 Tesla”. In: *Appl. Phys. Lett.* 117.12 (2020), p. 120502. URL: https://aip.scitation.org/doi/10.1063/5.0018012.

[65] Marta Pita-Vidal et al. “Gate-Tunable Field-Compatible Fluxonium”. In: *Phys. Rev. Applied* 14 (6 Dec. 2020), p. 064038. DOI: 10.1103/PhysRevApplied.14.064038. URL: https://link.aps.org/doi/10.1103/PhysRevApplied.14.064038.

[66] Patrick Winkel et al. “Implementation of a Transmon Qubit Using Superconducting Granular Aluminum”. In: *Phys. Rev. X* 10 (3 Aug. 2020), p. 031032. DOI: 10.1103/PhysRevX.10.031032. URL: https://link.aps.org/doi/10.1103/PhysRevX.10.031032.

[67] Matthias Mergenthaler et al. “Circuit Quantum Electrodynamics with Carbon-Nanotube-Based Superconducting Quantum Circuits”. In: *Phys. Rev. Applied* 15 (6 June 2021), p. 064050. DOI: 10.1103/PhysRevApplied.15.064050. URL: https://link.aps.org/doi/10.1103/PhysRevApplied.15.064050.

[68] Andre Schneider, Tim Wolz, Marco Pfirrmann, Martin Spiecker, Hannes Rotzinger, Alexey V. Ustinov, and Martin Weides. “Transmon qubit in a magnetic field: Evolution of coherence and transition frequency”. In: *Phys. Rev. Research* 1 (2 Sept. 2019), p. 023003.

DOI: 10.1103/PhysRevResearch.1.023003. URL: https://link.aps.org/doi/10.1103/PhysRevResearch.1.023003.

[69] Hanhee Paik et al. "Observation of High Coherence in Josephson Junction Qubits Measured in a Three-Dimensional Circuit QED Architecture". In: *Phys. Rev. Lett.* 107 (24 Dec. 2011), p. 240501. DOI: 10.1103/PhysRevLett.107.240501. URL: https://link.aps.org/doi/10.1103/PhysRevLett.107.240501.

[70] Chad Rigetti et al. "Superconducting qubit in a waveguide cavity with a coherence time approaching 0.1 ms". In: *Phys. Rev. B* 86 (10 Sept. 2012), 100506(R). DOI: 10.1103/PhysRevB.86.100506. URL: https://link.aps.org/doi/10.1103/PhysRevB.86.100506.

[71] Abdufarrukh A Abdumalikov Jr, Johannes M Fink, Kristinn Juliusson, Marek Pechal, Simon Berger, Andreas Wallraff, and Stefan Filipp. "Experimental realization of non-Abelian non-adiabatic geometric gates". In: *Nature* 496.7446 (2013), pp. 482–485. URL: https://www.nature.com/articles/nature12010.

[72] G. J. Dolan. "Offset masks for lift-off photoprocessing". In: *Applied Physics Letters* 31.5 (1977), pp. 337–339. URL: https://doi.org/10.1063/1.89690.

[73] For this thesis, the supplemental material is included to the appendix of the respective chapter and provides experimental details and additional data and analysis supporting the claims in the chapter's main text.

[74] Chen Wang et al. "Measurement and control of quasiparticle dynamics in a superconducting qubit". In: *Nat Commun* 5.1 (2014), p. 5836. DOI: 10.1038/ncomms6836.

[75] Jaseung Ku, Zack Yoscovits, Alex Levchenko, James Eckstein, and Alexey Bezryadin. "Decoherence and radiation-free relaxation in Meissner transmon qubit coupled to Abrikosov vortices". In: *Phys. Rev. B* 94 (16 Oct. 2016), p. 165128. DOI: 10.1103/PhysRevB.94.165128. URL: https://link.aps.org/doi/10.1103/PhysRevB.94.165128.

[76] M. D. Hutchings et al. "Tunable Superconducting Qubits with Flux-Independent Coherence". In: *Phys. Rev. Applied* 8 (4 Oct. 2017), p. 044003. DOI: 10.1103/PhysRevApplied.8.044003. URL: https://link.aps.org/doi/10.1103/PhysRevApplied.8.044003.

[77] Florian Lüthi. "Circuit Quantum Electrodynamics in a Magnetic Field". PhD thesis. Delft University of Technology, 2019. URL: https://doi.org/10.4233/uuid:5986ee2b-e9e6-42ed-a932-bddd5e78648e.

[78] A Potts, GJ Parker, JJ Baumberg, and PAJ de Groot. "CMOS compatible fabrication methods for submicron Josephson junction qubits". In: *IEE Proceedings-Science, Measurement and Technology* 148.5 (2001), pp. 225–228. URL: https://www.np.phy.cam.ac.uk/uploads/2001/ieee01-submicronjj.pdf.

[79] X. Wu, J. L. Long, H. S. Ku, R. E. Lake, M. Bal, and D. P. Pappas. "Overlap junctions for high coherence superconducting qubits". In: *Applied Physics Letters* 111.3 (2017), p. 032602. URL: https://doi.org/10.1063/1.4993937.

[80] Willemijn Uilhoorn et al. “Quasiparticle trapping by orbital effect in a hybrid superconducting-semiconducting circuit”. In: *arXiv:2105.11038* (2021). URL: https://arxiv.org/abs/2105.11038.

[81] P. Kumar et al. “Origin and Reduction of $1/f$ Magnetic Flux Noise in Superconducting Devices”. In: *Phys. Rev. Applied* 6 (4 Oct. 2016), 041001(R). URL: https://link.aps.org/doi/10.1103/PhysRevApplied.6.041001.

[82] G. Catelani, X. S. Wu, and P. W. Adams. “Fermi-liquid effects in the gapless state of marginally thin superconducting films”. In: *Phys. Rev. B* 78 (10 Sept. 2008), p. 104515. URL: https://link.aps.org/doi/10.1103/PhysRevB.78.104515.

[83] D. Bothner, T. Gaber, M. Kemmler, D. Koelle, R. Kleiner, S. Wünsch, and M. Siegel. “Magnetic hysteresis effects in superconducting coplanar microwave resonators”. In: *Phys. Rev. B* 86 (1 July 2012), p. 014517. DOI: 10.1103/PhysRevB.86.014517. URL: https://link.aps.org/doi/10.1103/PhysRevB.86.014517.

[84] C. Song et al. “Microwave response of vortices in superconducting thin films of Re and Al”. In: *Phys. Rev. B* 79 (17 May 2009), p. 174512. DOI: 10.1103/PhysRevB.79.174512. URL: https://link.aps.org/doi/10.1103/PhysRevB.79.174512.

[85] Gheorghe Stan, Stuart B. Field, and John M. Martinis. “Critical Field for Complete Vortex Expulsion from Narrow Superconducting Strips”. In: *Phys. Rev. Lett.* 92 (9 Mar. 2004), p. 097003. DOI: 10.1103/PhysRevLett.92.097003. URL: https://link.aps.org/doi/10.1103/PhysRevLett.92.097003.

[86] N. Pompeo and E. Silva. “Reliable determination of vortex parameters from measurements of the microwave complex resistivity”. In: *Phys. Rev. B* 78 (9 Sept. 2008), p. 094503. URL: https://link.aps.org/doi/10.1103/PhysRevB.78.094503.

[87] B Chiaro et al. “Dielectric surface loss in superconducting resonators with flux-trapping holes”. In: *Superconductor Science and Technology* 29.10 (Aug. 2016), p. 104006. URL: https://doi.org/10.1088/0953-2048/29/10/104006.

[88] Jonas Bylander et al. “Noise spectroscopy through dynamical decoupling with a superconducting flux qubit”. In: *Nat. Phys.* 7.7 (May 2011), pp. 565–570. ISSN: 1745-2473. URL: http://dx.doi.org/10.1038/nphys1994.

[89] Chen Wang et al. “Surface participation and dielectric loss in superconducting qubits”. In: *Applied Physics Letters* 107.16 (2015), p. 162601. URL: https://aip.scitation.org/doi/abs/10.1063/1.4934486.

[90] J. Bardeen, L. N. Cooper, and J. R. Schrieffer. “Theory of Superconductivity”. In: *Phys. Rev.* 108 (5 Dec. 1957), pp. 1175–1204. URL: https://link.aps.org/doi/10.1103/PhysRev.108.1175.

[91] Gianluigi Catelani, Robert J Schoelkopf, Michel H Devoret, and Leonid I Glazman. “Relaxation and frequency shifts induced by quasiparticles in superconducting qubits”. In: *Phys. Rev. B* 84.6 (2011), p. 064517. URL: https://journals.aps.org/prb/abstract/10.1103/PhysRevB.84.064517.

[92] A. A. Clerk and D. Wahyu Utami. "Using a qubit to measure photon-number statistics of a driven thermal oscillator". In: *Phys. Rev. A* 75 (4 Apr. 2007), p. 042302. URL: https://link.aps.org/doi/10.1103/PhysRevA.75.042302.

[93] J. G. Kroll. "Magnetic field compatible hybrid circuit quantum electrodynamics". PhD thesis. Delft University of Technology, 2019. URL: https://doi.org/10.4233/uuid:d72c0db9-8463-4098-a796-457aaa88eaa3.

[94] Sebastian Krinner et al. "Engineering cryogenic setups for 100-qubit scale superconducting circuit systems". In: *EPJ Quantum Technology* 6.1 (2019), p. 2. URL: https://epjquantumtechnology.springeropen.com/articles/10.1140/epjqt/s40507-019-0072-0.

[95] BL Al'Tshuler, AG Aronov, and BZ Spivak. "The Aaronov-Bohm effect in disordered conductors". In: *ZhETF Pisma Redaktsiiu* 33 (1981), p. 101. URL: http://jetpletters.ru/ps/1501/article_22943.shtml.

[96] M. Gijs, C. Van Haesendonck, and Y. Bruynseraede. "Quantum oscillations in the superconducting fluctuation regime of cylindrical A1 films". In: *Phys. Rev. B* 30 (5 Sept. 1984), pp. 2964–2967. DOI: 10.1103/PhysRevB.30.2964. URL: https://link.aps.org/doi/10.1103/PhysRevB.30.2964.

[97] V. Chandrasekhar, M. J. Rooks, S. Wind, and D. E. Prober. "Observation of Aharonov-Bohm Electron Interference Effects with Periods $\frac{h}{e}$ and $\frac{h}{2e}$ in Individual Micron-Size, Normal-Metal Rings". In: *Phys. Rev. Lett.* 55 (15 Oct. 1985), pp. 1610–1613. DOI: 10.1103/PhysRevLett.55.1610. URL: https://link.aps.org/doi/10.1103/PhysRevLett.55.1610.

[98] F. Pierre, A. B. Gougam, A. Anthore, H. Pothier, D. Esteve, and Norman O. Birge. "Dephasing of electrons in mesoscopic metal wires". In: *Phys. Rev. B* 68 (8 Aug. 2003), p. 085413. DOI: 10.1103/PhysRevB.68.085413. URL: https://link.aps.org/doi/10.1103/PhysRevB.68.085413.

[99] Efrat Shimshoni, Paul M. Goldbart, and Nigel Goldenfeld. "Josephson interference phenomena above T_c". In: *Phys. Rev. B* 48 (13 Oct. 1993), pp. 9865–9868. DOI: 10.1103/PhysRevB.48.9865. URL: https://link.aps.org/doi/10.1103/PhysRevB.48.9865.

[100] Dennis Willsch et al. "Observation of Josephson Harmonics in Tunnel Junctions". In: *Nat. Phys.* (2024). URL: https://doi.org/10.1038/s41567-024-02400-8.

[101] Morten Kjaergaard, Mollie E. Schwartz, Jochen Braumüller, Philip Krantz, Joel I.-J. Wang, Simon Gustavsson, and William D. Oliver. "Superconducting Qubits: Current State of Play". In: *Annu. Rev. Condens. Matter Phys.* 11.1 (2020), pp. 369–395. URL: https://doi.org/10.1146/annurev-conmatphys-031119-050605.

[102] Alexander PM Place et al. "New material platform for superconducting transmon qubits with coherence times exceeding 0.3 milliseconds". In: *Nat Commun* 12.1 (2021), p. 1779. URL: https://doi.org/10.1038/s41467-021-22030-5.

[103] K. Serniak et al. “Hot Nonequilibrium Quasiparticles in Transmon Qubits”. In: *Phys. Rev. Lett.* 121 (15 Oct. 2018), p. 157701. DOI: 10.1103/PhysRevLett.121.157701. URL: https://link.aps.org/doi/10.1103/PhysRevLett.121.157701.

[104] Matt McEwen et al. “Resolving catastrophic error bursts from cosmic rays in large arrays of superconducting qubits”. In: *Nat. Phys.* 18.1 (2022), pp. 107–111. URL: https://doi.org/10.1038/s41567-021-01432-8.

[105] R.-P. Riwar, A. Hosseinkhani, L. D. Burkhart, Y. Y. Gao, R. J. Schoelkopf, L. I. Glazman, and G. Catelani. “Normal-metal quasiparticle traps for superconducting qubits”. In: *Phys. Rev. B* 94 (10 Sept. 2016), p. 104516. DOI: 10.1103/PhysRevB.94.104516.

[106] Simon Gustavsson et al. “Suppressing relaxation in superconducting qubits by quasiparticle pumping”. In: *Science* 354.6319 (2016), pp. 1573–1577. DOI: 10.1126/science.aah5844. URL: https://www.science.org/doi/abs/10.1126/science.aah5844.

[107] R.-P. Riwar and G. Catelani. “Efficient quasiparticle traps with low dissipation through gap engineering”. In: *Phys. Rev. B* 100 (14 Oct. 2019), p. 144514. DOI: 10.1103/PhysRevB.100.144514.

[108] Matt McEwen et al. “Resisting High-Energy Impact Events through Gap Engineering in Superconducting Qubit Arrays”. In: *Phys. Rev. Lett.* 133 (24 Dec. 2024), p. 240601. DOI: 10.1103/PhysRevLett.133.240601. URL: https://link.aps.org/doi/10.1103/PhysRevLett.133.240601.

[109] Fabio Henriques et al. “Phonon traps reduce the quasiparticle density in superconducting circuits”. In: *Appl. Phys. Lett.* 115.21 (2019), p. 212601. DOI: 10.1063/1.5124967. URL: https://doi.org/10.1063/1.5124967.

[110] V. Iaia et al. “Phonon downconversion to suppress correlated errors in superconducting qubits”. In: *Nat Commun* 13 (1 2022), p. 6425. DOI: 10.1038/s41467-022-33997-0. URL: https://doi.org/10.1038/s41467-022-33997-0.

[111] Xianchuang Pan et al. “Engineering superconducting qubits to reduce quasiparticles and charge noise”. In: *Nat Commun* 13 (1 2022), p. 7196. DOI: 10.1038/s41467-022-34727-2. URL: https://doi.org/10.1038/s41467-022-34727-2.

[112] R. T. Gordon et al. “Environmental radiation impact on lifetimes and quasiparticle tunneling rates of fixed-frequency transmon qubits”. In: *Appl. Phys. Lett.* 120.7 (Feb. 2022), p. 074002. ISSN: 0003-6951. DOI: 10.1063/5.0078785. URL: https://doi.org/10.1063/5.0078785.

[113] Antti P Vepsäläinen et al. “Impact of ionizing radiation on superconducting qubit coherence”. In: *Nature* 584.7822 (2020), pp. 551–556. URL: https://doi.org/10.1038/s41586-020-2619-8.

[114] Laura Cardani et al. “Reducing the impact of radioactivity on quantum circuits in a deep-underground facility”. In: *Nat Commun* 12.1 (2021), p. 2733. URL: https://doi.org/10.1038/s41467-021-23032-z.

[115] J. Krause et al. “Magnetic Field Resilience of Three-Dimensional Transmons with Thin-Film Al/AlO_x/Al Josephson Junctions Approaching 1 T”. In: *Phys. Rev. Applied* 17 (3 Mar. 2022), p. 034032. DOI: 10.1103/PhysRevApplied.17.034032. URL: https://link.aps.org/doi/10.1103/PhysRevApplied.17.034032.

[116] D. Ristè, C. C. Bultink, M. J. Tiggelman, R. N. Schouten, K. W. Lehnert, and L. DiCarlo. “Millisecond charge-parity fluctuations and induced decoherence in a superconducting transmon qubit”. In: *Nat. Commun.* 4 (2013), p. 1913. URL: https://doi.org/10.1038/ncomms2936.

[117] C Kurter et al. “Quasiparticle tunneling as a probe of Josephson junction barrier and capacitor material in superconducting qubits”. In: *npj Quantum Inf* 8.1 (2022), p. 31. URL: https://doi.org/10.1038/s41534-022-00542-2.

[118] Daniel M. Tennant et al. “Low-Frequency Correlated Charge-Noise Measurements Across Multiple Energy Transitions in a Tantalum Transmon”. In: *PRX Quantum* 3 (3 July 2022), p. 030307. DOI: 10.1103/PRXQuantum.3.030307. URL: https://link.aps.org/doi/10.1103/PRXQuantum.3.030307.

[119] Thomas Connolly et al. “Coexistence of Nonequilibrium Density and Equilibrium Energy Distribution of Quasiparticles in a Superconducting Qubit”. In: *Phys. Rev. Lett.* 132 (21 May 2024), p. 217001. DOI: 10.1103/PhysRevLett.132.217001. URL: https://link.aps.org/doi/10.1103/PhysRevLett.132.217001.

[120] Giampiero Marchegiani, Luigi Amico, and Gianluigi Catelani. “Quasiparticles in Superconducting Qubits with Asymmetric Junctions”. In: *PRX Quantum* 3 (4 Dec. 2022), p. 040338. DOI: 10.1103/PRXQuantum.3.040338. URL: https://link.aps.org/doi/10.1103/PRXQuantum.3.040338.

[121] K. Serniak et al. “Direct Dispersive Monitoring of Charge Parity in Offset-Charge-Sensitive Transmons”. In: *Phys. Rev. Applied* 12 (1 July 2019), p. 014052. DOI: 10.1103/PhysRevApplied.12.014052. URL: https://link.aps.org/doi/10.1103/PhysRevApplied.12.014052.

[122] A. A. Houck et al. “Controlling the Spontaneous Emission of a Superconducting Transmon Qubit”. In: *Phys. Rev. Lett.* 101 (8 Aug. 2008), p. 080502. DOI: 10.1103/PhysRevLett.101.080502. URL: https://link.aps.org/doi/10.1103/PhysRevLett.101.080502.

[123] B. G. Christensen et al. “Anomalous charge noise in superconducting qubits”. In: *Phys. Rev. B* 100 (14 Oct. 2019), p. 140503. DOI: 10.1103/PhysRevB.100.140503. URL: https://link.aps.org/doi/10.1103/PhysRevB.100.140503.

[124] Peter Fulde. “High field superconductivity in thin films”. In: *Adv. Phys.* 22.6 (1973), pp. 667–719. DOI: 10.1080/00018737300101369. URL: https://doi.org/10.1080/00018737300101369.

[125] R. Meservey and P.M. Tedrow. “Spin-polarized electron tunneling”. In: *Phys. Rep.* 238.4 (1994), pp. 173–243. ISSN: 0370-1573. DOI: https://doi.org/10.1016/0370-1573(94)90105-8. URL: https://www.sciencedirect.com/science/article/pii/0370157394901058.

[126] P. Chubov, V. Eremenko, and Y. A. Pilipenko. “Dependence of the critical temperature and energy gap on the thickness of superconducting aluminum films”. In: *Sov. Phys. JETP* 28 (1969), p. 389. URL: http://jetp.ras.ru/cgi-bin/e/index/e/28/3/p389?a=list.

[127] R. Meservey and P. M. Tedrow. “Properties of Very Thin Aluminum Films”. In: *J. Appl. Phys.* 42.1 (1971), pp. 51–53. DOI: 10.1063/1.1659648. URL: https://doi.org/10.1063/1.1659648.

[128] G. Catelani. “Parity switching and decoherence by quasiparticles in single-junction transmons”. In: *Phys. Rev. B* 89 (9 Mar. 2014), p. 094522. DOI: 10.1103/PhysRevB.89.094522. URL: http://link.aps.org/doi/10.1103/PhysRevB.89.094522.

[129] M. Houzet, K. Serniak, G. Catelani, M. H. Devoret, and L. I. Glazman. “Photon-Assisted Charge-Parity Jumps in a Superconducting Qubit”. In: *Phys. Rev. Lett.* 123 (10 Sept. 2019), p. 107704. DOI: 10.1103/PhysRevLett.123.107704. URL: https://link.aps.org/doi/10.1103/PhysRevLett.123.107704.

[130] P.B. Fischer and G. Catelani. “Nonequilibrium quasiparticle distribution in superconducting resonators: Effect of pair-breaking photons”. In: *SciPost Phys.* 17 (2024), p. 070. DOI: 10.21468/SciPostPhys.17.3.070. URL: https://scipost.org/10.21468/SciPostPhys.17.3.070.

[131] David J Van Woerkom, Attila Geresdi, and Leo P Kouwenhoven. “One minute parity lifetime of a NbTiN Cooper-pair transistor”. In: *Nat. Phys.* 11.7 (2015), pp. 547–550. URL: https://doi.org/10.1038/nphys3342.

[132] O Rafferty, S Patel, CH Liu, S Abdullah, CD Wilen, DC Harrison, and R McDermott. “Spurious antenna modes of the transmon qubit”. In: *arXiv:2103.06803* (2021). URL: https://arxiv.org/pdf/2103.06803.pdf.

[133] C. H. Liu et al. “Quasiparticle Poisoning of Superconducting Qubits from Resonant Absorption of Pair-Breaking Photons”. In: *Phys. Rev. Lett.* 132 (1 Jan. 2024), p. 017001. DOI: 10.1103/PhysRevLett.132.017001.

[134] Jens Hedegaard Nielsen et al. *QCoDeS/Qcodes: QCoDeS 0.43.0*. Version v0.43.0. Jan. 2024. DOI: 10.5281/zenodo.10459033. URL: https://doi.org/10.5281/zenodo.10459033.

[135] Michiel Adriaan Rol et al. “Quantify: An open-source framework for operating quantum computers in the NISQ era”. In: *APS March Meeting Abstracts*. Vol. 2021. 2021, pp. M34–001. URL: https://ui.adsabs.harvard.edu/abs/2021APS..MARM34001R/abstract.

[136] Damien Crielaard et al. “Quantify-scheduler: An open-source hybrid compiler for operating quantum computers in the NISQ era”. In: *APS March Meeting Abstracts*. Vol. 2022. 2022, Q36–010. URL: https://ui.adsabs.harvard.edu/abs/2022APS..MARQ36010C/abstract.

[137] J.R. Johansson, P.D. Nation, and Franco Nori. "QuTiP 2: A Python framework for the dynamics of open quantum systems". In: *Comput. Phys. Commun.* 184.4 (Apr. 2013), pp. 1234–1240. DOI: 10.1016/j.cpc.2012.11.019. URL: https://doi.org/10.1016%2Fj.cpc.2012.11.019.

[138] R. Weiss et al. *hmmlearn python package - Hidden Markov Models in Python, with scikit-learn like API.* https://github.com/hmmlearn/hmmlearn.

[139] F. Motzoi, J. M. Gambetta, P. Rebentrost, and F. K. Wilhelm. "Simple Pulses for Elimination of Leakage in Weakly Nonlinear Qubits". In: *Phys. Rev. Lett.* 103 (11 Sept. 2009), p. 110501. DOI: 10.1103/PhysRevLett.103.110501. URL: https://link.aps.org/doi/10.1103/PhysRevLett.103.110501.

[140] J. M. Chow, L. DiCarlo, J. M. Gambetta, F. Motzoi, L. Frunzio, S. M. Girvin, and R. J. Schoelkopf. "Optimized driving of superconducting artificial atoms for improved single-qubit gates". In: *Phys. Rev. A* 82 (4 Oct. 2010), p. 040305. DOI: 10.1103/PhysRevA.82.040305. URL: https://link.aps.org/doi/10.1103/PhysRevA.82.040305.

[141] M. Reed. "Entanglement and quantum error correction with superconducting qubits". PhD Dissertation. Yale University, 2013.

[142] O. A. E. Cherney and J. Shewchun. "Enhancement of superconductivity in thin aluminium films". In: *Can. J. Phys.* 47.10 (1969), pp. 1101–1106. DOI: 10.1139/p69-138. URL: https://doi.org/10.1139/p69-138.

[143] A. Barone and G. Paternò. *Physics and applications of the Josephson effect.* Wiley, New York, 1982.

[144] D. Ristè, S. Poletto, M. -Z. Huang, A. Bruno, V. Vesterinen, O. -P. Saira, and L. DiCarlo. "Detecting bit-flip errors in a logical qubit using stabilizer measurements". In: *Nat Commun* 6 (2015), p. 6983. DOI: 10.1038/ncomms7983. URL: https://doi.org/10.1038/ncomms7983.

[145] U. Vool et al. "Non-Poissonian Quantum Jumps of a Fluxonium Qubit due to Quasiparticle Excitations". In: *Phys. Rev. Lett.* 113 (24 Dec. 2014), p. 247001. DOI: 10.1103/PhysRevLett.113.247001. URL: https://link.aps.org/doi/10.1103/PhysRevLett.113.247001.

[146] Leonid Glazman and Gianluigi Catelani. "Bogoliubov quasiparticles in superconducting qubits". In: *SciPost Phys. Lect. Notes* 31 (2021). URL: https://doi.org/10.21468/SciPostPhysLectNotes.31.

[147] Michael J. Peterer et al. "Coherence and Decay of Higher Energy Levels of a Superconducting Transmon Qubit". In: *Phys. Rev. Lett.* 114 (1 Jan. 2015), p. 010501. DOI: 10.1103/PhysRevLett.114.010501. URL: http://link.aps.org/doi/10.1103/PhysRevLett.114.010501.

[148] A. Morvan et al. "Qutrit Randomized Benchmarking". In: *Phys. Rev. Lett.* 126 (21 May 2021), p. 210504. DOI: 10.1103/PhysRevLett.126.210504. URL: https://link.aps.org/doi/10.1103/PhysRevLett.126.210504.

[149] Timm Fabian Mörstedt et al. “Rapid on-demand generation of thermal states in superconducting quantum circuits”. In: *arXiv:2402.09594* (2024). URL: http://arxiv.org/abs/2402.09594.

[150] Aidar Sultanov, Marko Kuzmanović, Andrey V. Lebedev, and Gheorghe Sorin Paraoanu. “Protocol for temperature sensing using a three-level transmon circuit”. In: *Appl. Phys. Lett.* 119.14 (Oct. 2021), p. 144002. ISSN: 0003-6951. DOI: 10.1063/5.0065224. URL: https://doi.org/10.1063/5.0065224.

[151] G. E. Blonder, M. Tinkham, and T. M. Klapwijk. “Transition from metallic to tunneling regimes in superconducting microconstrictions: Excess current, charge imbalance, and supercurrent conversion”. In: *Phys. Rev. B* 25 (7 Apr. 1982), pp. 4515–4532. DOI: 10.1103/PhysRevB.25.4515. URL: https://link.aps.org/doi/10.1103/PhysRevB.25.4515.

[152] Felix Münning et al. “Quantum confinement of the Dirac surface states in topological-insulator nanowires”. In: *Nature Communications* 12.1 (Feb. 2021). ISSN: 2041-1723. DOI: 10.1038/s41467-021-21230-3. URL: http://dx.doi.org/10.1038/s41467-021-21230-3.

[153] Oliver Breunig and Yoichi Ando. “Opportunities in topological insulator devices”. In: *Nature Reviews Physics* 4.3 (Jan. 2022), pp. 184–193. ISSN: 2522-5820. DOI: 10.1038/s42254-021-00402-6. URL: http://dx.doi.org/10.1038/s42254-021-00402-6.

[154] Matthias Rößler et al. “Top-Down Fabrication of Bulk-Insulating Topological Insulator Nanowires for Quantum Devices”. In: *Nano Letters* 23.7 (Mar. 2023), pp. 2846–2853. ISSN: 1530-6992. DOI: 10.1021/acs.nanolett.3c00169. URL: http://dx.doi.org/10.1021/acs.nanolett.3c00169.

[155] Jakob Schluck, Ella Nikodem, Anton Montag, Alexander Ziesen, Mahasweta Bagchi, Fabian Hassler, and Yoichi Ando. *Protected gap closing and reopening in topological-insulator Josephson junctions*. 2024. arXiv: 2406.08265 [cond-mat.supr-con].

[156] Wolfgang Himmler et al. “Supercurrent interference in HgTe-wire Josephson junctions”. In: *Phys. Rev. Res.* 5 (4 Oct. 2023), p. 043021. DOI: 10.1103/PhysRevResearch.5.043021. URL: https://link.aps.org/doi/10.1103/PhysRevResearch.5.043021.

[157] Patrick Zellekens et al. *Flux-periodic supercurrent oscillations in an Aharonov-Bohm-type nanowire Josephson junction*. 2024. arXiv: 2402.13880 [cond-mat.mes-hall].

[158] Tobias W. Schmitt et al. “Integration of Topological Insulator Josephson Junctions in Superconducting Qubit Circuits”. In: *Nano Letters* 22.7 (Mar. 2022), pp. 2595–2602. ISSN: 1530-6992. DOI: 10.1021/acs.nanolett.1c04055. URL: http://dx.doi.org/10.1021/acs.nanolett.1c04055.

[159] Xiaopei Sun et al. “Realization of superconducting transmon qubits based on topological insulator nanowires”. In: *Applied Physics Letters* 122.15 (Apr. 2023), p. 154001. ISSN: 0003-6951. DOI: 10.1063/5.0140079. eprint: https://pubs.aip.org/aip/apl/

article-pdf/doi/10.1063/5.0140079/16821343/154001_1_5.0140079.pdf. URL: https://doi.org/10.1063/5.0140079.

[160] Felix E. Schmidt, Mark D. Jenkins, Kenji Watanabe, Takashi Taniguchi, and Gary A. Steele. "A ballistic graphene superconducting microwave circuit". In: *Nature Communications* 9.1 (Oct. 2018). ISSN: 2041-1723. DOI: 10.1038/s41467-018-06595-2. URL: http://dx.doi.org/10.1038/s41467-018-06595-2.

[161] W. Chang, S. M. Albrecht, T. S. Jespersen, F. Kuemmeth, P. Krogstrup, J. Nygård, and C. M. Marcus. "Hard gap in epitaxial semiconductor–superconductor nanowires". In: *Nature Nanotechnology* 10.3 (Jan. 2015), pp. 232–236. ISSN: 1748-3395. DOI: 10.1038/nnano.2014.306. URL: http://dx.doi.org/10.1038/nnano.2014.306.

[162] Mengmeng Bai et al. "Novel self-epitaxy for inducing superconductivity in the topological insulator $(Bi_{1-x}Sb_x)_2Te_3$". In: *Phys. Rev. Mater.* 4 (9 Sept. 2020), p. 094801. DOI: 10.1103/PhysRevMaterials.4.094801. URL: https://link.aps.org/doi/10.1103/PhysRevMaterials.4.094801.

[163] Mengmeng Bai et al. "Proximity-induced superconductivity in $(Bi_{1-x}Sb_x)_2Te_3$ topological-insulator nanowires". In: *Communications Materials* 3.1 (Apr. 2022). ISSN: 2662-4443. DOI: 10.1038/s43246-022-00242-6. URL: http://dx.doi.org/10.1038/s43246-022-00242-6.

[164] E. Nikodem, J. Schluck, H. Legg, M. Bagchi, J. Klinovaja, D Loss, and Y. Ando. *Anomalous Little-Parks effect in proximitized topological-insulator nanowires.* in preparation (2024).

[165] M. L. Della Rocca, M. Chauvin, B. Huard, H. Pothier, D. Esteve, and C. Urbina. "Measurement of the Current-Phase Relation of Superconducting Atomic Contacts". In: *Phys. Rev. Lett.* 99 (12 Sept. 2007), p. 127005. DOI: 10.1103/PhysRevLett.99.127005. URL: https://link.aps.org/doi/10.1103/PhysRevLett.99.127005.

[166] Jorge Cayao, Pablo San-Jose, Annica M. Black-Schaffer, Ramón Aguado, and Elsa Prada. "Majorana splitting from critical currents in Josephson junctions". In: *Phys. Rev. B* 96 (20 Nov. 2017), p. 205425. DOI: 10.1103/PhysRevB.96.205425. URL: https://link.aps.org/doi/10.1103/PhysRevB.96.205425.

[167] Harry J. Levinson, F. Greuter, and E. W. Plummer. "Experimental band structure of aluminum". In: *Phys. Rev. B* 27 (2 Jan. 1983), pp. 727–747. DOI: 10.1103/PhysRevB.27.727. URL: https://link.aps.org/doi/10.1103/PhysRevB.27.727.